Chemical reactivity of group 14 $[E_9]^{4-}$ and 15 $[E'_7]^{3-}$ Zintl ions

A thesis submitted in partial fulfilment of the requirements for the degree

Doctor of Philosophy at the University of Oxford

Gabriela Espinoza Quintero

St. Anne's College

Oxford

August 2015

Abstract

Chemical reactivity of group 14 $[E_9]^{4-}$ and 15 $[E'_7]^{3-}$ Zintl ions

Gabriela Espinoza Quintero — Doctor of Philosophy

St. Anne's College — Trinity 2015

This thesis describes the reactivity of Zintl ions of groups 14 $[E_9]^{4-}$ (E = Ge and Sn) and 15 $[E'_7]^{3-}$ (E' = P and As) towards a number or transition, post-transition and main group reagents. The synthesis and characterisation of the resulting novel cluster anions is described herein.

Coordination compounds of group 14 Zintl ions were synthesised when K_4Ge_9 was reacted with $Zn[N(SiMe_3)_2]_2$ to give the simple coordination compound $[Ge_9ZnN(SiMe_3)_2]^{3-}$. The heavier analogue K_4Sn_9 reacts with the same metal precursor to give the paramagnetic species $[Sn_9ZnNSiMe_3]^{3-}$ where a trimethylsilyl group has been lost.

K_4Ge_9 reacts with $[Ru(COD)(\eta^3\text{-}CH_2C(CH_3)CH_2)_2]$ to form the paramagnetic endohedral compound $[Ru@Ge_{12}]^{3-}$ and with $[Co(PEt_2Ph)_2(mes)_2]$ to form the prolate

endohedral compound $[Co_2@Ge_{16}]^{4-}$, which has two metal centres encapsulated inside the sixteen atom germanium cage.

Regarding group 15 Zintl ion reactivity, the reactions between pyridine solutions of $[HP_7]^{2-}$ and $E[N(SiMe_3)_2]_2$ (E = Ge, Sn and Pb) have been found to yield coordination compounds of the type $[P_7E(N(SiMe_3)_2]^{2-}$. The germanium containing species $[P_7GeN(SiMe_3)_2]^{2-}$ quickly decomposes at room temperature to give rise to the thermodynamic product $[(P_7)_2Ge_2N(SiMe_3)_2]^{3-}$, a process that involves the loss of an amide moiety.

Activation products were also synthesised from the reaction of $[E'_7]^{3-}$ with varying stoichiometries of VCp_2. The reaction with 0.7 equivalents of VCp_2 yields the sandwich complexes $[CpV(\eta^5\text{-}E'_5)]^{n-}$ (E' = P: n = 1; E' = As, n = 1 and 2) whereas with 2.5 equivalents the products are the triple-decker sandwich complexes $[(CpV)_2(\eta^x\text{-}E'_x)]^-$ (E' = P: x = 6; E' = As: x = 5).

Acknowledgements

Firstly I want to thank my mum, for her unconditional love and encouragement and the rest of my family, especially my aunt Rocio. Without her help I simply would not have been able to come here.

Thanks to my supervisor, Dr. José Goicoechea, for giving me the opportunity to immerse myself into the Zintl world. Thanks for all his advice and words of wisdom when Zintls were making me feel desperate.

I want to thank all the people who trained me to do all the synthetic work and characterisation techniques: Dr. Market for giving me a new name, Dr. Robert for all the English tips and goat-related chat and Dr. Caroline for the long hours in crystallography. Thanks to all the proof-readers, who probably hate me a little because I can't tell the difference between “this” and “these” and I have no idea how to place a comma. Particularly: Andy for always having a smile on his face to make our days go smoother; Dr. Tom for his thousand different ways of calling out my name and closing with "smells"; Gordy, for his unplanned humour; and to all for the numerous unplanned fun U.C. trips.

I must thank the part II's I supervised. Mike Connolly for his DFT calculations and coming to capoeira, Izzy Paterson-Tayor for her contribution to Chapter 4 and making me laugh, Jack Duckworth who only gave me computational analysis and I didn't even have to supervise him in the lab, and Jamie for being an excellent source of gossip and his additional methods to synthesise polyphosphides.

I want to acknowledge all the people who helped me with this project: Dr. Nick Rees for the NMR help, Colin Sparow and James Wickens for unblocking the mass-spec capillary about a million times, Dr. Will Myers for all the EPR assistance and simulations, Prof. John McGrady for the DFT calculations and Dr. Rémi Trifoin for the help running the electrochemical measurements.

And well, I want thank everyone who I had the fortune to share the lovely S11 with, especially the ones who told me some gossip when I asked for it: Dr. Binbin Zhou, Becca Musgrave, Phil McCullough, Melissa Raybould, Doruk Ergöçmen, Bethan Coulson, Benji Clough, Mikey Geeson, Dave Gillot, Gemma Trott, Lajoy Tucker, Éléonore de la Garanderie, David Lo, Oli Crossley, James Holl, Marcel Schorpp and Dan de la Rosa. Thanks to Girl Talk, Bounce Happy Hardcore, Captain Jack and Neil Young for making us all happier.

Thanks also to the lunch club, Adán, Mido and Pierr for all the burrito-thursdays, momiércoles, ATS etc. trips and hearing me when Zintls were being difficult and when my feelings were not real.

Thanks to CONACyT for the funding.

Last but by no means least, I want to thank Charlie, who not only has been the best partner through my whole DPhil, but as well, helped me with the proof-reading and editing of this thesis, sometimes against my will.

List of Abbreviations

Å	Ångstrom
@	centred
°	degree
°C	degrees Celsius
δ	chemical shift
η	hapticity
μ	bridge
μL	microlitre
15-crown-5	1,4,7,10,13-pentaoxacyclopentadecane
18-crown-6	1,4,7,10,13,16-hexaoxacyclooctadecane
2,2,2-crypt	4,7,13,16,21,24-hexaoxa-1,10-diazabicyclo[8.8.8]hexacosane
A	alkali metal
Ad	adamantyl
^{t}Am	2-methylbutyl
Anal.	Analysis
Anthacenide	$[C_{14}H_9]^-$

Ar	2,6-$mes_2C_6H_3$
Ar'	C_6H_3-2,6-(C_6H_3-2,6-Pr^i_2)$_2$
av	average (mean)
bipy	2,2-bipyridine
Calcd.	calculated
CCD	charge-coupled device
COD	1,5-cyclooctadiene
COSY	correlation spectroscopy
COT	cyclooctatetraene
Cp	cyclopentadienyl
Cp*	pentamethylcyclopentadienyl
CpBIG	(4-n-Bu-C_6H_4)$_5$cyclopentadienyl
CSD	Cambridge Structural Database
CW	continuous wave
d	doublet
DFT	density functional theory
Dipp	2,6-diisopropylphenyl (2,6-$^i Pr_2C_6H_3$)
DMF	*N*,*N*-dimethylformamide
en	ethylenediamine
ESI	electrospray-ionisation
EPR	electron paramagnetic resonance

Et	ethyl
exp	experimental
eV	electronvolt
Fc	ferrocene or ferrocenyl
FT-IR	Fourier transform infrared
g	gram
g	g-factor
G	Gauss
h	hour
Hex	Hexyl
HOMO	highest occupied molecular orbital
Hz	hertz
^{i}Bu	isobutyl
^{i}Pr	isopropyl
I	nuclear spin quantum number
i	ipso
IR	infrared
J	scalar coupling constant
K	Kelvin
KHMDS	potassium bis(trimethylsilyl)amide
kJ	kilojoule

L	ligand
LUMO	lowest occupied molecular orbital
M	molar
m	mass, meta
m	multiplet
Me	methyl
mes	mesityl (2,4,6-$Me_3C_6H_2$)
mg	milligram
mL	millilitre
mol	mole
MS	mass spectrometry
^{n}Bu	n-butyl
nbe	norbornene (bicyclo[2.2.1]hept-2-ene)
NBO	natural bond order
NMR	nuclear magnetic resonance
Norbornene	bicyclo[2,2,1]heptane
^{n}Pr	n-propyl
o	ortho
p	para
Ph	phenyl
ppm	parts per million

py	pyridine
s	singlet
^{s}Bu	*sec*-butyl
SOMO	singly occupied molecular orbital
t	triplet
Ts	tosylate
^{t}Bu	*tert*-butyl
THF	tetrahydrofuran
tol	toluene
Ts	($CH_3C_6H_4SO$)
UV	ultraviolet

Contents

Chapter 1: Introduction 1

1.1 Historical background of Zintl clusters 1

1.2 Structure and bonding 3

1.1.1 $[E_9]^{x-}$: Nine-atom group 14 Zintl ions 3

1.1.2 $[E'_7]^{3-}$: Seven-atom group 15 Zintl ions 6

1.3 Previous solution reactivity 7

1.1.3 Group 14 $[E_9]^{4-}$ Zintl ions 8

1.1.3.1 Oxidative-coupling reactions of group 14 $[E_9]^{4-}$ clusters 8

1.1.3.2 *Exo*-functionalisation and vertex substitution reactions of group 14 $[E_9]^{4-}$ clusters with main group reagents 10

1.1.3.3 *Exo*-functionalisation reactions of group 14 $[E_9]^{4-}$ clusters with organic reagents 12

1.1.3.4 Reactions where the group 14 $[E_9]^{4-}$ clusters act as ligands towards metal centres 14

1.1.3.5 Reactions of group 14 $[E_9]^{4-}$ clusters towards metallic complexes where cluster activation occurs 31

1.3.1.1.1 Functionalised endohedral clusters 32

1.3.1.1.2 Substituent-free endohedral clusters 36

1.1.3.5.1.1 Nine-atom endohedral clusters 36

1.1.3.5.1.2 Ten-atom endohedral clusters 38

1.1.3.5.1.3 Twelve-atom endohedral clusters 40

1.1.3.5.1.4 High-nuclearity endohedral clusters 43

1.3.1.1.3 Non-deltahedral endohedral clusters 49

1.1.4 Group 15 $[E'_7]^{3-}$ Zintl ions 50

1.1.4.1 Oxidative coupling reactions of group 15 $[E'_7]^{3-}$ Zintl ions 50

1.1.4.2 *Exo*-functionalisation of group 15 $[E'_7]^{3-}$ clusters with main group reagents 52

1.1.4.3 *Exo*-functionalisation of group 15 $[E'_7]^{3-}$ clusters with organic fragments 54

1.1.4.4 Reactions where group 15 $[E'_7]^{3-}$ clusters act as ligands towards metals 57

1.3.1.1.4 η^1 coordination of the $[E'_7]^{3-}$ cage 58

1.3.1.1.5 η^2 coordination of the $[E'_7]^{3-}$ cage 59

1.3.1.1.6 η^4 coordination of the $[E'_7]^{3-}$ cage 72

1.1.4.5 Reaction of the group 15 $[E'_7]^{3-}$ clusters towards metal complexes where cluster fragmentation occurs 79

1.4 References 89

Chapter 2: Coordination chemistry of group 14 Zintl ions $[E_9]^{4-}$ 99

2.1 Summary 99

2.2 Introduction 100

2.3 Results and discussion 104

2.3.1 Reactivity of K_4E_9 towards $Zn[N(SiMe_3)_2]_2$ (E = Ge and Sn) 104

2.3.1.1 Synthesis of $[Ge_9ZnN(SiMe_3)_2]^{3-}$ (**1**) 104

2.3.1.2 Structure of $[Ge_9ZnN(SiMe_3)_2]^{3-}$ (**1**) 105

2.3.1.3 NMR spectroscopic studies on $[Ge_9ZnN(SiMe_3)_2]^{3-}$ (**1**) 109

2.3.1.4 Mass spectrometric studies on $[Ge_9ZnN(SiMe_3)_2]^{3-}$ (**1**) 109

2.3.1.5 Synthesis of $[Sn_9ZnNSiMe_3]^{3-}$ (**2**) 111

2.3.1.6 Structure of $[Sn_9ZnNSiMe_3]^{3-}$ (**2**) 112

2.3.1.7 EPR spectroscopic studies on $[Sn_9ZnNSiMe_3]^{3-}$ (**2**) 114

2.3.1.8 Mass spectrometric studies on $[Sn_9ZnNSiMe_3]^{3-}$ (**2**) 115

2.3.1.9 DFT calculations 116

2.3.2 Further reactivity studies 120

2.3.2.1 Reaction of **1** with CsF 120

2.3.2.2 Reaction of **1** with $HNPh_2$ 122

2.4 Conclusions 124

2.5 References 125

Chapter 3 Endohedral group 14 clusters 127

3.1 Summary 127

3.2 Introduction 128

3.3 Results and discussion 134

3.3.1 Reactivity of K_4Ge_9 towards $[Ru(1,5\text{-}COD)(\eta^3\text{-}CH_3C(CH_2)_2)_2]$ 134

3.3.1.1 Synthesis of $[Ru@Ge_{12}]^{3-}$ (**5**) 134

3.3.1.2 Structure of $[Ru@Ge_{12}]^{3-}$ (**5**) 135

3.3.1.3 Mass spectrometric studies on $[Ru@Ge_{12}]^{3-}$ (**5**) 138

3.3.1.4 EPR spectroscopic studies on $[Ru@Ge_{12}]^{3-}$ (**5**) 139

3.3.1.5 DFT calculations on $[Ru@Ge_{12}]^{3-}$ (**5**) 140

3.3.2 Reactivity of K_4Ge_9 towards $[Co(PPhEt_2)_2(mes)_2]$ 144

3.3.2.1 Synthesis of $[Co_2@Ge_{16}]^{4-}$ (**6**) 144

3.3.2.2 Structure of $[Co_2@Ge_{16}]^{4-}$ (**6**) 145

3.3.2.3 Mass spectrometric studies on $[Co_2@Ge_{16}]^{4-}$ (**6**) 145

3.3.2.4 DFT calculations on $[Co_2@Ge_{16}]^{4-}$ (**6**) 146

3.4 Conclusions 149

3.5 References 152

Chapter 4: Coordination chemistry of group 15 Zintl ions $[E'_7]^{3-}$ 155

4.1 Summary 155

4.2 Introduction 156

4.2.1 η^1 coordination of the $[E'_7]^{3-}$ cage 157

4.2.2 η^2 coordination of the $[E'_7]^{3-}$ cage 157

4.2.3 η^4 coordination of the $[E'_7]^{3-}$ cage 163

4.3 Results and discussion 166

4.3.1 Reactivity of $[HP_7]^{2-}$ towards $E[N(SiMe_3)_2]_2$ (E = Ge and Sn) 166

4.3.1.1 Synthesis of $[P_7EN(SiMe_3)_2]^{2-}$ (E = Ge (**7**) and Sn(**8**)) 166

4.3.1.2 Structures of $[P_7EN(SiMe_3)_2]^{2-}$ (E = Ge (**7**) and Sn(**8**)) 167

4.3.1.3 NMR spectroscopic studies on $[P_7EN(SiMe_3)_2]^{2-}$ (E = Ge (**7**) and Sn(**8**)) 171

4.3.1.4 Mass spectrometric studies on $[P_7EN(SiMe_3)_2]^{2-}$ (E = Ge (**7**) and Sn(**8**)) 177

4.3.1.5 Reactions between $[HP_7]^{2-}$ and $Pb[N(SiMe_3)_2]$ 178

4.3.1.6 Reactions between $[HAs_7]^{2-}$ and $E[N(SiMe_3)_2]$ (E = Ge, Sn and Pb) 179

4.3.1.7 Transformation of **7** to $[(P_7)_2Ge_2N(SiMe_3)_2]^{3-}$ (**10**) 180

4.3.1.8 Synthesis of $[(P_7)_2Ge_2N(SiMe_3)_2]^{3-}$ (**10**) 180

4.3.1.9 Structure of $[(P_7)_2Ge_2N(SiMe_3)_2]^{3-}$ (**10**) 181

4.3.1.10 NMR spectroscopic studies on $[(P_7)_2Ge_2N(SiMe_3)_2]^{3-}$ (**10**) 184

4.3.1.11 Mass spectrometric studies on $[(P_7)_2Ge_2N(SiMe_3)_2]^{3-}$ (**10**) 187

4.4 Conclusions 188

4.5 References 188

Chapter 5 Transition metal mediated activation of group 15 $[E'_7]^{3-}$ clusters 191

5.1 Summary 191

5.2 Introduction 191

5.2.1 Cyclic $[E'_5]$ and $[E'_6]$ ligands 194

5.2.1.1 $[E'_5]^-$ ligands 194

5.2.1.1.1 $[E'_5]^-$ sandwich compounds 194

5.2.1.1.2 $[E'_5]^-$ triple-decker compounds 197

5.2.1.2 $[E'_6]$ ligands 199

5.3 Results and discussion 202

5.3.1 Solution reactivity of $[E'_7]^{3-}$ towards VCp_2 (E' = P and As) 202

5.3.1.1 Reactivity of $[K(18\text{-crown-}6)]_3[P_7]$ towards VCp_2 203

5.3.1.1.1 Synthesis of $[CpV(\eta^5\text{-}P_5)]^-$ (**11**) and $[(CpV)_2(\eta^6\text{-}P_6)]^-$ (**12**) 203

5.3.1.1.2 Structures of $[CpV(\eta^5\text{-}P_5)]^-$ (**11**) and $[(CpV)_2(\eta^6\text{-}P_6)]^-$ (**12**) 204

5.3.1.1.3 Mass spectrometric studies on $[CpV(\eta^5\text{-}P_5)]^-$ (**11**) and $[(CpV)_2(\eta^6\text{-}P_6)]^-$ (**12**) 210

5.3.1.1.4 EPR spectroscopic studies on $[(CpV)_2(\eta^6\text{-}P_6)]^-$ (**12**) 211

5.3.1.1.5 Cyclic voltammetry studies on $[CpV(\eta^5\text{-}P_5)]^-$ (**11**) and $[(CpV)_2(\eta^6\text{-}P_6)]^-$ (**12**) 212

5.3.1.2 Reactivity of K_3As_7 towards VCp_2 215

5.3.1.2.1 Synthesis of $[CpV(\eta^5\text{-}As_5)]^{n-}$ (**13**) and $[(CpV)_2(\eta^5\text{-}As_5)]^-$ (**14**) 215

5.3.1.2.2 Structures of $[CpV(\eta^5\text{-}As_5)]^{2-}$ (**13**) and $[(CpV)_2(\eta^5\text{-}As_5)]^-$ (**14**) 217

5.3.1.2.3 Mass spectrometric studies on $[CpV(\eta^5\text{-}As_5)]^{2-}$ (**13**) and $[(CpV)_2(\eta^5\text{-}As_5)]^-$ (**14**) 222

5.3.1.2.4 EPR spectroscopic studies on $[CpV(\eta^5\text{-}As_5)]^{2-}$ (**13**) 223

5.3.1.2.5 Cyclic voltammetry studies on $[CpV(\eta^5\text{-}As_5)]^{2-}$ (**13**) and $[(CpV)_2(\eta^5\text{-}As_5)]^{-}$ (**14**) 224

5.4 Conclusions 227

5.5 References 228

Chapter 6 Conclusions 231

6.1 References 232

Chapter 7 Experimental 234

7.1 General synthetic considerations 234

7.1.1 Manipulation of air- and moisture-sensitive compounds 234

7.2 Syntheses 236

7.2.1 Zintl phases 236

7.2.2 Zintl Ions Precursors 236

7.2.2.1 $[K(18\text{-crown-}6)]_2[HP_7]$ 236

7.2.2.2 $[K(15\text{-crown-}5)_2]_2[HP_7]$ 237

7.2.2.3 $[K(18\text{-crown-}6)]_3[P_7]$ 237

7.2.3 Organometallic precursors 238

7.2.3.1 $Zn[N(SiMe_3)_2]_2$ 238

7.2.3.2 $[Ru(COD)(\eta^3\text{-}CH_2C(CH_3)CH_2)_2]$ 238

7.2.3.3 $[Co(PEt_2Ph)_2(mes)_2]$ 239

7.2.3.4 $Ge[N(SiMe_3)_2]_2$ 239

7.2.3.5 $Pb[N(SiMe_3)_2]_2$ 240

7.2.4 Compounds discussed in Chapter two 240

7.2.4.1 $[K(2,2,2\text{-crypt})]_3[Ge_9ZnN(SiMe_3)_2] \cdot 3tol$ (**1**) 240

7.2.4.2 $[K(2,2,2\text{-crypt})]_3[Sn_9ZnNSiMe_3] \cdot 3tol$ (**2**) 241

7.2.4.3 Synthesis of $Cs[K(2,2,2\text{-crypt})]_3[Ge_9ZnNSiMe_3]$ (**3**) 242

7.2.4.4 $[K(2,2,2\text{-crypt})]_3[Ge_9ZnNPh_2]$ (**4**) 242

7.2.5 Compounds discussed in Chapter three 243

7.2.5.1 $[K(2,2,2\text{-crypt})]_3[Ru@Ge_{12}]\cdot 4py$ (**5**) 243

7.2.5.2 $[K(2,2,2\text{-crypt})]_4[Co_2@Ge_{16}]\cdot 2en$ (**6**) 243

7.2.6 Compounds discussed in Chapter four 244

7.2.6.1 $[K(18\text{-crown-}6)]_2[P_7GeN(SiMe_3)_2] \cdot 2py$ (**7**) 244

7.2.6.2 $[K(18\text{-crown-}6)]_2[P_7SnN(SiMe_3)_2] \cdot 2py$ (**8**) 245

7.2.6.3 $[K(18\text{-crown-}6)]_2[P_7Pb(N(SiMe_3)_2]$ (**9**) 246

7.2.6.4 $[K(15\text{-crown-}5)_2]_3[(P_7)_2Ge_2N(SiMe_3)_2]$ (**10**) 247

7.2.7 Compounds discussed in Chapter five 247

7.2.7.1 $[K(2,2,2\text{-crypt})][CpV(\eta^5\text{-}P_5)]$ (**11**) 247

7.2.7.2 $[K(2,2,2\text{-crypt})][(CpV)_2(\eta^6\text{-}P_6)] \cdot 2THF$ (**12**) 248

7.2.7.3 $[K(2,2,2\text{-crypt})]_2[CpV(\eta^5\text{-}As_5)]$ (**13**) 249

7.2.7.4 $[K(2,2,2\text{-crypt})][(CpV)_2(\eta^5\text{-}As_5)] \cdot 2THF$ (**14**) 249

7.3 Characterisation techniques 250

7.3.1 Single Crystal X-Ray diffraction 250

7.3.2 Electrospray Ionisation Mass Spectrometry 251

7.3.3 NMR spectroscopy 251

7.3.4 Elemental Analysis 252

7.3.5 DFT calculations 252

7.3.5.1 $[K(2,2,2\text{-crypt})]_3[Sn_9ZnNSiMe_3] \cdot 3tol$ (**2**) and

$[K(2,2,2\text{-crypt})]_3[Ge_9ZnN(SiMe_3)_2] \cdot 3tol$ (**1**) 252

7.3.5.2 $[K(2,2,2\text{-crypt})]_3[\ [Ru@Ge_{12}] \cdot 4py$ (**5**) 253

7.3.5.3 $[K(2,2,2\text{-crypt})]_4[Co_2@Ge_{16}] \cdot 2en$ (**6**) 254

7.1.1.1.1 $[K(18\text{-crown-}6)]_2[P_7EN(SiMe_3)_2] \cdot 2py$ (E = Ge (**7**), Sn (**8**),

Pb (**9**)) and $[K(15\text{-crown-}5)_2]_3[(P_7)_2Ge_2N(SiMe_3)_2]$ (**10**) 254

7.1.1.1.2 $[K(2,2,2\text{-crypt})][(CpV)_2(\eta^6\text{-}P_6)] \cdot 2THF$ (**12**) 255

7.3.6 EPR 255

7.3.7 Cyclic Voltammetry 256

7.4 References 257

Appendix I 259

Appendix II 264

Chapter 1 Introduction

1.1 Historical background of Zintl clusters

The chemistry of Zintl ions began in 1891 when Joannis discovered that it was possible to dissolve elemental lead in liquid ammonia in the presence of sodium to yield a highly coloured green solution.[1–3] Kraus later studied these lead anions and suggested a stoichiometry of $NaPb_{2.25}$ (Na_4Pb_9).[4] Peck performed similar studies for sodium-antimony solutions and suggested a stoichiometry of $NaSb_{2.33}$ (Na_3Sb_7).[5] Finally in 1930 the German chemist Eduard Zintl carried out potentiometric titration experiments on a series of group 14 and 15 polyanions in solution demonstrating that the anionic species possessed the formulae $[E_9]^{4-}$ (E = Ge, Sn and Pb) or $[E'_7]^{3-}$ (E' = As and Sb).[6–10] This family of homoatomic polyanions was posthumously named after Zintl to honour his contribution to the field. The charge and structure of these group 14 and 15 Zintl ions was confirmed in 1976 and 1972, respectively, by the subsequent determination of their crystal structures.[11–15]

All the investigations carried out in the intervening 55 years were attempts to improve the synthesis of these species. The most popular technique used is a solid-state synthesis where, by reacting stoichiometric amounts of an alkali metal and a post-transition metal at high temperatures, a compound (which is termed "Zintl phase") with the general

formula A_xE_y (A = electropositive element and E = p-block element) can be prepared. In these reactions electron-transfer from element A to element E is assumed to take place, forming anionic $[E_y]^{x-}$ species in the lattice.

Several of these Zintl phases (those which contain isolated anions in the crystal lattice) were found to be soluble in liquid ammonia at very low temperatures. It was discovered later that other aprotic solvents with high dielectric constants could also be used, such as ethylenediamine, pyridine or *N*,*N*-dimethylformamide, making the manipulation of such species more straightforward at room temperature.

Alkali metal ion-sequestering agents, such as 2,2,2-crypt or 18-crown-6 play a very important role in the study of the Zintl ions because they bind strongly to the alkali metal cations encapsulating them. They increase the solubility of the metal phase, aiding solution studies. Sequestering agents also encapsulate the cation, preventing the transfer of electrons from the anionic species to the cations and thus stabilising the clusters. Finally, they aid in the crystallisation of the Zintl ions due to their spherical shape and comparable sizes.[15]

This thesis will focus mainly on the reactivity of the group 14, $[E_9]^{4-}$ (E = Ge and Sn), and seven-atom group 15, $[E'_7]^{3-}$ (E' = P and As), species. Other examples of group 14 homoatomic Zintl clusters include $[E_4]^{4-}$, $[E_5]^{2-}$ and $[E_9]^{4-}$ (E = Si, Ge, Sn and Pb) (Figure 1.1).[16–19]

The reactivity of the K_4E_9 (E = Ge, Sn and Pb) Zintl phases and the resulting $[E_9]^{4-}$ clusters that are available in solution has been studied extensively, whereas that of the analogous silicon cluster, $[Si_9]^{4-}$, has not been studied as much.[16,20] This is because the only silicon containing intermetallic phase available has the formula $A_{12}Si_{17}$, and

contains two soluble anions $[Si_4]^{4-}$ and $[Si_9]^{4-}$ in a 2:1 ratio (*i.e.* $K_{12}(Si_9)(Si_4)_2$) which can only be extracted into liquid ammonia.[21] Group 15 Zintl clusters such as $[E'_7]^{3-}$ (E' = P, As, Sb and Bi), $[E'_{11}]^{3-}$ (E' = P, As, Sb and Bi) and $[E'_4]^{2-}$ (E' = P, As, Sb and Bi) have also been characterised.[15–32]

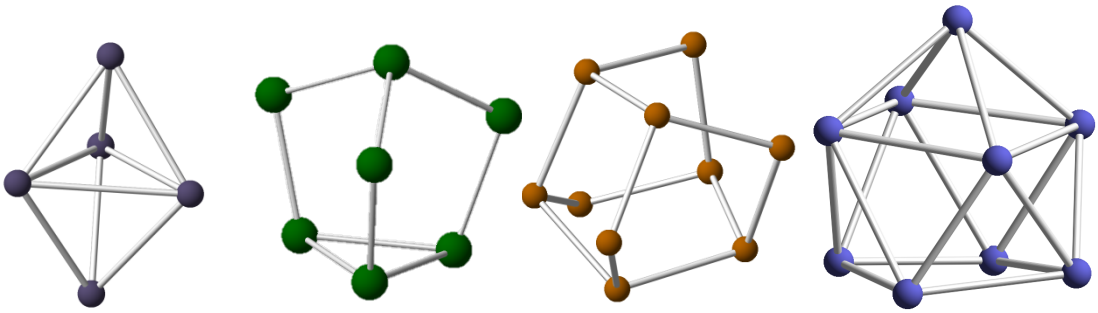

a) $[Ge_5]^{2-}$ b) $[As_7]^{3-}$ c) $[Sb_{11}]^{3-}$ d) $[Ge_9]^{4-}$

Figure 1.1: Selected examples of Zintl clusters.

1.2 Structure and bonding

1.2.1 $[E_9]^{x-}$: Nine-atom group 14 Zintl ions

The $[E_9]^{x-}$ ions possess a deltahedral structure and are electron-deficient and so the Wade-Mingos rules can be used to rationalise their electronic structure, assuming a total delocalisation of the valence electrons throughout the whole of the cluster framework (Table 1.1).[33–35] These clusters are isolobal to deltahedral boranes. Each group 14 atom is considered to be sp^3 hybridised and isolobal with a B–H fragment, contributing three orbitals and two electrons to cluster bonding. The other two electrons form a lone pair and are pointing radially away from the cluster.[33–35]

Name	Electron count	Structure
closo-	2n + 2	n vertices
nido-	2n + 4	n + 1 vertices with 1 missing vertex
arachno-	2n + 6	n + 2 vertices with 2 missing vertices

Table 1.1: Wade-Mingos rules for bonding in electron-deficient deltahedral clusters.

$[E_9]^{x-}$ clusters are fluxional in solution. They can accommodate different numbers of electrons due to a relatively high lying orbital and consequently can exist with three charges: from 2– to 4–. The equilibrium pictured in Scheme 1.1 can occur when they are in solution in solvents such as ethylenediamine or liquid ammonia. The solvated electrons can react with ethylenediamine to generate an amide and dihydrogen. The fluxionality of the $[Sn_9]^{4-}$ cluster has been confirmed by solution ^{119}Sn NMR spectroscopy in liquid ammonia at –40°C. These studies by Rudolph showed that only one ^{119}Sn NMR resonance was observed, implying that on the NMR timescale all nine atoms are equivalent.[36]

$$E_9^{4-} \rightleftharpoons E_9^{3-} + e^- \rightleftharpoons E_9^{2-} + 2e^-$$

Scheme 1.1:Equilibrium of the different oxidation states of the $[E_9]^{x-}$ cluster in solution.

The structures of these nine atom clusters vary according to their overall charge. The $[E_9]^{4-}$ clusters possess a *nido* geometry (*i.e.* 2 × 9 + 4 = 2n + 4) with a monocapped square antiprismatic shape (C_{4v}), whereas the $[E_9]^{2-}$ clusters possess *closo* geometry (*i.e.* 2 × 9 + 2 = 2n + 2) with a tricapped trigonal prismatic geometry (D_{3h}). The paramagnetic $[E_9]^{3-}$ cluster has 2n + 3 skeletal electrons and has a geometry halfway between a *closo* and a *nido*, which is a distorted tricapped prismatic structure (C_{2v}) (Scheme 1.2).

Such fluxionality is possible because the energy barriers between the different geometries are very low. As shown in Scheme 1.2, interconversion between the clusters with different charges can readily occur by elongating the trigonal prismatic edges parallel to the three-fold axis of an idealised D_{3h} cluster. For $[E_9]^{3-}$ most of the clusters exhibit a distorted tricapped trigonal prismatic structure with one or two elongated prismatic heights parallel to the three-fold axis.

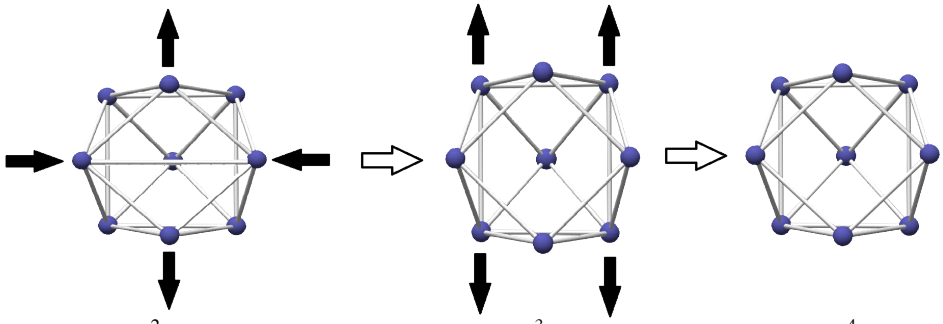

Scheme 1.2: Geometric relation between $[E_9]^{x-}$ clusters with different net charges.

Although in solution there is an equilibrium between clusters with three possible charges, a given cluster can be targeted by controlling the amount of sequestering agent added to the solution. Bearing in mind that a sequestered K^+ cation, $[K(2,2,2\text{-crypt})]^+$, is 56 times larger than the free K^+ cation, crystal packing effects can be exploited to selectively crystallise a specific charged anion. For example, if one wants to crystallise the $[E_9]^{4-}$ anion, it is possible to add three equivalents of 2,2,2-crypt and pack around the cluster three sequestered $[K(2,2,2\text{-crypt})]^+$ ions and one free K^+ cation.[12,37] If four equivalents of 2,2,2-crypt are added, the cluster crystallises as $[E_9]^{3-}$ because all of the four K^+ cations are sequestered, but they do not pack effectively alongside the cage in the crystal lattice.[38]

1.2.2 $[E'_7]^{3-}$: Seven-atom group 15 Zintl ions

Unlike group 14 Zintl ions, $[E'_7]^{3-}$ clusters are electron-precise. Their bonding structure can be explained using the two-centre, two-electron model where E' and E'$^-$ are isolobal with C–H and CH_2, respectively. The $[E'_7]^{3-}$ cluster has a nortricyclane-like structure (C_{3v}) consisting of a basal three-membered ring (E'5, E'6 and E'7), three two-connected atoms, each bearing a single negative charge (E'2, E'3 and E'4) and one three-connected E' atom at the apex (E'1) (Figure 1.2).

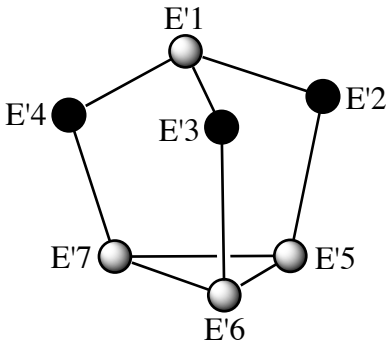

Figure 1.2: Ball and stick diagram of $[E'_7]^{3-}$. Atoms in black carry a formal negative charge.

Despite the electron-precise nature of the $[E'_7]^{3-}$ cluster it is fluxional in both solution and the solid-state. This has been confirmed by ^{31}P NMR spectroscopic studies on $[P_7]^{3-}$ where at 50 °C only one resonance at δ = –119 ppm is observed, showing that all of the phosphorus atoms are equivalent on the NMR timescale.[39,40] If the spectrum is recorded below –35 °C, it is possible to distinguish all three magnetically inequivalent phosphorus atoms. The three resonances are observed at δ = –57.0 (P1), –103.0 (P2, P3 and P4) and –161.7 (P5, P6 and P7) ppm with an intensity ratio of 1:3:3, respectively.

This fluxionality is as a result of a reversible valence tautomerism process analogous to the degenerate Cope rearrangement in the hydrocarbon bullvalene. The strained basal

three-membered ring reduces the energy required for the rearrangement to take place. This rearrangement consists of the cleavage of one of the bonds at the basal ring and the formation of a new bond between one of the three two-connected phosphorus atoms as shown in Scheme 1.3.[41–43] Due to the lack of a spectroscopic handle, similar rearrangements have not been studied for the $[As_7]^{3-}$ and $[Sb_7]^{3-}$ clusters, however, it is reasonable to assume that they have an analogous behaviour due to their very similar structure.

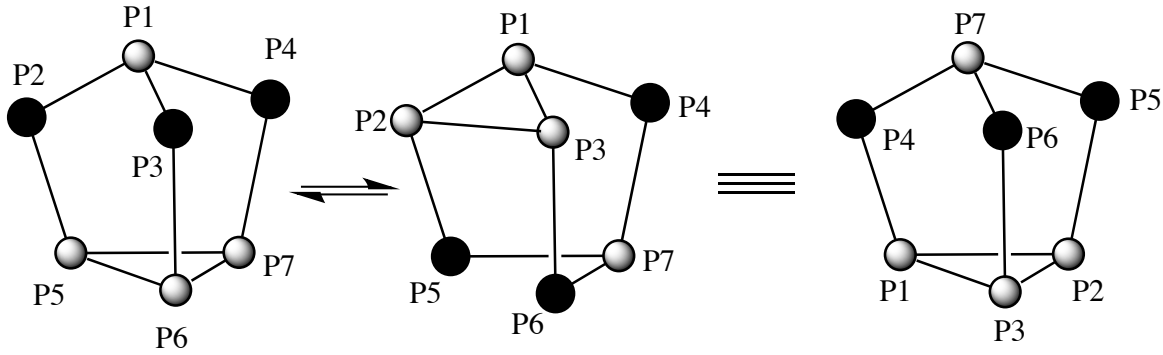

Scheme 1.3: Diagram illustrating the rearrangement taking place in $[P_7]^{3-}$.

1.3 Previous solution reactivity

$[E_9]^{4-}$ and $[E'_7]^{3-}$ ions can react with a range of different electrophilic species to give rise to novel cluster anions. A variety of bonding modes are observed for these anions, which have been studied by single-crystal X-ray diffraction and theoretical studies.[20] Since the focus of this thesis is on group 14 $[E_9]^{4-}$ and group 15 $[E'_7]^{3-}$ Zintl ions, this chapter will provide an overview of their solution reactivity towards different reagents and the established bonding modes available of such clusters.

1.3.1 Group 14 $[E_9]^{4-}$ Zintl ions

1.3.1.1 Oxidative-coupling reactions of group 14 $[E_9]^{4-}$ clusters

Group 14 Zintl $[E_9]^{4-}$ ions can be oxidised to form oligomeric species with several linked clusters.

The polymers that can be formed can be as small as a dimer ($[Ge_9–Ge_9]^{6-}$) where two nonagermanide units are linked together with a conventional two-centre, two-electron *exo*-bond (approximately 2.51 Å). There are two different structures that have been reported in the past for this dimer, one where the two clusters form a bond through the vertices of the open faces of the monocapped antiprisms with an "up-down" conformation (Figure 1.3, left) and another where the bond between the nonagermanide units is pointing radially towards the cluster centre (Figure 1.3, right).[44–46]

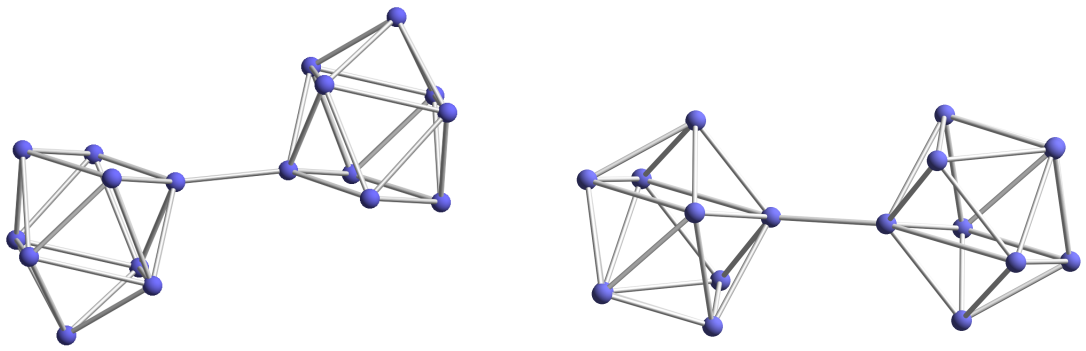

Figure 1.3: Ball and stick diagram of the two reported conformations of $[Ge_9–Ge_9]^{6-}$.

Trimers, such as $[Ge_9=Ge_9=Ge_9]^{6-}$ (Figure 1.4), have also been prepared by the addition of a mild oxidising agent such as PPh_3 or $AsPh_3$ to solutions of $[Ge_9]^{4-}$ at 70 °C.[47] In these species there are two *exo*-bonds formed between each tricapped trigonal prismatic cluster, as opposed to the dimeric species, which are linked by a single bond. The bond lengths in these trimers (approximately 2.59 Å) are longer than for the dimeric species

mentioned above. Fenske-Hall and extended-Hückel calculations were performed on the trimer and it was shown that the six negative charges are evenly distributed along the three cluster units, indicating some degree of delocalisation throughout the whole oligomer.

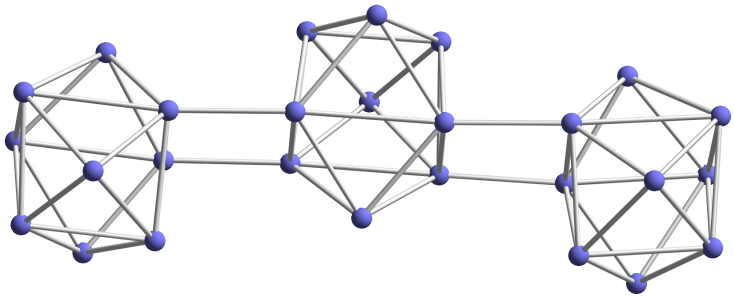

Figure 1.4: Ball and stick diagram of $[Ge_9{=}Ge_9{=}Ge_9]^{6-}$.

Tetramers such as $[Ge_9{=}Ge_9{=}Ge_9{=}Ge_9]^{8-}$ can also be prepared using the Rb_4Ge_9 Zintl phase by adding 18-crown-6 and heating to 50 ºC. The tetramers are similar to the trimers, they have two *exo*-bonds between each tricapped trigonal prismatic cluster and have their eight negative charges evenly distributed along the four cluster units. Again, the bonds are longer than the *exo*-bonds in the dimeric species.[48] The crystal structure revealed an interaction between the sequestered $[Rb(18\text{-crown-}6)]^+$ cations and the tetrameric species. The potassium analogue has also been prepared *via* the reaction of the K_4Ge_9 Zintl phase with GeI_2 and one equivalent of elemental potassium.[49]

Infinite one-dimensional chains $_\infty[-Ge_9-]$, have also been crystallised by dissolving K_4Ge_9 and a bidimentional sequestering agent in ethylenediamine and toluene.[50–52] The one-dimensional chains show clusters with monocapped square antiprismatic geometry linked with single *exo*-bonds (approximately 2.48 Å) with an alternating "up–down" arrangement.

1.3.1.2 *Exo*-functionalisation and vertex substitution reactions of group 14 $[E_9]^{4-}$ clusters with main group reagents

Following the isolation of oligomers of group 14 Zintl ions, it seemed reasonable to assume that such clusters might react with mild oxidising main group reagents to give rise to *exo*-functionalised species.

The reactivity of the K_4Ge_9 Zintl phase with EPh_4 (E = Ge and Sn) was first studied by Sevov and co-workers. The reaction of K_4Ge_9 with $SnPh_4$ yielded the *bis*functionalised anion $[Ph_3Sn–Ge_9–SnPh_3]^{2-}$.[53] The analogous product was not accessible when $GePh_4$ was employed. In an attempt to synthesise the germanium *bis*functionalised analogue, $GePh_3Cl$ was used, but due to oxidation of the $[Ge_9]^{4-}$ cluster (to provide the electrons necessary for the reduction of $GePh_3Cl$), $[Ph_3Ge–Ge_9–Ge_9–GePh_3]^{4-}$ was isolated instead.

To improve this reaction, elemental potassium was added to the ER_3Cl reagent before mixing it with K_4Ge_9. This way monofunctionalised compounds of the form $[Ge_9–SnR_3]^{3-}$ (R = Ph and Me) and the *bis*functionalised compounds $[R_3E–Ge_9–ER_3]^{3-}$ (E = Ge and Sn: R = Ph and Me) were prepared. These results show that these reactions occur *via* a nucleophilic addition to vertices at the elongated edges of the distorted tricapped trigonal prism of the cage.[53]

The E–Ge bonds in the majority of these anions can be described as covalent two-centre, two-electron bonds. The E atom is bonded to the nonagermanide unit by the elongated prismatic edge of the cluster. In the $[Ge_9–SnPh_3]^{3-}$ cluster the tin atom appears to be bonded to two germanium atoms forming a delocalised three-centre, two-electron bond.

$[Ge_9]^{4-}$ Zintl ion can react with group 15 species of the type $E'Ph_3$ (E' = Sb and Bi) in ethylenediamine and in the presence of 2,2,2-crypt.[54,55] These reactions yield the *exo*-functionalised clusters $[Ph_2E'–Ge_9–E'Ph_2]^{2-}$ (Figure 1.5). This reaction can be described as a nucleophilic addition of the $[E'Ph_2]^-$ ion to the cluster. DFT calculations were performed in order to confirm this hypothesis. ^{1}H NMR spectroscopic studies of these clusters proved inconclusive, showing many phenyl species in solution. The reaction with $SbPh_3$ also yielded the clusters $[Ph–Ge_9–SbPh_2]^{2-}$ and $[Ph_2Sb–Ge_9–SbPh_2]^{4-}$.

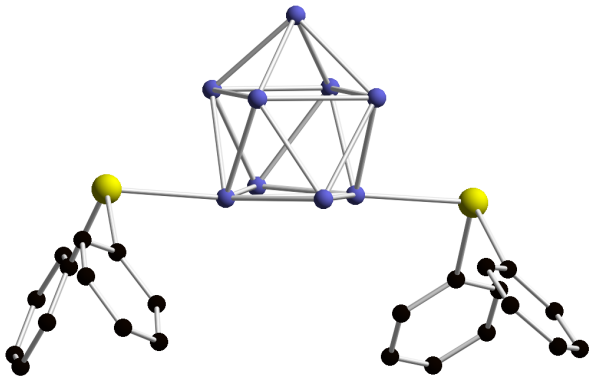

Figure 1.5: Ball and stick diagram of $[Ph_2Bi–Ge_9–BiPh_2]^{2-}$ (Ge atoms are shown in purple, Bi atoms in yellow and C atoms in black). H atoms are omitted for clarity.

The Sevov group additionally attempted to prepare the analogous compounds with lighter $E'Ph_2$ reagents (E' = P and As) unsuccesfully. The products obtained instead were oligomers of the $[Ge_9]^{4-}$ cluster due to oxidative coupling.

Reactions between $E'Ph_3$ (E' = Sb and Bi) and K_4Ge_9 can lead to the substitution of a germanium atom in the cluster. Subsequent dimerisation upon heating the reaction mixture at 75 ºC for 3 days resulted in the formation of $[E'Ge_8–Ge_8E']^{4-}$ (Figure 1.6).[56] The charge of the $[E'Ge_8–Ge_8E']^{4-}$ dimers is smaller than that of $[Ge_9–Ge_9]^{6-}$ because each antimony atom contributes an extra electron for cluster bonding. Additional heating of the reaction mixtures (100 ºC for 3 days) yields the *bis*substituted species $[Sb_2Ge_7]^{2-}$,

and sonication of the reaction mixture lead to the formation of the $[SbGe_8–SbPh_2]^{2–}$ anion.

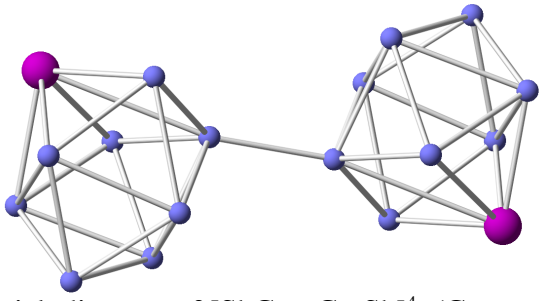

Figure 1.6: Ball and stick diagram of $[SbGe_8–Ge_8Sb]^{4–}$ (Ge atoms are shown in purple and Sb atoms in pink).

1.3.1.3 *Exo*-functionalisation reactions of group 14 $[E_9]^{4–}$ clusters with organic reagents

As with the main group reagents discussed in Section 1.3.1.2 , group 14 clusters can also be *exo*-functionalised using alkyl halides (R–X). Reactions between the K_4Ge_9 Zintl phase and RCl (R = ^{t}Bu, ^{s}Bu, ^{n}Bu and ^{t}Am) reported by Sevov *et al*. in 2007, yielded dimeric products which are also *exo*-functionalised by organic fragments (*i.e*. $[R–Ge_9–Ge_9–R]^{4–}$).[57]

In addition to these alkylation reactions, the Sevov group also reported *exo*-functionalisation products through reactions of the $[Ge_9]^{4–}$ cluster with alkynes after undergoing partial hydrogenation by the solvent.[58] The alkynes studied include FcC≡CFc, [FcC≡C]K, PhC≡CH, ^{t}BuC≡CH, PhC≡CPh, and 4-MeO–PhC≡CH. Crystallographic analysis of the $[Fc–CH=CH–Ge_9–CH=CH–Fc]^{2–}$ cluster (Figure 1.7) revealed a *bis-exo*-functionalised cage with a tricapped trigonal prismatic geometry and one elongated edge. Both CH=CH–Fc moieties adopt a *cis* conformation. As in the majority of the *exo*-bonds reported, these are covalent single bonds. These reactions were

studied using mass spectrometry, both with and without sequestering agents, and revealed the formation of the mono- and *bis*functionalised analogues. In the same year Sevov reported the reaction of the $[Ge_9]^{4-}$ anion with two equivalents of $Me_3Si–C\equiv C–SiMe_3$ yielding the *bis*functionalised $[H_2C=CH–Ge_9–CH=CH_2]^{2-}$ product that, due to its very low charge, is soluble in non-polar solvents.[59] X-ray crystallography has confirmed that the Ge–C bonds formed are single covalent two-centre, two-electron bonds.

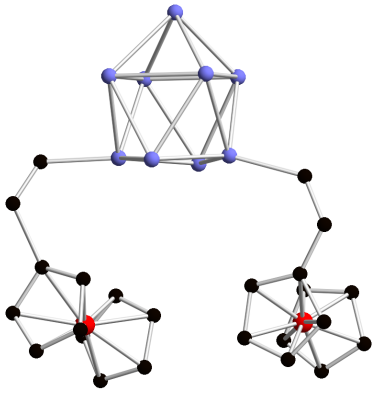

Figure 1.7: Ball and stick diagram of $[Fc–CH=CH–Ge_9–CH=CH–Fc]^{2-}$ (Ge atoms are shown in purple, Fe atoms in red and C atoms in black). H atoms are omitted for clarity.

K_4Sn_9 reacts with RCl (R = ^{t}Bu, ^{n}Bu and ^{s}Bu) in the presence of 2,2,2-crypt yielding the monosubstiuted products $[Sn_9–R]^{3-}$.[60] X-ray crystallography studies of $[Sn_9–^t Bu]^{3-}$ revealed a similar geometry to the germanium analogues. Single crystals suitable for X-ray crystallography of the ^{n}Bu and ^{s}Bu substituted products could not be obtained, however, mass spectrometric studies confirmed the formation of the monosubstituted clusters. Reactions of the K_4Sn_9 Zintl phase with alkynes such as $Me_3Si–C\equiv C–SiMe_3$ and Ph–C≡CH result in the formation of the monosubstituted anions $[Sn_9–CH=CH_2]^{3-}$ and $[Sn_9–C=CH–Ph]^{3-}$. In these reaction of *exo*-functionalisation, one electron is required to reductively cleave the bond in the reagents. There is no change in the overall number of skeletal electrons or geometry of the cluster when an –R group is bonded to the

substituent; one extra valence electron is contributed to cluster bonding, which is compensated for with a decrease of the overall charge.

1.3.1.4 Reactions where the group 14 $[E_9]^{4-}$ clusters act as ligands towards metal centres

The first coordination compound of group 14 clusters was reported by Eichhorn *et al*. K_4Sn_9 reacts with $[Cr(CO)_3(mesitylene)]$ in ethylenediamine and in the presence of 2,2,2-crypt to form $[Sn_9Cr(CO)_3]^{4-}$.[61] The chromium atom has an formal oxidation state of zero and is acting as a 10th vertex in a capping position in a *closo* cluster with a bicapped square antiprismatic geometry. The cluster is coordinated to the metal in an η^4 mode. The overall charge suggests that the neutral fragment $[Cr(CO)_3]$ is coordinated by the tetraanionic cage resulting in the $[Sn_9Cr(CO)_3]^{4-}$ complex. The cluster has 22 skeletal electrons (2n + 2) corresponding to a *closo* cluster as was observed by X-ray crystallography. Additionally, the chromium has an eighteen-electron configuration (six electrons provided by the cluster, six provided by the carbonyl groups and six from the metal valence electrons). This compound was studied by IR spectroscopy, revealing extensive Cr–CO π back-donation shown by the lower frequency of the carbonyl ligands compared to the starting material. This suggestion is corroborated by X-ray crystallography where the lengthening of the C–O bonds is observed.

Other examples of $[E_9M(CO)_3]^{4-}$ (E = Sn: M = Cr, Mo and W; E = Pb: M = Mo and W) have also been synthesised by similar methods (Figure 1.8).[62–65] In most of these examples the metal binds to the cluster in an η^4 fashion and all of them possess similar properties to the $[Sn_9Cr(CO)_3]^{4-}$ system described in the previous paragraph.

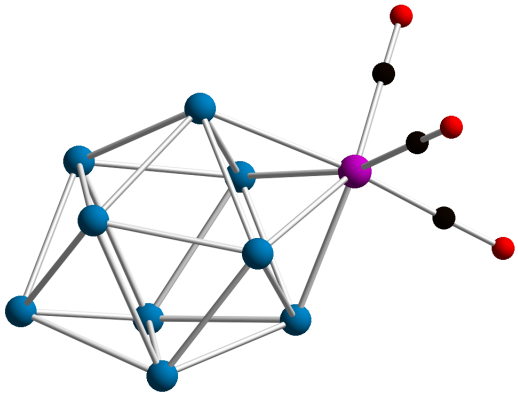

Figure 1.8: Ball and stick diagram of $[Sn_9W(CO)_3]^{4-}$ (Sn atoms are shown in blue, the W atom in pink, C atoms in black and O atoms in red).

^{119}Sn and ^{117}Sn NMR spectroscopic studies performed by Schrobilgen *et al*. in 2002 on $[Sn_9M(CO)_3]^{4-}$ (M = Cr, Mo and W) revealed the presence of three different tin environments with relative intensities 1:4:4, corresponding to the capping tin atom, the four tin atoms placed in the square closest to the $M(CO)_3$ fragment and the four atoms above them.[64] This is in contrast to the $[Sn_9]^{4-}$ anion where fluxionality is observed on the NMR timescale, showing only one resonance.

In 2001 a different binding mode for the $[Sn_9W(CO)_3]^{4-}$ complex was reported. η^5 coordination was observed in a cluster synthesised by the reaction of K_4Sn_9 and $[W(CO)_3(\text{mesitylene})]$ (Figure 1.9).[63] The tungsten atom is occupying a different position in the 10-vertex cluster, in contrast to the previous η^4 analogues. It is situated in a waist position, but the electron count remains the same. The cluster has C_s symmetry.

^{119}Sn NMR spectroscopy of a mixture of the $[(\eta^5\text{-}Sn_9)W(CO)_3]^{4-}$ and the $[(\eta^4\text{-}Sn_9)W(CO)_3]^{4-}$ compound reveals a dynamic equilibrium between the η^5 and the η^4 species, showing only the three resonances corresponding to the C_{4v}-symmetric isomer. Additionally, ^{13}C NMR spectroscopy shows only one carbonyl resonance at δ = 239 ppm. The NMR spectra of solutions of the pure crystalline sample of $[(\eta^4\text{-}Sn_9)W(CO)_3]^{4-}$

are identical. Eichhorn *et al*. monitored these reactions at different times by solid-state IR. They proposed that the η^4 and η^5 isomers are in equilibrium and do not represent kinetic and thermodynamic products of an irreversible transformation.

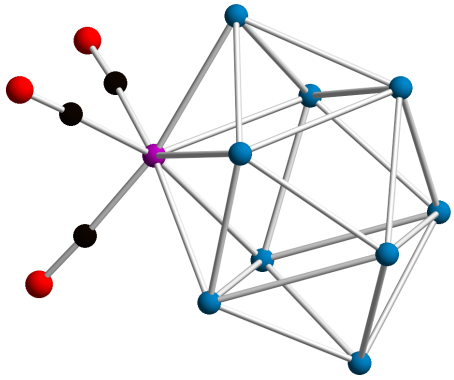

Figure 1.9: Ball and stick diagram of $[(\eta^5\text{-}Sn_9)W(CO)_3]^{4-}$ (Sn atoms are shown in blue, the W atom in pink, C atoms in black and O atoms in red).

In 2005 Fässler *et al*. reported the reaction between the $[Pb_9]^{4-}$ cage and $Mo(CO)_3(MeCN)_3$ in the presence of 2,2,2-crypt, yielding the η^5 coordination compound $[(\eta^5\text{-}Pb_9)Mo(CO)_3]^{4-}$.[65]

In 2010 Goicoechea and Zhou reported the reaction of the K_4Ge_9 Zintl phase with the organometallic reagent $Fe(COT)(CO)_3$ in the presence of 2,2,2-crypt to yield $[Ge_8Fe(CO)_3]^{3-}$ (Figure 1.10).[66] In contrast to the reaction involving the d^6 $M(CO)_3L$ compounds, this reaction does not proceed as a simple ligand displacement by the nine-atom cage.

This structure represents an unprecedented functionalised germanium Zintl anion in which the nine-atom precursor cluster has lost an atom, which in turn has been replaced with an $Fe(CO)_3$ fragment coordinated to a *nido* Ge_8 cage in an η^4 mode. The cluster anion has a monocapped square antiprismatic geometry with the iron tricarbonyl moiety occupying one of the vertices of the open square face. The chemically reduced

organometallic species $[Fe(\eta^3\text{-}C_8H_8)(CO)_3]^-$ was also isolated as a side product from this reaction as the $[K(2,2,2\text{-crypt})]^+$ salt.

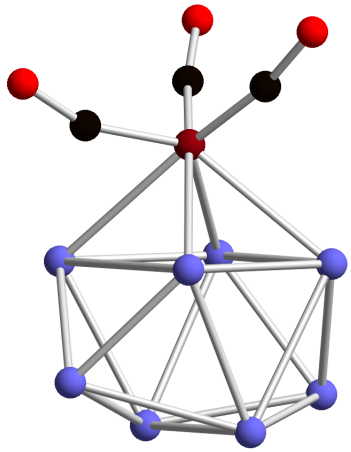

Figure 1.10: Ball and stick diagram of $[Ge_8Fe(CO)_3]^{3-}$ (Ge atoms are shown in purple, the Fe atom in dark red, C atoms in black and O atoms in red).

The $Fe(CO)_3$ fragment contributes three orbitals and two electrons to cluster bonding, making it isolobal to a germanium vertex. This would mean that the $[Ge_8Fe(CO)_3]^{3-}$ cluster is isolobal to the paramagnetic $[Ge_9]^{3-}$ cluster. It has 21 valence electrons and a geometry that is somewhere between that of a *closo* tricapped trigonal prism and a *nido* monocapped square antiprism. Its paramagnetic character was confirmed by EPR spectroscopy. At room temperature a weak broad resonance was observed, which sharpens on cooling to 20 K. It has a *g* factor of 2.0200.

In 2010, another reaction between a Zintl phase and a carbonyl reagent was studied. K_4Ge_9 was reacted with $Mn_2(CO)_{10}$ in ethylenediamine in the presence of 2,2,2-crypt to form an unexpected coordination compound $[Ge_{10}Mn(CO)_4]^{3-}$ (Figure 1.11).[67] Unlike the other carbonyl compounds, the $Mn(CO)_4$ fragment coordinates to a single germanium atom. The cage undergoes a mild oxidation and gains an additional germanium atom to form the $[Ge_{10}]^{2-}$ cluster.

The $[Ge_{10}]^{2-}$ cage acts like a two-electron donor ligand and coordinates to the manganese centre *via* the lone pair of a germanium vertex. The *closo* cluster adopts the typical bicapped square antiprismatic geometry of the ten-vertex clusters, with a pseudo D_{4d} geometry. As expected, the $[Ge_{10}]^{2-}$ fragment has a total of 22 skeletal electrons. The manganese atom in the $[Mn(CO)_4]^-$ fragment has an eighteen-electron configuration, made up of its seven valence electrons, two from each CO ligand, two more from the cluster and one from the 1– charge. Similar to the other carbonyl complexes discussed in this section, the IR spectrum revealed strong back-donation from the negatively charged manganese atom to the antibonding π* orbitals of the carbonyl groups. X-ray crystallography supported this observation exhibiting longer C–O bonds than in the starting material. This implies that the $[Ge_{10}]^{2-}$ cluster is a poorer π acceptor than a carbonyl, or a better σ donor (or a combination of both effects).

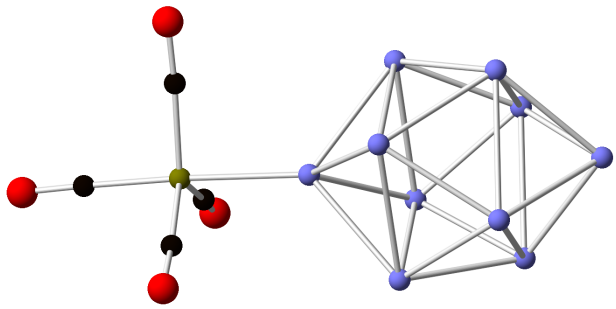

Figure 1.11: Ball and stick diagram of $[Ge_{10}Mn(CO)_4]^{3-}$ (Ge atoms are shown in purple, the Mn atom in green, C atoms in black and O atoms in red).

The final metal carbonyl species that will be discussed in this section is a nickel-containing system. In 2006, Sevov and Goicoechea reported the reaction of $Ni(CO)_2(PPh_3)_2$ with K_4Ge_9 at room temperature, where a simple ligand displacement reaction takes place leading to the formation of $[Ge_9Ni(CO)]^{3-}$ (Figure 1.12).[68] The cluster has a bicapped square antiprismatic geometry with a nickel atom acting as a 10th vertex. Despite the fact that the cluster was observed with a *closo* conformation, it only

has 21 skeletal electrons. The calculated SOMO – HOMO–1 gap was only 0.7 eV, which is indicative that this cluster should be susceptible to both oxidation and reduction.

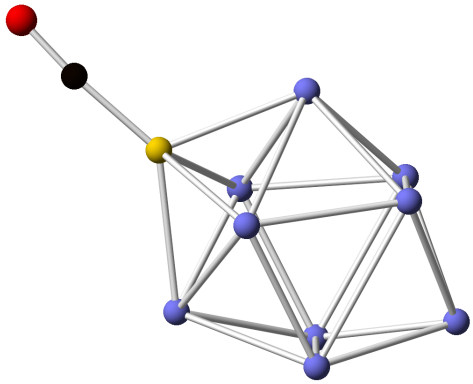

Figure 1.12: Ball and stick diagram of $[Ge_9Ni(CO)]^{3-}$ (Ge atoms are shown in purple, the Ni atom in yellow, the C atom in black and the O atom in red).

A similar molecule has been reported whereby the nine-atom cage coordinates in an η^4 mode to an $[Ir(COD)]^+$ moiety generated by the fragmentation of $[Ir(COD)Cl]_2$ in the presence of 2,2,2-crypt, namely $[E_9Ir(COD)]^{3-}$ (E = Sn and Pb) (Figure 1.13).[69] It is believed that such reactions proceed by the dissociation of the organometallic precursor to Cl^- and the electrophilic compound $[Ir(COD)]^+$. The latter attacks the electron-rich $[E_9]^{4-}$, forming the coordination compound $[E_9Ir(COD)]^{3-}$.

The structure of the cage is very similar to the previously mentioned $[E_9M(CO)_3]^{4-}$ systems. The iridium atom is positioned as the 10th vertex of a *closo* cage, with 22 skeletal electrons, including one electron donated by the $[Ir(COD)]^+$ moiety. The cluster has pseudo-C_{4v} symmetry, with a bicapped square antiprismatic geometry. ^{13}C NMR spectroscopy revealed that the COD ligand resonances are more deshielded than those of the starting material. Additionally, the longer C–C bond distances in the ligand observed by X-ray crystallography suggest that there is substantial metal-ligand back-donation

between the d valence orbitals and the empty π* antibonding molecular orbitals of the COD ligand.

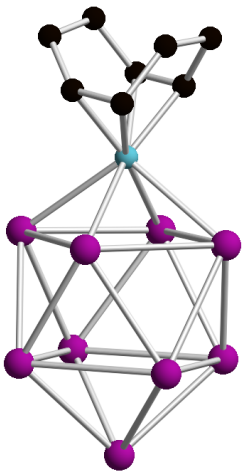

Figure 1.13: Ball and stick diagram of $[Pb_9Ir(COD)]^{3-}$ (Pb atoms are shown in pink, the Ir atom in blue and C atoms in black). H atoms are omitted for clarity.

In 2006, Goicoechea and Sevov reported a series of coordination compounds of the form $[E_9ZnPh]^{3-}$ (E = Si, Ge, Sn and Pb) prepared by reactions of K_4E_9 (E = Ge, Sn and Pb) or $K_{12}Si_{17}$ with $ZnPh_2$ (Figure 1.14).[70] In this reactions the heterolytic cleavage of a Zn–Ph bond takes place, giving rise to a radical $[ZnPh]^{\bullet}$ and a phenyl anion, the latter abstracts a proton from the solvent to form benzene. The radical formed attacks the electron-rich cage to form the η^4 coordination compounds $[E_9ZnPh]^{3-}$. This report is the first complete series of group 14 $[E_9]^{4-}$ clusters (Si–Pb) functionalised with the same fragment, and the very first example of a functionalised $[Si_9]^{4-}$ cluster.

Each E atom is sp^3 hybridised and donates three orbitals and two electrons to cluster bonding. The zinc atom donates one valence electron to the Zn–Ph bond and the other valence electron to the cluster. Each E atom contributes two electrons to the skeletal bonding, plus three from the overall charge and the zinc valence electron gives a total of

22 skeletal electrons corresponding to a *closo* cluster. A *closo* bicapped square antiprismatic geometry was confirmed by single crystal X-ray diffraction.

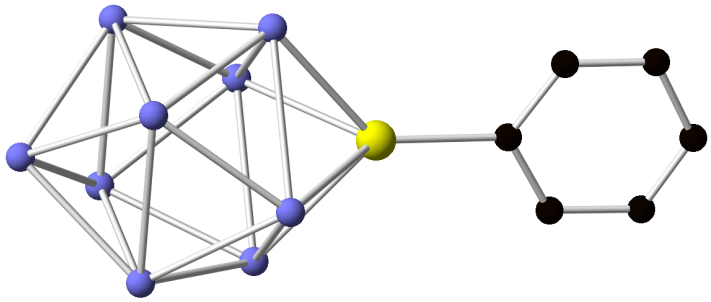

Figure 1.14: Ball and stick diagram of $[Ge_9ZnPh]^{3-}$ (Ge atoms are shown in purple, the Zn atom in yellow and C atoms in black). H atoms are omitted for clarity.

A frontier orbital analysis of $[E_9ZnPh]^{3-}$ revealed that the cage has three filled molecular orbitals with appropriate symmetry to interact with the zinc atom. The zinc is sp hybridised and one of the sp orbitals plus the p_x and p_y orbitals have the correct symmetry to interact with the cage (Figure 1.15). A more detailed discussion about this will be given in Chapter 2.

In 2009, Goicoechea and co-workers extended this work by preparing similar coordination compounds $[E_9ZnR]^{3-}$ (E = Ge, Sn and Pb: R = mes and ^{i}Pr) by reacting the K_4E_9 Zintl phases and the organometallic compounds ZnR_2, proving the versatility of this route to form novel mixed-metal clusters with *exo*-bonds to organic substituents.[71]

In 2008, the work was extended further to the heavier group 12 metal cadmium. By reacting K_4E_9 (E = Sn and Pb) with the organometallic species $CdPh_2$, clusters of the form $[E_9CdPh]^{3-}$ were isolated. These species exhibit similar properties to the zinc analogues.[72]

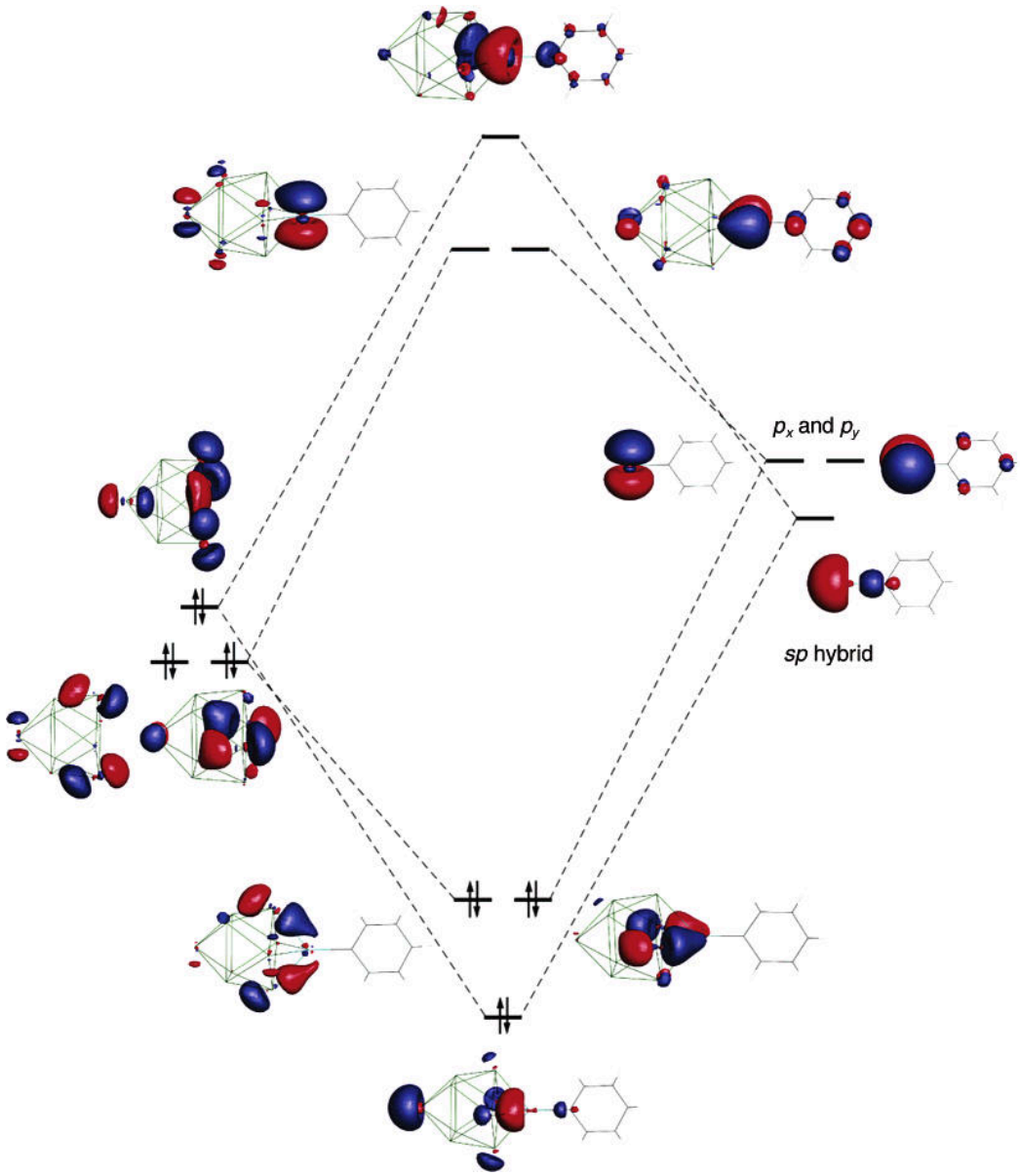

Figure 1.15: Qualitative fragment analysis of the interactions between the frontier orbitals of nine-atom cluster (left) and the ZnPh fragment (right) in the formation of $[E_9ZnPh]^{3-}$.[70]

The reaction between $[Sn_9CdPh]^{3-}$ towards tributyltinhydride in pyridine was also investigated. This reaction yields the tin-functionalised cluster $[Sn_9CdSn^nBu]^{3-}$ (Figure 1.16), along with free benzene generated from the loss of the phenyl group. This proved that the highly reactive functionalised clusters, which were thought to be very reductive,

are possible "inert" ligands, opening the possibility to use such systems as organometallic ligands.

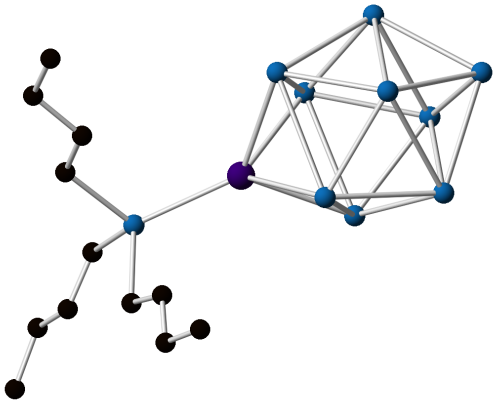

Figure 1.16: Ball and stick diagram of $[Sn_9CdSn^nBu]^{3-}$ (Sn atoms are shown in blue, the Cd atom in purple and C atoms in black).

While attempting to expand this work, the Goicoechea group reacted the K_4Pb_9 with $Cd(mes)_2$ in ethylenediamine, yielding the $[Pb_9Cd–CdPb_9]^{6-}$ anion.[73] This anion consists of two *closo* clusters with a cadmium atom in each capping position linked together by a Cd–Cd bond. Prior to this report, there was only one Cd–Cd bond reported in a molecular species characterised crystallographically, namely Ar'Cd–CdAr', in this case bulky *m-tert*phenyl substituents were used to sterically protect the bond.[74] The Cd–Cd bond reported by Goicoechea is 0.08 Å longer.

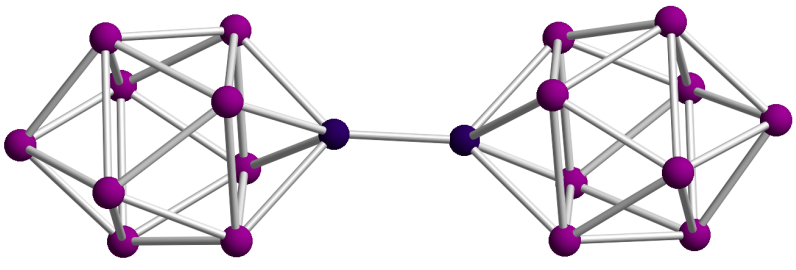

Figure 1.17: Ball and stick diagram of $[Pb_9Cd–CdPb_9]^{6-}$ (Pb atoms are shown in pink and Cd atoms in purple).

The mechanism for this reaction was postulated as follows: the free solvated electrons from the typical equilibrium of the group 14 cages in solution can reductively cleave the Cd–C bonds to initially form $[Pb_9Cd(mes)]^{3-}$. Further cleavage of the second Cd–C bond occurs by the same electrons to give rise to a $[Pb_9Cd]^{3-}$ fragment which subsequently couples to another fragment to give a Cd–Cd bridged dimer $[Pb_9Cd–CdPb_9]^{6-}$. The mystery of why the reactions between K_4Pb_9 and $Cd(mes)_2$ or $CdPh_2$ proceed differently remains unsolved. One suggestion is that the bond enthalpy of $Cd(mes)_2$ is slightly smaller than that of $CdPh_2$.[75]

The two halves of the $[Pb_9Cd–CdPb_9]^{6-}$ (Figure 1.17) dimer are in an eclipsed conformation, giving the structure an overall D_{4h} symmetry. Regarding the electron count, each cadmium atom donates one valence electron to the Cd–Cd bond and the other is contributed to cluster bonding. This, plus the 3– charge of each unit gives a total of 22 skeletal electrons, consistent with the *closo* geometry observed by X-ray crystallography.

DFT calculations revealed that the optimised structure and the structure determined by X-ray crystallographically are very similar. The main difference being that the Cd–Cd bond is slightly longer in the calculated structure. The HOMO–4 was found to have significant Cd–Cd σ bond character.

Interesting reactivity of the $[Ge_9]^{4-}$ cage towards mercury compounds has also been reported. K_4Ge_9 reacts with elemental mercury to form a polymeric species $^1_\infty[HgGe_9]^{2-}$ (Figure 1.18) in ethylenediamine and in DMF.[76,77] The polymer consists of nine-atom cages linked linearly by mercury atoms. The *exo*-bonds are formed using diagonally

opposite germanium vertices of the open square bases of the square antiprismatic monomers.

These species can be seen as covalent species –([Ge_9]$^{2-}$)–Hg–([Ge_9]$^{2-}$)–Hg or with formal charges ([Ge_9]$^{4-}$)–(Hg^{2+})–([Ge_9]$^{4-}$)–(Hg^{2+}). Each cluster has 22 skeletal electrons available for bonding.

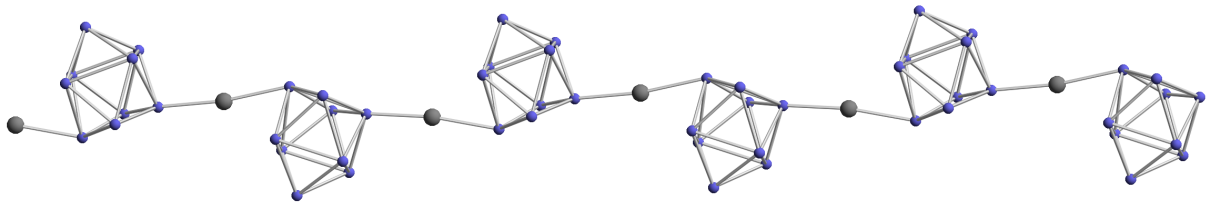

Figure 1.18: Ball and stick diagram of $^{1}_{\infty}[HgGe_9]^{2-}$ (Ge atoms are shown in purple and Hg atoms in gray).

K_4Ge_9 reacts with $HgPh_2$ to form the nanorod [Ge_9–Hg–Ge_9–Hg–Ge_9–Hg–Ge_9]$^{10-}$. The mechanism proposed is similar to the formation of [E_9MR]$^{3-}$ and is as follows: The nine-atom cage in solution, due to the equilibrium gives electrons to cleave all the Hg–C bonds affording Hg^{2+} and the phenyl anions. The phenyl anions subsequently extract of a proton from the solvent to form benzene. The overall charge supports the idea of the loss of six electrons to cleave the Hg–C bonds. Four cages and three mercury atoms link together to form the nanorod [Ge_9–Hg–Ge_9–Hg–Ge_9–Hg–Ge_9]$^{10-}$ (Figure 1.19), which has a length of 3 nm. X-ray analysis revealed that the central mercury atom sits a crystallographic inversion centre.

K_4Ge_9 reacts differently with $HgPh_2$ than with the other group 12 MPh_2 (M = Zn and Cd) compounds.[78] The different reactivity of the group 12 MPh_2 compounds could be attributed to the difference in bond dissociation energy, as M–C bonds get weaker as the metal becomes heavier.[75]

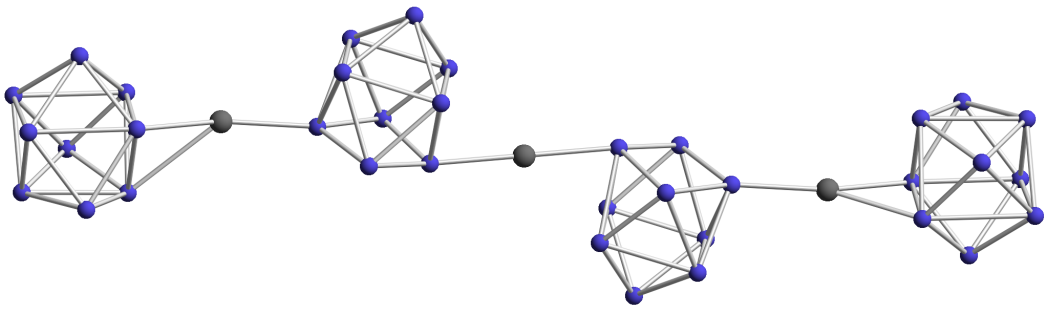

Figure 1.19: Ball and stick diagram of $[Ge_9–Hg–Ge_9–Hg–Ge_9–Hg–Ge_9]^{10–}$ (Ge atoms are shown in purple and Hg atoms in gray).

The nine-atom cages at the extremes are distorted tricapped trigonal prisms whereas the other two have monocapped square antiprismatic geometries. The external cages are linked to the adjacent mercury atoms in an η^2 fashion and the central mercury atom is forming single covalent bonds with two cages. The anion can be rationalised as two monofunctionalised 3– cages and two *bis*functionalised 2– cages. Recrystallisation of the sample from pyridine leads to the formation of the polymeric species mentioned previously in this section.

The reaction between K_4Sn_9 and elemental mercury in ethylenediamine has been also investigated. It leads to the formation of the coordination compound $[Sn_9–Hg–Sn_9]^{6–}$ (Figure 1.20). The mercury atom sits on an inversion centre of the cluster. The two cages coordinate to the mercury atom cage in an η^2 mode.[79]

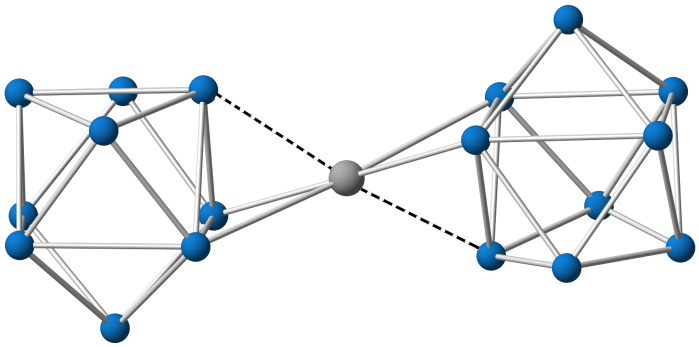

Figure 1.20: Ball and stick diagram of $[Sn_9–Hg–Sn_9]^{6–}$ (Sn atoms are shown in blue and the Hg atom in gray).

This constitutes one of the few examples where a nine-atom group 14 cage is bonded to a metal atom in an η^2 manner. Both cages have a tricapped trigonal prismatic geometry.

The reactions of K_4Ge_9 and $CuCl(PR_3)$ (R = ^{i}Pr and Cy) in DMF yield $[Ge_9Cu(PR_3)]^{3-}$.[80] These products are obtained by crystallisation from NH_3 at –70 ºC. However, when the reaction is stored at –40 ºC, a different substituent-free product was isolated $[(\eta^1\text{-}Ge_9)Cu(\eta^4\text{-}Ge_9)]^{7-}$ (Figure 1.21).

In both cases the $[Ge_9Cu]$ moiety constitutes a typical case of η^4 coordination where the cage is acting like a six-electron donor and the copper atom is capping the cluster as the 10th vertex of the bicapped square antiprism with 22 skeletal electrons and a *closo* geometry.

In the second and more interesting product, $[(\eta^1\text{-}Ge_9)Cu(\eta^4\text{-}Ge_9)]^{7-}$, there are two cages coordinated with different hapticities to the metal atom. One is a six-electron donor in an η^4 fashion, and the second is coordinated in an η^1 manner to the copper centre. The second cluster has tricapped trigonal prismatic geometry and is acting as two-electron donor. The copper has an eighteen-electron configuration taking into account its ten valence electrons, plus six from one cage and two from the other. The whole compound can be seen as two $[Ge_9]^{4-}$ fragments bonded to a Cu^+ cation.

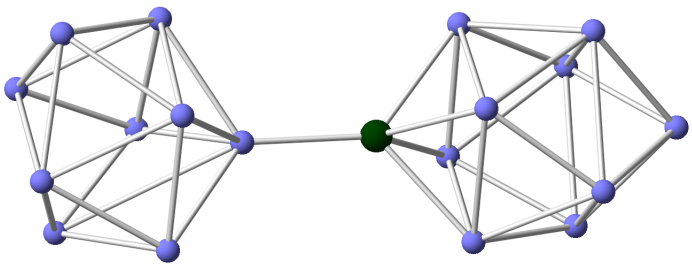

Figure 1.21: Ball and stick diagram of $[(\eta^1\text{-}Ge_9)Cu(\eta^4\text{-}Ge_9)]^{7-}$ (Ge atoms are shown in purple and the Cu atom in dark green).

Going down group 11, the reaction of K_4Sn_9 with $[Ag(mes)]_4$ in ethylenediamine and in the presence of 2,2,2-crypt affords $[Ag(Sn_9)_2]^{5-}$ (Figure 1.22).[81] In this cluster the two cages are linked through a normal two-centre, two-electron *exo*-bond and additionally, they coordinate in an η^3 fashion to the metal centre through one of the triangular faces.

Both cages are tricapped trigonal prisms and they have three elongated three-fold prismatic edges. This structure can be seen as a dimer $[Sn_9–Sn_9]^{6-}$ linked to a Ag^+ cation. One silver atom is bonded to six different tin atoms and all the bond lengths are longer than a single Ag–Sn bond.[82]

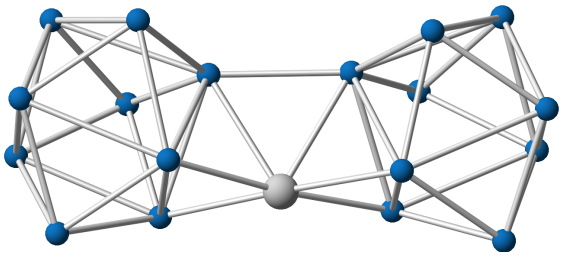

Figure 1.22: Ball and stick diagram of $[Ag(Sn_9)_2]^{5-}$ (Sn atoms are shown in blue and the Ag atom in silver)

The reaction between the Zintl ion $[Ge_9]^{4-}$ and $[Au(PPh_3)Cl]$ yielded two different products: $[Au_3Ge_{18}]^{5-}$ and $[Au_3Ge_{45}]^{9-}$.[83,84] By stirring K_4Ge_9 with $[Au(PPh_3)Cl]$ for one hour before mixing it with the 2,2,2-crypt, a dimer was isolated with the formula $[Au_3Ge_{18}]^{5-}$ (Figure 1.23, left), where two cages are coordinating to a central Au_3 triangle.

DFT calculations performed on these molecules suggested that there are covalent bonding interactions between the gold atoms and the germanium atoms, but only very weak Au–Au interactions. Each nine-atom cage coordinates to the gold atoms through a triangular face, matching the shape of the Au_3 triangle.

Each gold atom is coordinated in an almost linear manner to two germanium atoms. Interestingly, both of the cages are not crystallographically equivalent. One of the cages has a distorted monocapped square antiprismatic geometry with a 4– charge and the other a distorted tricapped square prismatic geometry with a 3– charge.

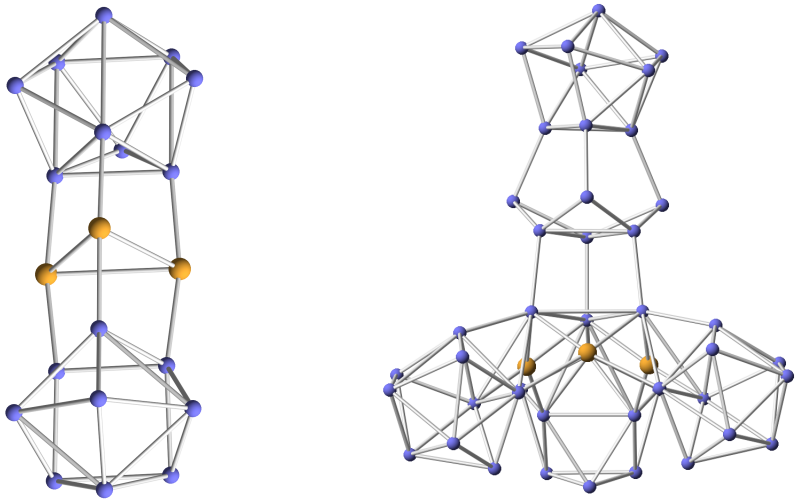

Figure 1.23: Ball and stick diagrams of $[Au_3Ge_{18}]^{5-}$ (left) and $[Au_3Ge_{45}]^{9-}$ (right) (Ge atoms are shown in purple and Au atoms in yellow).

The second product formed was $[Au_3Ge_{45}]^{9-}$ (Figure 1.23, right). This was obtained after stirring the solution for fourteen hours. This cluster consists of three gold atoms, four nine-atom cages and nine separate germanium atoms coordinated to the gold atoms. The three basal nine-atom cages are almost identical and can be described as tricapped trigonal prisms, whereas the top one is better described as a monocapped square antiprism. The basal cages are bonded to two gold atoms each. The three gold atoms and the three clusters form a cyclic unit with near threefold symmetry. Also, the basal cages form one *exo*-bond each to the three adjacent germanium atoms. These germanium atoms act as a bridge to the gold atoms and establish covalent contacts and are roughly in a tetrahedral environment. Each gold atom bonds to four germanium atoms in a square planar coordination mode, which is indicative of Au^{3+} species, rather than Au^{+}. Four germanium atoms coordinate the three gold atoms individually in a trapezoidal fashion.

The asymmetric unit contains two independent cluster units $[Au_3Ge_{45}]^{9-}$, sixteen $[K(2.2.2\text{-crypt})]^+$ units, and two K^+ ions.

A very different reaction profile has been reported for the reaction of K_4Ge_9 and the group 13 organometallic compound $InPh_3$.[85] This reaction, performed in ethylenediamine, yielded three different products: $[In(Ge_9)_2]^{5-}$, $[(Ge_9)_2InPh]^{4-}$ and $[Ge_9(InPh_3)_2]^{4-}$ (Figure 1.24).

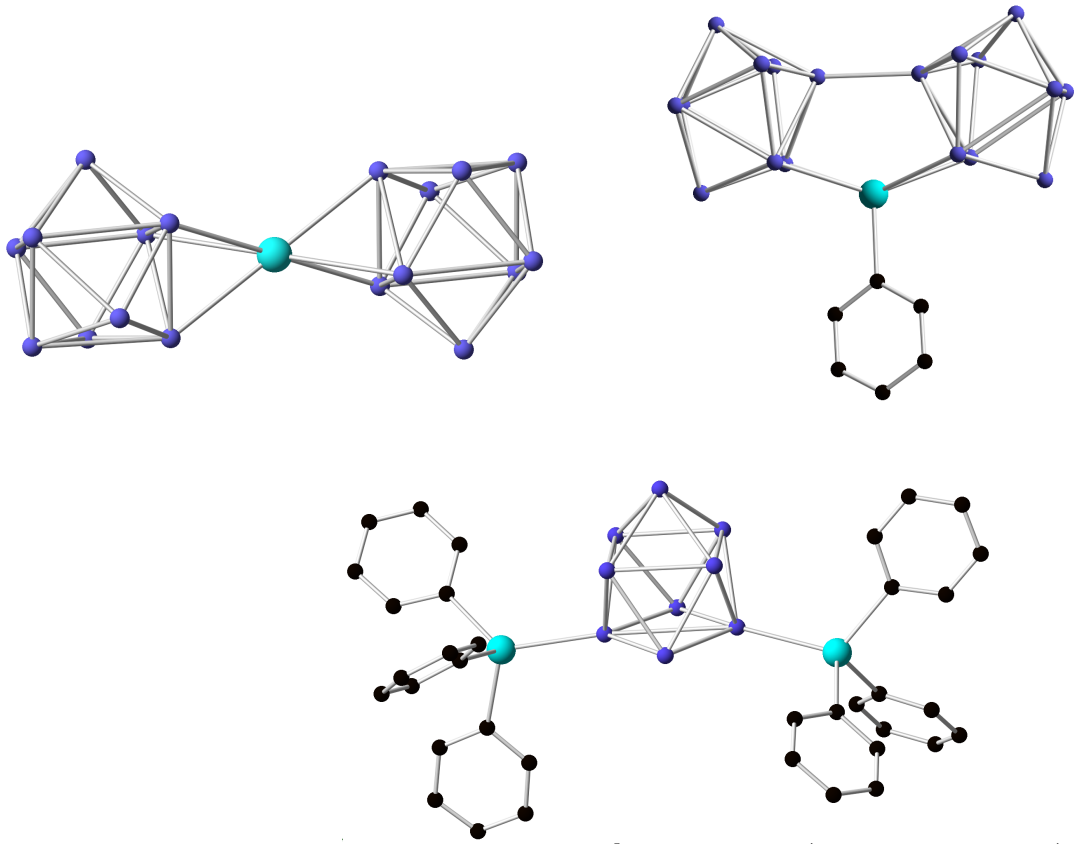

Figure 1.24: Ball and stick diagram of $[In(Ge_9)_2]^{5-}$, $[(Ge_9)_2InPh]^{4-}$ and $[Ge_9(InPh_3)_2]^{4-}$ (Ge atoms are shown in purple, In atoms in cyan and C atoms in black). H atoms are omitted for clarity.

The first product is the "sandwich" compound $[In(Ge_9)_2]^{5-}$, that was prepared by adding two equivalents of $[Ge_9]^{4-}$ to one of $InPh_3$. For this reaction the cleavage of all three In–C bonds has been observed. The total charge of the cluster is 5–, which is consistent with two $[Ge_9]^{4-}$ cluster anions (total charge of 8–) breaking three In–C bonds. The indium

atom exhibits an octahedral geometry coordinated by two $[Ge_9]^{4-}$ cages through triangular faces in an η^3 mode. The cages are in an "up-down" and staggered configuration and each cage has a nearly perfect D_{3d} symmetry.

A similar reaction, performed in a 2:1 ratio of $InPh_3$ to K_4Ge_9 produced $[(Ge_9)_2InPh]^{4-}$ as a minor product. This compound shows an $[InPh]^+$ fragment coordinated by a $[Ge_9–Ge_9]^{6-}$ dimer. Each one of the two clusters coordinates to the indium atom in an η^2 mode. It is postulated that this product may be formed *via* an oxidatively-coupled dimer $[Ge_9–Ge_9]^{6-}$ prior to the reaction of this species with $InPh_3$. Oxidative coupling of two such clusters would release the two electrons needed to cleave two of the In–C bonds in $InPh_3$. Both of the cages are in an "up-up" configuration.

When more than two equivalents of $InPh_3$ were added to the K_4Ge_9 mixture a third product was isolated, namely $[Ge_9(InPh_3)_2]^{4-}$. In this compound the lone pairs of the cluster act as Lewis bases towards two $InPh_3$ molecules forming an *exo*-functionalised cluster. The η^1 coordination mode observed in the molecule can be related to the one observed in $[Ge_{10}Mn(CO)_4]^{3-}$ or in $[(\eta^4\text{-}Ge_9)Cu(\eta^1\text{-}Ge_9)]^{7-}$.[67,80] The structure of the nine-atom cage is somewhere in between a monocapped square antiprism and a tricapped trigonal prism.

1.3.1.5 Reactions of group 14 $[E_9]^{4-}$ clusters towards metallic complexes where cluster activation occurs

Studies have shown that interstitial metal centres are able to stabilise clusters of greater nuclearities than those that are accessible in the absence of an interstitial atom. In the reactions described this far, the maximum number of atoms per cluster observed has

been ten, however, the use of transition metal reagents allows the isolation of endohedral clusters with up to eighteen group 14 atoms. These reactions proceed *via* the cleavage of all the M–L bonds of an organometallic reagent. In the resulting product a metal atom sits in the centre of the cluster, forming the so-called endohedral clusters. There are also cases of ligand stabilised endohedral clusters. Perhaps interestingly, there are also some reports of endohedral clusters containing more than one metal in the central cavity and having external frameworks with greater nuclearities. For these compounds the @ symbol is employed here to refer to an interstitial metal.

1.3.1.5.1 Functionalised endohedral clusters

The first endohedral cluster was reported by Eichhorn in 1996. It was synthesised when reacting $Ni(CO)_2(PPh_3)_2$ with K_4Ge_9 at 118 ºC. X-ray crystallography studies supported the presence of the $[Ge_9Ni(PPh_3)]^{2-}$ cluster with residual electron-density at the centre, which was initially assigned to a germanium atom as $[Ge@Ge_9Ni(PPh_3)]^{2-}$.[86,87] It was not until 2006 when that with the aid of mass spectrometry, the formula of the cluster was correctly reassigned to $[Ni@Ge_9Ni(PPh_3)]^{2-}$ (Figure 1.25).

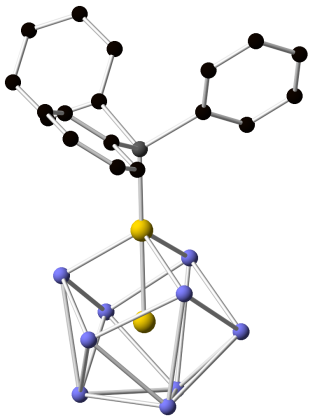

Figure 1.25: Ball and stick diagram of $[Ni@Ge_9Ni(PPh_3)]^{2-}$ (Ge atoms are shown in purple, Ni atoms in yellow, the P atom in grey and C atoms in black). H atoms are omitted for clarity.

The formation of this cluster proceeds *via* the loss of both (CO) ligands from the organometallic precursor and subsequent incorporation of a $Ni(PPh_3)$ unit as a 10^{th} vertex to form a hyper-*closo* system that has an open "*nido*-type" architecture. The capping nickel atom does not interact in a conventional η^4 fashion through the open face. Instead it coordinates through one of the two triangular bases of the tricapped trigonal prism after the cleavage of three Ge–Ge bonds. The central nickel atom does not contribute any electrons to cluster bonding as it has a d^{10} closed-shell configuration.

When the same reaction is performed at lower temperatures (40 ºC) a larger endohedral cluster could be isolated, $[Ni_6Ge_{13}(CO)_5]^{4-}$ (Figure 1.26). This cluster can be seen as two interpenetrating icosahedral units that share a central $Ge_3Ni_2(CO)_2$ pentagonal ring. Each unit has an endohedral nickel atom at the centre of the cluster. Both icosahedral fragments have different compositions: one is $Ge_7Ni_2(CO)_2$ and the other is $Ge_9Ni_2(CO)_2$.

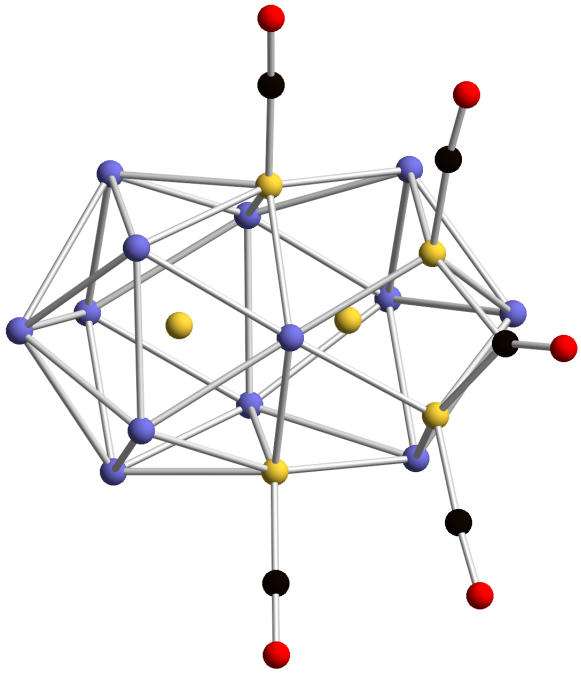

Figure 1.26: Ball and stick diagram of $[Ni_6Ge_{13}(CO)_5]^{4-}$ (Ge atoms are shown in purple, Ni atoms in yellow, C atoms in black and O atoms in red).

In 2006, Sevov published the formation of very similar clusters to those discussed above exhibiting different ligands on the capping nickel atom. By first reacting K_4Ge_9 with $Ni(COD)_2$ followed by the addition of one equivalent of $Ni(CO)_2(PPh_3)_2$ they were able to isolate $[Ni@Ge_9Ni(CO)]^{2-}$. The labile CO ligand could then be substituted with C≡C–Ph or ethylenediamine (increasing the charge to 3– for ethylenediamine).[68]

In 2009, Wang *et al*. published the insertion of a nickel atom into the previously reported $[Ge_9Pd(PPh_3)]^{3-}$ cluster, prepared by the reaction of K_4Ge_9 with $Pd(PPh_3)_4$ in the presence of 2,2,2-crypt.[88] The insertion is performed by the reaction of $[Ge_9Pd(PPh_3)]^{3-}$ with one equivalent of $Ni(PPh_3)_4$ to yield the endohedral cluster $[Ni@Ge_9Pd(PPh_3)]^{2-}$. Although the original cluster exhibited conventional η^4 coordination mode through the open square face, in the endohedral cluster the coordination changed to one similar to the $[Ni@Ge_9Ni(PPh_3)]^{2-}$ cluster mentioned above.

Descending group 14, in 2002 Eichhorn studied the reaction of the K_4Sn_9 Zintl phase towards $Ni(CO)_2(PPh_3)_2$ to form $[Ni@Sn_9Ni(CO)]^{3-}$ (Figure 1.27).[89] Despite the fact that this cluster has a similar composition to the germanium analogue reported by Sevov ($[Ni@Ge_9Ni(CO)]^{2-}$), the charge reported for the tin cluster is 3–. The geometry of the cluster also differs from the germanium species. It displays a "normal" bicapped square antiprismatic geometry in which the carbonyl group is collinear with the two nickel atoms and the capping tin atom. This gives rise to a total of 21 valence electrons giving a slightly distorted, 10-vertex *closo* geometry. EPR confirmed the paramagnetic nature of this cluster showing a five-line pattern due to the 4.8 G hyperfine interactions involving all the nine tin atoms.

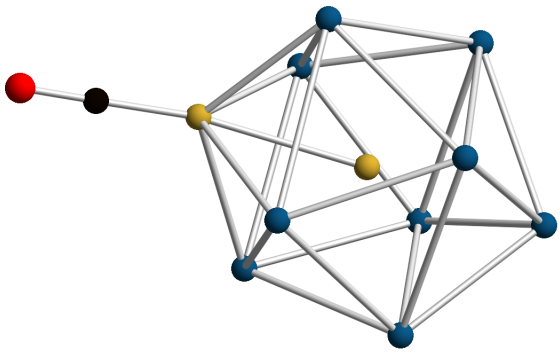

Figure 1.27: Ball and stick diagram of $[Ni@Sn_9Ni(CO)]^{3-}$ (Sn atoms are shown in blue, Ni atoms in yellow, the C atom in black and the O atom in red).

In the same study the $[Pt@Sn_9Pt(PPh_3)]^{2-}$ cluster is shown to be accessible through the reaction between K_4Sn_9 and $Pt(PPh_3)_4$ and to exhibit the same "alternative" geometry as $[Ni@Ge_9Ni(PPh_3)]^{2-}$.[89] $[Pt@Sn_9Pt(PPh_3)]^{2-}$ displays a structure consistent with an elongated tricapped trigonal prism with a capping $Pt(PPh_3)$ unit and an interstitial platinum atom. The cluster has a total of 20 valence electrons and a 10-vertex hyper-*closo* structure. ^{119}Sn NMR spectroscopy revealed that the structure is fluxional in solution on the NMR timescale, exhibiting only one signal.

Eichhorn has also shown that alternative tin precursors are applicable for endohedral cluster synthesis. $[Sn_9–SnCy_3]^{3-}$ (prepared by reacting K_4Sn_9 with $[Cy_3SnCl]$) was shown to react with $[Pd(PPh_3)_4]$ to form two different endohedral clusters: $[Pd@Sn_9–SnCy_3]^{3-}$ and $[Pd@Sn_9Pd(SnCy_3)]^{3-}$ *via* the addition of one or two equivalents of the palladium reagent, respectively.[90] For $[Pd@Sn_9–SnCy_3]^{3-}$ only the insertion of a palladium atom to the cavity is observed, whereas for $[Pd@Sn_9Pd(SnCy_3)]^{3-}$ an interstitial palladium atom plus a capping $Pd(SnCy_3)$ fragment are incorporated into the cluster. The $[Pd@Sn_9PdSnCy_3]^{3-}$ cluster displays the same coordination mode as the previously discussed $[Ni@Ge_9Ni(PPh_3)]^{2-}$ cluster.

1.3.1.5.2 Substituent-free endohedral clusters

As mentioned in the introduction, some endohedral clusters are ligand-free, and consist of an external framework with a metal within the internal cavity. To date the simplest endohedral cluster reported has nine atoms and an interstitial metal atom and the largest has eighteen E atoms. The larger cluster anions can accommodate anywhere between one and three interstitial metal atoms depending on the size of the cavity.

1.3.1.5.3 Nine-atom endohedral clusters

The most fundamental endohedral cluster consist of a $[E_9]^{4-}$ cluster with a single interstitial atom: $[M@E_9]^{n-}$ (M = Ni: E = Ge and Sn: n = 3; M = Cu: E = Sn, Pb: n = 3).

The "naked" clusters $[Ni@E_9]^{3-}$ (E = Ge and Sn) (Figure 1.28) were synthesised *via* the reaction of the respective nine-atom cage and $Ni(COD)_2$ in ethylenediamine in the presence of 2,2,2-crypt.[68,91,92] The solid-state structures of these clusters, revealed a tricapped trigonal prismatic geometry with two or three elongated prismatic heights parallel to the three-fold rotation axis for the germanium or tin analogues, respectively. Upon insertion of a nickel atom these clusters suffer a distortion and become almost spherical compared to the $[E_9]^{3-}$ precursors. The interstitial nickel atoms have a d^{10} closed-shell configuration and therefore donate no electrons to cluster bonding. The clusters have a total of 21 skeletal electrons, analogous to the empty $[E_9]^{3-}$ species, and can be described as $[Ni^0@(E_9)^{3-}]$. Moreover, all of the Ni–E distances are very similar, optimising the interaction between the nickel atom and the cluster framework.

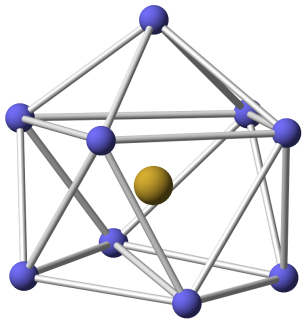

Figure 1.28: Ball and stick diagram of $[Ni@Ge_9]^{3-}$ (Ge atoms are shown in purple and the Ni atom in yellow).

Further reactivity of the naked $[Ni@E_9]^{3-}$ (E = Ge and Sn) clusters was reported by Sevov in 2011. The reactions of TlCp and $[Ni@E_9]^{3-}$ led to the *closo* 10-vertex cluster $[Ni@E_9Tl]^{3-}$ (E = Ge and Sn) with a bicapped square antiprismatic geometry (Figure 1.29).[93] The same product can also be isolated *via* the reaction between $[Sn_9]^{4-}$ and TlCp followed by the addition of $Ni(COD)_2$. Interestingly, the nickel atom remains in the centre of the tin cluster, whether the thallium atom is present or not.

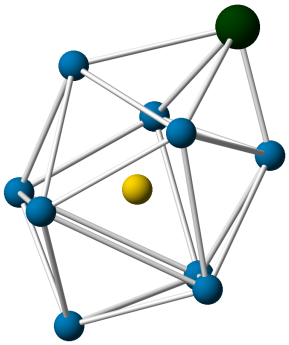

Figure 1.29: Ball and stick diagram of $[Ni@Sn_9Tl]^{3-}$ (Sn atoms are shown in blue, the Ni atom in yellow and the Tl atom in dark green).

The thallium vertex contributes only one electron to the skeletal bonding, making a total of 22 electrons giving a *closo* cluster.

Endohedral $[Cu@E_9]^{3-}$ (E = Sn and Pb) clusters have been synthesised in DMF and in the presence of 2,2,2-crypt by reacting the respective K_4E_9 Zintl phases with

$[Cu(mes)]_5$.[94] The clusters adopt an elongated tricapped trigonal prismatic geometry with almost perfect D_{3h} symmetry. All the Cu–E distances are very similar. However, for the copper atom at the centre of the cluster to have a closed-shell d^{10} configuration it needs to be Cu^+, which was confirmed by DFT calculations on the cluster $[Cu^+@(E_9)^{3-}]$. This makes the $[Cu@E_9]^{3-}$ cluster diamagnetic, allowing NMR measurements to be performed. ^{119}Sn NMR spectroscopy revealed that all the E atoms in the spherical cluster are equivalent on the NMR timescale, showing a quartet at δ = 1440 ppm due to the coupling to the copper atom (^{63}Cu 69% and ^{65}Cu 31%: I = 3/2). Additionally, due to the coupling with ^{117}Sn, satellites were also observed. ^{63}Cu NMR studies show one sharp resonance at δ = –330 that shows the typical $^{117/119}$Sn coupling satellites.

Although most examples of naked endohedral clusters can be prepared from the reaction of the corresponding Zintl phase and an organometallic precursor in solution, there are some examples of clusters that were prepared by alternative methods. $[Ni@Sn_9]^{4-}$ and $[Co@Sn_9]^{5-}$ were prepared by the solid-state reaction of the elements in the melt.[95] The Zintl phases $Na_{12}Ni_{1-x}Sn_{17}$ and $K_{13-x}Co_{1-x}Sn_{17}$ were prepared and they were subsequently dissolved in ethylenediamine in the presence of a sequestering agent to yield the respective clusters. $[Ni@Sn_9]^{4-}$ has been also prepared by the dissolution of the Zintl phase $K_4Sn_9Ni_3$ in ethylenediamine in the presence of 18-crown-6.[92]

1.3.1.5.4 **Ten-atom endohedral clusters**

The reaction of $Ni(COD)_2$ and the K_4E_9 Zintl phases (E = Ge and Sn) yields the nine-atom cluster mentioned in previous section, namely $[Ni@E_9]^{3-}$.[68,91,92] However, the analogous reaction with the K_4Pb_9 Zintl phase results in cluster activation and two different products can be isolated $[Ni@Pb_{10}]^{2-}$ and the minor side product, $[Ni@Pb_{12}]^{2-}$

(Figure 1.30).[96,97] The resulting 10-atom cluster has a total of 22 skeletal electrons, which corresponds to a *closo* cluster. The structure was confirmed by single crystal X-ray crystallography. It has a bicapped trigonal antiprismatic geometry with a D_{4d} symmetry. The d^{10} closed-shell nickel atom does not contribute any electrons to the skeletal bonding.

Similar to other lead clusters, ^{207}Pb NMR spectroscopy showed that all lead atoms are equivalent on the NMR timescale, revealing cluster fluxionality. The mechanism for formation of this cluster still remains unclear, however, it is known that during the reaction, the COD ligand is reduced to cyclooctene, which was detected by mass spectrometric measurements.

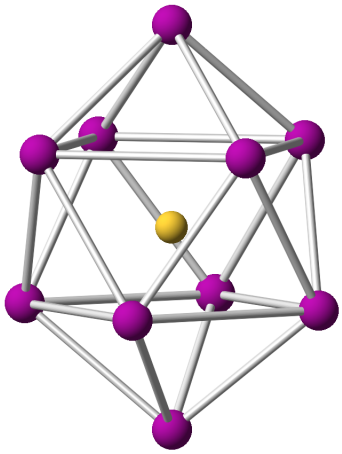

Figure 1.30: Ball and stick diagram of $[Ni@Pb_{10}]^{2-}$ (Pb atoms are shown in magenta and the Ni atom in yellow).

The reaction between K_4Sn_9 and $[Fe(mes)_2]_2$ led to the formation of the $[Fe@Sn_{10}]^{3-}$ endohedral cluster.[98] X-ray crystallography studies were very challenging due to the spherical shape of the cluster and rotational disorder: it has two components (60% to 40%) exhibiting similar geometries. It exhibits a C_s geometry but is not too far from a distorted D_{4d} symmetry (similarly to the $[Ni@Pb_{10}]^{2-}$ cluster). It has 23 skeletal electrons

and is paramagnetic. EPR measurements revealed a weak and a broad resonance centred at g = 2.0229. Since the solid-state structure was severely disordered, DFT calculations had to be performed in order to confirm its structure. The studies showed that there is some degree of back-donation from the iron centre to the cage and its structural global minimum lies on a very flat surface connecting D_{4d}, C_{2v} and C_{3v}-symmetric minima. This suggests a very plastic structure that may be easily deformed by the surrounding crystal environment.

1.3.1.5.5 **Twelve-atom endohedral clusters**

The reaction of $[Sn_9]^{4-}$ with [Ir(COD)Cl] yielded the coordination compound $[Sn_9Ir(COD)]^{3-}$, which was subsequently oxidised in the presence of PPh_3 or dppe ($Ph_2PCH_2CH_2PPh_2$) to yield the nearly perfect I_h symmetric cluster $[Ir@Sn_{12}]^{3-}$ (Figure 1.31).[99]

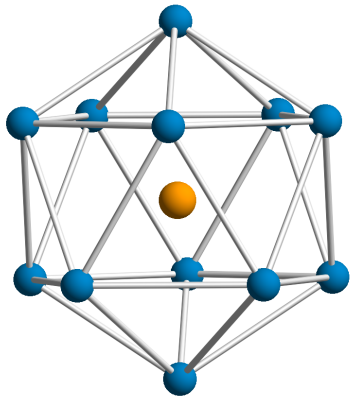

Figure 1.31: Ball and stick diagram of $[Ir@Sn_{12}]^{3-}$ (Sn atoms are shown in blue and the Ir atom in orange).

DFT calculations suggested that the iridium atom is negatively polarised and can be considered as an iridium (–I) with the formula $[Ir^{-}@(Sn_{12})^{2-}]$. The iridium (–I) ion has a d^{10} configuration and does not contribute any electrons to cluster bonding. The skeletal

electron count is 26 electrons, corresponding to a *closo* cluster. This *closo* geometry was confirmed by single crystal X-ray crystallography. Similar to other endohedral clusters, all the Ir–Sn distances are very similar and are significantly longer than conventional Ir–Sn single bonds. This is indicative of a small degree of interaction between the interstitial iridium atom and the cage.

A series of compounds were reported with the general formulae $[M@Pb_{12}]^{2-}$ (M = Pd, Pt and Ni).[97,100] These clusters were prepared by reacting the K_4Pb_9 Zintl phase with $M(PPh_3)_4$ (M = Pd and Pt) and $Ni(COD)_2$, respectively. It is worth noting that $[Ni@Pb_{12}]^{2-}$ was only observed as a minor product alongside $[Ni@Pb_{10}]^{2-}$. For the palladium and platinum centred clusters, it is believed that the PPh_3 ligands are the oxidising agents that drive the reaction, similar to the $[Ir@Sn_{12}]^{3-}$ cluster.[99] ^{207}Pb NMR spectroscopic studies on $[M@Pb_{12}]^{2-}$ (M = Ni, Pd and Pt) revealed an unusually deshielded resonance presumably associated with a σ-aromatic effect caused by the high symmetry. This is reflected in the difference between the chemical shift observed for $[Ni@Pb_{12}]^{2-}$ which is observed over 2000 ppm more deshielded than the $[Ni@Pb_{10}]^{2-}$ cluster ($[Ni@Pb_{12}]^{2-}$: δ = 1167; $[Ni@Pb_{10}]^{2-}$: δ = –996). For each of these clusters ^{207}Pb NMR spectroscopy exhibited only one resonance, and in the case of the $[Pt@Pb_{12}]^{2-}$, coupling of the twelve lead atoms with the platinum atom was observed and verified by ^{195}Pt NMR spectroscopy.

As observed by X-ray crystallography, the *closo* shape of the I_h symmetric $[M@Pb_{12}]^{2-}$ clusters is consistent with an electron count at 26 skeletal electrons. All of the bond lengths decrease, as the endohedral metal gets smaller. However, as the interstitial metal gets smaller the cluster becomes more distorted with bond lengths that are more dissimilar. The platinum atom appears to be the metal that best fits into the internal

cavity, as all the Pt–Pb and Pb–Pb distances are virtually identical. This is consistent with the observation that nickel, being the smallest metal, prefers to be encapsulated by ten lead atoms rather than by twelve.

The highly distorted cluster with an unconventional geometry, $[Mn@Pb_{12}]^{3-}$ (Figure 1.32), is the product of the reaction between K_4Pb_9 and $[Mn(mes)_2]_3$ in ethylenediamine and in the presence of 2,2,2-crypt.[101] The reaction is thought to proceed *via* the reductive cleavage of the Mn–C bonds. Elemental lead is observed as a metallic precipitate as a side product of the reaction.

An X-ray crystallographic analysis showed that there are three $[Mn@Pb_{12}]^{3-}$ clusters in the unit cell. Two of the clusters exhibit a C_{2h} symmetry and the third one a D_{2h} symmetry, which deviates from the I_h symmetry observed in the other clusters reported. Furthermore unlike the other $[M@E_{12}]^{n-}$ clusters, the Mn–Pb distances are not equal, there are three sets of different Mn–Pb distances.

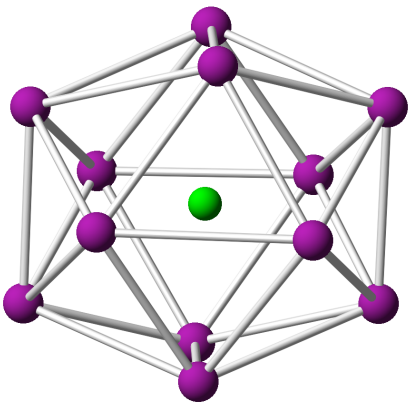

Figure 1.32: Ball and stick diagram of $[Mn@Pb_{12}]^{3-}$ (Pb atoms are shown in magenta and the Mn atom in green).

EPR measurements confirmed the paramagnetic character of $[Mn@Pb_{12}]^{3-}$, featuring a broad resonance with a *g* factor of 2.0095. The broad nature of the resonance is likely to

be indicative of a fast relaxation effect owing to spin-orbit coupling. The distorted geometry of this cluster was confirmed by DFT calculations. The optimised computed geometry revealed a global minimum with D_{3d} symmetry, although there is a D_{2h} stationary point lying only 0.2 eV above it. The experimental values obtained for the D_{2h} cluster and the calculated ones were in agreement and the structural differences between the two D_{3d} and D_{2h} are very small. Additionally, the perfect I_h cluster lays 0.46 eV above the minimum. DFT calculations indicate that cage prolation is due to a substantial transfer of electron-density from the formally Mn^- centre to the low-lying vacant orbitals of the $[Pb_{12}]^{2-}$ cage.

1.3.1.5.6 **High-nuclearity endohedral clusters**

Interestingly, when reacting $Ni(COD)_2$ with either K_4Ge_9 or K_4Sn_9 in a 1:1 ratio the product is $[Ni@E_9]^{3-}$, (Section 1.3.1.5.3) but if an excess (3:1) of the metal precursor is added different products can be accessed. The reaction of K_4Ge_9 and three equivalents of $Ni(COD)_2$ yields $[Ni_3@(Ge_9)_2]^{4-}$ (Figure 1.33, left).[91] This compound that can be considered as two nine-atom germanium clusters interconnected by a nickel atom. Additionally, each cluster contains an interstitial nickel atom. This cluster could also be considered as a linear Ni_3 unit with two D_{3h}-symmetric nonagermanide cages surrounding each of the terminal nickel atoms. Both cages are in a staggered conformation.

The analogous reaction with K_4Sn_9 yielded the endohedral $[Ni_2@Sn_{17}]^{4-}$ cluster consisting of two nickel-centred tin clusters, fused by a single tin vertex, presenting a D_{2d} symmetry (Figure 1.33, right).[102] ^{119}Sn NMR experiments on $[Ni_2@Sn_{17}]^{4-}$ showed that the cluster exhibits high fluxionality. Variable temperature experiments at –64 ºC

revealed four distinct tin environments with 4:8:4:1 relative intensities. Upon gradually heating the solution to 44 ºC, the three more intense resonances broaden and eventually disappear into the baseline. The fourth resonance, corresponding to the linking tin atom, is present at all temperatures. At 60 ºC a second resonance appears, this is indicative that at higher temperatures all the tin atoms in the cluster interchange apart from the linking tin atom.

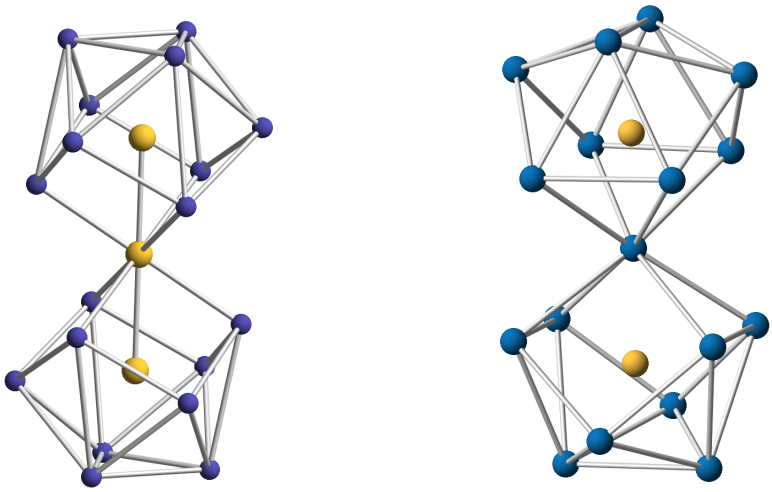

Figure 1.33: Ball and stick diagram of $[Ni_3@(Ge_9)_2]^{4-}$ (left) and $[Ni_2@Sn_{17}]^{4-}$ (right) (Ge atoms are shown in purple, Sn atoms in blue and Ni atoms in yellow.

A cluster isostructural with $[Ni_2@Sn_{17}]^{4-}$ with cobalt in place of nickel, was reported by Fässler in 2012 $[Co_2@Sn_{17}]^{5-}$.[103] This cluster was not prepared by the solution reactivity of the K_4Sn_9, but was extracted from a new Zintl phase with the formula $K_{5-x}Co_{2-x}Sn_9$. Later on, another Zintl phase was discovered to also yield $[Co_2@Sn_{17}]^{5-}$ in solution, namely $K_{4.79}Co_{0.79}Sn_9$.[104] Dissolution of this Zintl phase in ethylenediamine lead to the extraction of $[Co_2@Sn_{17}]^{5-}$ and $[Co_{0.68}@Sn_9]^{4-}$. The latter consists of overlaying $[Co@Sn_9]^{4-}$ and $[Sn_9]^{4-}$ cluster anions forming infinite $K[Co_{0.68}@Sn_9]$ chains. $[Co_2@Sn_{17}]^{5-}$ was studied by EPR and DFT calculation confirming its stability.

In 2011, Sevov reported the synthesis of $[\{Ni@Sn_8(\mu–Ge)_{1/2}\}_2]^{4–}$, a cluster similar to $[Ni_2@Sn_{17}]^{4–}$ but with a germanium atom linking the two $[Ni@Sn_8]$ units.[92] This was prepared by mixing the tertnary precursor "$K_4Ge_{4.5}Sn_{4.5}$", which is known to produce heteroatomic $Ge_{9–x}Sn_x$ clusters, with $Ni(COD)_2$.

The $[Pt_2@Sn_{17}]^{4–}$ (Figure 1.34) cluster can be formed by the reactions of K_4Sn_9 with $Pt(nbe)_3$ or $Pt(PPh_3)$.[105] The latter gives a range of products including $[Sn_9Pt(PPh_3)_x]^{4–}$, $[Pt@Sn_9Pt(PPh_3)]^{2–}$, $[Pt_2@Sn_{17}]^{4–}$ and $[Pt@Sn_9H_3]^{–}$. Solid-state studies revealed a very different structure to the previously discussed $[Ni_2@Sn_{17}]^{2–}$ cluster, despite their isoelectronic relationship. $[Pt_2@Sn_{17}]^{4–}$ shows a "capsule" like cluster which can be seen as two $[PtSn_6]$ moieties linked together by a central planar $[Sn_5]$ ring. The Pt–Pt distance suggests that there is no bonding interaction between the interstitial platinum atoms. The difference in structure between $[Pt_2@Sn_{17}]^{4–}$ and $[Ni_2@Sn_{17}]^{2–}$ is likely to be due to the greater steric demands of the platinum atoms, resulting in a larger cluster. It is important to remark that the same metallic precursor, $Pt(PPh_3)_4$, reacted with the K_4Pb_9 Zintl phase in a very different way forming $[Pt@Pb_{12}]^{2–}$.[100]

Interestingly, ^{119}Sn NMR spectroscopy showed that on the NMR timescale all the tin atoms are equivalent in $[Pt_2@Sn_{17}]^{4–}$, showing only one resonance. This shows that the cluster is fluxional in solution and all tin atoms participate in a quick and dynamic exchange at room temperature and at –60 ºC. Additionally, in the ^{195}Pt NMR spectrum one resonance was observed with coupling to all seventeen tin atoms. This observation allows us to consider the cluster as two platinum atoms at the core surrounded by a liquid-like tin shell.

Electronically, the cluster has 38 skeletal electrons according to Wade's rules. Clusters of this size are too large, compared to those normally described by rules for bonding in electron-deficient clusters. Such rules do not account for bonding in multifocus clusters. Therefore $[Pd_2@Sn_{17}]^{4-}$ does not fit into a classical deltahedral bonding model.

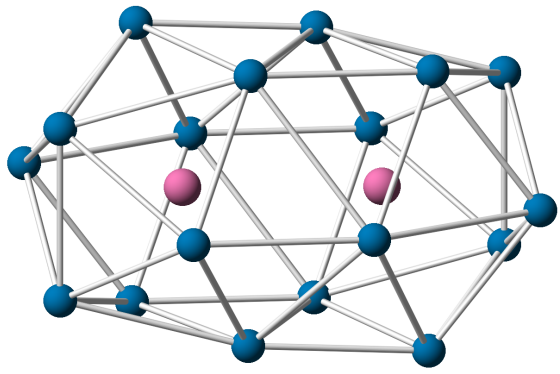

Figure 1.34: Ball and stick diagram of $[Pt_2@Sn_{17}]^{4-}$ (Sn atoms are shown in blue and Pt atoms in pink).

The largest endohedral cages prepared by the solution reactivity of a K_4E_9 Zintl phase known to date are $[Pd_2@E_{18}]^{4-}$ (E = Ge and Sn) (Figure 1.35).[106–108] These clusters were synthesised by the reaction of a K_4E_9 Zintl phase with $Pd(PPh_3)_4$ in ethylenediamine. The analogous reaction with the K_4Pb_9 Zintl phase affords a much smaller cluster $[Pd@Pb_{12}]^{2-}$. The 18-atom cages are capsule-like and can be described as two $[PdE_6]$ units connected by a central E_6 central ring. The d^{10} platinum atoms do not contribute any electrons to cluster bonding; therefore the 18-vertex cluster has a total of 40 skeletal electrons. This would suggest a *nido* cluster, which is inconsistent with the crystallographic data. The cluster can be seen as two Pd^0 surrounded by a $[E_{18}]^{4-}$ cage. The Pd–Pd distances are smaller in the germanium analogue, but in both cases it is not considered as a bonding interaction. ^{117}Sn NMR studies on $[Pd_2@Sn_{18}]^{4-}$ revealed similar behaviour to $[Pd_2@Sn_{17}]^{4-}$, where only one resonance was observed between –50 ºC to

+10 ºC for all of the tin atoms of the cage. This again suggests a dynamic process in which all the atoms rapidly interchange.

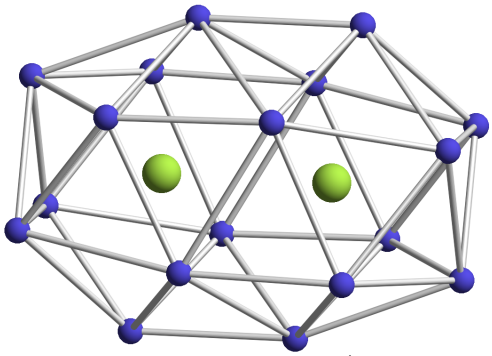

Figure 1.35: Ball and stick diagram of $[Pd_2@Ge_{18}]^{4-}$ (Pd atoms are shown in green and Ge atoms in purple.)

There is a theory behind the formation of these large clusters: the reaction of K_4Ge_9 and $CuCl(P^iPr_3)$ in liquid ammonia leads to two different products: $[Cu(\eta^4\text{-}Ge_9)(P^iPr_3)]^{3-}$ at –70 ºC and $[Cu(\eta^4\text{-}Ge_9)(\eta^1\text{-}Ge_9)]^{7-}$ at –40 ºC.[80] For the latter, loss of a P^iPr_3 ligand is observed and it is replaced by an η^1-Ge_9 cluster. This may suggest that molecules similar to $[Cu(\eta^4\text{-}Ge_9)(\eta^1\text{-}Ge_9)]^{7-}$ may be formed as intermediaries to the capsule-like clusters and then rearrange to form endohedral clusters. The number of atoms involved in the external cluster depends on the nature or size of the interstitial heteroatom at the core.[109] This can be supported by the previous reports where metal atoms are both capping and filling a cluster, like $[Ni@Sn_9Ni(CO)]^{2-}$ or $[Pt@Sn_9Pt(PPh_3)]^{2-}$.[89]

Figure 1.36 shows the resemblance of $[Ni@Ge_9Ni(PPh_3)]^{2-}$ to $[Ni_3@(Ge_9)_2]^{4-}$ after a PPh_3 ligand has been replaced by a $Ni@Ge_9$ unit and subsequent formation of bonds between the adjacent clusters to form $[Pd_2@Ge_{18}]^{4-}$.

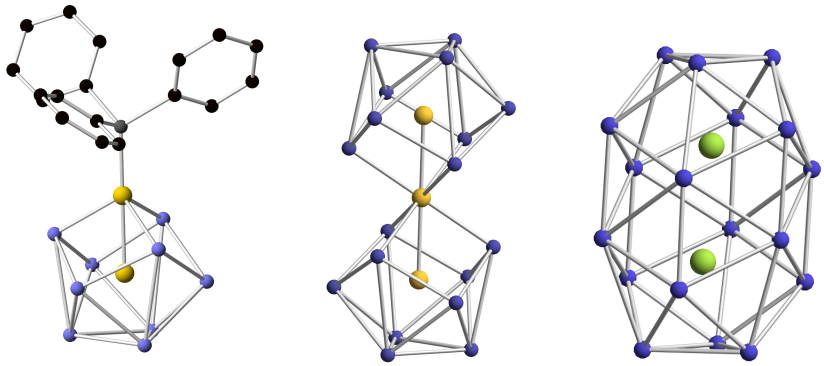

Figure 1.36: Ball and stick diagram of $[Ni@Ge_9Ni(PPh_3)]^{2-}$, $[Ni_3@(Ge_9)_2]^{4-}$ and $[Pd_2@Ge_{18}]^{4-}$ (Ge atoms are shown in purple, Ni atoms in yellow, Pd atoms in green and C atoms in black) H atoms are omitted for clarity.

The largest endohedral compound reported was not prepared by the reaction in solution of the K_4Sn_9 Zintl phase. A ternary Zintl phase was prepared with the formula $A_{12}Cu_{12}Sn_{21}$ (A = Na to Cs) with a reaction in the solid-state.[110] Upon dissolving the Zintl phase the $[Sn@Cu_{12}@Sn_{20}]^{12-}$ (Figure 1.37) cluster was found in solution.

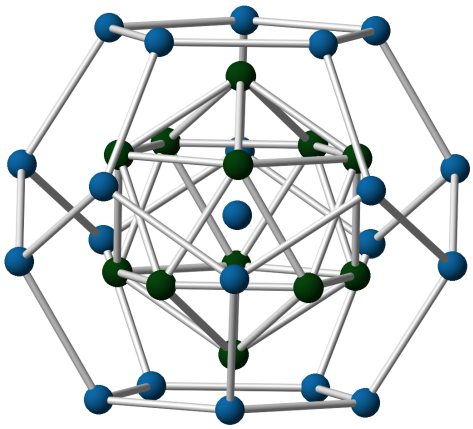

Figure 1.37: Ball and stick diagram of $[Sn@Cu_{12}@Sn_{20}]^{12-}$ (Sn atoms are shown in blue and Cu atoms in dark green).

The X-ray crystallography studies revealed an "onion"-like cluster where at the core of the cluster there is a single tin atom surrounded by a $[Cu_{12}]$ icosahedron, and an external layer, which is a $[Sn_{20}]$ pentagonal dodecahedra cluster.

1.3.1.5.7 **Non-deltahedral endohedral clusters**

Whereas most endohedral complexes to date have exhibited deltahedral structures, in 2009, Goicoechea and Fässler reported the first non-deltahedral clusters $[M@Ge_{10}]^{3-}$ (M = Fe and Co) (Figure 1.38).[111,112] The clusters were synthesised by the reaction between the K_4Ge_9 Zintl phase and $FeAr_2$ or $[Co(C_8H_{12})(C_8H_{13})]$, respectively.

The clusters do not have triangular faces and each germanium is three-connected; more similar to an electron-precise species. Their solid-state structures exhibit a pentagonal prismatic D_{5h} geometry with an interstitial metal atom in the central cavity. For $[Fe@Ge_{10}]^{3-}$, the Fe–Ge distances are the longest Fe–Ge bonds to be reported, implying that there is only weak interaction between the cage and the interstitial metal.

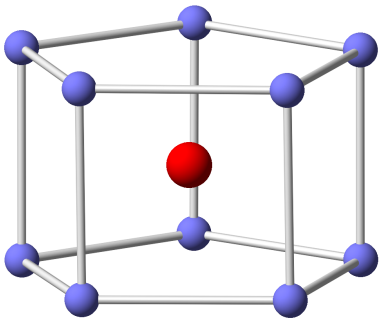

Figure 1.38: Ball and stick diagram of $[Fe@Ge_{10}]^{3-}$ (Ge atoms are shown in purple and the Fe atom in red).

DFT calculations performed on $[Co@Ge_{10}]^{3-}$ suggest that the interstitial cobalt atom carries a 1.05– charge, with a d^{10} closed-shell configuration. This implies that the cobalt atom has an additional electron available for cluster bonding. For the paramagnetic $[Fe@Ge_{10}]^{3-}$ species, DFT calculations revealed that the deltahedral D_{4d} geometry lies 0.58 eV higher in energy than the observed D_{5h} geometry. It was shown that when going from a deltahedral D_{4d} symmetry to the D_{5h} symmetry, four empty cluster-based orbitals could overlap with high-lying metal d orbitals. This stabilises these unoccupied orbitals

and transfers some ß-spin density onto the cage. The pentagonal prism-like structure is caused by a transfer of density from the iron atom to the cage.

These species are especially interesting in respect to their electronic structure. If each germanium atom contributes two electrons to the skeletal cluster bonding (the two electrons in the lone pair pointing radially away from the cluster that do not participate in cluster bonding), there are a total of 23 electrons, contributed by the outer cluster including the 3– charge. The interstitial atom contributes eight valence electrons summing to a total of 31 electrons. This is one too many electrons for an electron-precise structure for which 30 electrons to form 15 conventional two-centre, two-electron bonds are needed without taking into account the interstitial atoms. There are also too few electrons to be a deltahedral cluster missing seven vertices (36 electrons). Interestingly, calculations performed on $[M@Ge_{10}]^{2-}$ (M = Pd and Pt) revealed that these clusters would also adopt a D_{5h} geometry as well, but they have yet to be synthesised.

1.3.2 Group 15 $[E'_7]^{3-}$ Zintl ions

1.3.2.1 Oxidative coupling reactions of group 15 $[E'_7]^{3-}$ Zintl ions

Similarly to group 14 Zintl ions, group 15 clusters can also form higher nuclearity species by oxidative processes. Von Schnering and co-workers reported in 1981 the first synthesis of $[P_{16}]^{2-}$ by mixing Na_3P_7 with $[PPh_4]Cl$ in THF.[113] This cluster consists of two seven-atom cages bridged by a $[P_2]$ fragment. Both of the cages are pointing in the same direction with an "up-up" conformation. Baudler, in 1985, reported another two syntheses for the $[P_{16}]^{2-}$ anion via the disproportionation of the monoprotonated $[HP_7]^{2-}$ cage in THF and by reacting white phosphorus with $LiPH_2$.[114,115] The ^{31}P NMR spectrum

of this species shows six resonances (δ = 60, 38, 6, –34, –134 and –172 ppm) with relative intensities of 2:1:1:1:1:2.

There are reports of other polypnictide cages that contain seven-atom cages, but their synthesis has not used the $[P_7]^{3-}$ anion as a precursor. All of these clusters show the same electronic features as the $[P_7]^{3-}$ cage, they have conventional two-centre, two-electron bonds and the negative charges are localised on the two-connected atoms. Similar to the $[Ge_9–Ge_9]^{6-}$ dimer, Korber reported a dimeric species $[E'_7–E'_7]^{4-}$ (E' = P and As), but as mentioned earlier, they were not synthesised using a Zintl phase. The phosphorus dimer was synthesised by the reduction of white phosphorus with lithium in liquid ammonia, whereas the arsenic analogue was synthesised by the reduction of Rb_4As_6 with $SbPh_3$ in the presence of 18-crown-6.[116] These cages are linked by a single conventional covalent bond and the clusters are arranged in an alternating "up-down" motif.

In 2006, Miluykov reported an alternative synthesis for the $[P_{14}]^{4-}$ dimer. It was obtained either by refluxing PCl_3 and elemental sodium or by mixing elemental sodium and red phosphorus in ethylenediamine.[117] No ^{31}P NMR spectra have been reported for this dimer to date.

A larger polyphosphide can be formed by oxidative coupling of three $[P_7]^{3-}$ cages affording $[P_{21}]^{3-}$ (Figure 1.39). $[P_{21}]^{3-}$ was synthesised by reacting white phosphorus with substoichiometric amounts of sodium in DME or THF.[118] The ^{31}P NMR spectrum of $[P_{21}]^{3-}$ shows seven resonances (δ = 72, 61, –15, –108, –118, –146 and –169 ppm) with relative intensities 2:8:2:1:2:2:4.

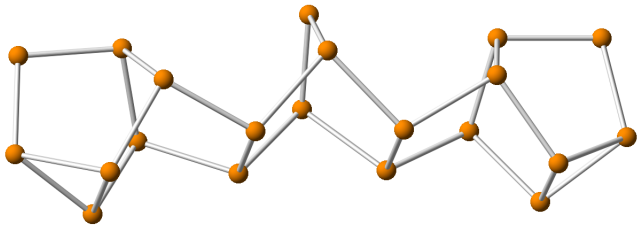

Figure 1.39: Ball and stick diagram of $[P_{21}]^{3-}$.

In 1995, Guerin and Richeson reported a redox interconversion between $[P_{16}]^{2-}$ and $[P_{21}]^{3-}$.[119] K_2P_{16} was dissolved in THF and ^{31}P NMR spectroscopy and X-ray fluorescence proved the full conversion to $[P_{21}]^{3-}$ and elemental phosphorus. Upon removing the THF and dissolving the remaining solid in ethanol conversion back into $[P_{16}]^{2-}$ was confirmed by ^{31}P NMR spectroscopy.

1.3.2.2 *Exo*-functionalisation of group 15 $[E'_7]^{3-}$ clusters with main group reagents

Reactions between $[E'_7]^{3-}$ anions and selected main group compounds have been studied and, similarly to the group 14 reactions mentioned in Section 1.3.1.2 , they yield *exo*-functionalised clusters.

Both $[P_7]^{3-}$ and $[As_7]^{3-}$ anions have been *exo*-functionalised by the nucleophilic substitution with main group ER_3X reagents (E = Si, Ge and Sn: X = Cl, Br and I) yielding novel neutral compounds of the form $E'_7(ER)_3$ (E' = P: E = Si: R = H_3, H_2Me, Me_3, Me_2PEt_3 and Ph_3; E' = P: E = Ge and Sn: R = Me_3; E' = As: E = Si: R = Me_3) (Figure 1.40).[120–122]

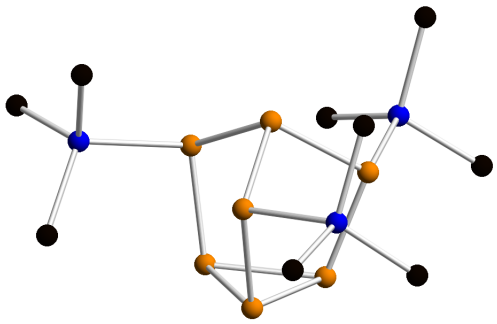

Figure 1.40: Ball and stick diagram of $P_7(SiMe_3)_3$ (P atoms are shown in orange, Si atoms in blue and C atoms in black). H atoms are omitted for clarity.

*Tris*functionalised heptapnictide cages can have two possible isomers described as either symmetric or asymmetric (Figure 1.41). The symmetric isomer would show only three resonances by ^{31}P NMR spectroscopy, whereas the asymmetric isomer would show seven resonances due to the magnetically inequivalent phosphorus nuclei. ^{31}P NMR spectra for the reactions mentioned in the last paragraph revealed only three resonances confirming the formation only of the symmetric isomers. X-ray crystallography has corroborated such observations.

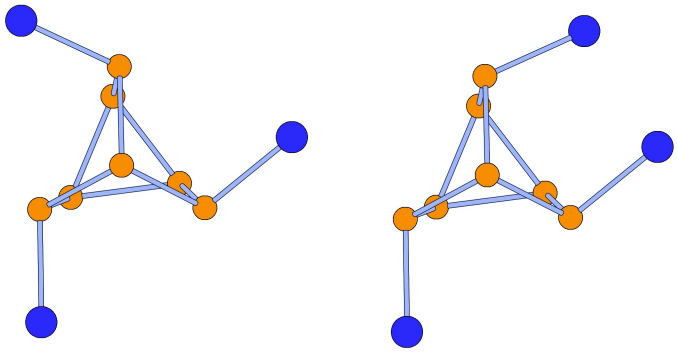

Symmetric isomer Asymmetric isomer

Figure 1.41: The two possible isomers of a $[E'R_3]$ cage.

Group 15 reagents have been studied as well. $[P_7]^{3-}$ has formed *tris*functionalised neutral species $[P_7(E''Bu_2)_3]$ when reacted with $P'Bu_2F$ and $Sb'Bu_2F$.[123] Both ^{31}P NMR

spectroscopy and X-ray crystallography revealed that only the symmetric isomer is formed.

1.3.2.3 *Exo*-functionalisation of group 15 $[E'_7]^{3-}$ clusters with organic fragments

In addition to *exo*-functionalisation with main group fragments, $[E'_7]^{3-}$ (E' = P and As) cages can be *exo*-functionalised with organic fragments. Starting with the rare monosubstituted cages, the simplest example is the monoprotonated cage $[HE'_7]^{2-}$ (Figure 1.42). This can be prepared by simple protonation of the Zintl phase $K_3E'_7$ with water in the presence of two equivalents of a sequestering agent in pyridine.[124,125] The monoprotonated $[HE'_7]^{2-}$ cages have been studied by single crystal X-ray crystallography.

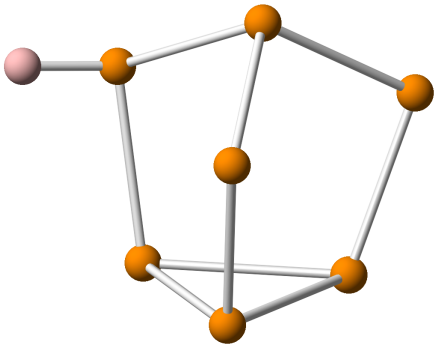

Figure 1.42: Ball and stick diagram of $[HP_7]^{2-}$ (P atoms shown in orange and the H atom in pink).

For monosubstituted derivatives two enantiomers can be formed, *S*-enantiomer and *R*-enantiomer (Figure 1.43). When monosubstituted cages have been prepared, they yield a racemic mixture. For the $[P_7R]^{2-}$ cages all the phosphorus are inequivalent and the cluster displays some fluxionality in solution at room temperature on the NMR timescale.

$[P_7(SiMe_3)]^{2-}$ can be formed by ligand redistribution by mixing $[P_7(SiMe_3)_3]$ and $[P_7]^{3-}$ in a 1:2 ratio.[126] Another example that illustrates the racemic character of these cages is $[P_7SiMe(SiMe_3)_2]^{2-}$ which constitutes the only monosubstituted cluster that has been studied using X-ray crystallography and both enantiomers have been found as a racemic mixture.[127]

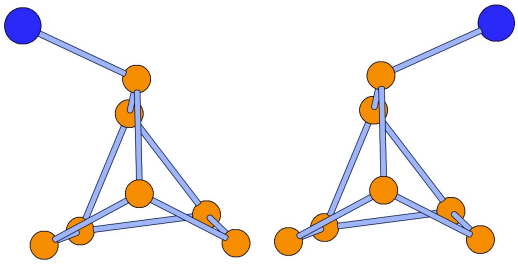

S-enantiomer R-enantiomer

Figure 1.43: The two enantiomers of a monosubstituted heptapnictide cage viewed from the apical vertex.

Some *bis*functionalised derivatives $[E'_7R_2]^-$ have been prepared by reacting $[E'_7]^{3-}$ with tetraalkylammonium salts $[RR'_3N]X$ (R,R' = Me, Et and Bu, X = Cl, Br and I; R = $PhCH_2$, $EtOCOCH_2$ and EtOCOCHMe: R' = Me; X = Cl, Br and I).[128,129] For *bis*functionalised cages there is the possibility for three different isomers (Figure 1.44). Isomer A and B would have a C_s point group with mirror planes running between the alkyl groups, resulting in two pairs of equivalent E' atoms and three unique atomic positions. For the third isomer C, all seven E' atoms are inequivalent.

All these reactions are stereospecific and when monitored by ^{31}P NMR spectroscopy revealed five resonances. This implies formation of isomer A or B, although due to sterics it is reasonable to conclude that isomer A is the more plausible option. X-ray crystallography confirmed this hypothesis.

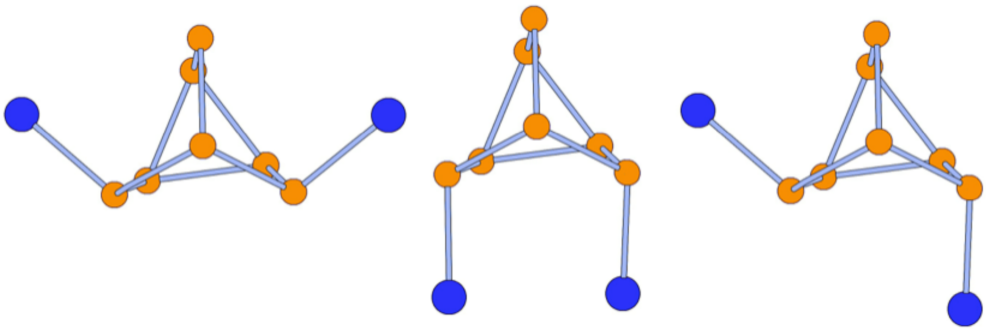

Isomer A Isomer B Isomer C

Figure 1.44: Different isomers for *bis*functionalised $[E'_7]^-$ clusters.

A proposed reaction mechanism is the nucleophilic attack by the cage to one of the α-carbon atoms of the ammonium salt. Another set of *bis*functionalised cages was reported by Muluykov. He studied *bis*alkylations by reacting the $[P_7]^{3-}$ cage with two equivalents of RTs to form $[R_2P_7]^-$ (R = ^{i}Pr and ^{i}Bu).[130] ^{31}P NMR spectroscopy showed the formation of isomer A. If three equivalents of the RTs (R = ^{i}Pr, ^{n}Bu, ^{i}Bu, 3-C_5H_{11} and C_6H_{13}) are added it is possible to form the *tris*functionalised neutral cage.

*Tris*functionalised compounds have been prepared by reacting $[P_7]^{3-}$ with three equivalents of RBr (R = Me, Et, ^{i}Pr, ^{i}Bu).[120,121,131] ^{31}P NMR spectroscopy showed ten resonances meaning that these reactions are not stereospecific and that the reactions give rise to the formation of both isomers. Sterics ultimately define which isomer is formed as the major product.

Goicoechea and Turbervill reported in 2012 a series of hydrophosphination of carbodiimides.[132] The Zintl ion precursor used is the monoprotonated cage $[HP_7]^{2-}$; the latter reacts with RN=C=NR (R = Dipp, ^{i}Pr and Cy) affording the monofunctionalised species $[P_7C(NHR)(NR)]^{2-}$. The Dipp derivative (Figure 1.45) can be protonated to form $[HP_7C(NHDipp)(NDipp)]^-$ which can subsequently be functionalised a second time to

result in the formation of $\{[P_7[C(NHDipp)(NDipp)][C(NHR')(NR')]\}^-$ (R' = Dipp, ^{i}Pr and Cy).[133] Furthermore, $[HE'_7]^{2-}$ (E' = P and As) can react with isocyanates (O=C=NAd) to afford the amide-derivatised cluster anions $[E_7C(CO)(NHAd)]^{2-}$.

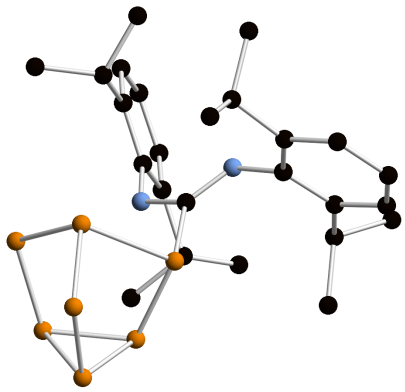

Figure 1.45: Ball and stick diagram of $[P_7C(NHDipp)(NDipp)]^{2-}$ (P atoms are shown in orange, N atoms in blue and C atoms in black). H atoms are omitted for clarity.

1.3.2.4 Reactions where group 15 $[E'_7]^{3-}$ clusters act as ligands towards metals

Zintl ions are versatile reagents, and can coordinate to Lewis acidic metal centres. Eichhorn, Fenske and Goicoechea, amongst others, have reported numerous studies on the coordination chemistry of Zintl ions over the last few years and such species are discussed herein.[134] The coordination chemistry of the Zintl ions can be divided into three different binding modes. The cage can coordinate in an η^1 fashion through one E' atom donating two electrons to the metal centre, in an η^2 (or κ^2) fashion through two E' atoms donating two electrons from each atom (four in total) and finally in an η^4 fashion where a mild activation of the cage occurs and one of the basal bonds (E'5–E'6) breaks to give a norbornadiene-like geometry. In this mode the cage donates a total of six electrons. Figure 1.46 shows the numbering scheme that will be used in this thesis.

While the generally accepted literature term for the two-vertex binding mode has been η^2, this implies that there is a bond between the two coordinating E' vertices that is not present. Arguably a better description of the bonding mode could be κ^2: the cage simply coordinates through two independent E' donor functionalities to a single metal centre.

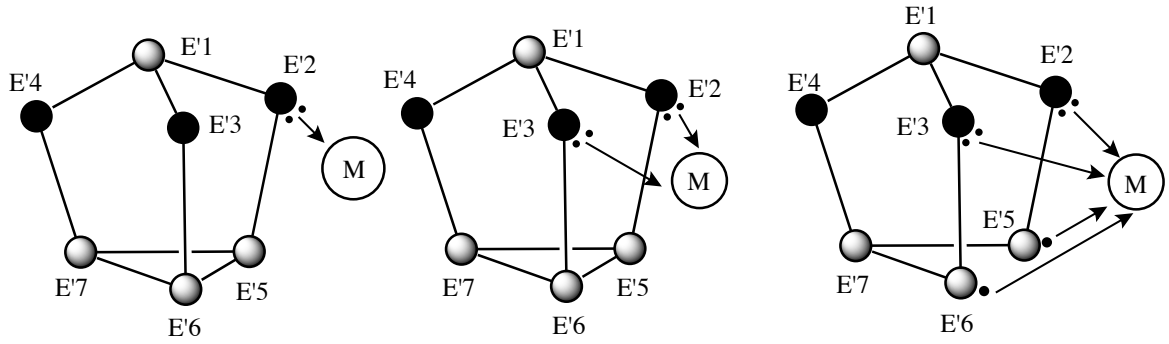

η^1 coordination mode η^2 coordination mode η^4 coordination mode

Figure 1.46: Diagram showing the three possible bonding modes of the $[E'_7]^{3-}$ cage. Atoms possessing a formal negative charge are highlighted in black.

1.3.2.4.1 η^1 coordination of the $[E'_7]^{3-}$ cage

To date there is only one report of a neutral *tris*functionalised species $[E_7'R_3]$ with a metal fragment. By reacting the Li_3P_7 Zintl phase with three equivalents of $[FeCp(CO)_2Br]$ the $[P_7\{FeCp(CO)_2\}_3]$ (Figure 1.47) neutral compound can be prepared.[135] Of the two possible isomers available for a *tris*functionalised species $[E'_7R_3]$ (Figure 1.41), this reaction proceeds forming exclusively the symmetric isomer due to the steric demand of the $FeCp(CO)_2$ fragment. This can be confirmed by ^{31}P NMR spectroscopy where only three resonances are observed (δ = 47.7 ppm for the apical phosphorus atom, δ = –48.7 ppm for the three basal phosphorus atoms and δ = –159.3 ppm for the three phosphorus atoms bonded to the $FeCp(CO)_2$ moieties).

X-ray crystallographic studies show that the structure of the heptaphosphide cage remains intact. Each of the two-connect phosphorus atoms is bonded to a cationic $[FeCp(CO)_2]^+$ moiety, yielding a neutral product.

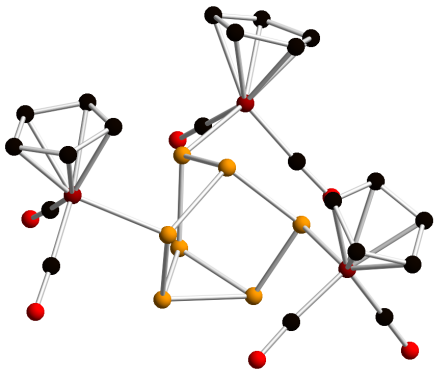

Figure 1.47: Ball and stick diagram of $[P_7(FeCp(CO)_2)_3]$ (P atoms are shown in orange, Fe atoms in dark red, C atoms in black and O in red). H atoms are omitted for clarity.

1.3.2.4.2 η^2 coordination of the $[E'_7]^{3-}$ cage

The simplest compound of this family of coordination compounds is $[TlE'_7]^{2-}$ (E' = P and As) (Figure 1.48).[135] This compound was prepared by mixing the $K_3E'_7$ Zintl phase and one equivalent of TlCl in ethylenediamine and in the presence of 2,2,2-crypt (for the phosphorus compound) or 18-crown-6 (for the arsenic analogue).

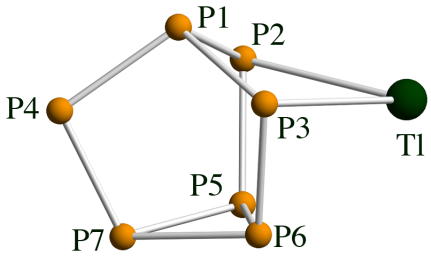

Figure 1.48: Ball and stick diagram of $[TlP_7]^{2-}$.

In contrast to what has been reported for the group 14 $[TlE_9]^{3-}$ cluster discussed in Section 1.3.1.4 , where the thallium atom was coordinated in an η^4 fashion by the anionic

cage, in the analogous group 15 cluster compound the metal is coordinated by two E' atoms. This has been demonstrated by single crystal X-ray diffraction.

In the $[TlE'_7]^{2-}$ cluster the bonding E'–Tl distances (P2–Tl = 2.819(2) Å, P3–Tl = 2.871(2) Å; As2–Tl = 2.921(2) Å, As3–Tl = 2.939(2) Å) are notably shorter than the distances from the basal E' atoms nearest to the thallium atom (P5–Tl = 3.113(2) Å, P6–Tl = 3.174(2) Å; As5–Tl = 3.147(2) Å, As6–Tl = 3.182(2) Å). Additionally, cleavage of the basal E'–E' bond is not observed. Nevertheless the distance between the two basal E' atoms (P5–P6 = 2.313(3) Å; As5–As6 = 2.629(2) Å) is significantly longer than the other two distances in the ring (P5–P7 = 2.225(3) Å, P6–P7 = 2.249(3); As5–As7 = 2.479(2) Å, P6–P7 = 2.576(2) Å) which implies that there is certain degree of interaction between the thallium atom and the basal E' atoms. The arsenic analogue has shorter distances between the basal atoms and the thallium atom, suggesting that this molecule has a higher η^4 character.

Solution ^{31}P NMR spectroscopic studies on $[TlP_7]^{2-}$ at –50 ºC show only two broad resonances, plus some unreacted $[HP_7]^{2-}$ and $[P_{21}]^{3-}$. A resonance at δ = 99.0 ppm was assigned to P1 and P7, the other resonance, δ = –147.2 ppm, was assigned to the four phosphorus atoms closest to the thallium atom (P2, P3, P5 and P6). The missing P4 resonance is believed to be overlapping with one of the $[P_{21}]^{3-}$ resonances, which was observed at δ = 58.2 ppm. This suggests that P2, P3 and P5, P6 are equivalent, like P1 and P7, implying that there is a fluxionality between the two binding modes *via* η^4 bond intermediate (Scheme 1.4).

The overall charge suggests that a trianionic $[E'_7]^{3-}$ cage bonds to a Tl^+ ion resulting in a 2– charge. The thallium atom has a lone pair which points radially away from the cluster.

DFT calculations on this compound showed that the HOMO for both analogues is mainly composed by the thallium lone pair with some mixing of the cage orbitals. The HOMO–1 is largely constituted of the lone pair on the additional negatively charged E'4 atom.

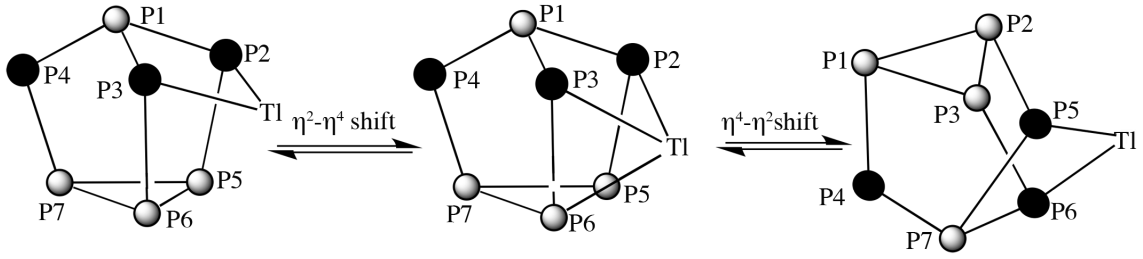

Scheme 1.4: Diagram showing the proposed η^2–η^4–η^2 transition taking place in $[TlP_7]^{2-}$. Atoms possessing a formal negative charge are shown in black.

The reaction of one equivalent of the homoleptic organometallic compound $InPh_3$ and the $K_3E'_7$ Zintl phase yielded the η^2 coordination compound $[E'_7InPh_2]^{2-}$ (E' = P and As) (Figure 1.49).[136] Single crystals suitable for X-ray diffraction were obtained only for the phosphorus analogue, however, the identity of the arsenic cluster was corroborated by NMR spectroscopy and mass spectrometry.

In this molecule the $[E'_7]^{3-}$ cage acts as a four-electron donor towards the indium centre, and one In–Ph bond is reductively cleaved in the process. The resulting free Ph^- abstracts a proton from the ethylenediamine and forms benzene, as demonstrated by ^1H NMR studies.

The solid-state structure of $[P_7InPh_2]^{2-}$ reveals an intact $[P_7]^{3-}$ cage coordinated to a four valence electron $[InPh_2]^+$ fragment. In total the indium atom possesses eight valence electrons, and has a distorted tetrahedral geometry (P2–In1–P3 80.33(4)°, P2–In1–C1

114.00(15)°, P2–In1–C7 113.85(14)°, P3–In1–C1 114.02(14)°, P3–In1–C7 120.46(15)° and C1–In1–C7 111.00(20)°).

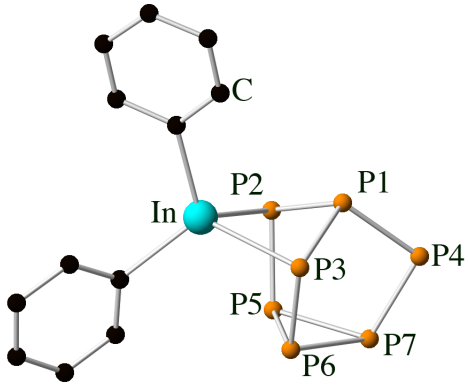

Figure 1.49: Ball and stick diagram of $[P_7InPh_2]^{2-}$. H atoms are omitted for clarity.

Solution ^{1}H NMR studies showed that there are six different phenyl resonances suggesting that both groups are chemically inequivalent. ^{31}P NMR spectroscopy revealed the expected number of resonances for an η^2 coordination compound at δ = 3.6, –50.7, –67.8, –76.8 and –170.0 ppm with relative intensities 2:1:1:1:2. These resonances were assigned to P2 and P3, P1, P4, P7 and P5 and P6, respectively.

Reactions of $[Pt(PPh_3)_2(C_2H_4)]$ with $[E'_7]^{3-}$ (E' = P and As) in ethylenediamine were found to afford the η^2 coordination compound $[E'_7PtH(PPh_3)]^{2-}$ (Figure 1.50).[137] In this reaction the organometallic starting material loses a PPh_3 ligand and is coordinated by two of the two-connect atoms of the cage, additionally, the platinum centre gains a hydride from the solvent. The hydride could not be located by X-ray crystallography, but was observed with deuterium labelling studies. It was proved that ethylenediamine, acetonitrile, DMSO and DMF can also act as hydrogen sources.

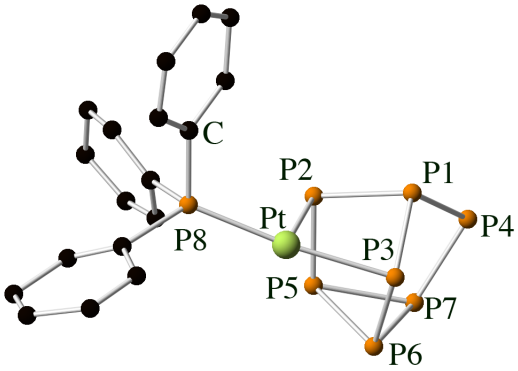

Figure 1.50: Ball and stick diagram of $[P_7PtH(PPh_3)]^{2-}$. Hydride could not be located by X-ray crystallography. H atoms are omitted for clarity.

The solid-state structure shows that the structure of the cage is intact, and the $[E'_7]^{3-}$ cage is coordinated to a twelve-electron $[PtH(PPh_3)]^+$ fragment. The geometry of the platinum atom is square planar and has sixteen valence electrons.

^{31}P NMR spectroscopic studies at –78 ºC showed five multiplets, corresponding to the different phosphorus environments of the cage, as well as free unreacted $[P_7]^{3-}$ and a resonance corresponding to the PPh_3 ligand. Variable temperature studies show that P2, P3, P5 and P6 coalesce at –20 ºC into one resonance that integrates to four; P1 and P7 coalesce into one resonance at –60 ºC, the P4 resonance remains unique and that finally the PPh_3 resonance changes from a doublet to a quintet at 25 ºC.

Solution ^1H NMR studies show the resonances corresponding to the hydride at $\delta = -10.1$ and –10.8 ppm in the phosphorus and arsenic clusters, respectively. The multiplicity of these resonances changes from a doublet of multiplets at –78 ºC to a single multiplet at 25 ºC. All this evidence suggests that, as with the $[TlP_7]^{2-}$ anion, there is a fluxionality between the η^2 and η^4 the coordination modes.

Metal complexes have also been synthesised where two $[E'_7]^{3-}$ cages coordinate in an η^2 mode to a single metal centre, namely $[M(E'_7)_2]^{x-}$ (E = P and As: M = Zn and Cd: x = 4; E = P and As: M = In: x = 3) (Figure 1.51).[135,136,138]

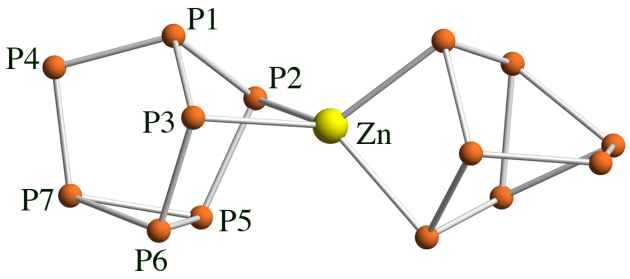

Figure 1.51: Ball and stick diagram of $[Zn(P_7)_2]^{4-}$.

The group 12 analogues were prepared by reacting 0.5 equivalents of the organometallic reagent MPh_2 (M = Zn and Cd) complex and one equivalent of $[E'_7]^{3-}$.[136] These reactions proceed *via* the reductive cleavage of an M–C bond of the metal reagent. When attempting to complete the series and synthesise the $[Cd(As_7)_2]^{4-}$ analogue, the mass spectrum did not show any evidence of its formation. However, it was later prepared by Sen and co-workers by reacting the K_3As_7 Zintl phase with cadmium cyclohexanebutyrate.[138]

The analogous compound $[In(P_7)_2]^{3-}$ was prepared by the simple salt-metathesis of $InCl_3$ and two equivalents of the $K_3E'_7$ (E' = P and As) Zintl phase.[135]

X-ray crystallography revealed very similar structures for all of these compounds. Each one of the two $[E'_7]^{3-}$ cages coordinates to a central metal in an η^2 fashion resulting in a distorted tetrahedral geometry around the metal centre with both of the cages in a staggered conformation. The cage acts as a four-electron donor towards the metal centre. In the case of the zinc and cadmium analogues, the metal centres are in a 2+ oxidation state with a d^{10} electron configuration and eighteen valence electrons. Whereas for the

indium analogue the overall oxidation state of the indium atom is 3+ with a valence electron count of eight electrons. These clusters have C_2 symmetry with a two-fold axis running through the central metal atom.

^{31}P NMR spectroscopic studies revealed five resonances with relative intensities 2:1:1:1:2, corresponding to the chemically inequivalent phosphorus atoms. A summary of the NMR data for the clusters anions is provided in Table 1.2.

Compound	P2, P3	P1	P4	P7	P5, P6
$[Zn(P_7)_2]^{4-}$	–14.9	–42.9	–56.3	–104.7	–162.3
$[Cd(P_7)_2]^{4-}$	–4.5	–36.0	–82.1	–134.7	–161.0
$[In(P_7)_2]^{3-}$	42.3	–51.3	–57.1	–104.2	–173.0

Table 1.2: ^{31}P NMR chemical shift values for $[M(P_7)_2]^{x-}$ in ppm.

DFT calculations for $[In(P_7)_2]^{3-}$ were performed to study its electronic structure. These found that the HOMO and the HOMO–1 are predominantly composed of lone-pair on the P4 atom. A geometry optimisation was performed employing a continuum dielectric to model the presence of the cations in the crystal lattice. A pseudo-tetrahedral coordination geometry around the central indium atom allows for a strong σ-bonding interaction between the metal and the lone pairs on P2 and P3 from both cages (HOMO–23). The corresponding antibonding orbital is the LUMO. The indium p orbitals can also interact with the s orbitals on P2 and P3 from both cages, giving rise to three bonding orbitals (HOMO–22, HOMO–14 and HOMO–13). DFT calculations showed that there is a slightly positive Mulliken spin density on the indium centre (0.3857), with negative spin densities on all of the phosphorus atoms. The most negative spin density values were obtained for the formally anionic phosphorus atoms, P4.

In 2011, the Goicoechea group reported the formation of another type of coordination compound with group 11 metals. The reaction of K_3P_7 and $[M(nbe)_3][SbF_6]$ or MCl (M = Ag and Au) in a 1:1 ratio in the presence of 2,2,2-crypt yields the protonated $[M_2(HP_7)_2]^{2-}$ in very low yields.[139] Since the proton was originally abstracted from trace amounts of water in the ethylenediamine solvent, stoichiometric addition of a proton source ($[NH_4][BPh_4]$) increased the yield for the reaction significantly. The reaction of the $[As_7]^{3-}$ Zintl ion and an alternative gold precursor $[(PPh_3)AuCl]$ has also been studied, yielding the deprotonated cluster $[M_2(As_7)_2]^{4-}$ (Figure 1.52).[140,141] These compounds are light sensitive and were isolated in low crystalline yields.

X-ray crystallographic studies for the three compounds revealed very similar structures. The compounds feature a central $[M_2]^{2+}$ fragment with "T-shaped" coordination environment around each metal. Each $[HE'_7]^{2-}$ cage is bonded to one of the metal atoms in an η^1 fashion by one of the two-connect E' atoms. The two bridging metal atoms and the E' atoms which comprise their immediate coordination sphere are coplanar and give rise to an “H-shaped” motif. This is in contrast to the $[E'_{15}M]^{3-}$ (M = Sn, Pb and Hg) species which are isostructural with the $[P_{16}]^{2-}$ anion and have a "bent" geometry. Additionally, both of the cages are in an "up-down" configuration, possibly because of crystal packing effects, since it was shown by DFT calculations that the energy barrier between both isomers for this type of molecule is very small (0.4 kJ/mol for $[Ag_2(HP_7)_2]^{2-}$ and 2.4 kJ/mol for $[Au_2(HP_7)_2]^{2-}$). In the examples reported by Goicoechea, $[M_2(HP_7)_2]^{2-}$, the two remaining two-connect phosphorus atoms are protonated, whereas in the $[Au_2(As_7)_2]^{4-}$ example reported by Sen and Weiss they are not, presumably because the phosphorus has a significantly enhanced basicity compared to the arsenic analogue.

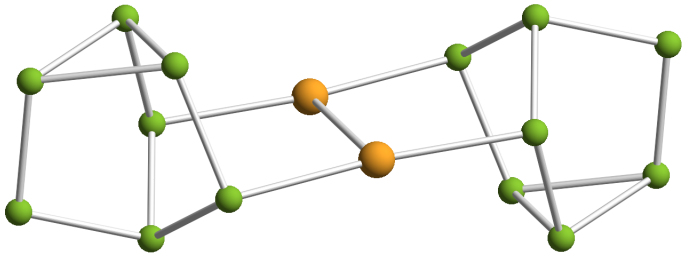

Figure 1.52: Ball and stick diagram of $[Au_2(As_7)_2]^{4-}$ (As atoms are shown in green and Au in gold).

The position of the protons in $[M_2(HP_7)_2]^{2-}$ was determined by studying the residual electron-densities in the asymmetric units of the crystal structures after all non-hydrogen atomic positions had been determined and refined anisotropically and the initial hydrogen positions of the $[K(2,2,2\text{-crypt})]^+$ cations had been determined. Some of the largest residual Q peaks were observed close to the two-connect phosphorus atoms in chemically viable positions. The final proton positions were consistent with a pyramidal coordination environment at the two-connect phosphorus atoms.

^{31}P NMR spectroscopic studies proved very challenging for these compounds due to their light sensitivity, and show evidence of the formation of the decomposition products $[P_{16}]^{2-}$ and PH_3. However, seven resonances that can be assigned to the $[M_2(HP_7)_2]^{2-}$ compound could be observed.

The aforementioned reactions between the organometallic compounds $ZnPh_2$ and $CdPh_2$ with the $[E'_7]^{3-}$ Zintl cages afford the $[Zn(E'_7)_2]^{4-}$ and $[Cd(E'_7)_2]^{4-}$, respectively.[136] Going down the group, the reaction of $[As_7]^{3-}$ and $HgPh_2$ was also studied, which yielded two different products, namely $[Hg_2(As_7)_2]^{4-}$ and $[HgAs_{15}]^{3-}$.[138,142] If gallium was added to the reaction mixture $[Hg_2(As_7)_2]^{4-}$ could be formed exclusively, and if the stoichiometry of $HgPh_2$ was reduced to 0.5 equivalents the formation of $[HgAs_{15}]^{3-}$ was favoured.

$[HgAs_{15}]^{3-}$ is isostructural to a series of $[ME'_{15}]^{3-}$ clusters (E' = P: M = Sn and Pb; E' = As; M = Sn, Pb and Hg) and therefore will be discussed along those compounds.

X-ray crystallography of $[Hg_2(As_7)_2]^{4-}$ (Figure 1.53) reveals a central $[Hg_2]^{2+}$ unit coordinated linearly by two $[E'_7]^{3-}$ cages. This is in contrast to the $[M_2(HP_7)_2]^{2-}$ (M = Au and Ag) discussed previously in this section. Each cage is coordinated to only one mercury atom on each side in an η^2 (or κ^2) fashion.

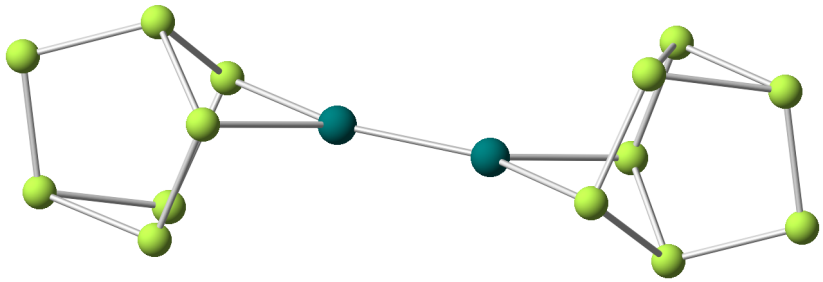

Figure 1.53: Ball and stick diagram of $[Hg_2(As_7)_2]^{4-}$ (As atoms are shown in green and Hg atoms are shown in blue).

The reaction between the $[As_7]^{3-}$ cage and $Pd(PCy_3)_2$ in the presence of 2,2,2-crypt affords two different activation products namely $[Pd_7As_{16}]^{4-}$ and $[Pd_2(As_7)_2]^{4-}$ (Figure 1.54).[143]

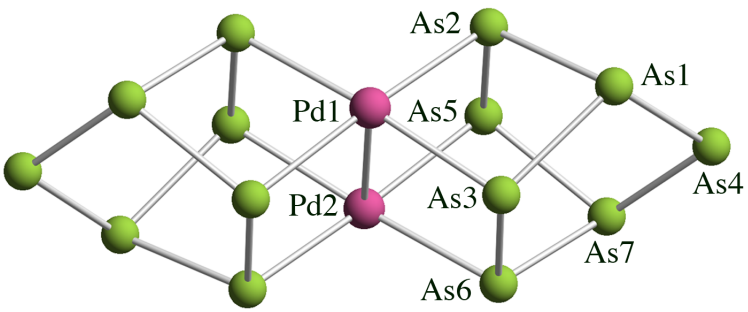

Figure 1.54: Ball and stick diagram of $[Pd_2(As_7)_2]^{4-}$.

X-ray crystallography of $[Pd_2(As_7)_2]^{4-}$ reveals a mild activation of the $[As_7]^{3-}$ cage and a central $[Pd_2]^{2+}$ fragment; the As5–As6 basal bond has been cleaved and As2 and As3 are

bond to one of the palladium atoms, while As5 and As6 bond to the other palladium atom. Both palladium atoms have a distorted square planar geometry and a strong bonding interaction between the two palladium atoms (Pd–Pd = 2.714(1) Å).

One possible mechanism for the formation of this molecule is *via* a complex similar to $[P_7PtH(PPh_3)]^{2-}$.[144] $[As_7PdH(PCy_3)]^{2-}$ could be formed initially and then through a redox process the final compound could be formed (Scheme 1.5). This is consistent with the release of H_2 gas observed during this reaction, however, this intermediate has not been isolated.

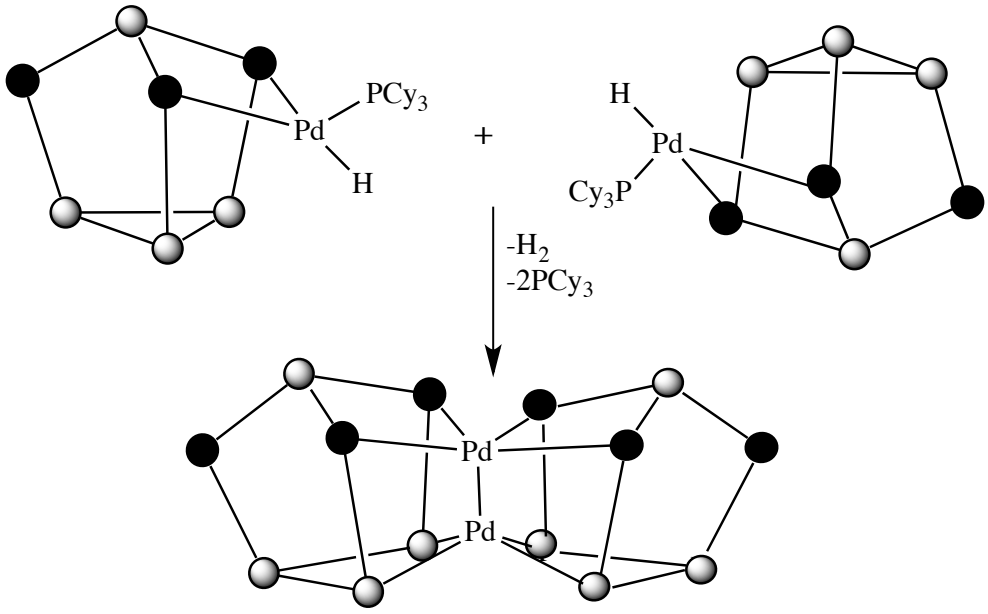

Scheme 1.5: Diagram showing the hypothetical formation of $[Pd_2(As_7)_2]^{4-}$ from $[As_7PdH(PCy_3)]^{2-}$. Atoms possessing a formal negative charge are shown in black.

The reaction between the $K_3E'_7$ Zintl phase and 0.2 equivalents of the $[Cu(mes)]_5$ organometallic compound yields a bimetallic bridged compound, namely $[Cu_2(E'_7)_2]^{4-}$ (E' = P and As) (Figure 1.55).[136]

Only single crystals of $[Cu_2(As_7)_2]^{4-}$ suitable for X-ray crystallography could be obtained. Although the isolated crystals of $[Cu_2(P_7)_2]^{4-}$ were too small to be suitable for X-ray

diffraction, its identity was corroborated by ^{31}P NMR spectroscopy. The crystal structure of $[Cu_2(As_7)_2]^{4-}$ revealed a diatomic $[Cu_2]^{2+}$ moiety bridging two $[E'_7]^{3-}$ units. Unlike the $[Pd_2(As_7)_2]^{4-}$ discussed above, the $[Cu_2]^{2+}$ unit is not arranged symmetrically with respect to the two $[As_7]^{3-}$ cages. Each copper atom has strong bonding interactions with all four E' atoms of one cage (η^4) and to one E' (η^1) in the adjacent cage. This gives each copper atom a coordination number of six. The cluster has a C_i symmetry with a centre of inversion in the centre of the Cu–Cu bond making both moieties crystallographically equivalent. In the formation of $[Cu_2(As_7)_2]^{4-}$ the As5–As6 bond length has been significantly lengthened but not cleaved (2.772(1) Å).

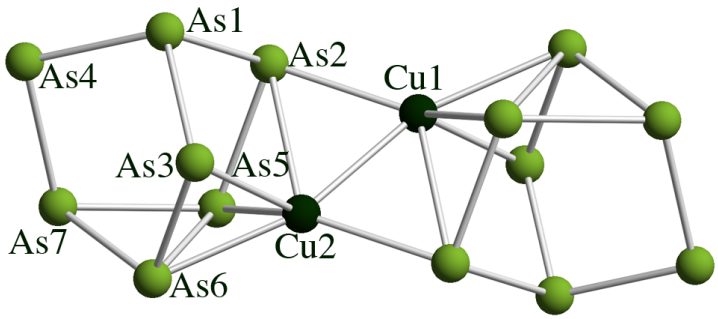

Figure 1.55: Ball and stick diagram of $[Cu_2(As_7)_2]^{4-}$.

^{31}P NMR spectroscopic studies revealed that the phosphorus analogue is fluxional in solution. At –50 ºC it shows three very broad resonances with intensities 1:2:4. The resonance at δ = –28.8 ppm was assigned to P1, the triplet at δ = –39.1 ppm was assigned to P7 and P4 and the final resonance at δ = –81.0 ppm was to assigned all the copper-bonded phosphorus atoms P2, P3, P5 and P6.

Separately, the syntheses of compounds of the type $[ME'_{15}]^{3-}$ (E' = P: M = Sn and Pb; E' = As; M = Sn, Pb and Hg) were reported by the Goicoechea group and the Weiss and Sen group.[135,138,142] The synthesis reported by Goicoechea involves in the reaction of the

$K_3E'_7$ Zintl phases and MI_2 (M = Sn and Pb), and the synthesis reported by Weiss and Sen involves the reaction of $[As_7]^{3-}$ with 0.5 equivalents of $HgPh_2$.

The resulting anions are sixteen atom clusters isostructural with the polyphosphide $[P_{16}]^{2-}$, which consists of two heptaphosphide units bridged by a $[P_2]$ moiety. In this molecule fourteen phosphorus atoms are three-connected, only two are bonded to two nearest neighbours giving rise to the 2– charge. In $[ME'_{15}]^{3-}$ one of the bridging two-connected phosphorus atoms is replaced with a negatively charged metal, affording the cluster a total charge of 3–. The group 14 element is bonded to two E' atoms and has an *exo*-lone pair.

In the solid-state single crystal X-ray crystallographic studies of $[MP_{15}]^{3-}$ (M = Sn and Pb) a statistical disorder of the group 14 element in both bridging positions was observed. The best refinement parameters were found when the molecules were modelled for 50% occupancy for the phosphorus atom and 50% occupancy for the group 14 elements in each one of the bridging positions. This, in addition to the evident 3– charge of the cluster anion, confirms the formation of $[ME'_{15}]^{3-}$. The solid-state structure of $[HgAs_{15}]^{3-}$ (Figure 1.56) was found to be fully ordered.

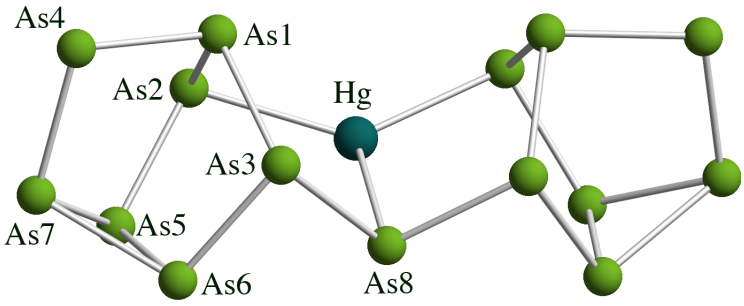

Figure 1.56: Ball and stick diagram of $[HgAs_{15}]^{3-}$.

The phosphorus-containing species were studied using ^{31}P NMR spectroscopy and revealed a total of eight resonances, arising from all the magnetically inequivalent phosphorus atoms with relative intensities of 2:2:2:1:2:2:2:2 (Table 1.3). These resonances were assigned by means of a ^{31}P–^{31}P COSY experiment.

Compound	P2	P1	P3	P8	P7	P4	P6	P5
$[SnP_{15}]^{3-}$	50.6	22.8	–31.7	–54.0	–61.5	–115.8	–152.1	–176.3
$[PbP_{15}]^{3-}$	49.5	33.0	–40.0	–50.6	–64.8	–122.7	–153.4	–175.4

Table 1.3: ^{31}P NMR chemical shift values for $[ME'_{15}]^{3-}$ in ppm.

DFT calculations on $[SnAs_{15}]^{3-}$ showed that the HOMO and HOMO–1 mostly consist of lone pair contributions from As4, while the HOMO–2 possesses significant tin lone pair character. A Mulliken spin density analysis showed that all of the arsenic atoms possess negative spin densities, with the most negative spin density values obtained for the formally anionic arsenic atoms, As4 (–0.5815 and –0.5812 for each cage). The Mulliken spin density for the tin atom was found to be slightly positive, however, a Hirschfield charge analysis gave some negative spin density on the tin atom, as expected from the Lewis structure. An NBO analysis was consistent with each interaction in $[SnAs_{15}]^{3-}$ being a two-centre, two-electron bond.

1.3.2.4.3 η^4 coordination of the $[E'_7]^{3-}$ cage

Analogously to the $[E_9M(CO)_3]^{4-}$ compounds isolated for group 14 clusters (Section 1.3.1.4) group 15 $[E'_7]^{3-}$ cages can react with $[M(CO)_3L]$ (M = Cr, W: L = mesitylene; M = Mo: L = cycloheptatriene) to afford coordination compounds of the type $[E'_7M(CO)_3]^{3-}$ (E' = P, As and Sb; M = Cr, Mo and W).[145,146] The $[Sb_7Mo(CO)_3]^{3-}$ complex was formed by reacting the $[Sb_7]^{3-}$ cage and $[Mo(CO)_4(bipy)]$.[147] In these coordination compounds

the $[E'_7]^{3-}$ cage is bound to the $M(CO)_3$ fragment in an η^4 fashion, donating six electrons to the zero-valent metal centre. As evidenced by X-ray crystallography studies, when the $[E'_7]^{3-}$ cages coordinate to the metal they undergo a mild activation. It might be expected that a basal E'–E' bond is cleaved and the whole cluster bonds to the $M(CO)_3$ fragment symmetrically and that the E'5–E'4 and E'6–E'7 distances within the cluster are equal, but this is not always the case. In some examples there is cleavage of an E'–E' bond in the basal triangle, but in others only a significant lengthening is observed.

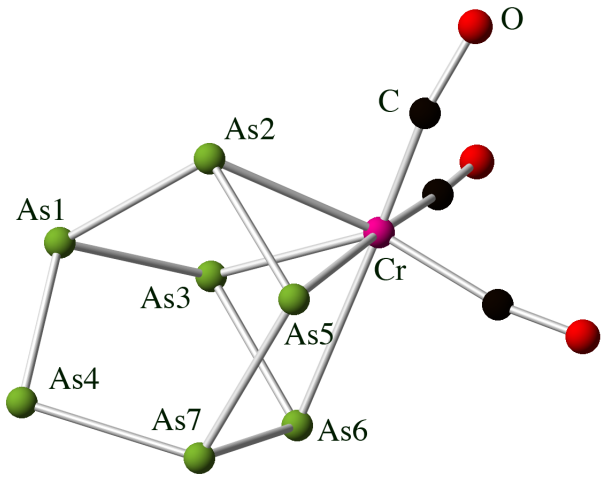

Figure 1.57: Ball and stick diagram for $[As_7Cr(CO)_3]^{3-}$.

It has been observed that the M–E' interatomic distances are not the same for all of the atoms of the cluster that interact with the metal centre. The molecule closest to this case is $[As_7Cr(CO)_3]^{3-}$ (Figure 1.57), where it is assumed that there is an optimal overlap between the orbitals of the cage and the $Cr(CO)_3$ fragment. Fenske-Hall molecular orbital calculations using both the idealised completely symmetrical geometry, C_{2v} geometry, and the C_s observed in the experimental structures, show that the $[\eta^4\text{-}E'_7]^{3-}$ fragment and rectangular distorted cyclobutadiene dianion fragment are isoelectronic. They possess four orbitals of the π- type symmetry (π_1, π_2, π_3 and π_4), where like in the cyclobutadiene dianion, the π_1 and π_2 bonding orbitals are lower in energy than the π_3 and π_4 antibonding

orbitals (Figure 1.58). The main interaction between the $[E'_7]^{3-}$ cage and the $M(CO)_3$ fragment is π type, with the primary interactions between the π_2 and π_3 orbitals of the cage with the $M(CO)_3$ fragment.

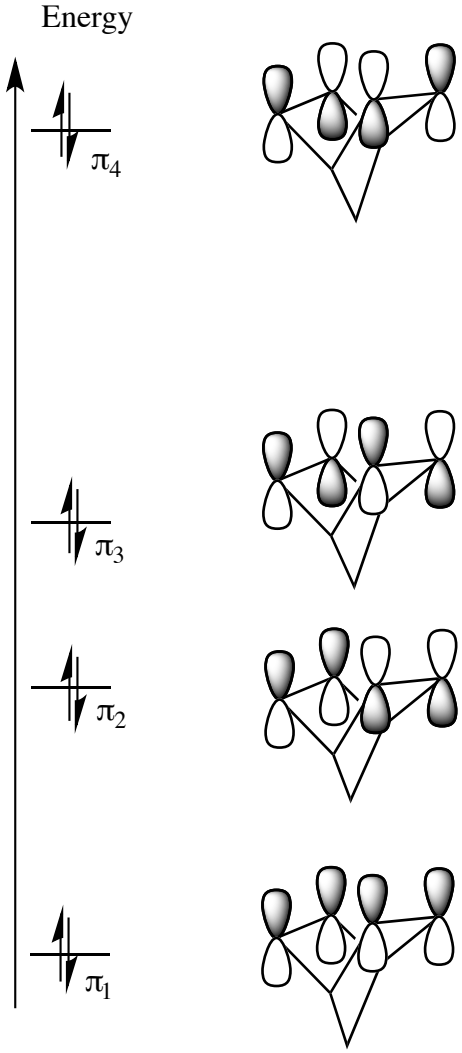

Figure 1.58: Simplified molecular orbital diagram for $[\eta^4\text{-}E'_7]^{3-}$. In the case of the $[Sb_7]^{3-}$ the relative energies from π_2 and π_3 are reversed, which has been attributed to poorer π overlap on descending the group (a consequence of the so-called double-bond rule).

When going down group 15, the strength of π bonding decreases, causing stabilisation of π_3 and destabilisation of π_2. In the case of the $[Sb_7]^{3-}$ anion, π_2 and π_3 are almost degenerate, and show greater similarity to the undistorted limit for cyclobutadiene. This would imply that the lack of symmetry in the $[E'_7M(CO)_3]^{3-}$ cluster is due to a lower

energy from the C_s point group isomer caused by additional orbital mixing within the cluster cage. This distortion has been attributed to a second-order Jahn-Teller effect. This theory has been confirmed by DFT calculations.

IR spectroscopy revealed low C–O stretching frequencies, meaning that there is a substantial charge transfer from the negatively charged cage to the $M(CO)_3$ moiety. This leads to a greater degree of back-bonding into the C–O π^* orbitals weakening the C–O bonds.

The asymmetrical nature the $[P_7Cr(CO)_3]^{3-}$ cluster as determined by single crystal X-ray diffraction is not observed by ^{31}P NMR spectroscopy. Even at low temperatures, only three resonances are observed with 1:2:4 relative intensities (δ = 199 ppm (P4), δ = –21 ppm (P1 and P7) and δ = –143 ppm (P2, P3, P5 and P6)). This indicates that all the Cr–P bonds are equivalent on the NMR timescale. This fluxionality can be described by an intermolecular "wagging" (Scheme 1.6).

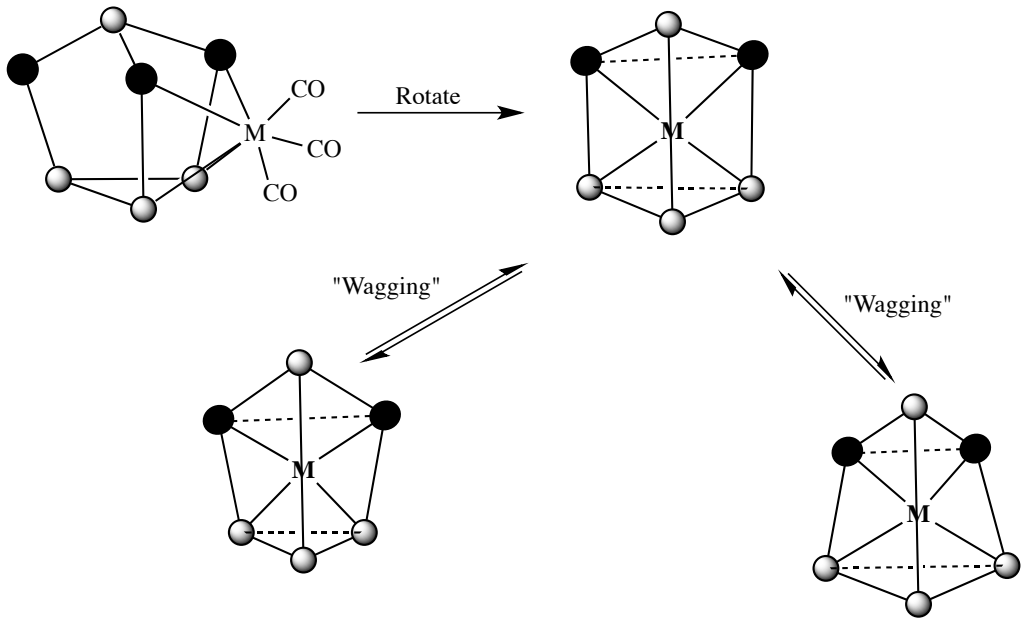

Scheme 1.6: Diagram showing the intra-molecular "wagging" process taking place in $[P_7M(CO)_3]^{3-}$. Atoms possessing a formal negative charge are shown in black.

It is possible to protonate these species with acids with a pK_a value of less than eighteen to give rise to the $[HP_7M(CO)_3]^{2-}$ coordination compounds. These can subsequently be deprotonated by MeO^- to afford the original complexes.[148] Some functionalisation reactions have also been reported for the $[P_7W(CO)_3]^{3-}$ compound to form $[RP_7W(CO)_3]^{2-}$ (R = Me, Et, Bu, $PhCH_2$, Me_3Si, Bu_3Si, Hex_3Si, Ph_3Si, Et_3Ge, Ph_3Ge, Et_3Sn, Bu_3Sn, Cy_3Sn, Ph_3Sn, Ph_3Pb and $(en)(CO)_3W$).[128,149,150] While being studied by ^{31}P NMR spectroscopy, only four resonances were found at –50 ºC, and when the temperature was increased to 90 ºC, two of the resonances coalesced to one giving a three resonance spectrum due to the pyramidal inversion at the functionalised position.

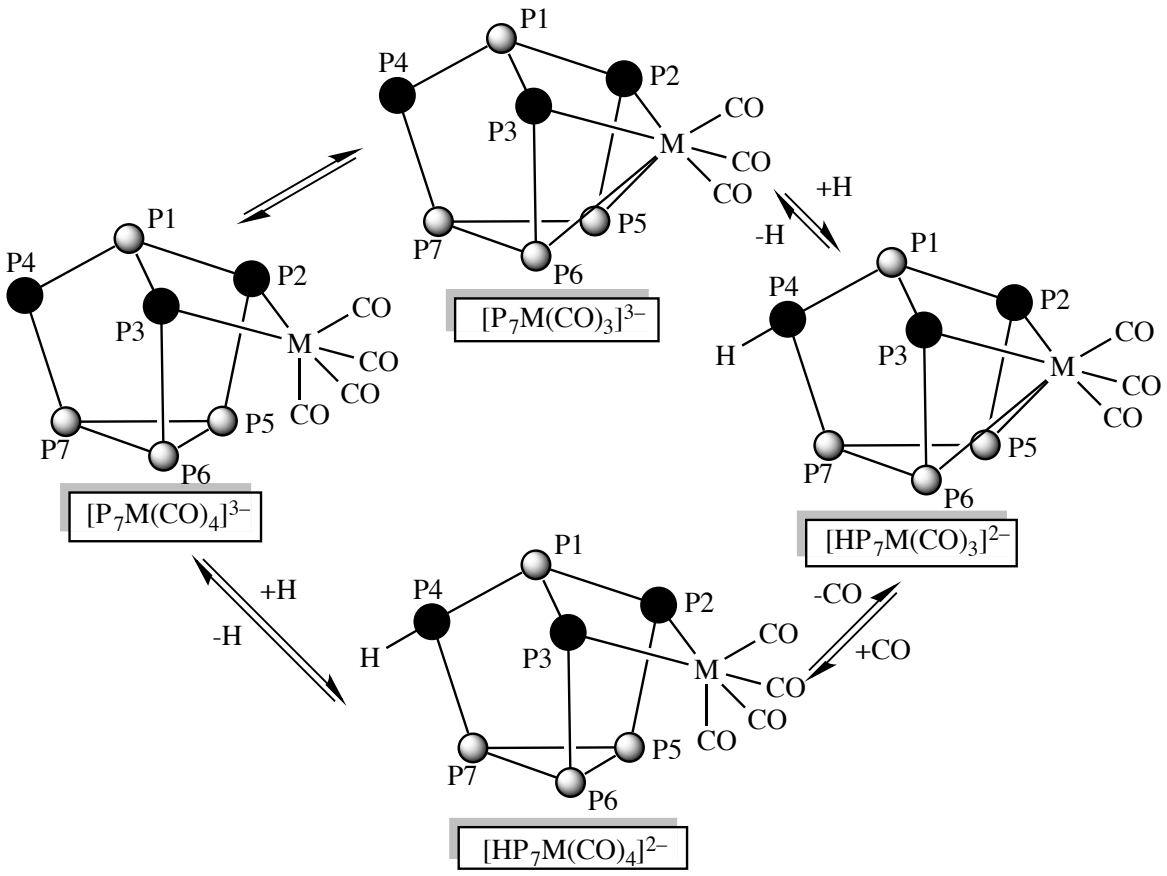

Scheme 1.7: Diagram showing the interconversion between $[P_7M(CO)_3]^{3-}$, $[HP_7M(CO)_3]^{2-}$, $[HP_7M(CO)_4]^{2-}$ and $[P_7M(CO)_4]^{3-}$. Atoms possessing a formal negative charge are shown in black.

Furthermore, the addition of an extra CO ligand to the metal to form $[P_7M(CO)_4]^{3-}$ (M = Mo, and W) has been studied, where the $[P_7]^{3-}$ cage is forced to change its coordination mode and switches from η^4 to η^2 coordination in order to preserve the eighteen-electron configuration at the metal centre. The $[E'_7]^{3-}$ reverts back to its original nortricyclane structure. However, the product is unstable, and tends to lose a CO ligand when exposed to nitrogen.[151] These species show five resonances in their ^{31}P NMR spectra, as expected for an η^2 coordinated cluster with the relative intensities 1:1:1:2:2.

In 1996, Eichhorn *et al*. published the interconversion between the $[P_7M(CO)_3]^{3-}$, the protonated or alkylated $[(H/R)P_7M(CO)_3]^{3-}$, and the further carbonylated form $[HP_7M(CO)_4]^{2-}$ as shown in Scheme 1.7.[151]

The reaction of the $[P_7]^{3-}$ cage and $[Ni(CO)_2(PPh_3)_2]$ has also been studied, yielding the η^4 coordination compound $[P_7Ni(CO)]^{3-}$ (Figure 1.59).[144] Just like in the previously discussed species, $[E'_7M(CO)_3]^{3-}$, the cage acts as a six-electron donor. Consequently, the nickel centre has eighteen valence electrons.

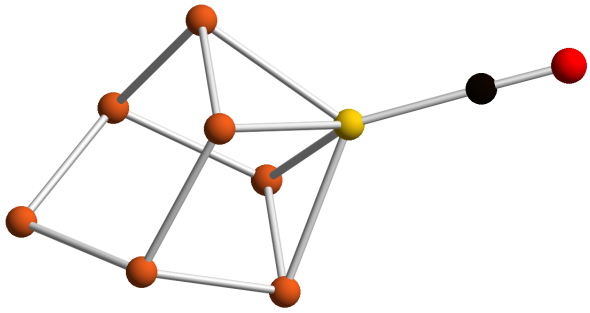

Figure 1.59: Ball and stick representation of $[P_7Ni(CO)]^{3-}$ (P atoms are shown in orange, the Ni atom in yellow, the C atom in black and the O atom in red).

The solid-state structure reveals a highly symmetrical structure, unlike the $[E'_7M(CO)_3]^{3-}$ anions. This is also corroborated by ^{31}P NMR spectroscopy, where only three resonances are observed, with the relative intensities of 1:2:4. This anion can be protonated by slow

addition of MeOH at –50 ºC to give rise to the complex $[HP_7Ni(CO)]^{2-}$. The IR spectrum reveals similar behaviour to the $[E'_7M(CO)_3]^{3-}$ anions. A low stretching frequency is observed, indicating that there is significant electron-donation to the Ni(CO) fragment from the $[P_7]^{3-}$ cage, which weakens the C–O bond.

In 2011 Goicoechea published a phosphorus-based Zintl ion analogue of ferrocene, $[Fe(HP_7)]^{2-}$ (Figure 1.60). This complex was synthesised by the simple salt-metathesis reaction of $FeCl_2$ and the Zintl phase K_3P_7.[152] The original yield was very low due to the lack of a proton source. H^+ was originally abstracted from the ethylenediamine, or adventitious moisture. It was later discovered that by adding two equivalents of $[NH_4][BPh_4]$ to the reaction mixture, the yield could be improved significantly.

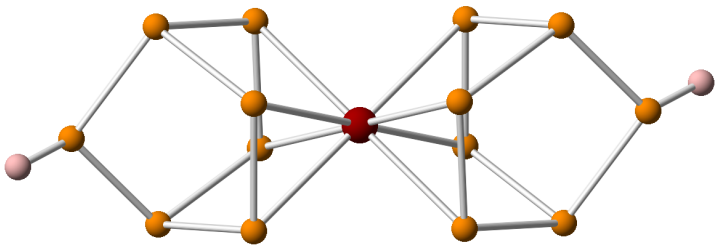

Figure 1.60: Ball and stick diagram of $[Fe(HP_7)_2]^{2-}$ (P atoms are shown in orange, the Fe atom in red and H atoms in pink).

X-ray crystallography revealed two protonated $[HP_7]^{2-}$ cages bridged by an iron centre in an η^4 fashion, each donating six electrons to the metal centre. The Fe^{2+} centre has a total of eighteen valence electrons. Both of the $[HP_7]^{2-}$ cages are disordered over two positions each with 50% occupancy, while the iron atom sits on a crystallographic centre of inversion. For this reasons it was not possible to determine whether the two cages are staggered or eclipsed by X-ray crystallography.

Calculations on the $[HP_7]^{2-}$ cage revealed four frontier orbitals of π-type symmetry (HOMO–9, HOMO–1, HOMO and LUMO), three of which are full. These orbitals are of

comparable symmetry to those of the cyclobutadienyl dianion and are able to interact with a transition metal centre. A fifth frontier orbital (HOMO–11) was found to mainly consist of P–H bonding orbital character. The principal frontier orbitals for both isomers of $[Fe(HP_7)_2]^{2-}$ have significant metal d orbital character. The HOMO for both isomers are non-bonding and are mainly composed of iron d_{z^2} orbital. The HOMO–1 and HOMO–2 have significant d_{xy} and $d_{x^2-y^2}$ character, respectively. For the staggered isomer, these two orbitals are quasi-degenerate, while in the case of the eclipsed isomer, the d_{xy} orbital is no bonding and mixes with the HOMO. The LUMO and LUMO+1 were found to have predominantly d_{xz} and d_{yz} orbital character, respectively. The corresponding π bonding orbitals are the HOMO–4 and HOMO–11 for the staggered isomer, and HOMO–4 and HOMO–9 for the eclipsed isomer. DFT calculations on the staggered and eclipsed isomers of $[Fe(HP_7)_2]^{2-}$ were performed revealing an energy difference of 40 kJ/mol, with the staggered isomer being lower in energy.

The ^{31}P NMR spectrum shows four resonances with the relative intensities of 1:2:2:2. The proton attached to the apical phosphorus atom could be observed by ^{1}H NMR as a doublet at δ = 6.56 ppm.

1.3.2.5 Reaction of the group 15 $[E'_7]^{3-}$ clusters towards metal complexes where cluster fragmentation occurs

Cluster activation is a more common type of reactivity for group 14 clusters than for those of group 15. The dissociation energy of the E'–E' bond is a good indication of how readily a $[E'_7]^{3-}$ cluster cluster can activate. The Sb–Sb bond dissociation energy (121 kJ/mol) is lower than the As–As (146 kJ/mol) and P–P (146 kJ/mol) bond dissociation energies. This is reflected in the fact that the $[Sb_7]^{3-}$ cage exhibits the greatest number of

examples of cluster activation, followed by the $[As_7]^{3-}$ and to date, there is only one example of activation of the $[P_7]^{3-}$ cage reported in the literature.

The first activation product of an $[E'_7]^{3-}$ cage was synthesised serendipitously when von Schnering was attempting to synthesise Rb_3As_7 from the solid-state reaction of three equivalents of elemental rubidium and seven equivalents of elemental arsenic in niobium tubes. The isolated product was instead the $[NbAs_8]^{3-}$ anion (Figure 1.61).[153] After this, a series of compounds based on the latter were synthesised with the formulae $[ME'_8]^{n-}$ (E' = As: M = Mo: n = 2; E' = As: M = Cr and Nb: n = 3; E' = Sb: M = Mo, and Nb: n = 3).[154–156] These clusters were prepared by the reaction of $[E'_7]^{3-}$ (E' = As and Sb) with $M(Ar'')_2$ (M = Nb: Ar'' = toluene; M= Cr: Ar'' = naphthalene; M = Mo: Ar'' = Me-naphthalene).

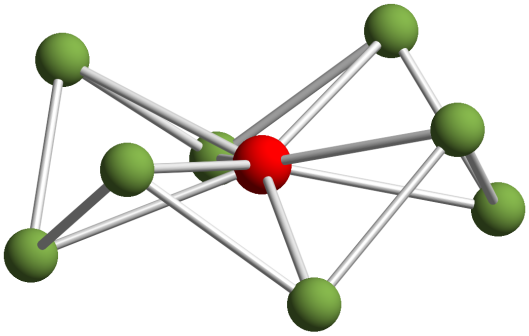

Figure 1.61: Ball and stick diagram of $[NbAs_8]^{3-}$ (The Nb atom is shown in red and As atoms in green).

In the solid-state, these species adopt a crown-like *cyclo*-$[E'_8]^{8-}$ structure, isoelectronic with S_8, giving oxidation states of the metallic centres as M^{5+} (for n = 3) and M^{6+} (for n = 2). Group 6 metals, molybdenum and chromium, have been found with different oxidation states, this can be explained by the fact that 4d transition metals adopt higher oxidation states relative to 3d metals. Single crystal X-ray diffraction studies revealed that the size of the ring changes depending on the metal it is hosting inside. In $[MoAs_8]^{2-}$

and $[MoSb_8]^{3-}$ the central molybdenum ion has different oxidation states. This can be explained by the fact that $[As_8]$ ring is more electronegative than $[Sb_8]$, and can stabilise the higher oxidation state Mo^{6+}. $[NbAs_8]^{3-}$, $[NbSb_8]^{3-}$ and $[MoAs_8]^{3-}$ have been formally characterised as sixteen-electron diamagnetic compounds whereas $[MoSb_8]^{3-}$ and $[CrAs_8]^{3-}$ are seventeen-electron paramagnetic species, as confirmed by EPR spectroscopy.

The missing member of this family, $[CrSb_8]^{n-}$, has not been synthesised. A possible explanation could be that the chromium atom is too small to properly interact with a large $[Sb_8]^{8-}$ ring.

The reaction between $[Ni(CO)_2(PPh_3)_2]$ and the $[Sb_7]^{3-}$ cage yielded the activation compound $[Sb_7Ni_3(CO)_3]^{3-}$ (Figure 1.62).[157] Interestingly, the geometry of this compound can be considered as an electron-deficient cluster with a *nido* geometry and rationalised using Wade-Mingos rules. It is a ten-vertex cluster in which each antimony atom contributes three electrons to cluster bonding, which in addition to the three electrons of the overall charge gives a total of 24 electrons (2n + 4). However, as was observed by solid-state studies not all the faces in the cluster are triangular. There are two four-membered rings fused along a common edge (*nido*-10(iv+iv) structure). An alternative way of defining this cluster involves a 24-electron $[Sb_7Ni(CO_3)]$ cuneane-core with an Sb–Ni blade edge. This cuneane core is electron-precise with twelve two-centre, two-electron bonds. Two additional Ni(CO) fragments cap the open faces to generate $[Sb_7Ni_3(CO)_3]^{3-}$.

The formation of $[Sb_7Ni_3(CO)_3]^{3-}$ may involve a $[Sb_7Ni(CO)]^{3-}$ intermediate, which is electronically equivalent to the structurally characterised $[Sb_7M(CO)_3]^{3-}$ complexes (M =

Cr, Mo and W).[146] Formation of $[Sb_7Ni_3(CO)_3]^{3-}$ can be accomplished by adding two additional Ni(CO) fragments plus further rearrangement. The exact mechanism of this transformation is not known.

Although three equivalents of Ni(CO) are inserted in the $[Sb_7]^{3-}$ cage, if the reaction is performed with three equivalents of the $[Ni(CO)_2(PPh_3)_2]$ instead of one, the product is not observed.

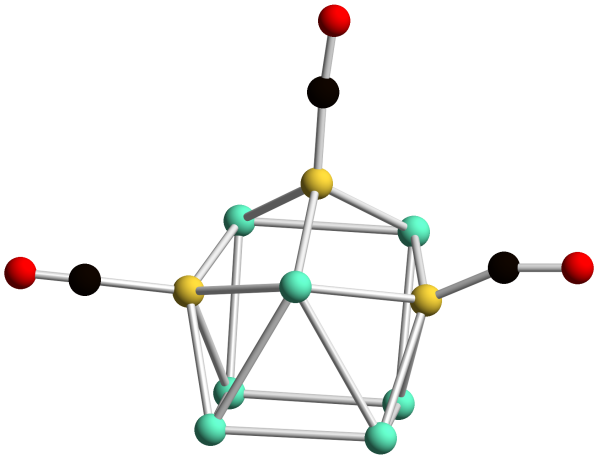

Figure 1.62: Ball and stick diagram of $[Sb_7Ni_3(CO)_3]^{3-}$ (Sb atoms are shown in green and Ni atoms in yellow, C atoms in black and O atoms in red).

In 2003, Eichhorn and co-workers published the synthesis of $[As@Ni_{12}@As_{20}]^{3-}$ (Figure 1.63).[158] This species was prepared from the reaction of $[As_7]^{3-}$ and $Ni(COD)_2$ in ethylenediamine. It consists of a nearly perfect I_h $[As_{20}]$ cage with a $[Ni_{12}]$ cage inside and a single arsenic atom residing in the centre of the "onion"-like cluster. The $[As_{20}]$ cage has pentagonal faces with the lone pairs pointing radially way from the cluster, similar to an electron-precise structure. The $[Ni_{12}]$ cage is an electro-deficient cage. Each arsenic atom of the $[As_{20}]$ cage caps a $[Ni_3]$ triangular face and each $[As_5]$ ring is centred by a nickel atom.

Electronically, the $[As_{20}]$ cage has thirty covalent two-centre, two-electron bonds, which require sixty electrons. Additionally, each arsenic atom has a lone pair pointing away from the cluster (forty electrons in total). This gives a total of one hundred electrons for the external $[As_{20}]$ unit. There is no significant degree of interaction between the electrons in the As–As single bonds and the $[As@Ni_{12}]^{3-}$ fragment, nevertheless, the twenty lone pairs do interact with twenty p-type orbitals (with some s character) of the same symmetry.

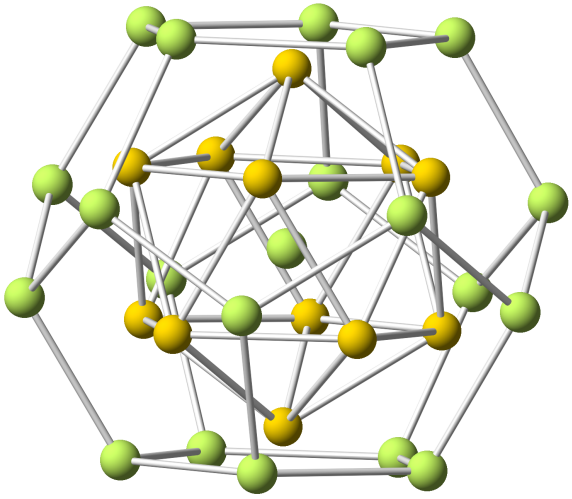

Figure 1.63: Ball and Stick diagram of $[As@Ni_{12}@As_{20}]^{3-}$ (As atoms are shown in green and Ni atoms in yellow).

The $[As@Ni_{12}]^{3-}$ fragment has a total of 128 electrons, ten valence electron from each nickel atom, five from the central arsenic and three of the overall charge. These 128 valence electrons, plus the 40 electrons from the As_{20} lone pairs sums up to 168 valence electrons, providing a diamagnetic electronic structure.

Mass spectrometric studies revealed peaks corresponding to the entire $[As@Ni_{12}@As_{20}]^{3-}$ cluster, as well as the peaks corresponding to the fragmentation $[Ni_{12}As_x]$ (x = 0 – 21).

In 2007, the reaction of the heavier Zintl ion $[Sb_7]^{3-}$ with $Ni(COD)_2$ was reported.[159] This reaction forms the $[Ni_5Sb_{17}]^{4-}$ anion with a very similar structure to the $[ME'_8]^{n-}$ clusters mentioned above (Figure 1.64). Crystals of this species were obtained along with $[K(2,2,2\text{-crypt})]_4[(Sb_7)_2Ni_x(Ni_2Sb_2)_2]$ which is similar to $[Ni_5Sb_{17}]^{4-}$ but with a partially occupied interstitial nickel atom of variable occupancy.

The $[Ni_5Sb_{17}]^{4-}$ anion contains a Ni(*cyclo*-Ni_4Sb_4) ring unit that resides inside a bowl-shaped $[Sb_{13}]$ unit. The nickel atom in the centre, with a square pyramidal geometry, is bonded to the four antimony atoms in the ring and also to one antimony atom of the bowl-shaped $[Sb_{13}]$ unit. The electronic configuration of the central nickel can be seen as a d^8 metal plus two electrons per antimony atom giving a total of 18 valence electrons.

The four nickel atoms in the structure have bonding distances of 2.540(2) to 2.590(2) Å, which are indicative of a Ni–Ni bonding interaction. However, DFT calculations revealed that there is little (if any) direct Ni–Ni interaction.

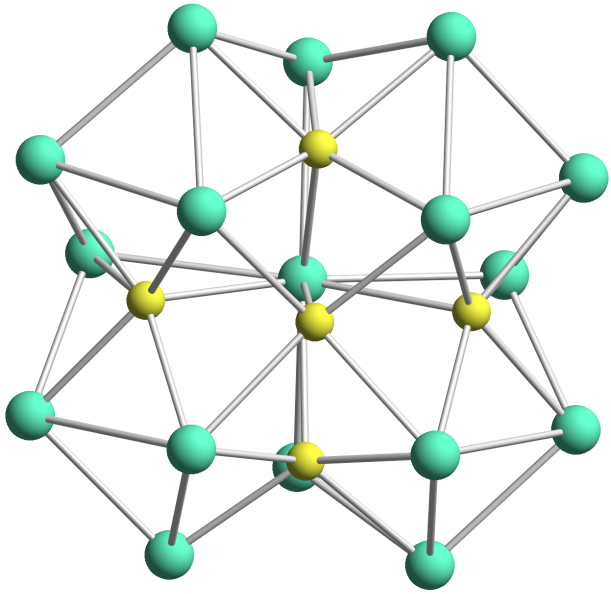

Figure 1.64: Ball and stick diagram of $[Ni_5Sb_{17}]^{4-}$ (Ni atoms are shown in yellow and Sb atoms in green).

The $[Ni_5Sb_{17}]^{4-}$ anion has a total of 139 valence electrons, which is indicative of a paramagnetic species. Nevertheless EPR measurements did not reveal a resonance at room temperature. DFT calculations were attempted in both S = 1/2 and 3/2 electronic configuration, but only the latter converged, which is consistent with the EPR observation.

The reaction between the $[As_7]^{3-}$ Zintl ion and $Pd(Cy_3)_2$ yields the simpler $[Pd_2(As_7)_2]^{4-}$ anion discussed on Section 1.3.2.4.2 , plus the minor activation product $[Pd_7As_{16}]^{4-}$ (Figure 1.65).[143] The latter consists of a bowl-like moiety $[Pd_2As_{12}]$, a cyclic $[Pd_4As_4]$ subunit and a central palladium atom. The central palladium atom is electronically unsaturated with a total of 16 valence electrons (eight from the valence electrons, plus two electrons per coordinated arsenic). This makes the palladium atom capable of forming Pd–Pd bonds, as demonstrated by DFT calculations.

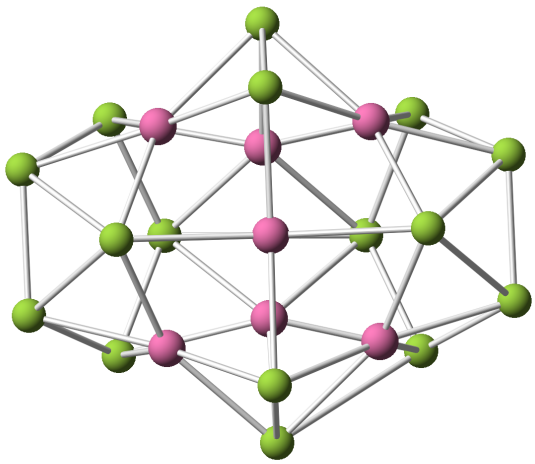

Figure 1.65: Ball and stick diagram of $[Pd_7As_{16}]^{4-}$ (As atoms are shown in green and Pd atoms in pink).

This molecular structure has C_{2v} symmetry, with a $[Pd_7]$ core, two $[As_5]^-$ rings, two $[As_2]^{2-}$ units and two As^{3-} atoms. The $[Pd_7]$ core can be seen as a distorted capped trigonal prism or two cyclopentane-like rings fused at a common edge sharing a common

vertex. In the core there are six Pd^{+} ions in the trigonal prism and a Pd^{2+} with a square-planar geometry capping one face of the trigonal prism.

K_3P_7 reacts with $Co(mes)_2(PEt_2Ph)_2$ in ethylenediamine and in the presence of 2,2,2-crypt to form $[Co(\eta^5\text{-}P_5)\{\eta^2\text{-}P_2H(mes)\}]^{2-}$ (Figure 1.66).[160] The latter is the first activation product of a $[P_7]^{3-}$ cage. It is worth pointing out that the number of E' atoms remains the same in the starting material and in the product, which is not usually the case.

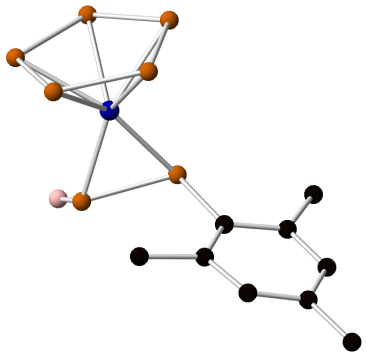

Figure 1.66: Ball and stick diagram of $[Co(\eta^5\text{-}P_5)\{\eta^2\text{-}HP_2(mes)\}]^{2-}$ (P atoms are shown in orange, the Co atom in blue, C atoms in black and H atom in pink). H atoms in the mes group are omitted for clarity.

The product features a cyclic $[P_5]^{-}$ ring, coordinating in an η^5 fashion to the cobalt atom and a (mes)P=PH fragment coordinating to the cobalt atom through both phosphorus atoms. The $[P_5]^{-}$ ring can be considered isolobal to a cyclopentadienyl group. The isomer formed in the (mes)P=PH moiety (*cis* or *trans*), is not clear because the proton could not be located by X-ray crystallography. However, DFT calculations showed that the *trans* isomer is 15 kJ/mol lower in energy than the *cis*. ^{31}P NMR spectroscopic studies showed a singlet at δ = 157.6 ppm that integrates to five for the $[P_5]^{-}$ ring and two doublets that can be assigned to the (mes)P=PH fragment at δ = –12.6 and –105.9 ppm.

There are two possible extremes models that can be used to rationalise the electronic structure of $[Co(\eta^5\text{-}P_5)\{\eta^2\text{-}P_2H(mes)\}]^{2-}$. It can be considered as a Co^{1-} complex with a

$[P_5]^-$ and a neutral (mes)P=PH. This supports the long P=P bond which due to extensive π back-bonding from an electron-rich Co^{1-} centre to the π* orbital, resulting in the lengthening of the bond. Alternatively $[Co(\eta^5\text{-}P_5)\{\eta^2\text{-}P_2H(mes)\}]^{2-}$ can be considered as a Co^{1+} complex, with a $[P_5]^-$ and a diphosphanediide $[(mes)P\text{–}PH]^{2-}$. In this model the short P–P bond in $[(mes)P\text{–}PH]^{2-}$ would be attributed to the reduction in the electrostatic repulsion between the two phosphorus atoms upon coordination to a Co^{1+} core.

$Co(mes)_2(PEt_2Ph)_2$ reacts with K_3As_7 in ethylenediamine and in the presence of 2,2,2-crypt to form the activation product $[Co(\eta^3\text{-}As_3)\{\eta^4\text{-}As_4(mes)_2\}]^{2-}$ (Figure 1.67).[161] Similar to the analogous $[P_7]^{3-}$ reaction, the nuclearity of the final product is the same as in the starting material. X-ray crystallographic studies revealed the formation of a novel $[As_4(mes)_2]^{2-}$ ligand (1,4-diaryltetraarsenabutadienediide) along with the previously reported *cyclo* triarsenide ring coordinated to a cobalt centre. The metallic centre has a total of 18 valence electrons. Nine electrons from the d^9 metal ion, plus three electrons from the $[As_3]$ unit, four electrons from the $\eta^4\text{-}As_4(mes)_2$ moiety and two electrons from the overall charge.

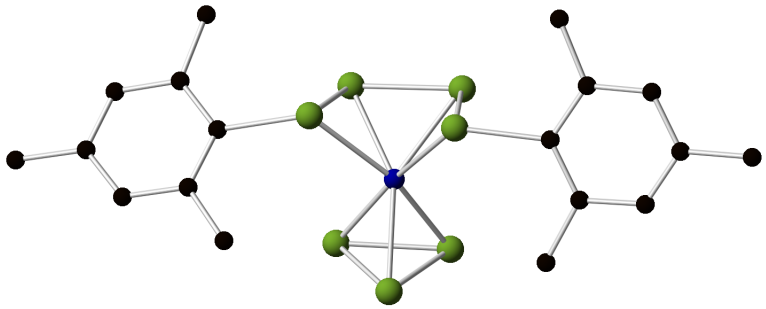

Figure 1.67: Ball and stick diagram of $[Co(\eta^3\text{–}As_3)\{\eta^4\text{–}As_4(mes)_2\}]^{2-}$(As atoms are shown in green, the Co atom in blue and C atoms in black). H atoms are omitted for clarity.

There are three possible oxidation states for the cobalt atom. The first is Co^{1+} which interacts with a neutral $\eta^4\text{-}As_4(mes)_2$ and a $[As_3]^{3-}$ unit. A Co^{3+} centre could be envisaged

interacting with a $[\eta^4\text{-}As_4(mes)_2]^{2-}$ and a $[As_3]^{3-}$. Finally a Co^{1-} is interacting with $[\eta^4\text{-}As_4(mes)_2]^{2-}$ and a $[As_3]^{+}$ ligand.

The butadiene like $[\eta^4\text{-}As_4(mes)_2]$ does not have alternating short-long-short bond lengths, implying that there is delocalisation in the ligand. This provides evidence that the ligand is dianionic.

Despite the fact that most of the examples of activation of $[E'_7]^{3-}$ cages have been metal mediated, there are reports of alternative methods to activate the cages. In 2012, Turbervill and Goicoechea reported the activation of the $[E'_7]^{3-}$ Zintl cages (E' = P and As) by reacting them with alkynes (R–C≡C–R') (R, R' = H; R = R' = Ph; R = H: R' = Ph) yielding the 1,2,3-tripnictolide monoanions $[E'_3C_2RR']^-$.[162,163] Additionally, these species have been studied as ligands and they are able to displace more labile ligands. And finally in 2013, Jupp and Goicoechea reported the reaction of the $[P_7]^{3-}$ cage with CO to yield the phosphaethynolate monoanion (PCO^-).[164]

This thesis will describe the reactivity of group 14, $[E_9]^{4-}$ (E = Ge and Sn), and group 15, $[E'_7]^{3-}$ (E' = P and As), Zintl ions towards metal and semi-metal complexes that have not been explored before. Most of the reactivity reported in the past, used as a metal source either metal alkyl complexes (MR_y) or metal halides (MX_y) as a metal source. Two chapters of this thesis (Chapter 2 and Chapter 4) will describe the reactivity of group 14 and 15 Zintl phases towards metal and semi-metal amides $(MNR_2)_y$. Chapters 3 and 5 will describe the metal-mediated activation of group 14 and 15 Zintl ions.

1.4 References

(1) Joannis, A. *Ann. Chim. Phys.* **1906**, *7*, 75.

(2) Joannis, A. *C. R. Hebd. Seances Acad. Sci.* **1891**, *113*, 795.

(3) Joannis, A. *C. R. Hebd. Seances Acad. Sci.* **1892**, *113*, 587.

(4) Kraus, C. A. *J. Am. Chem. Soc.* **1925**, *47*, 43.

(5) Peck, E. B. *J. Am. Chem. Soc.* **1918**, *40*, 335.

(6) Zintl, E.; Kaiser, H. *Z. Anorg. Allg. Chem.* **1933**, *211* (1-2), 113–131.

(7) Zintl, E.; Dullenkopf, W. *Z. Phys. Chem., Abt. B.* **1932**, *16*, 183.

(8) Zintl, E.; Goubeau, J.; Dullenkopf, W. *Z. Phys. Chem., Abt. A.* **1931**, *154*, 1.

(9) Zintl, E.; Harder, A. *Z. Phys. Chem., Abt. A* **1931**, *154*, 47.

(10) Zintl, E.; Harder, A. Neumayr, S. *Z. Phys. Chem., Abt. A* **1931**, *154*, 92.

(11) Diehl, L.; Khodadadeh, K.; Kummer, D.; Strahle, J. *Z. Naturforschung Sect. B- J. Chem. Sci.* **1976**, *31* (4), 522–524.

(12) Critchlow, S. C.; Corbett, J. D. *J. Am. Chem. Soc.* **1983**, *105* (17), 5715–5716.

(13) Fässler, T. F.; Schütz, U. *Inorg. Chem.* **1999**, *38* (8), 1866–1870.

(14) Somer, M.; Carrillo-Cabrera, W.; Peters, E. M.; Peters, K.; Schnering, H. G. *Z. Anorg. Allg. Chem.* **1998**, *624* (11), 1915–1921.

(15) Corbett, J. D.; Adolphson, D. G.; Merryman, D. J.; Edwards, P. A.; Armatis, F. J. *J. Am. Chem. Soc.* **1975**, *97* (21), 6267–6268.

(16) Scharfe, S.; Kraus, F.; Stegmaier, S.; Schier, A.; Fässler, T. F. *Angew. Chem. Int. Ed.* **2011**, *50* (16), 3630–3670.

(17) Fässler, T. F. *Angew. Chem. Int. Ed.* **2001**, *40* (22), 4161–4165.

(18) Corbett, J. D. *Chem. Rev.* **1985**, *85* (5), 383–397.

(19) Corbett, J. D. *Angew. Chem. Int. Ed.* **2000**, *39* (4), 670–690.

(20) Sevov, S. C.; Goicoechea, J. M. *Organometallics* **2006**, *25* (24), 5678–5692.

(21) Nolan, B. M.; Henneberger, T.; Waibel, M.; Fässler, T. F.; Kauzlarich, S. M. *Inorg. Chem.* **2014**.

(22) Manriquez, V.; Hönle, W.; von Schnering, H. G. *Z. Anorg. Allg. Chem.* **1986**, *539* (8), 95–109.

(23) Santandrea, R. P.;Mensing, C.; von Schnering, H.G. *Thermochim. Acta* **1986**, *98*, 301–311.

(24) Meyer, T.; Hönle, W.; von Schnering, H. G. *Z. Anorg. Allg. Chem.* **1987**, *552* (9), 69–80.

(25) Emmerling, F.; Rohr, C. *Z. Naturforsch. 57 b* **2002**, 963–975.

(26) Hirschle, C.; Röhr, C. *Z. Anorg. Allg. Chem.* **2000**, *626* (9), 1992–1998.

(27) Wichelhaus, W.; von Schnering, H. G. *Naturwissenschaften* **1973**, *60* (2), 104–104.

(28) Von Schnering, H. G.; Somer, M.; Kliche, G.; Hönle, W.; Meyer, T.; Wolf, J.; Ohse, L.; Kempa, P. B. *Z. Für Anorg. Allg. Chem.* **1991**, *601* (1), 13–30.

(29) Dahlmann, W.; von Schnering, H. G. *Naturwissenschaften* **1972**, *59* (9), 420–420.

(30) Dahlmann, W.; von Schnering, H. G. *Naturwissenschaften* **1973**, *60* (9), 429–429.

(31) Schmettow, W.; von Schnering, H. G. *Angew. Chem. Int. Ed. Engl.* **1977**, *16* (12), 857–857.

(32) Weinert, B.; Eulenstein, A. R.; Ababei, R.; Dehnen, S. *Angew. Chem. Int. Ed.* **2014**, *53* (18), 4726–4726.

(33) Mingos, D. M. P. *Acc. Chem. Res.* **1984**, *17* (9), 311–319.

(34) Mingos, D. M. P. *Nature* **1972**, *236* (68), 99–102.

(35) Wade, K. *J. Chem. Soc. D* **1971**, *15*, 792.

(36) Rudolph, R. W.; Wilson, W. L.; Parker, F.; Taylor, R. C.; Young, D. C. *J. Am. Chem. Soc.* **1978**, *100* (14), 4629–4630.

(37) Belin, C. H. E.; Corbett, J. D.; Cisar, A. *J. Am. Chem. Soc.* **1977**, *99* (22), 7163–7169.

(38) Campbell, J.; Dixon, D. A.; Mercier, H. P. A.; Schrobilgen, G. J. *Inorg. Chem.* **1995**, *34* (23), 5798–5809.

(39) Sen, T.; Poupko, R.; Fleischer, U.; Zimmermann, H.; Luz, Z. *J. Am. Chem. Soc.* **2000**, *122* (5), 889–896.

(40) Baudler, M. *Angew. Chem. Int. Ed. Engl.* **1982**, *21* (7), 492–512.

(41) Poupko, R.; Zimmermann, H.; Müller, K.; Luz, Z. *J. Am. Chem. Soc.* **1996**, *118* (34), 7995–8005.

(42) Oth, J. F. M.; Müllen, K.; Gilles, J.-M.; Schröder, G. *Helv. Chim. Acta* **1974**, *57* (5), 1415–1433.

(43) Schröder, G. *Angew. Chem. Int. Ed. Engl.* **1963**, *2* (8), 481–482.

(44) Xu, L.; Sevov, S. C. *J. Am. Chem. Soc.* **1999**, *121* (39), 9245–9246.

(45) Hauptmann, R.; Fässler, T. F. *Z. Anorg. Allg. Chem.* **2003**, *629* (12-13), 2266–2273.

(46) Nienhaus, A.; Hoffmann, S. D.; Fässler, T. F. *Z. Anorg. Allg. Chem.* **2006**, *632* (10-11), 1752–1758.

(47) Ugrinov, A.; Sevov, S. C. *J. Am. Chem. Soc.* **2002**, *124* (37), 10990–10991.

(48) Ugrinov, A.; Sevov, S. C. *Inorg. Chem.* **2003**, *42* (19), 5789–5791.

(49) Yong, L.; Hoffmann, S. D.; Fässler, T. F. *Z. Anorg. Allg. Chem.* **2004**, *630* (12), 1977–1981.

(50) Downie, C.; Mao, J.-G.; Parmar, H.; Guloy, A. M. *Inorg. Chem.* **2004**, *43* (6), 1992–1997.

(51) Downie, C.; Tang, Z.; Guloy, A. M. *Angew. Chem. Int. Ed.* **2000**, *39* (2), 337–340.

(52) Ugrinov, A.; Sevov, S. C. *Comptes Rendus Chim.* **2005**, *8* (11–12), 1878–1882.

(53) Ugrinov, A.; Sevov, S. C. *Chem. Eur. J.* **2004**, *10* (15), 3727–3733.

(54) Ugrinov, A.; Sevov, S. C. *J. Am. Chem. Soc.* **2003**, *125* (46), 14059–14064.

(55) Ugrinov, A.; Sevov, S. C. *J. Am. Chem. Soc.* **2002**, *124* (11), 2442–2443.

(56) Gillett-Kunnath, M. M.; Oliver, A. G.; Sevov, S. C. *J. Am. Chem. Soc.* **2011**, *133* (17), 6560–6562.

(57) Hull, M. W.; Ugrinov, A.; Petrov, I.; Sevov, S. C. *Inorg. Chem.* **2007**, *46* (7), 2704–2708.

(58) Hull, M. W.; Sevov, S. C. *Angew. Chem. Int. Ed.* **2007**, *46* (35), 6695–6698.

(59) Hull, M. W.; Sevov, S. C. *Inorg. Chem.* **2007**, *46* (26), 10953–10955.

(60) Chapman, D. J.; Sevov, S. C. *Inorg. Chem.* **2008**, *47* (13), 6009–6013.

(61) Eichhorn, B. W.; Haushalter, R. C.; Pennington, W. T. *J. Am. Chem. Soc.* **1988**, *110* (26), 8704–8706.

(62) Yong, L.; Hoffmann. S. D.; Fassler, T. F. *Z. Krist. New Cryst. St.* **2005**, *1* (220), 53.

(63) Kesanli, B.; Fettinger, J.; Eichhorn, B. W. *Chem. Eur. J.* **2001**, *7* (24), 5277–5285.

(64) Campbell, J.; Mercier, H. P. A.; Franke, H.; Santry, D. P.; Dixon, D. A.; Schrobilgen, G. J. *Inorg. Chem.* **2001**, *41* (1), 86–107.

(65) Yong, L.; Hoffmann, S. D.; Fässler, T. F. *Eur. J. Inorg. Chem.* **2005**, *2005* (18), 3663–3669.

(66) Zhou, B.; Goicoechea, J. M. *Chem. Eur. J.* **2010**, *16* (36), 11145–11150.

(67) Rios, D.; Sevov, S. C. *Inorg. Chem.* **2010**, *49* (14), 6396–6398.

(68) Goicoechea, J. M.; Sevov, S. C. *J. Am. Chem. Soc.* **2006**, *128* (12), 4155–4161.

(69) Downing, D. O.; Zavalij, P.; Eichhorn, B. W. *Eur. J. Inorg. Chem.* **2010**, *2010* (6), 890–894.

(70) Goicoechea, J. M.; Sevov, S. C. *Organometallics* **2006**, *25* (19), 4530–4536.

(71) Zhou, B.; Denning, M. S.; Jones, C.; Goicoechea, J. M. *Dalton Trans.* **2009**, No. 9, 1571–1578.

(72) Zhou, B.; Denning, M. S.; Chapman, T. A. D.; Goicoechea, J. M. *Inorg. Chem.* **2009**, *48* (7), 2899–2907.

(73) Zhou, B.; Denning, M. S.; Chapman, T. A. D.; McGrady, J. E.; Goicoechea, J. M. *Chem. Commun.* **2009**, No. 46, 7221–7223.

(74) Zhu, Z.; Brynda, M.; Wright, R. J.; Fischer, R. C.; Merrill, W. A.; Rivard, E.; Wolf, R.; Fettinger, J. C.; Olmstead, M. M.; Power, P. P. *J. Am. Chem. Soc.* **2007**, *129* (35), 10847–10857.

(75) Huheey, J.E.; Keiter, E. A.; Keiter, R. L. New York, 1993.

(76) Nienhaus, A.; Hauptmann, R.; Fässler, T. F. *Angew. Chem. Int. Ed.* **2002**, *41* (17), 3213–3215.

(77) Boeddinghaus, M. B.; Hoffmann, S. D.; Fässler, T. F. *Z. Anorg. Allg. Chem.* **2007**, *633* (13-14), 2338–2341.

(78) Denning, M. S.; Goicoechea, J. M. *Dalton Trans.* **2008**, No. 43, 5882–5885.

(79) Yong, L.; Boeddinghaus, M. B.; Fässler, T. F. *Z. Anorg. Allg. Chem.* **2010**, *636* (7), 1293–1296.

(80) Scharfe, S.; Fässler, T. F. *Eur. J. Inorg. Chem.* **2010**, *2010* (8), 1207–1213.

(81) Wang, J.-Q.; Wahl, B.; Fässler, T. F. *Angew. Chem. Int. Ed.* **2010**, *49* (37), 6592–6595.

(82) Pyykkö, P.; Atsumi, M. *Chem. Eur. J.* **2009**, *15* (1), 186–197.

(83) Spiekermann, A.; Hoffmann, S. D.; Kraus, F.; Fässler, T. F. *Angew. Chem. Int. Ed.* **2007**, *46* (10), 1638–1640.

(84) Spiekermann, A.; Hoffmann, S. D.; Fässler, T. F.; Krossing, I.; Preiss, U. *Angew. Chem. Int. Ed.* **2007**, *46* (28), 5310–5313.

(85) Hansen, D. F.; Zhou, B.; Goicoechea, J. M. *J. Organomet. Chem.* **2012**, *721–722*, 53–61.

(86) Gardner, D. R.; Fettinger, J. C.; Eichhorn, B. W. *Angew. Chem. Int. Ed. Engl.* **1996**, *35* (23-24), 2852–2854.

(87) Esenturk, E. N.; Fettinger, J.; Eichhorn, B. W. *Polyhedron* **2006**, *25* (2), 521–529.

(88) Sun, Z.-M.; Zhao, Y.-F.; Li, J.; Wang, L.-S. *J. Clust. Sci.* **2009**, *20* (3), 601–609.

(89) Kesanli, B.; Fettinger, J.; Gardner, D. R.; Eichhorn, B. W. *J. Am. Chem. Soc.* **2002**, *124* (17), 4779–4786.

(90) Kocak, F. S.; Zavalij, P.; Eichhorn, B. W. *Chem. Eur. J.* **2011**, *17* (17), 4858–4863.

(91) Goicoechea, J. M.; Sevov, S. C. *Angew. Chem. Int. Ed.* **2005**, *44* (26), 4026–4028.

(92) Gillett-Kunnath, M. M.; Paik, J. I.; Jensen, S. M.; Taylor, J. D.; Sevov, S. C. *Inorg. Chem.* **2011**, *50* (22), 11695–11701.

(93) Rios, D.; Gillett-Kunnath, M. M.; Taylor, J. D.; Oliver, A. G.; Sevov, S. C. *Inorg. Chem.* **2011**, *50* (6), 2373–2377.

(94) Scharfe, S.; Fässler, T. F.; Stegmaier, S.; Hoffmann, S. D.; Ruhland, K. *Chem. Eur. J.* **2008**, *14* (15), 4479–4483.

(95) Hlukhyy, V.; Stegmaier, S.; van Wüllen, L.; Fässler, T. F. *Chem. Eur. J.* **2014**, 12157–12168.

(96) Esenturk, E. N.; Fettinger, J.; Eichhorn, B. W. *Chem. Commun.* **2005**, No. 2, 247–249.

(97) Esenturk, E. N.; Fettinger, J.; Eichhorn, B. W. *J. Am. Chem. Soc.* **2006**, *128* (28), 9178–9186.

(98) Krämer, T.; Duckworth, J. C. A.; Ingram, M. D.; Zhou, B.; McGrady, J. E.; Goicoechea, J. M. *Dalton Trans.* **2013**, *42* (34), 12120–12129.

(99) Wang, J.-Q.; Stegmaier, S.; Wahl, B.; Fässler, T. F. *Chem. Eur. J.* **2010**, *16* (6), 1793–1798.

(100) Esenturk, E. N.; Fettinger, J.; Lam, Y.-F.; Eichhorn, B. W. *Angew. Chem. Int. Ed.* **2004**, *43* (16), 2132–2134.

(101) Zhou, B.; Kräemer, T.; Thompson, A. L.; McGrady, J. E.; Goicoechea, J. M. *Inorg. Chem.* **2011**, *50* (17), 8028–8037.

(102) Esenturk, E. N.; Fettinger, J. C.; Eichhorn, B. W. *J. Am. Chem. Soc.* **2005**, *128* (1), 12–13.

(103) Hlukhyy, V.; He, H.; Jantke, L.-A.; Fässler, T. F. *Chem. Eur. J.* **2012**, *18* (38), 12000–12007.

(104) He, H.; Klein, W.; Jantke, L.-A.; Fässler, T. F. *Z. Anorg. Allg. Chem.* **2014**, *640* (14), 2864–2870.

(105) Kesanli, B.; Halsig, J. E.; Zavalij, P.; Fettinger, J. C.; Lam, Y.-F.; Eichhorn, B. W. *J. Am. Chem. Soc.* **2007**, *129* (15), 4567–4574.

(106) Goicoechea, J. M.; Sevov, S. C. *J. Am. Chem. Soc.* **2005**, *127* (21), 7676–7677.

(107) Kocak, F. S.; Zavalij, P.; Lam, Y.-F.; Eichhorn, B. W. *Inorg. Chem.* **2008**, *47* (9), 3515–3520.

(108) Sun, Z.-M.; Xiao, H.; Li, J.; Wang, L.-S. *J. Am. Chem. Soc.* **2007**, *129* (31), 9560–9561.

(109) Scharfe, S.; Kraus, F.; Stegmaier, S.; Schier, A.; Fässler, T. F. *Angew. Chem. Int. Ed.* **2011**, *50* (16), 3630–3670.

(110) Stegmaier, S.; Fässler, T. F. *J. Am. Chem. Soc.* **2011**, *133* (49), 19758–19768.

(111) Zhou, B.; Denning, M. S.; Kays, D. L.; Goicoechea, J. M. *J. Am. Chem. Soc.* **2009**, *131* (8), 2802–2803.

(112) Wang, J.-Q.; Stegmaier, S.; Fässler, T. F. *Angew. Chem. Int. Ed.* **2009**, *48* (11), 1998–2002.

(113) Von Schnering, H. G.; Manriquez, V.; Hönle, W. *Angew. Chem. Int. Ed. Engl.* **1981**, *20* (6-7), 594–595.

(114) Baudler, M.; Heumüller, R.; Hahn, J. *Z. Anorg. Allg. Chem.* **1985**, *529* (10), 7–14.

(115) Baudler, M.; Exner, O. *Chem. Ber.* **1983**, *116* (3), 1268–1270.

(116) Hanauer, T.; Aschenbrenner, J. C.; Korber, N. *Inorg. Chem.* **2006**, *45* (17), 6723–6727.

(117) Miluykov, V.; Kataev, A.; Sinyashin, O.; Lönnecke, P.; Hey-Hawkins, E. *Z. Anorg. Allg. Chem.* **2006**, *632* (10-11), 1728–1732.

(118) Baudler, M.; Düster, D.; Langerbeins, K.; Germeshausen, J. *Angew. Chem. Int. Ed. Engl.* **1984**, *23* (4), 317–318.

(119) Guerin, F.; Richeson, D. *Inorg. Chem.* **1995**, *34* (11), 2793–2794.

(120) Fritz, G.; Hoppe, K. D.; Hönle, W.; Weber, D.; Mujica, C.; Manriquez, V.; Schnering, H. G. *J. Organomet. Chem.* **1983**, *249* (1), 63–80.

(121) Fritz, G.; Schneider, H.-W. *Z. Anorg. Allg. Chem.* **1990**, *584* (1), 12–20.

(122) Von Schnering, H. G.; Fenske, D.; Hönle, W.; Binnewies, M.; Peters, K. *Angew. Chem. Int. Ed. Engl.* **1979**, *18* (9), 679–679.

(123) Fritz, G.; Layher, E.; Goesmann, H.; Hanke, D.; Persau, C. *Z. Für Anorg. Allg. Chem.* **1991**, *594* (1), 36–46.

(124) Aschenbrenner, J. C.; Korber, N. *Z. Anorg. Allg. Chem.* **2004**, *630* (1), 31–32.

(125) Dai, F.-R.; Xu, L. *Inorg. Chim. Acta* **2006**, *359* (13), 4265–4273.

(126) Fritz, G.; Härer, J.; Matern, E. *Z. Anorg. Allg. Chem.* **1983**, *504* (9), 38–46.

(127) Noblet, P.; Cappello, V.; Tekautz, G.; Baumgartner, J.; Hassler, K. *Eur. J. Inorg. Chem.* **2011**, *2011* (1), 101–109.

(128) Charles, S.; Fettinger, J. C.; Eichhron, B. W. *J. Am. Chem. Soc.* **1995**, *117* (19), 5303–5311.

(129) Mattamana, S. P.; Promprai, K.; Fettinger, J. C.; Eichhorn, B. W. *Inorg. Chem.* **1998**, *37* (24), 6222–6228.

(130) Milyukov, V. A.; Kataev, A. V.; Hey-Hawkins, E.; Sinyashin, O. G. *Russ. Chem. Bull.* **2007**, *56* (2), 298–303.

(131) Baudler, M.; Faber, W.; Hahn, J. *Z. Anorg. Allg. Chem.* **1980**, *469* (1), 15–21.

(132) Turbervill, R. S. P.; Goicoechea, J. M. *Organometallics* **2012**, *31* (6), 2452–2462.

(133) Turbervill, R. S. P.; Goicoechea, J. M. *Eur. J. Inorg. Chem.* **2014**, *2014* (10), 1660–1668.

(134) Turbervill, R. S. P.; Goicoechea, J. M. *Chem. Rev.* **2014**, *114* (21), 10807–10828.

(135) Knapp, C. M.; Large, J. S.; Rees, N. H.; Goicoechea, J. M. *Dalton Trans.* **2010**, *40* (3), 735–745.

(136) Knapp, C.; Zhou, B.; Denning, M. S.; Rees, N. H.; Goicoechea, J. M. *Dalton Trans.* **2009**, *39* (2), 426–436.

(137) Kesanli, B.; Charles, S.; Lam, Y.-F.; Bott, S. G.; Fettinger, J.; Eichhorn, B. W. *J. Am. Chem. Soc.* **2000**, *122* (45), 11101–11107.

(138) Mandal, S.; Reber, A. C.; Qian, M.; Liu, R.; Saavedra, H. M.; Sen, S.; Weiss, P. S.; Khanna, S. N.; Sen, A. *Dalton Trans.* **2012**, *41* (40), 12365–12377.

(139) Knapp, C. M.; Jackson, C. S.; Large, J. S.; Thompson, A. L.; Goicoechea, J. M. *Inorg. Chem.* **2011**, *50* (9), 4021–4028.

(140) Qian, M.; Reber, A. C.; Ugrinov, A.; Chaki, N. K.; Mandal, S.; Saavedra, H. M.; Khanna, S. N.; Sen, A.; Weiss, P. S. *ACS Nano* **2009**, *4* (1), 235–240.

(141) Chaki, N. K.; Mandal, S.; Reber, A. C.; Qian, M.; Saavedra, H. M.; Weiss, P. S.; Khanna, S. N.; Sen, A. *ACS Nano* **2010**, *4* (10), 5813–5818.

(142) Mandal, S.; Reber, A. C.; Qian, M.; Liu, R.; Saavedra, H. M.; Sen, S.; Weiss, P. S.; Khanna, S. N.; Sen, A. *Dalton Trans.* **2012**, *41* (18), 5454–5457.

(143) Moses, M. J.; Fettinger, J.; Eichhorn, B. W. *J. Am. Chem. Soc.* **2002**, *124* (21), 5944–5945.

(144) Charles, S.; Fettinger, J. C.; Bott, S. G.; Eichhorn, B. W. *J. Am. Chem. Soc.* **1996**, *118* (19), 4713–4714.

(145) Eichhorn, B. W.; Haushalter, R. C.; Huffman, J. C. *Angew. Chem. Int. Ed. Engl.* **1989**, *28* (8), 1032–1033.

(146) Charles, S.; Eichhorn, B. W.; Rheingold, A. L.; Bott, S. G. *J. Am. Chem. Soc.* **1994**, *116* (18), 8077–8086.

(147) Bolle, U.; Tremel, W. *J. Chem. Soc. Chem. Commun.* **1994**, No. 2, 217–219.

(148) Charles, S.; Danis, J. A.; Mattamana, S. P.; Fettinger, J. C.; Eichhorn, B. W. *Z. Anorg. Allg. Chem.* **1998**, *624* (5), 823–829.

(149) Charles, S.; Danis, J. A.; Fettinger, J. C.; Eichhorn, B. W. *Inorg. Chem.* **1997**, *36* (17), 3772–3778.

(150) Kesanli, B.; Mattamana, S. P.; Danis, J.; Eichhorn, B. W. *Inorg. Chim. Acta* **2005**, *358* (11), 3145–3151.

(151) Charles, S.; Fettinger, J. C.; Eichhorn, B. W. *Inorg. Chem.* **1996**, *35* (6), 1540–1548.

(152) Knapp, C. M.; Large, J. S.; Rees, N. H.; Goicoechea, J. M. *Chem. Commun.* **2011**, *47* (14), 4111–4113.

(153) Von Schnering, H. G.; Wolf, J.; Weber, D.; Ramirez, R.; Meyer, T. *Angew. Chem. Int. Ed. Engl.* **1986**, *25* (4), 353–354.

(154) Kesanli, B.; Fettinger, J.; Scott, B.; Eichhorn, B. W. *Inorg. Chem.* **2004**, *43* (13), 3840–3846.

(155) Eichhorn, B. W.; Mattamana, S. P.; Gardner, D. R.; Fettinger, J. C. *J. Am. Chem. Soc.* **1998**, *120* (37), 9708–9709.

(156) Kesanli, B.; Fettinger, J.; Eichhorn, B. W. *J. Am. Chem. Soc.* **2003**, *125* (24), 7367–7376.

(157) Charles, S.; Eichhorn, B. W.; Bott, S. G. *J. Am. Chem. Soc.* **1993**, *115* (13), 5837–5838.

(158) Moses, M. J.; Fettinger, J. C.; Eichhorn, B. W. *Science* **2003**, *300* (5620), 778–780.

(159) Moses, M. J.; Fettinger, J. C.; Eichhorn, B. W. *Inorg. Chem.* **2007**, *46* (4), 1036–1038.

(160) Knapp, C. M.; Westcott, B. H.; Raybould, M. A. C.; McGrady, J. E.; Goicoechea, J. M. *Angew. Chem. Int. Ed.* **2012**, *51* (36), 9097–9100.

(161) Knapp, C. M.; Westcott, B. H.; Raybould, M. a. C.; McGrady, J. E.; Goicoechea, J. M. *Chem. Commun.* **2012**, *48* (100), 12183–12185.

(162) Turbervill, R. S. P.; Goicoechea, J. M. *Chem. Commun.* **2012**, *48* (49), 6100–6102.

(163) Turbervill, R. S. P.; Jupp, A. R.; McCullough, P. S. B.; Ergöçmen, D.; Goicoechea, J. M. *Organometallics* **2013**, *32* (7), 2234–2244.

(164) Jupp, A. R.; Goicoechea, J. M. *Angew. Chem. Int. Ed.* **2013**, *52* (38), 10064–10067.

Chapter 2 Coordination chemistry of group 14 Zintl ions $[E_9]^{4-}$

2.1 Summary

To date, the coordination chemistry of Zintl ions has focused primarily on their interaction with transition metals. The most successful reactions involve the use of organometallic reagents (MR_n), while metal halides (MX_n) frequently give rise to undesired redox reactions and cluster decomposition. In our research group we have recently decided to study the reactivity of $M(NR_2)_2$ species towards Zintl ions.

Sevov and Goicoechea have studied the reactivity of group 14 Zintl ions towards ZnR_2 (R = Ph, mes and ^{i}Pr), which results in the formation of the η^4 coordination compounds $[E_9ZnR]^{3-}$.[1,2] These products are formed by the heterolytic cleavage of an Zn–C bond. In these compounds, the group 14 cages acts as a six-electron donor towards the metal centre.

This chapter will describe the reactivity of the group 14 Zintl cages $[E_9]^{4-}$ (E = Ge and Sn) towards $Zn[N(SiMe_3)_2]_2$. To our surprise, the products from these reactions are not analogous to those obtained using ZnR_2. The K_4Ge_9 reaction yields the simple metal functionalised product $[Ge_9ZnN(SiMe_3)_2]^{3-}$ (**1**), whereas with K_4Sn_9 the loss of a

trimethylsilyl group is observed, causing the formation of the paramagnetic compound $[Sn_9ZnNSiMe_3]^{3-}$ (**2**). The further solution-phase reactivity of **1** will be also discussed.

2.2 Introduction

The first compounds synthesised from reactions of group 14 $[E_9]^{4-}$ Zintl phases with metal reagents were coordination complexes. In the majority of the cases the Zintl ions coordinate to the metal centres as six-electron donors, in an η^4 fashion through the open face. However, there are a handful of examples where coordination occurs in an alternative manner: the cage can coordinate through one of the triangular faces in an η^2 or η^3 fashion, through only one E atom in a η^1 fashion, or in an η^5 fashion. In most cases, the nuclearity of the cage remains the same, however cluster activation has also been observed in a limited number of examples.

In the η^4 coordination compounds, the $[E_9]^{4-}$ Zintl ions act as six-electrons donors towards a metal centre and their geometry is retained forming a 10-vertex *closo* bicapped square antiprism. This type of coordination has been observed for compounds such as $[E_9M(CO)_3]^{4-}$ (E = Sn: M = Cr, Mo and W; E = Pb: M = Mo and W),[3–7] $[E_9Ir(COD)]^{3-}$ (E = Sn and Pb),[8] $[E_9MR]^{3-}$ (E = Si, Ge, Sn and Pb: M = Zn: R = Ph; E = Ge, Sn and Pb: M = Zn and Cd: R = mes and ^{i}Pr),[1,2,9] and $[Ge_9Ni(CO)]^{3-}$.[10]

The formation of the $[E_9MR]^{3-}$ (E = Si, Ge, Sn and Pb: M = Zn: R = Ph; E = Ge, Sn and Pb: M = Zn and Cd: R = mes and ^{i}Pr) clusters will be reviewed since the compounds discussed in this chapter are closely related.[1,2,9] In 2006, Goicoechea and Sevov reported a series of coordination compounds of the form $[E_9ZnPh]^{3-}$ (E = Si, Ge, Sn and Pb) (Figure 2.1) obtained by reaction of K_4E_9 with $ZnPh_2$.[1] This report

describes the first complete series of group 14 $[E_9]^{4-}$ clusters functionalised with the same fragment, and the very first example of a functionalised silicon cluster.

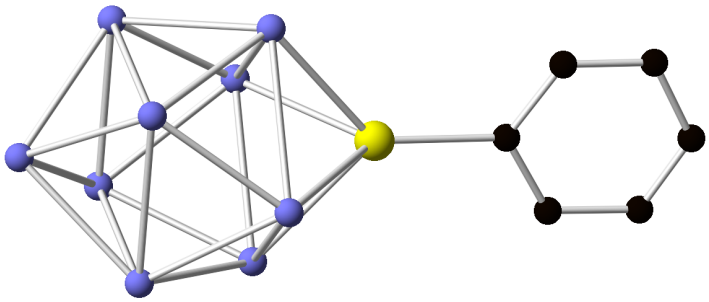

Figure 2.1: Ball and stick diagram of $[Ge_9ZnPh]^{3-}$ (Ge atoms are shown in purple, the Zn atom in yellow and C atoms in black). H atoms are omitted for clarity.

These reactions can be explained by the fact that, in solution, $[E_9]^{x-}$ (x = 2–4) clusters exist in equilibria between clusters of varying charges and free solvated electrons. These electrons reductively cleave the M–C bonds giving rise to an $[MR]^{\bullet}$ radical and an R^- anion. The latter subsequently deprotonates the solvent to form RH. The radical formed attacks the electron-rich cage through the open square face to form the 10-vertex cluster.

In these $[E_9ZnPh]^{3-}$ clusters each group 14 atom is sp^3 hybridised and donates three orbitals and two electrons for cluster bonding. The zinc atom donates one electron to the Zn–Ph bond and the other valence electron to the cluster. These compounds have a total of 22 skeletal electrons, including two electrons from each group 14 atom in the cluster, three from the overall charge and the zinc valence electron. 22 electrons corresponds to a *closo* cluster, according to Wade-Mingos rules, and this was corroborated by X-ray crystallography.

In 2009, Goicoechea *et al*. extended this work by preparing similar coordination compounds with the formulae $[E_9MR]^{3-}$ (E = Ge, Sn and Pb: M = Zn: R = mes and ^{i}Pr;

E = Ge, Sn and Pb: M = Cd: R = Ph, mes and ^{i}Pr) which incorporated different R groups and the heavier group 12 metal cadmium.[2,9] Further reactivity of $[Sn_9CdPh]^{3-}$ towards tributyltinhydride was investigated. This reaction affords a cluster with a Sn–Cd bond namely, $[Sn_9CdSn^{n}Bu]^{3-}$ (Figure 2.2).

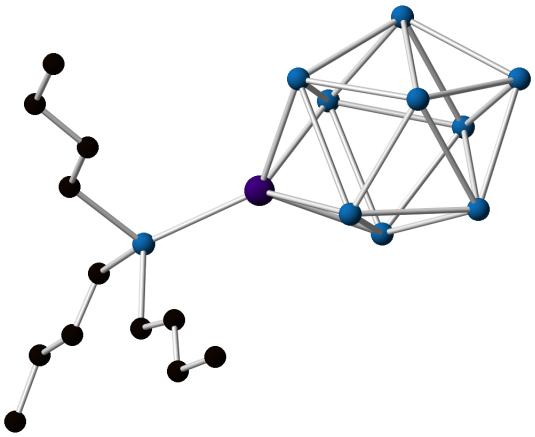

Figure 2.2: Ball and stick diagram of $[Sn_9CdSn^{n}Bu]^{3-}$ (Sn atoms are shown in blue, the Cd atom in purple and C atoms in black). H atoms are omitted for clarity.

The reactivity of other K_4E_9 Zintl phases towards further organometallic MR_2 compounds has been investigated in the past. The group 12 organometallic species $HgPh_2$ reacts with K_4Ge_9 to form the nanorod $[Ge_9–Hg–Ge_9–Hg–Ge_9–Hg–Ge_9]^{10-}$ (Figure 2.3).[11] The nine-atom cages at the extremes are distorted tricapped trigonal prisms whereas the other two are monocapped square antiprisms. The external cages are linked to the adjacent mercury atoms in an η^2 fashion while the central mercury atom is forming single covalent bonds with its two nearest neighbours.

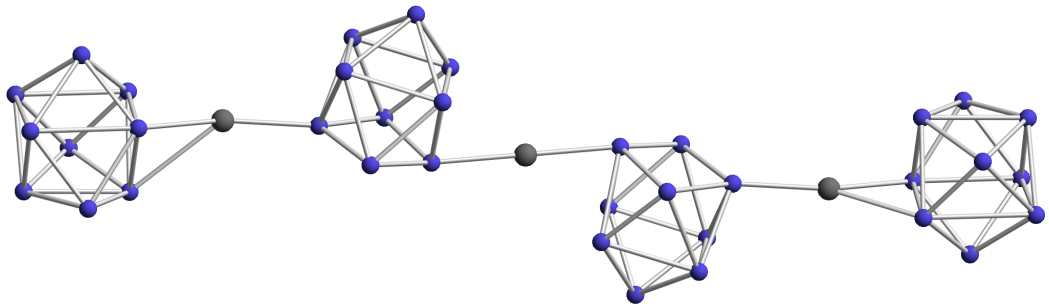

Figure 2.3: Ball and stick diagram of $[Ge_9–Hg–Ge_9–Hg–Ge_9–Hg–Ge_9]^{10–}$ (Ge atoms are shown in purple and Hg atoms in gray).

The reaction between K_4Sn_9 and elemental mercury in ethylenediamine has been also investigated. It leads to the formation of the coordination compound $[Sn_9–Hg–Sn_9]^{6–}$. The mercury atom sits on a crystallographic inversion centre and consequently, the two tin cages are identical. The two cages coordinate to the mercury atom cage in an η^2 mode.[12] The different reactivity of the group 12 MPh_2 compounds can be attributed to the difference in M–C bond dissociation energies, as M–C bonds get weaker as the metal becomes heavier.[13]

The reaction of K_4Sn_9 with $[Ag(mes)]_4$ affords $[Ag(Sn_9)_2]^{5–}$ (Figure 2.4), where two oxidatively-coupled cages are linked together through an *exo*-bond. The cages coordinate to the Ag^+ cation in an η^3 fashion.[14]

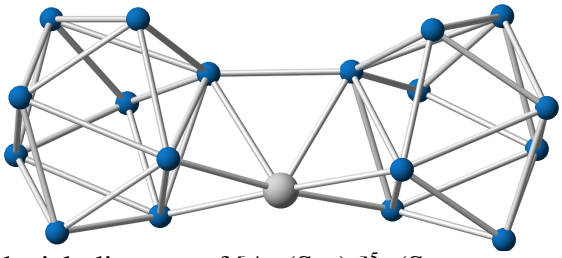

Figure 2.4: Ball and stick diagram of $[Ag(Sn_9)_2]^{5–}$ (Sn atoms are shown in blue and the Ag atom in silver).

2.3 Results and discussion

2.3.1 Reactivity of K_4E_9 towards $Zn[N(SiMe_3)_2]_2$ (E = Ge and Sn)

2.3.1.1 Synthesis of $[Ge_9ZnN(SiMe_3)_2]^{3-}$ (1)

Several reactions of K_4Ge_9 with $Zn[N(SiMe_3)_2]_2$ under a variety of conditions and stoichiometric loadings were monitored by mass spectrometry. After careful optimisation of the reaction conditions, it was found that a stoichiometric excess of $Zn[N(SiMe_3)_2]_2$ was needed for the reaction to reach completion (Scheme 2.1). The optimal synthesis consists of mixing one equivalent of K_4Ge_9 and four equivalents of 2,2,2-crypt in a Schlenk tube, dissolve the powders in 5 mL of ethylenediamine and leave the reaction mixture to stir for ten minutes. To this solution, three equivalents of $Zn[N(SiMe_3)_2]_2$ were added dropwise with a microsyringe resulting in the formation copious orange precipitate. The orange suspension was filtered and the filtrate was isolated. All the volatiles were removed under dynamic vacuum, and the resulting orange oil was washed with THF to remove any organic side products.

The resulting orange precipitate was characterised as containing the novel anionic species $[Ge_9ZnN(SiMe_3)_2]^{3-}$ (**1**) using NMR spectroscopy, mass spectrometry, X-ray crystallography and elemental analysis. The initial orange precipitate generated in the reaction mixture was characterised by mass spectrometry as $[Ge_9]^-$.

Crystals suitable for X-ray crystallography were grown from slow diffusion of toluene into a concentrated pyridine solution over the course of a week. The crystalline yield obtained for this reaction is 30%.

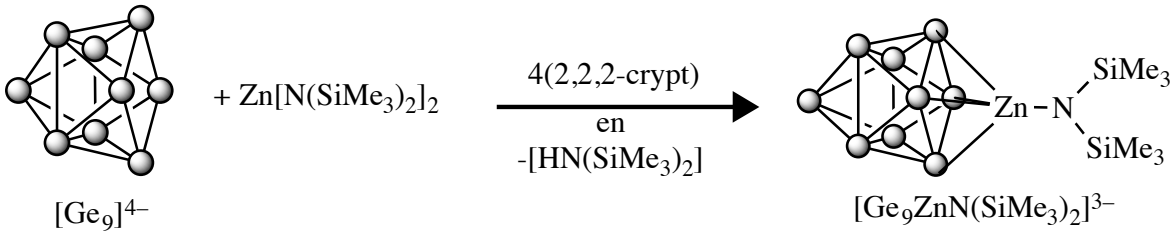

Scheme 2.1: Formation of **1**.

2.3.1.2 Structure of $[Ge_9ZnN(SiMe_3)_2]^{3-}$ (1)

The crystals used for X-ray crystallography were orange blocks with the formula $[K(2,2,2\text{-crypt})]_3[\mathbf{1}]\cdot 3tol$ (Figure 2.5).

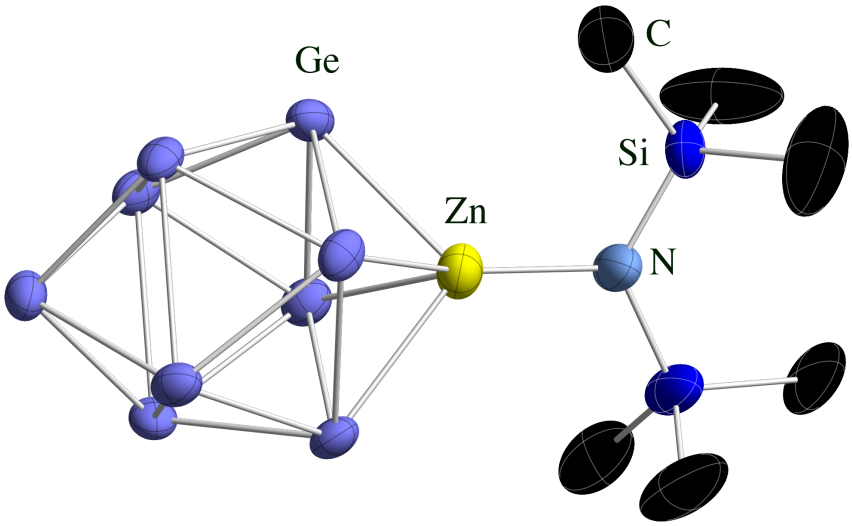

Figure 2.5: Thermal ellipsoid plot of **1**. Anisotropic displacement ellipsoids are pictured at 50% probability level. H atoms are omitted for clarity.

This reaction is very similar to previous reactions described in Section 2.2 involving a ZnR_2 reagent, where the reductive cleavage of a Zn–R bond takes place and η^4 coordination occurs (Scheme 2.2). In this case, the cleavage of a Zn–N bond takes place, yielding an amide $[N(SiMe_3)_2]^-$ which subsequently abstracts a proton from the ethylenediamine solvent to form the amine $HN(SiMe_3)_2$. This species can be removed under vacuum or extracted into THF. The resulting $[ZnN(SiMe_3)_2]^{\bullet}$ radical species subsequently interacts with $[Ge_9]^{3-}$ to form the coordination compound **1**.

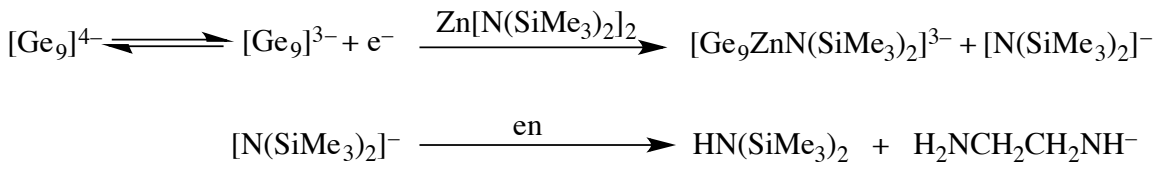

Scheme 2.2: Loss of one of an amide group by single electron reduction, leading to the formation of **1**, followed by the deprotonation of the ethylenediamine solvent to form an amide and an amine.

Goicoechea and Sevov reported a qualitative analysis of the frontier orbitals involved in bonding in $[E_9ZnPh]^{3-}$.[1] **1** exhibits an analogous electronic structure to these species.

A frontier orbital analysis of $[E_9ZnPh]^{3-}$ revealed that the cage has three filled molecular orbitals with appropriate symmetry to interact with the zinc atom. One of the zinc sp hybrid orbitals and two p_x and p_y orbitals have the correct symmetry to interact with the cage. One cluster orbital is predominantly made up of atomic orbitals at the four corners of the open base, which lie in the plane pointing towards the centre of the square face. The overlap between this cluster orbital and the sp orbital on the zinc centre gives rise to a σ bonding interaction. The p_x and p_y zinc orbitals also have their matches with orbitals on the open square face of the cluster. These two orbitals are quasi-degenerate and are composed of the out of phase combinations of p_π orbitals. Therefore, the $[E_9]^{4-}$ cage acts as a six-electron donor towards the zinc metal centre (Figure 2.6). The open square face of a $[E_9]^{4-}$ cluster can be considered as cyclopentadienyl analogue.

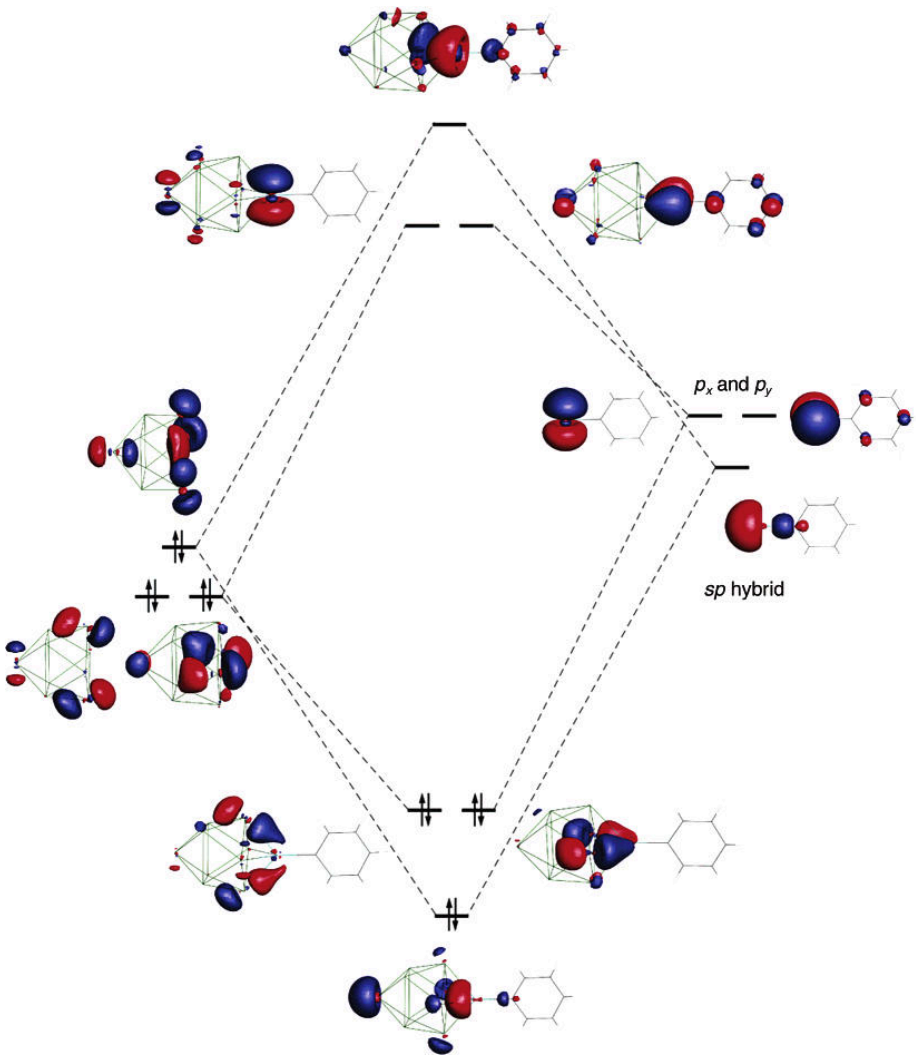

Figure 2.6: Qualitative fragment analysis of the interactions between the frontier orbitals of the nine-atom cluster (left) and the ZnPh fragment (right) in the formation of $[E_9ZnPh]^{3-}$.

The structure of the cluster is bicapped square antiprismatic, with the zinc acting as the 10th vertex. This is analogous to the $[E_9ZnPh]^{3-}$ clusters. The cluster has 22 skeletal electrons; two from each germanium atom, three of the overall charge and one from the $[ZnN(SiMe_3)_2]$ fragment. According to Wade-Mingos rules, 22 skeletal electrons for a ten-vertex cluster gives rise to a *closo* cluster, which is indeed what was observed in the X-ray crystallography studies. Table 2.1 shows selected bond lengths of **1**.

Bond in $[Ge_9ZnN(SiMe_3)_2]^{3-}$ (**1**)	Bond length (Å)
Ge1–Ge5	2.566(1)
Ge1–Ge4	2.571(1)
Ge1–Ge3	2.579(1)
Ge1–Ge2	2.581(1)
Ge2–Ge6	2.557(1)
Ge2–Ge9	2.570(1)
Ge2–Ge3	2.795(1)
Ge2–Ge5	2.881(1)
Ge3–Ge7	2.561(1)
Ge3–Ge6	2.574(1)
Ge3–Ge4	2.855(1)
Ge4–Ge8	2.552(1)
Ge4–Ge7	2.569(1)
Ge4–Ge5	2.807(1)
Ge5–Ge8	2.547(1)
Ge5–Ge9	2.554(1)
Ge6–Ge7	2.784(1)
Ge6–Ge9	2.786(1)
Ge7–Ge8	2.804(1)
Ge8–Ge9	2.789(1)
Ge9–Zn1	2.606(1)
Ge7–Zn1	2.590(1)
Ge8–Zn1	2.592(1)
Ge6–Zn1	2.596(1)
Zn1–N1	1.96(1)
N1–Si1	1.677(1)
N1–Si2	1.736(1)

Table 2.1: Selected bond lengths in **1**.

The Ge–Ge distances lie in the range of 2.547(1) to 2.881(1) Å, which are similar to those reported by Sevov for $[Ge_9ZnPh]^{3-}$ (2.543(1) to 2.838(1) Å).[1] The Zn–Ge distances lie in the narrow rage of 2.592(1) to 2.606(1) Å, which are similar to the $[Ge_9ZnPh]^{3-}$ compound (2.572(1) to 2.594(1) Å) and longer than the mean found in a Cambridge Structural Database (CSD) search: 2.521 (av) Å.[15] The sum of the covalent radii for a Zn–Ge single bond is 2.39 Å, which is shorter than the bond length found in **1** and is consistent with the electron-deficient nature of the cluster bonding.[16] The Zn–N bond is 1.962(4)Å which is similar to the mean for a single Zn–$N(SiMe_3)_2$ bond as

found in the CSD (1.934 Å) and slightly longer than to the sum of the covalent radii (1.89 Å).[17]

2.3.1.3 NMR spectroscopic studies on $[Ge_9ZnN(SiMe_3)_2]^{3-}$ (1)

Crystals of $[K(2,2,2\text{-crypt})]_3[\mathbf{1}]\cdot 3tol$ were dissolved in d_5-pyridine and characterised by ^1H and ^{13}C NMR spectroscopy. The ^1H NMR spectrum showed three resonances at δ = 3.44, 3.37 and 2.35 ppm corresponding to the 2,2,2-crypt protons. A fourth singlet at δ = 1.11 ppm was also observed corresponding to the methyl groups of the ligand.

^{13}C NMR spectroscopy showed three singlet resonances at δ = 71.2, 68.4 and 54.6 ppm corresponding to the 2,2,2-crypt and a singlet at δ = 10.2 ppm corresponding to the methyl groups of the amide functionality.

2.3.1.4 Mass spectrometric studies on $[Ge_9ZnN(SiMe_3)_2]^{3-}$ (1)

Mass spectrometry is a very useful tool for the study of group 14 Zintl ions, due to the variety of naturally occurring germanium isotopes (70, 72–74 and 76).[18] The isotopic distribution patterns of the mass envelopes in the spectra can be used to assign them unequivocally. Additionally zinc has five naturally occurring isotopes (64, 66–68 and 70).

Confirmation of the presence of the cluster anion in solution was obtained by electrospray mass spectrometry of DMF solutions of the reaction mixture. In the negative ion mode spectrum, a mass envelope corresponding to $[Ge_9ZnN(SiMe_3)_2]^-$ at 876.9 Da was observed (Figure 2.7). Other species found are listed on Table 2.2.

Molecular ion	Mass envelope (Da)	Relative intensity
$[Ge_9ZnN(SiMe_3)_2]^-$	876.9	100%
$[Ge_9]^-$	653.1	96.4%
$[K(Ge_9)]^-$	692.0	71.4%
$[K(Ge_9ZnN(SiMe_3)_2)]^-$	916.0	32.1%
$[Ge_9ZnNSiMe_3]^-$	809.6	28%
$\{[K(2,2,2\text{-crypt})][Ge_9ZnN(SiMe_3)_2]\}^-$	1294.2	27%
$[K(Ge_9ZnNSiMe_3)]^-$	846.9	27.1%
$\{[K(Ge_{10})]\}^-$	1070.1	23.6%
$\{[K(2,2,2\text{-crypt})][Ge_9]\}^-$	763.9	17.14%
$\{[K(2,2,2\text{-crypt})]_2[Ge_9ZnN(SiMe_3)_2)\}]^-$	1709.2	10%

Table 2.2: Mass envelopes observed in the mass spectrometric studies (negative ion mode) of the crude reaction mixture which afforded **1**.

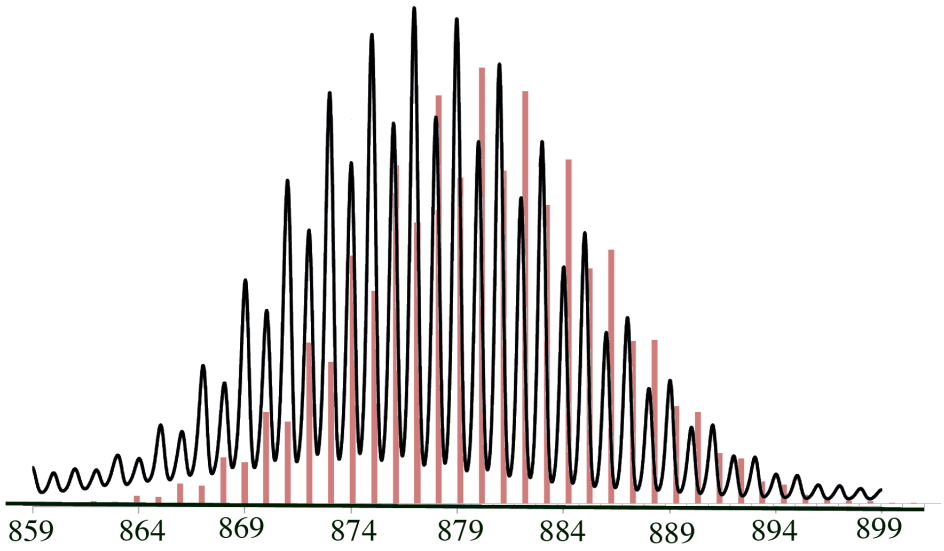

Figure 2.7: Negative ion mode electrospray mass envelope corresponding to $[Ge_9ZnN(SiMe_3)_2]^-$. Predicted isotopic distribution is shown in red and observed mass spectrometric data are shown in black.

In the positive ion mode spectrum less fragmentation is evident and very often the overall charge of the cluster can be determined. The mass envelope observed corresponds to the anion accompanied by the required number of cations to give an ion pair with 1+ charge. A mass envelope corresponding to $\{[K(2,2,2\text{-crypt})_4[Ge_9ZnN(SiMe_3)_2]\}^+$ was found at 2540.9 Da as the major species. Additionally, the mass envelope corresponding to {[K(2,2,2-

crypt)]$_4$[$Ge_9ZnNSiMe_3$]}$^+$ was observed as well at 2968.9 Da along with starting material.

A significant amount of fragmentation is observed in the negative ion mode, including starting material that was only observed in the mass spectrometer. The product resulting from the loss of a trimethylsilyl group ([$Ge_9ZnNSiMe_3$]$^-$) is also observed in both the positive and the negative mode, but not in the crystalline material.

2.3.1.5 Synthesis of $[Sn_9ZnNSiMe_3]^{3-}$ (2)

As with the K_4Ge_9 precursor, the reactivity of K_4Sn_9 towards $Zn[N(SiMe_3)_2]_2$ was investigated. Several reactions were monitored by mass spectrometry. After careful optimisation of the reaction conditions, it was found that the synthesis of $[Sn_9ZnNSiMe_3]^{3-}$ (**2**) involved reacting K_4Sn_9 and four equivalents of 2,2,2-crypt with one equivalent of $Zn[N(SiMe_3)_2]_2$ (Scheme 2.3). The black solution was filtered into a crystallisation ampoule and carefully layered with toluene. Large black block-like crystals were isolated after several days (yield 55%), and characterised as the paramagnetic compound **2** by single crystal X-ray diffraction, EPR spectroscopy, mass spectrometry and elemental analysis.

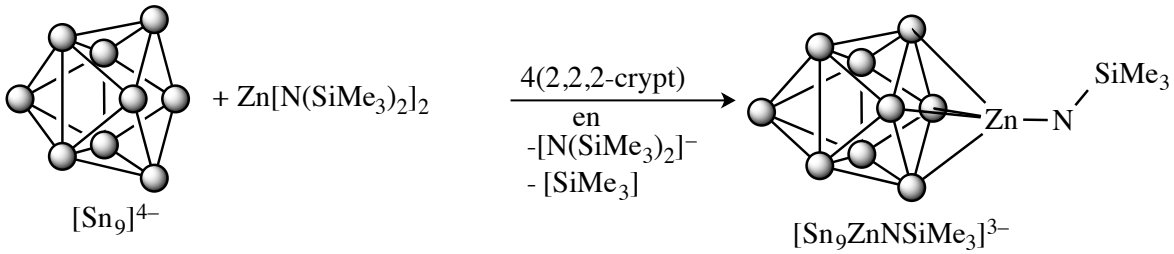

Scheme 2.3: Formation of **2**.

In contrast to the reaction with K_4Ge_9, a stoichiometric excess of the $Zn[N(SiMe_3)_2]_2$ reagent was not required for this reaction to proceed to completion.

2.3.1.6 Structure of $[Sn_9ZnNSiMe_3]^{3-}$ (2)

The novel trianionic cluster **2**, crystallised with the formula $[K(2,2,2\text{-crypt})]_3[\mathbf{2}]\cdot 3tol$ (Figure 2.8) as black block-like crystals in good yields. This crystalline phase is isomorphic with $[K(2,2,2\text{-crypt})]_3[\mathbf{1}]\cdot 3tol$. The structure suffers rotational disorder of one of the $[K(2,2,2\text{-crypt})]^+$ cations, but this can be modelled satisfactorily.

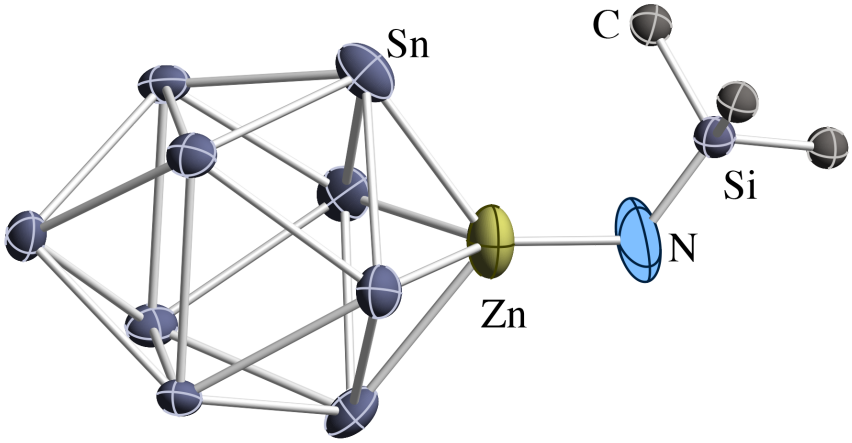

Figure 2.8: Thermal ellipsoid plot of **2**. Anisotropic displacement ellipsoids are pictured at 50% probability level. H atoms are omitted for clarity.

The reaction is believed to proceed as follows. The reductive cleavage of a Zn–N bond occurs first, yielding the amide $[N(SiMe_3)_2]^-$ plus the $[ZnN(SiMe_3)_2]^{\bullet}$ radical species. The latter subsequently attacks the $[Sn_9]^{3-}$ open face to form the coordination compound $[Sn_9ZnN(SiMe_3)_2]^{3-}$. This is followed by the loss of a trimethylsilyl radical. The mechanism of this reaction is not clear, or why the reactivity changes from the germanium to the tin analogue. It seems likely that a parallel radical pathway is operating in the case of the tin cluster giving rise to different reactivity to that observed for the germanium-containing species. We are unable to say whether radical dissociation of $[Sn_9ZnN(SiMe_3)_2]^{3-}$ to form **2** and trimethylsilyl radical (or Si_2Me_6) is taking place in solution or whether an alternative radical pathway is operational due to

the relatively quick rates with which this reaction takes place. The *closo* cluster **2** has the same E atom bonding properties as **1**, where the zinc atom is acting like a 10th vertex in a bicapped square antiprism. Table 2.3 shows selected bond lengths of **2**.

Bond in $[Sn_9ZnNSiMe_3]^{3-}$ (**2**)	Bond length (Å)
Sn1–Sn3	2.907(2)
Sn1–Sn2	2.928(2)
Sn1–Sn4	2.930 (2)
Sn1–Sn5	2.935(2)
Sn2–Sn7	2.915(2)
Sn2–Sn6	2.949(2)
Sn2–Sn4	3.146(1)
Sn2–Sn3	3.278(2)
Sn3–Sn6	2.903(2)
Sn3–Sn9	2.915(2)
Sn3–Sn5	3.180(1)
Sn4–Sn8	2.950(2)
Sn4–Sn7	2.962(2)
Sn4–Sn5	3.219(2)
Sn5–Sn8	2.936(2)
Sn5–Sn9	2.946(2)
Sn6–Sn7	3.142(2)
Sn6–Sn9	3.145(2)
Sn7–Sn8	3.116(2)
Sn8–Sn9	3.166(2)
Sn6–Zn1	2.764(2)
Sn7–Zn1	2.731(2)
Sn8–Zn1	2.798(2)
Sn9– Zn1	2.770(2)
Zn1–N1	1.880(2)
N1–Si1	1.61(3)

Table 2.3: Selected bond lengths in (**2**).

The Sn–Sn distances lie in the range of 2.903(1) to 3.278(1) Å, which are similar to the ones reported by Sevov for $[Sn_9ZnPh]^{3-}$ (2.896(1) to 3.264(1) Å).[1] The Sn–Zn distances are similar narrowly distributed from 2.731(2) to 2.798(2) Å, and are closely related to the values reported for $[Sn_9ZnPh]^{3-}$ (2.740(1) to 2.787(1) Å). The mean Zn–Sn single bond found in a search on the CSD is 2.892 (av) Å,[19] and the sum of the

covalent radii is 2.58 Å.[16] The Zn–N bond (1.880(14) Å) is abnormally short. The mean distance for a Zn–N single bond is 2.093 Å and the sum of the covalent radii is 1.89 Å. The Zn–N bond length found in **2** can be compared to $[AI^{Ar}]ZnN(SiMe_3)_2$ (Ar = 2,6-$^{i}Pr_2C_6H_3$) where a bidentate ligand is coordinating to a $ZnN(SiMe_3)_2$ fragment giving rise to an identical bong length (1.881(1) Å).[20] The Si–N bond is 1.61 Å, which is also shorter than the mean obtained from a search in the CSD (1.750 (av) Å).[21]

Comparing **1** and **2** the Zn–N bond length is 0.82 Å shorter for **2** and the N–Si bond length is 0.0965 Å shorter on average, showing how the loss of the trimethylsilyl group affects the electronic structure of the metal amide.

2.3.1.7 EPR spectroscopic studies on $[Sn_9ZnNSiMe_3]^{3-}$ (2)

Electron paramagnetic resonance spectroscopy (X- and W-band) was recorded at isotopic natural abundance in a solid-state sample of $[K(2,2,2\text{-crypt})]_3$[**2**]·3tol at 85 K to confirm its paramagnetic character. Experimental measurements are shown in Figure 2.9 in black. Panel a) shows the X-band measurement, panel b) the W-band measurements. Simulations performed by Dr. William Myers found $g_1 = 2.0948$, $g_2 = 2.0698$ and $g_3 = 1.9198$ (Figure 2.9: green line), related to a broad component of the spectrum. DFT calculations predicted values of $g_1 = 2.1820$, $g_2 = 2.0669$, $g_3 = 1.9903$ for **2** (Figure 2.9: red line). There is a close fit between the broad feature and the simulated g-values. The experimental spectrum also contained a sharp resonance with complex hyperfine structure, which proved difficult to assign. It may be that additional chemistry is occurring which is causing another paramagnetic species to give another signal.

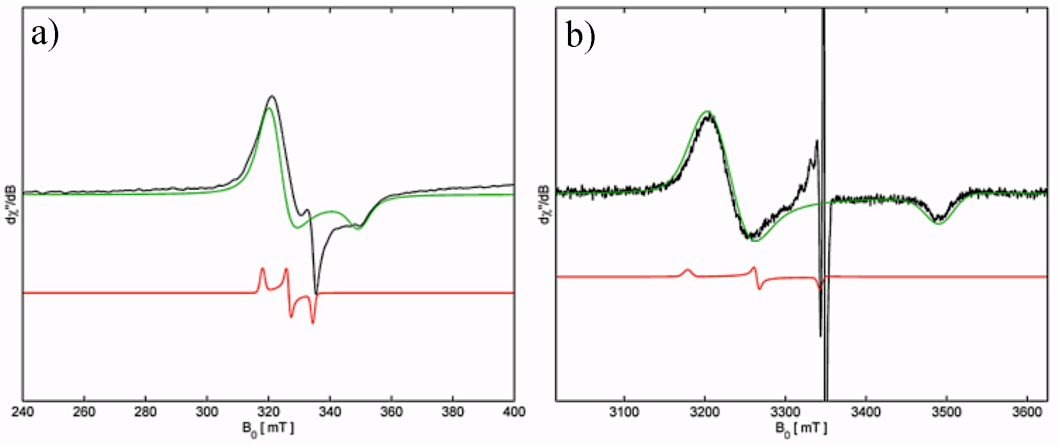

Figure 2.9: a) X-band and b) W-band EPR at 85K for solid samples of [K(2,2,2-crypt)]$_3$[**2**]·3tol.

The DFT predicted *g*-values are a poor match to the experimental observations, which may be caused by the effect of low lying excited states mixing with the ground state via the second order Zeeman effect. Investigations into these effects and the nature of the calculations are on-going.

2.3.1.8 Mass spectrometric studies on $[Sn_9ZnNSiMe_3]^{3-}$ (2)

As with germanium-containing species, the variety of naturally occurring tin isotopes (112, 114–120, 122 and 124) aids in the assignment of mass envelops for tin-containing Zintl clusters.[18]

Confirmation of the presence of the cluster anion in solution was possible by means of electrospray mass spectrometry of DMF solutions of the crude reaction mixtures. In the negative ion mode spectrum a mass envelope corresponding to $[Sn_9ZnNSiMe_3]^-$ was observed at 1222.8 Da (100%) (Figure 2.10). The ion paired species $\{[K(2,2,2\text{-crypt})][Sn_9ZnNSiMe_3]\}^-$ was also observed at 1637.2 Da (40%) along with some starting material.

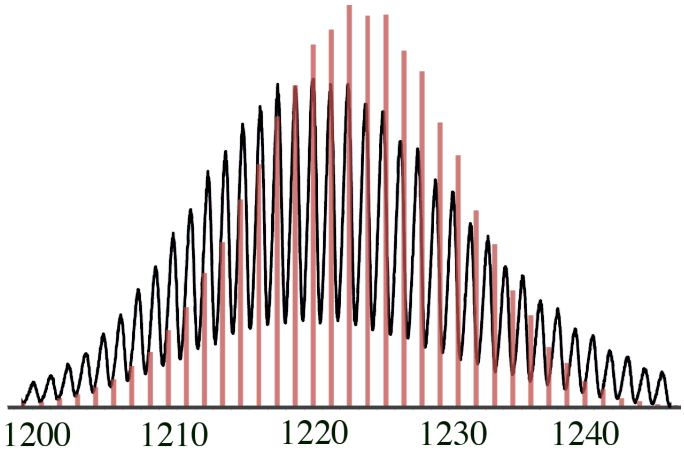

Figure 2.10: Negative ion-mode electrospray mass envelope corresponding to $[Sn_9ZnNSiMe_3]^-$. Predicted isotopic distributions are shown in red and observed mass spectrometric data are shown in black.

In the positive ion mode spectrum the mass envelope corresponding to $\{[K(2,2,2\text{-crypt})]_4[Sn_9ZnNSiMe_3]\}^+$ was observed at 2878.2 Da (100%) along with some starting material.

It is important to mention that the germanium analogue of $[Sn_9ZnNSiMe_3]^{3-}$ ($[GeZnNSiMe_3]^-$) was observed in the mass spectrum of reaction mixture of K_4Ge_9 and $Zn[N(SiMe_3)_2]_2$ but never observed in the crystalline material.

2.3.1.9 DFT calculations

DFT calculations were performed by Michael Connolly in order to study the electronic properties of **1** and **2**, in particular the interactions between the zinc and nitrogen atoms as well as the nitrogen and silicon atoms of the $ZnN(SiMe_3)_x$ (x = 1 and 2) functionalities.

For **1** the optimised geometry found is a good fit with the experimental data (Table 2.4). Analysis of the Kohn-Sham orbitals (Figure 2.11) shows that the HOMO and

LUMO are localised on the cage indicating that the interactions between the germanium atoms are weak compared to the bonds in the amide ligand.

Bond	Experimental	Calculated
Ge–Zn	2.591–2.606 Å	2.650–2.672 Å
Zn–N	1.962 Å	1.974 Å
N–Si	1.677–1.736 Å	1.737–1.739 Å

Table 2.4: Comparison of calculated and experimental selected bond lengths of **1**.

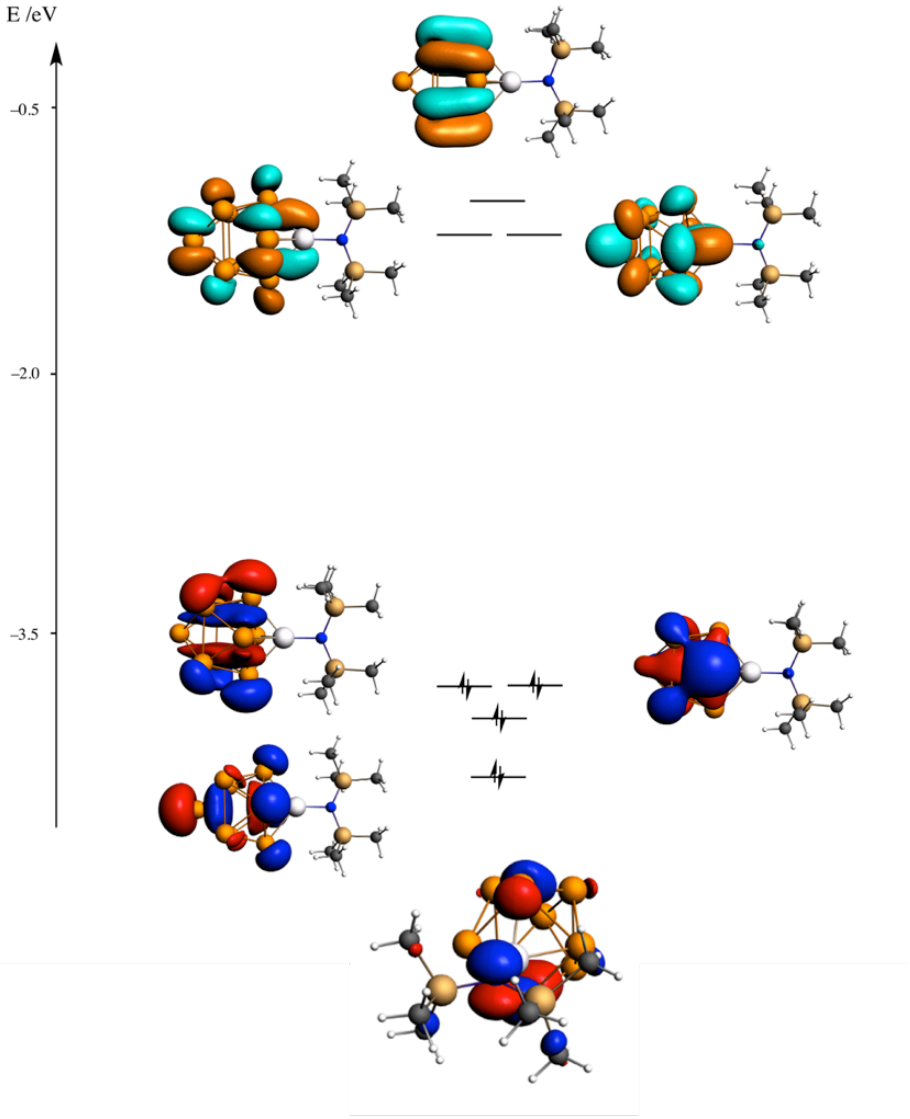

Figure 2.11: Selected frontier Kohn-Sham orbitals of **1**.

Table 2.5 shows the comparison between selected bond lengths from the computational analysis and the crystal structure of **2**, showing good fit.

Bond	Experimental	Calculated
Sn–Zn	2.731–2.798 Å	2.880–3.136 Å
Zn–N	1.880Å	1.858 Å
N–Si	1.61 Å	1.71 Å

Table 2.5: Comparison of calculated and experimental selected bond lengths of **2**.

The short N–Si bond in **2** could indicate some π character, as loss of a trimethylsilyl group would leave extra electron-density on the nitrogen atom. The relevant Kohn-Sham orbitals (Figure 2.12) show bonding and antibonding interactions between the p_x and p_y orbitals on the nitrogen and two Si–C σ* orbitals.

Selected Kohn-Sham orbitals for **2**, show that the HOMO–1 was found to be mainly composed of the electron pairs on the nitrogen atom. These are drawn into the Si–C antibonding orbitals. This reduced electron-density on the nitrogen atom reduces dπ–pπ interactions between the zinc atom and nitrogen atom leading to the shorter Zn–N bond. This implies that donation into one trimethylsilyl group is better than into two.

As shown in Figure 2.12, the SOMO is mainly composed of the tin cluster with some nitrogen atom character. The difference in reactivity may therefore be due to the enhanced stability of the tin cluster radical relative to the germanium analogue, which facilitates the radical-type mechanism in the formation of **2**.

The Kohn-Sham diagram shows the molecular orbitals corresponding to the π interactions between the nitrogen atom and the Si–C antibonding orbitals. They show how the electron-density is still mostly localised on the nitrogen atom. This could be

indicative of a presence of a N–Si multiple bond, nevertheless this is only partially present, because the localisation of the electron-density on the nitrogen atom would imply that there is only a small amount of triple bond character.

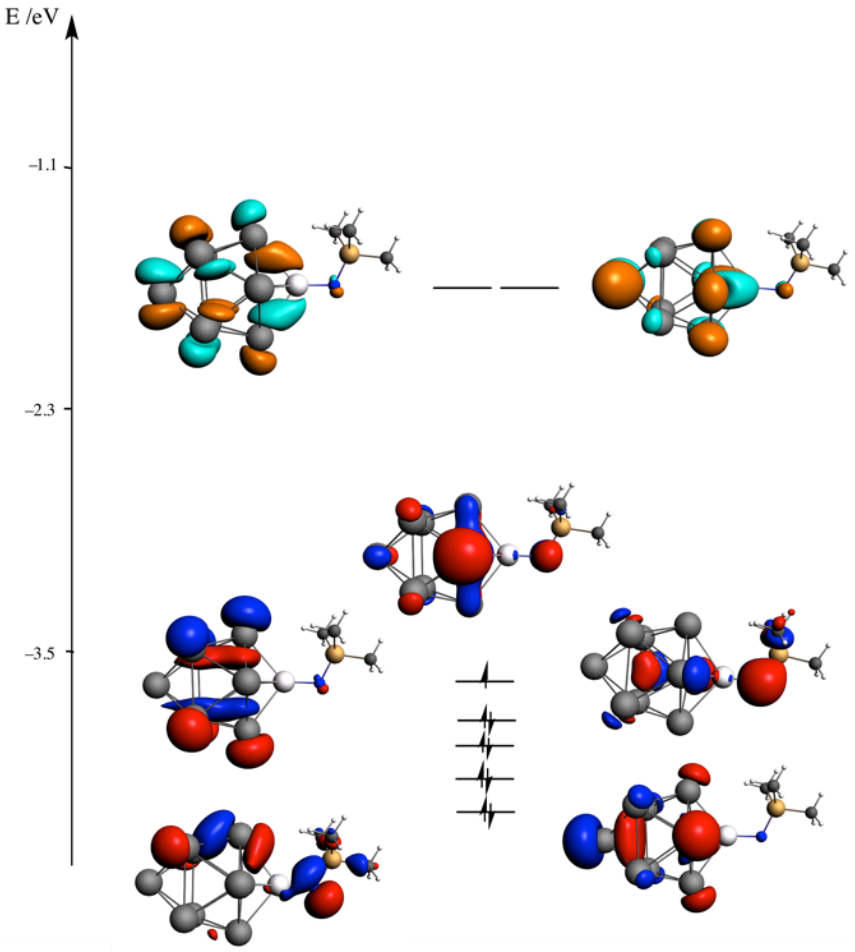

Figure 2.12: Selected Kohn-Sham orbitals of **2**.

Natural Bond Order analysis revealed that the N–Si bond had a much higher Mayer bond order than any other bond in the system. This could be an indication of π character of the bond. The Mayer bond order is a natural extension of the Wiberg bond order, which has proved extremely useful in bonding analysis using semi-empirical computational methods, and the Mulliken population analysis to *ab initio* theories.[22]

	Mayer Bond Order	Bond length (Å)
N–Si	1.4569	1.610
Si–C	0.7673–0.8504	1.685–2.174
Zn–N	0.8721	1.894

Table 2.6: Natural Bond Order analysis of **2**.

2.3.2 Further reactivity studies

2.3.2.1 Reaction of 1 with CsF

The solution-phase reactivity of **1** was studied in an attempt to isolate additional novel cluster anions. First in an attempt to obtain the germanium analogue of **2**, **1** was reacted with two equivalents of CsF to abstract a trimethylsilyl group and afford the tetraanionic compound $[Ge_9ZnNSiMe_3]^{4-}$ (**3**) (Scheme 2.4). This reaction was carried out in pyridine. After stirring the reaction mixture for approximately thirty minutes, all volatiles were removed under vacuum and the resulting solid was washed with diethyl ether.

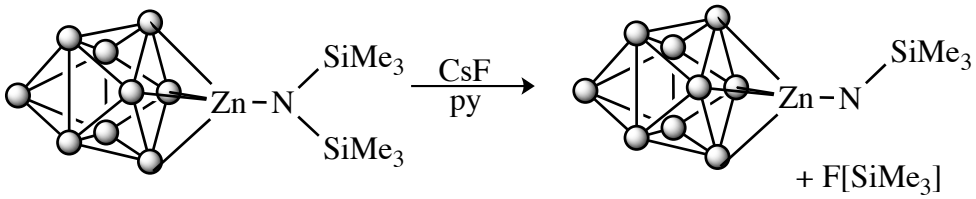

Scheme 2.4: Abstraction of a trimethylsilyl group from CsF to form **3**.

Despite the efficiency of this reaction, crystals could not be obtained. In the negative ion mode spectrum a mass envelope corresponding to $[Ge_9ZnNSiMe_3]^-$ at 809.6 Da was observed (Figure 2.13) and $[Ge_9ZnN(SiMe_3)_2]^-$ could no longer be seen (Figure 2.14). In the positive ion mode spectrum a mass envelope corresponding to {[K(2,2,2-

crypt)]$_4$[$Ge_9ZnNSiMe_3$]}$^+$ at 2468.4 Da was observed, despite the fact that {[K(2,2,2-crypt)]$_5$[$Ge_9ZnNSiMe_3$]}$^+$ was actually expected.

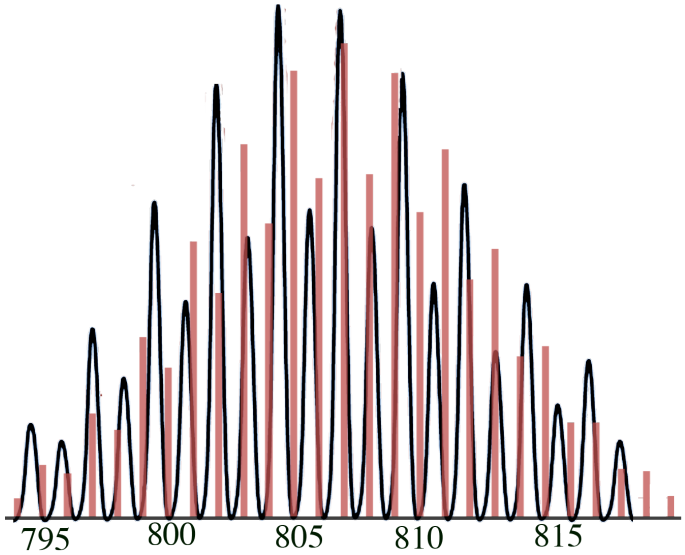

Figure 2.13: Negative ion mode electrospray mass envelope corresponding to [$Ge_9ZnNSiMe_3$]$^-$. Predicted isotopic distributions are shown in red and observed mass spectrometric data are shown in black.

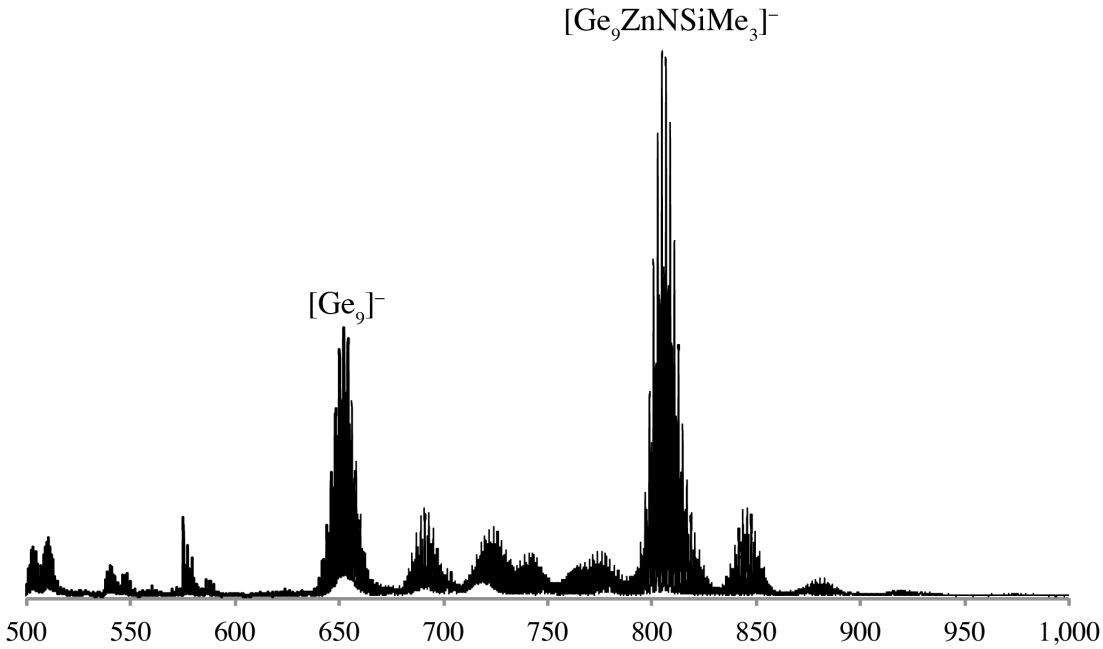

Figure 2.14: Negative ion mode of the reaction of **1** with CsF to form **3**.

NMR spectroscopic studies were performed to confirm the formation of **3**. ^{1}H NMR showed three resonances corresponding to the 2,2,2-crypt at δ = 3.44, 3.37 and 2.35

ppm. There was a singlet at δ = 1.15 ppm corresponding to the methyl group of the product.

^{13}C NMR spectroscopy showed three resonances corresponding to the 2,2,2-crypt at δ = 71.2, 68.4 and 54.6 ppm. An additional resonance at δ = 16.1 was observed corresponding to the methyl group in **3**. The resonance at δ = 10.2 ppm corresponding to the starting material was not observed.

2.3.2.2 Reaction of 1 with $HNPh_2$

The transamination of $[Ge_9ZnN(SiMe_3)_2]^{3-}$ with four equivalents $HNPh_2$ in pyridine was found to yield $[Ge_9ZnNPh_2]^{3-}$ (**4**) (Scheme 2.5). After stirring the reaction mixture for one hour, all volatiles were removed under vacuum and the remaining black oil was washed with THF to remove all organic side products. Clean conversion was observed in mass spectrometric studies along with formation of the some $[Ge_9]^-$. The presence of the latter was confirmed by X-ray crystallography studies on the crystalline material obtained from these crude reactions mixtures.

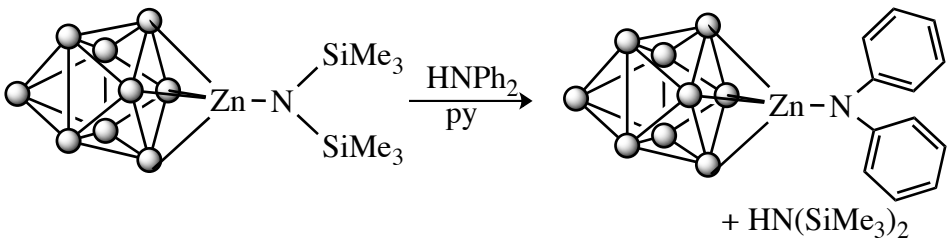

Scheme 2.5: Reaction of transamination of **1** with $HNPh_2$ to form **4**.

In the negative ion mode spectrum of the reaction mixture a mass envelope corresponding $[Ge_9ZnNPh_2]^-$ at 887.6 Da was observed (Figure 2.15) and $[Ge_9ZnN(SiMe_3)_2]^-$ could not longer be seen (Figure 2.16). In the positive ion mode

spectrum a mass envelope corresponding to {[K(2,2,2-crypt)]$_4$[Ge$_9$ZnNPh$_2$]} at 2549.7 was observed.

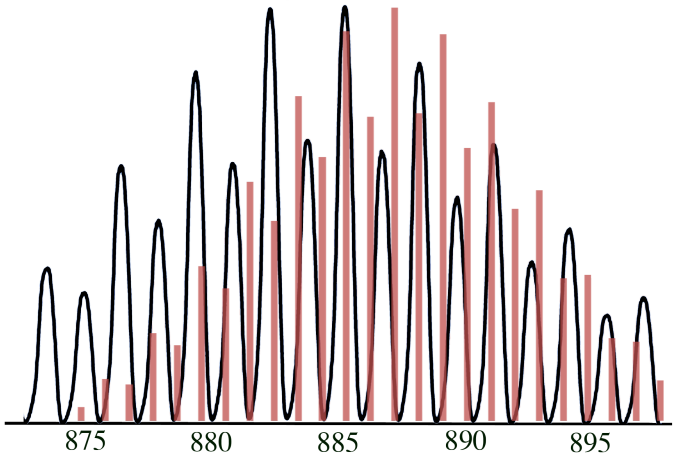

Figure 2.15: Negative ion mode electrospray mass envelope corresponding to [Ge$_9$ZnNPh$_2$]$^-$. Predicted isotopic distributions are shown in red and observed mass spectrometric data are shown in black.

No crystals of **4** suitable for single crystal X-ray diffraction could be obtained.

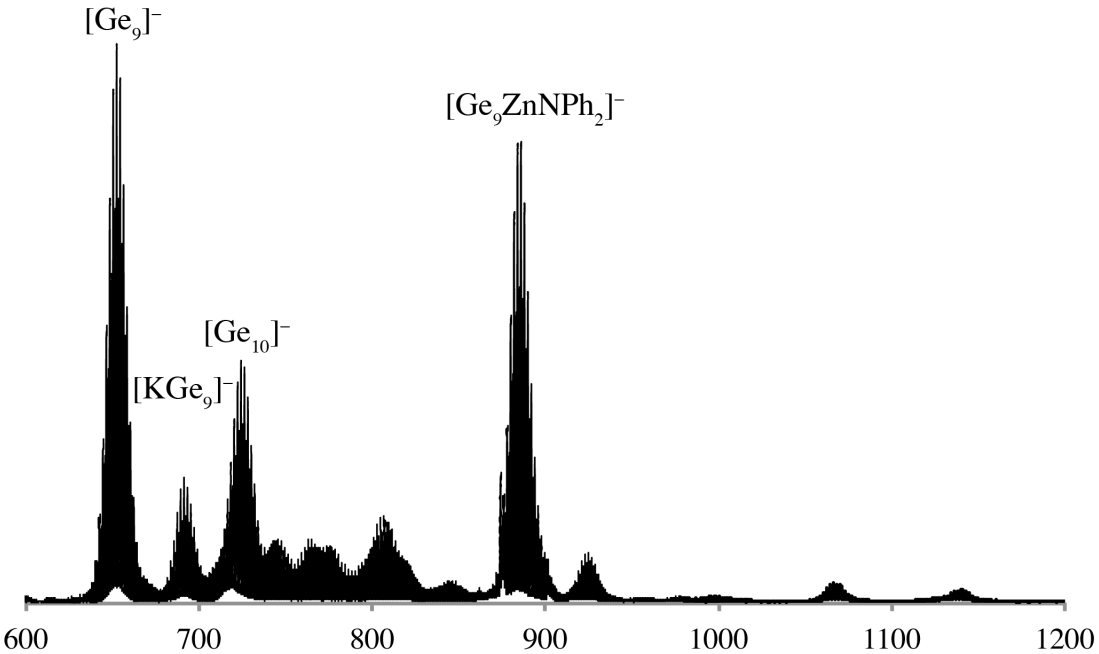

Figure 2.16: Negative ion mode electrospray of the reaction mixture of **1** and HNPh$_2$ to form **4**.

^{1}H NMR spectroscopy showed three resonances corresponding to the 2,2,2-crypt at δ = 3.44, 3.37 and 2.35 ppm. Additional resonances were observed in the aromatic region at δ = 6.80, 7.30 and 7.57 ppm corresponding to the protons in the *para, meta* and *ortho* positions, respectively.

^{13}C NMR spectroscopy supported the formation of **4** by showing four resonances in the aromatic region at δ = 117.6, 118.5, 130.0 and 149.8 ppm, corresponding to the carbon atoms in the *para, ortho, meta* and *ipso* position, respectively. Additionally the three resonances corresponding to the 2,2,2-crypt carbon atoms at δ = 71.2, 68.4 and 54.6 ppm were observed.

2.4 Conclusions

This chapter describes the synthesis and characterisation of four novel compounds. By mixing K_4Ge_9 with a stoichiometric excess of $Zn[N(SiMe_3)_2]_2$, the simple η^4 coordination compound $[Ge_9ZnN(SiMe_3)_2]^{3-}$ (**1**) is formed after the reductive cleavage of a Zn–N bond takes place. This compound was studied using X-ray crystallography, NMR spectroscopy, mass spectrometry and its purity was confirmed by elemental analysis.

Further reactivity of **1** was also investigated. **1** reacts with CsF to give rise to $[Ge_9ZnNSiMe_3]^{4-}$ (**3**). It also reacts with an excess of $HNPh_2$ to form the transamination product $[Ge_9ZnNPh_2]^{3-}$ (**4**). **3** and **4** were characterised using NMR spectroscopy and mass spectrometry.

Additionally, when K_4Sn_9 reacts with a stoichiometric amount of $Zn[N(SiMe_3)_2]_2$, an η^4 coordination compound $[Sn_9ZnNSiMe_3]^{3-}$ (**2**) is formed. In this cage a trimethylsilyl

group is lost, affording a paramagnetic compound. The radical character was confirmed using EPR spectroscopy. Additionally X-ray crystallography, mass spectrometry and elemental analysis were used to characterise this cluster.

DFT calculations revealed that the HOMO and LUMO of **1** have significant $[Ge_9]^{4-}$ cage character. Optimised geometries of **1** and **2** are a good fit with the experimental data. In **2**, the nitrogen atom has two lone pairs around it and one is drawn into the Si–C antibonding orbitals (HOMO–1). The short N–Si bond indicates some π character. The dπ–pπ interactions between the zinc and nitrogen are reduced leading to a shorter Zn–N bond. This implies that donation into one trimethylsilyl group is better than into two. The interaction between the nitrogen and the silicon atoms has some small degree of multiple bond character, but the electron-density mostly on the nitrogen atom.

2.5 References

(1) Goicoechea, J. M.; Sevov, S. C. *Organometallics* **2006**, *25* (19), 4530–4536.

(2) Zhou, B.; Denning, M. S.; Jones, C.; Goicoechea, J. M. *Dalton Trans.* **2009**, No. 9, 1571–1578.

(3) Yong, L.; Hoffmann. S. D.; Fassler, T. F. *Z. Krist. New Cryst. St.* **2005**, *1* (220), 53.

(4) Kesanli, B.; Fettinger, J.; Eichhorn, B. W. *Chem. Eur. J.* **2001**, *7* (24), 5277–5285.

(5) Campbell, J.; Mercier, H. P. A.; Franke, H.; Santry, D. P.; Dixon, D. A.; Schrobilgen, G. J. *Inorg. Chem.* **2001**, *41* (1), 86–107.

(6) Yong, L.; Hoffmann, S. D.; Fässler, T. F. *Eur. J. Inorg. Chem.* **2005**, *2005* (18), 3663–3669.

(7) Eichhorn, B. W.; Haushalter, R. C.; Pennington, W. T. *J. Am. Chem. Soc.* **1988**, *110* (26), 8704–8706.

(8) Downing, D. O.; Zavalij, P.; Eichhorn, B. W. *Eur. J. Inorg. Chem.* **2010**, *2010* (6), 890–894.

(9) Zhou, B.; Denning, M. S.; Chapman, T. A. D.; Goicoechea, J. M. *Inorg. Chem.* **2009**, *48* (7), 2899–2907.

(10) Goicoechea, J. M.; Sevov, S. C. *J. Am. Chem. Soc.* **2006**, *128* (12), 4155–4161.

(11) Denning, M. S.; Goicoechea, J. M. *Dalton Trans.* **2008**, No. 43, 5882–5885.

(12) Yong, L.; Boeddinghaus, M. B.; Fässler, T. F. *Z. Anorg. Allg. Chem.* **2010**, *636* (7), 1293–1296.

(13) Huheey, J.E.; Keiter, E. A.; Keiter, R. L. HarperCollins: New York, 1993.

(14) Wang, J.-Q.; Wahl, B.; Fässler, T. F. *Angew. Chem. Int. Ed.* **2010**, *49* (37), 6592–6595.

(15) . For 24 crystallographically characterised complexes containing a Zn–Ge single bond (CSD version 5.36, November 2014): d(min) = 2.373; d(max) = 2.715; d(mean) = 2.521; var(d) = 0.013; std. dev. = 0.115; mean dev. = 0.106;

(16) Pyykkö, P.; Atsumi, M. *Chem. Eur. J.* **2009**, *15* (1), 186–197.

(17) . For 179 crystallographically characterised complexes containing a Zn–$N(SiMe_3)_2$ single bond (CSD version 5.36, November 2014): d(min) = 1.812; d(max) = 2.131; d(mean) = 1.934; var(d) = 0.004; std. dev.= 0.059; mean dev. = 0.046;

(18) De Laeter, J. R.; Böhlke, J. K.; De Bièvre, P.; Hidaka, H.; Peiser, H. S.; Rosman, K. J. R.; Taylor, P. D. P. *Pure Appl. Chem.* **2003**, *75* (6).

(19) . For 26 crystallographically characterised complexes containing a Zn–Sn single bond (CSD version 5.36, November 2014): d(min) = 2.578; d(max) = 3.365; d(mean) = 2.892; var(d) = 0.055; std. dev. = 0.234; mean dev. = 0.196;

(20) Pang, K.; Rong, Y.; Parkin, G. *Polyhedron* **2010**, *29* (8), 1881–1890.

(21) . For 29770 crystallographically characterised complexes containing a Si–N single bond (CSD version 5.36, November 2014): d(min) = 1.429; d(max) = 3.117; d(mean) = 1.751; var(d) = 0.006; std. dev. = 0.076; mean dev. = 0.044;

(22) Bridgeman, A. J.; Cavigliasso, G.; Ireland, L. R.; Rothery, J. *J. Chem. Soc. Dalton Trans.* **2001**, No. 14, 2095–2108.

Chapter 3 Endohedral group 14 clusters

3.1 Summary

The chemistry of nine-atom deltahedral group 14 Zintl ions $[E_9]^{4-}$ is a rich and fascinating field of study. These species can be used as precursors to give rise to endohedral clusters that present varying nuclearities and conformations. The variety of structures available is remarkably large, even for systems that contain the same interstitial transition metal atom (*e.g.* $[Ge_9Ni(CO)]^{3-}$, $[Ni@Ge_9Ni(CCPh)]^{3-}$, $[Ni@Ge_9]^{3-}$, $[Ni_3@Ge_{18}]^{4-}$, $[Ni_2@Ge_{13}Ni_4(CO)_5]^{4-}$).[1–3] In particular, ligand-free endohedral clusters (also referred as "naked" systems) are especially interesting due to their close relationship with nanoparticles and fullerenes.[4,5] Of these species, those adopting non-deltahedral structures are of particular interest due to the challenges they pose in understanding their bonding and electronic properties (although it is worth noting that, to date, only a handful of such species have been reported).[6–8] One of the aims of this project was to study the reactivity of the $[E_9]^{4-}$ (E = Ge, Sn and Pb) cluster anions towards organometallic transition metal compounds, in an attempt to synthesise novel endohedral cages encapsulating transition metal atoms.

This chapter will describe the reaction of the K_4Ge_9 Zintl phase with the organometallic compound $[Ru(1,5\text{-}COD)(\eta^3\text{-}CH_3C(CH_2)_2)_2]$ which afforded the three-connected cluster

$[Ru@Ge_{12}]^{3-}$, featuring a rare non-deltahedral geometry. The reaction between K_4Ge_9 and $[Co(PPhEt_2)_2(mes)_2]$ yielded the expanded cluster $[Co_2@Ge_{16}]^{4-}$.[8,9] Due to the poor quality of the single crystal X-ray structure of this species, extensive DFT calculations were performed by the group of Prof. John McGrady at the University of Oxford to explore the structure and electronic properties of this cluster.

3.2 Introduction

In 1996, Eichhorn and co-workers reported the reaction between K_4Ge_9 and $Ni(CO)_2(PPh_3)_2$ at elevated temperatures, yielding the first example of an endohedral cluster: $[Ni@Ge_9Ni(PPh_3)]^{2-}$ (The @ symbol is employed here to refer to an interstitial metal, as shown in Figure 3.1)[3,10]. There are two nickel atoms in the structure; one in the central cavity and the other forming part of the ten-atom cage. The nine-atom germanium cage coordinates to the $Ni(PPh_3)$ moiety, forming a ten-vertex cluster with the $Ni(PPh_3)$ fragment as one of the vertices. This is in contrast to other ten-atom, group 14 coordination compounds of the form $[E_9ML]^{3-}$, where the $[E_9]^{4-}$ cage coordinates through the open face, forming a bicapped square antiprism. The interstitial nickel atom does not contribute any electrons to cluster bonding due to its d^{10} closed-shell configuration.

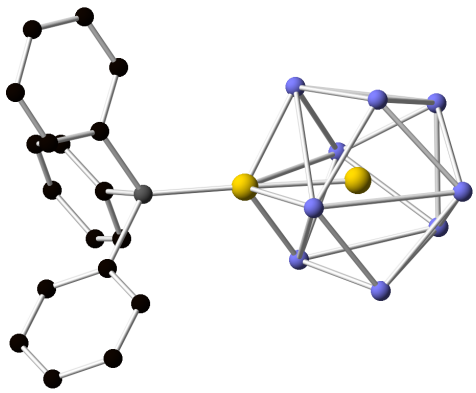

Figure 3.1: Ball and stick diagram of $[Ni@Ge_9Ni(PPh_3)]^{2-}$ (Ge atoms are shown in purple, Ni atoms in yellow, the P atom in grey and C atoms in black). H atoms are omitted for clarity.

$Ni(CO)_2(PPh_3)_2$ reacts with the $[Sn_9]^{4-}$ Zintl cage to afford the endohedral cluster $[Ni@Sn_9Ni(CO)]^{3-}$.[11] This cluster has a more common bicapped square antiprismatic geometry. In the same report, the $[Pt@Sn_9Pt(PPh_3)]^{2-}$ cluster was synthesised as the product of the reaction between K_4Sn_9 and $Pt(PPh_3)_4$. This species has the same geometry as $[Ni@Ge_9Ni(PPh_3)]^{2-}$.

The ligand-free clusters $[Ni@E_9]^{3-}$ (E = Ge and Sn) were accessed by reaction of K_4E_9 and an organometallic complex with two labile ligands, $Ni(COD)_2$, acting as an effective source of Ni^0.[1,2,12] The further reactivity of $[Ni@Ge_9]^{3-}$ was also studied. Reaction of the latter with $Ni(CO)_2(PPh_3)_2$ lead to the nickel-capped ten-atom cluster $[Ni@Ge_9Ni(CO)]^{2-}$, which has the same geometry as the aforementioned $[Ni@Ge_9Ni(PPh_3)]^{2-}$ species. Reactions between TlCp and $[Ni@E_9]^{3-}$ lead to another *closo* ten-atom cluster, namely $[Ni@E_9Tl]^{3-}$ (E = Ge and Sn) (Figure 3.2).[13]

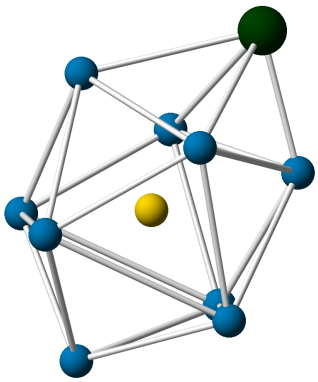

Figure 3.2: Ball and stick diagram of $[Ni@Sn_9Tl]^{3-}$ (Sn atoms are shown in blue, the Ni atom in yellow and the Tl atom in dark green).

Endohedral $[Cu@E_9]^{3-}$ (E = Sn and Pb) clusters have been synthesised in DMF in the presence of 2,2,2-crypt by reacting the relevant Zintl phases with $[Cu(mes)]_5$.[14] Single crystal X-ray spectroscopy revealed highly symmetrical tricapped trigonal prismatic

geometries for these species which are maintained in solution, as shown by multi-element NMR spectroscopic experiments.

Endohedral clusters with more than nine atoms have also been synthesised. The reaction of $Ni(COD)_2$ and the K_4Pb_9 Zintl phase results in the formation of *closo*-$[Ni@Pb_{10}]^{2-}$ and a minor side product, *closo*-$[Ni@Pb_{12}]^{2-}$ (Figure 3.3).[15] The $[Ni@Pb_{10}]^{2-}$ cluster has a bicapped square antiprismatic geometry (D_{4h}) whereas the $[Ni@Pb_{12}]^{2-}$ has an icosahedral geometry (I_h). In both cases the interstitial nickel atom has a d^{10} configuration and does not contribute any electrons to cluster bonding. Because of this, the *closo* ten-atom cluster has 22 skeletal electrons for bonding, consistent with its geometry. The metal centred clusters $[M@Pb_{12}]^{2-}$ (M = Pt and Pd) have also been synthesised by reacting K_4Pb_9 and $M(PPh_3)_4$.[16] Both of them have an almost perfect I_h geometry and exhibit no contribution from the metal atom to the cluster bonding.

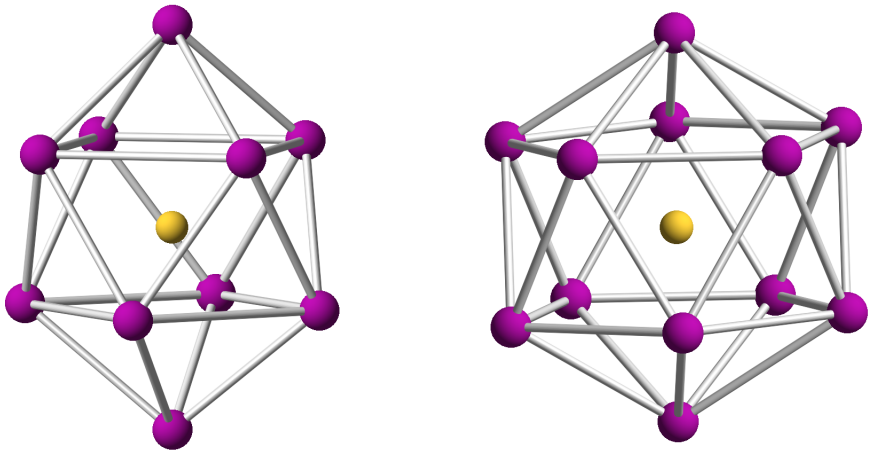

Figure 3.3: Ball and stick diagram of $[Ni@Pb_{10}]^{2-}$ (left) and $[Ni@Pb_{12}]^{2-}$ (right) (Pb atoms are shown in magenta and Ni atoms in yellow).

The reaction between K_4Sn_9 and $[Fe(mes)_2]_2$ leads to the formation of the $[Fe@Sn_{10}]^{3-}$ endohedral cluster.[17] Extensive disorder in the crystal structure made the crystallographic characterisation difficult, necessitating extensive DFT calculations. The authors found

that there is a significant degree of back-donation from the metal centre to the cage and that its global minimum lies on a very flat surface connecting D_{4d}, C_{2v} and C_{3v}-symmetric minima, suggesting a very plastic structure, easily deformed by the surrounding crystal environment.

The nearly perfect icosahedral cluster $[Ir@Sn_{12}]^{3-}$ (Figure 3.4, left) can be formed by the activation of the $[Sn_9Ir(COD)]^{3-}$ cluster in the presence of PPh_3 at 80 °C.[18,19] Electronically, if the iridium atom is considered as Ir^{1-} then it would have a d^{10} configuration and would not contribute electrons to cluster bonding. The skeletal electron count is 26 electrons, corresponding to a *closo* cluster. This *closo* geometry was confirmed by single crystal X-ray crystallography.

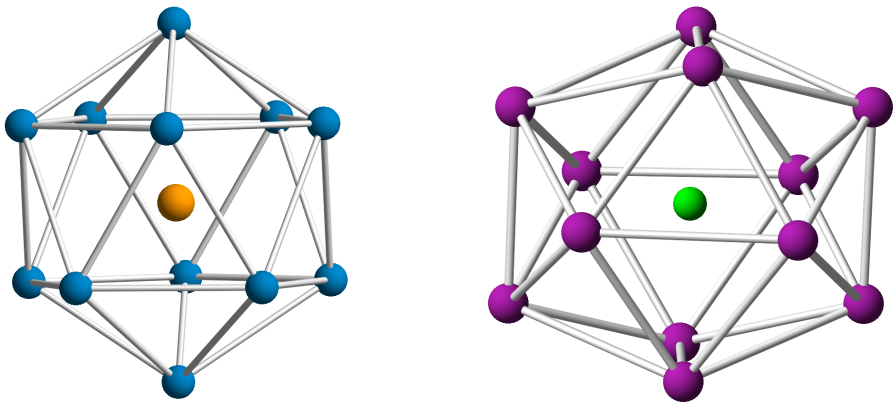

Figure 3.4: Ball and stick diagram of $[Ir@Sn_{12}]^{3-}$ (left) and $[Mn@Pb_{12}]^{3-}$ (right) (Sn atoms are shown in blue, the Ir atom in orange, Pb atoms in magenta and the Mn atom in green).

A closely-related, albeit highly distorted, cluster is $[Mn@Pb_{12}]^{3-}$ (Figure 3.4, right). This cluster is formed by reacting K_4Pb_9 with $[Mn(mes)_3]_3$.[20] Its geometry is highly distorted, as was suggested by X-ray crystallography and confirmed by DFT calculations. The cluster anion is considerably expanded compared to the 26 electron closed-shell analogue $[Ni@Pb_{12}]^{2-}$. The distortion causes lowere symmetry with respect to the idealised icosahedral geometry characteristic of related endohedral clusters. DFT calculations

indicate that the cage prolation is due to a substantial transfer of electron-density from the formally Mn^{1-} centre to the low-lying vacant orbitals of the $[Pb_{12}]^{2-}$ cage. This can also be understood in terms of a first order Jahn-Teller distortion.

Reactions of one equivalent of $Ni(COD)_2$ with either K_4Ge_9 or K_4Sn_9 afford $[Ni@E_9]^{3-}$, as mentioned above.[1,2,12] However, when a stoichiometric excess of $Ni(COD)_2$ is used (3:1), different products can be isolated. The reaction with K_4Ge_9 yielded $[Ni_3@(Ge_9)_2]^{4-}$ (Figure 3.5, left), which is a trimer that can be considered as two 10-vertex $[Ni@Ge_9Ni]$ clusters interconnected by the nickel atom on the cluster.[2] The reaction with K_4Sn_9 yielded the endohedral species $[Ni_2@Sn_{17}]^{4-}$ (Figure 3.5, right) consisting of two nickel-centred tin clusters $[Ni@Sn_9]$ fused by a single tin vertex and presenting a D_{2d} symmetry.[21]

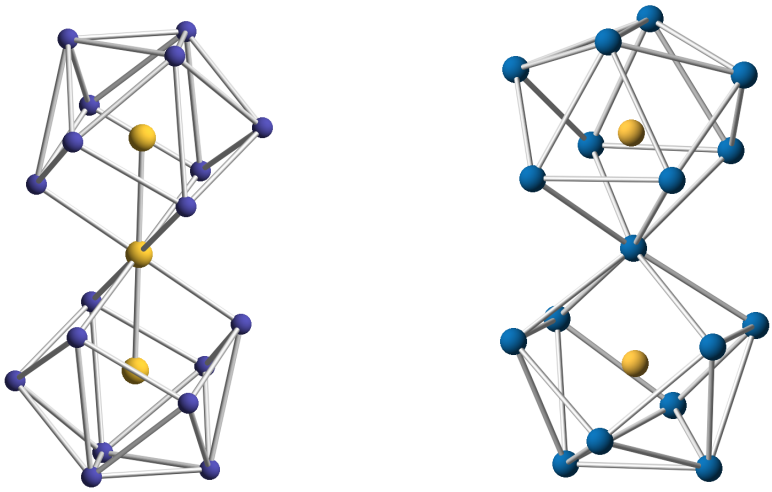

Figure 3.5: Ball and stick diagram of $[Ni_3@(Ge_9)_2]^{4-}$ (left) and $[Ni_2@Sn_{17}]^{4-}$ (right) (Ge atoms are shown in purple, Sn atoms in blue and Ni atoms in yellow).

Larger cages such as $[Pt_2@Sn_{17}]^{4-}$ (Figure 3.6) can be formed by reaction of K_4Sn_9 and $Pt(nbe)_3$.[22] The largest endohedral cages known to date are the $[Pd_2@E_{18}]^{4-}$ (E = Ge and Sn) clusters, formed by the reaction of the relevant Zintl phase and $Pd(PPh_3)_4$ in

ethylenediamine.[23–25] In these species there are two endohedral metal atoms which occupy the centre of the ellipsoidal-like cages of the group 14 elements.

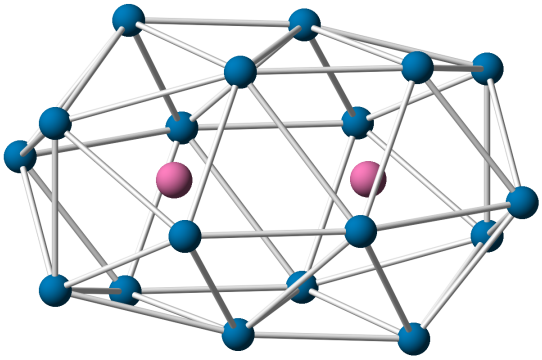

Figure 3.6: Ball and stick diagram of $[Pt_2@Sn_{17}]^{4-}$ (Sn atoms are shown in blue and Pt atoms in pink).

In 2009, a new family of cages was reported by Goicoechea and Fässler. $[M@Ge_{10}]^{3-}$ (M = Fe and Co) (Figure 3.7) are non-deltahedral clusters. They do not have triangular faces and every germanium atom is three-connected, more similar to electron-precise species.[6,7] They were prepared by reacting the K_4Ge_9 Zintl phase with $FeAr_2$ (Ar = 2,6-$Mes_2C_6H_3$) and $[Co(C_8H_{12})(C_8H_{13})]$, respectively. They exhibit a pentagonal prismatic D_{5h} geometry with an interstitial metal atom in the central cavity. The reason why these clusters preferentially adopt non-deltahedral geometries, as opposed to the more classical structures adopted by the other endohedral clusters reported to date, has been the subject of extensive theoretical studies.[17]

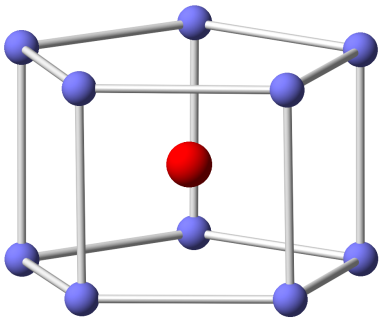

Figure 3.7: Ball and stick diagram of $[Fe@Ge_{10}]^{3-}$ (Ge atoms are shown in purple and the Fe atom in red).

3.3 Results and discussion

3.3.1 Reactivity of K_4Ge_9 towards [Ru(1,5-COD)(η^3-$CH_3C(CH_2)_2)_2$]

3.3.1.1 Synthesis of $[Ru@Ge_{12}]^{3-}$ (5)

A THF solution of the organometallic precursor [Ru(1,5-COD)(η^3-$CH_3C(CH_2)_2)_2$] was added dropwise to an ethylenediamine solution of K_4Ge_9 and three equivalents of 2,2,2-crypt. After monitoring several reactions by mass spectrometry and following careful optimisation of the reaction conditions, it was discovered that stirring the reaction for six hours at 65 °C led to the best product yield (Scheme 3.1). For reactions carried out at lower temperatures or shorter stirring times the main compound observed in mass spectrometric studies (Section 3.3.1.3) was the starting material (observed as $[Ge_9]^-$ in mass spectrometry). After stirring the reaction for six hours the reaction mixture was filtered, to separate the unidentified precipitate formed during this reaction, and all volatiles were removed under dynamic vacuum. The resulting brown oil, containing the novel cluster $[Ru@Ge_{12}]^{3-}$ (**5**), was washed with THF to remove all organic side products and dried under vacuum, affording a dark brown powder.

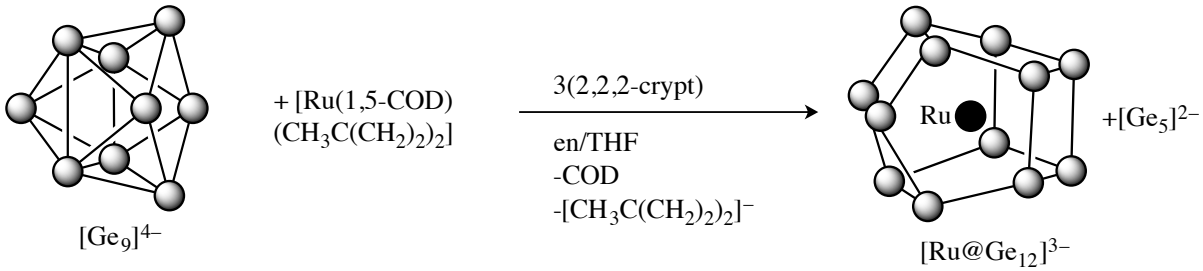

Scheme 3.1: Synthesis of **5**.

Crystals suitable for single crystal X-ray diffraction were obtained after one week by slow diffusion of toluene into a pyridine solution of the aforementioned dark brown

precipitate. The crystals formed include orange blocks of $[Ge_5]^{2-}$, alongside some black plates which were found to contain the novel endohedral cluster **5**. Fortunately, the different physical appearance of the crystalline samples allowed for the mechanical separation of both species under a microscope.

3.3.1.2 Structure of $[Ru@Ge_{12}]^{3-}$ (5)

X-ray crystallography studies revealed a single, crystallographically unique cluster anion in the asymmetric unit accompanied by three $[K(2,2,2\text{-crypt})]^+$ cations balancing the charge. **5** crystallises in space group $P2_1$ (No. 4) with the formula $[K(2,2,2\text{-crypt})]_3$[**5**]·4py (Figure 3.8).

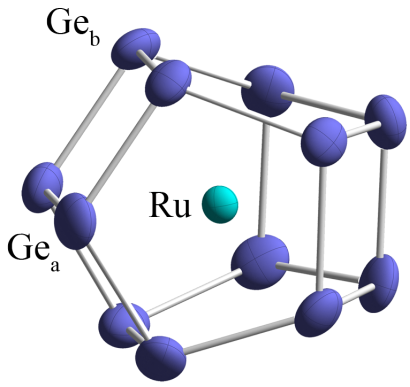

Figure 3.8: Thermal ellipsoid plot of **5**. Anisotropic displacement ellipsoids are pictured at 50% probability level.

Most of the endohedral Zintl ion clusters identified in the past have been *closo* deltahedral cages with a 2n + 2 skeletal electron-count (where n is the number of vertices). The first three-connected clusters reported in 2009 were the pentagonal prisms (D_{5h}) $[Fe@Ge_{10}]^{3-}$ and $[Co@Ge_{10}]^{3-}$.[6,7] These clusters are expected to have a 5n electron-count consistent with electron precise species such as Si_xR_x.[26–32] In these two cases the interstitial metal atoms donate electron-density to the ten-atom germanium cage, which

renders the three-connected geometry more favourable. Until our isolation of **5**, there was no previous report of a three-connected $[E_{12}]^{x-}$ Zintl ion cage.

This unprecedented Zintl ion exhibits a substituent-free twelve-atom germanium cage with an interstitial ruthenium atom in the central cavity. The reaction proceeds non-stoichiometrically, giving rise to a cluster of higher nuclearity than the precursor and forming a large amount of $[Ge_5]^{2-}$, which is observed both by mass spectrometry and in the crystalline material formed. Additionally, a certain degree of cluster decomposition must be occurring, as there is an insoluble precipitate presumed as elemental germanium present in the reaction vessel.

5 exhibits D_{2d} symmetry with a $4^4.5^4$ octahedrane-like germanium cage encapsulating a ruthenium atom.

Bond in $[Ru@Ge_{12}]^{3-}$ (**5**)	Bond length (Å)	Bond in $[Ru@Ge_{12}]^{3-}$ (**5**)	Bond length (Å)
Ru1–Ge1	2.764(1)	Ge1–Ge2	2.462(2)
Ru1–Ge2	2.734(1)	Ge1–Ge3	2.481(2)
Ru1–Ge3	2.713(1)	Ge1–Ge11	2.492(2)
Ru1–Ge4	2.677(1)	Ge2–Ge4	2.476(2)
Ru1–Ge5	2.686(1)	Ge2–Ge12	2.486(2)
Ru1–Ge6	2.672(1)	Ge3–Ge4	2.577(2)
Ru1–Ge7	2.725(1)	Ge3–Ge9	2.470(2)
Ru1–Ge8	2.722(1)	Ge4–Ge5	2.462(2)
Ru1–Ge9	2.709(1)	Ge5–Ge6	2.610(2)
Ru1–Ge10	2.704(1)	Ge5–Ge7	2.484(2)
Ru1–Ge11	2.714(1)	Ge6–Ge8	2.473(2)
Ru1–Ge12	2.657(1)	Ge6–Ge12	2.469(2)
		Ge7–Ge8	2.447(2)
		Ge7–Ge9	2.490(2)
		Ge8–Ge10	2.478(2)
		Ge9 –Ge10	2.600(2)
		Ge10–Ge11	2.475(2)
		Ge11 –Ge12	2.586(2)

Table 3.1: Bond lengths of **5**.

The Ge–Ge bond lengths in the cluster lie in the range of 2.442(2) to 2.601(2) Å. These are a similar length to those in the pentagonal prism $[Fe@Ge_{10}]^{3-}$, which lie in the range of 2.526(1) to 2.622(1) Å, but somewhat shorter than those of the $[Ge_9]^{3-}$ starting material (2.494(7) to 2.713(7) Å). They are of comparable magnitude to the sum of the covalent single bond radii for two germanium atoms (Ge–Ge: 2.42 Å).[33]

There are two symmetry-distinct positions of germanium atoms within **5** in a 4:8 ratio: Ge_a, which are further from the ruthenium atom and Ge_b, which are closer to it (Figure 3.8). Each one of the germanium atoms is adjacent to three other germanium atoms, giving a total of eighteen edges. The Ru–Ge_a distances lie in the range of 2.722(1) to 2.764(1) Å and the Ru–Ge_b distances lie in the range of 2.657(1) to 2.714(1) Å. These are close to the longest Ru–Ge single bond reported (2.715(1) Å), and significantly longer than the mean Ge–Ru single bond length (2.503 Å) according to a search on the CSD.[33,34]

5 has four pentagonal faces and four square faces. The bond angles within the pentagonal faces vary between 102.19(9)° and 114.39(9)° and those within the square faces vary between 87.37(8)° and 92.50(9)°.

This geometry can be related to a hexagonal prism in which six of the atoms are rotated by 90º about a C_2'' axis as illustrated in Figure 3.9. The cluster was found to crystallise in two different positions in a 72:28 ratio. This implies that bond metric data must be interpreted with caution; nevertheless the symmetry and connectivity of the cluster anion can be assigned unequivocally.

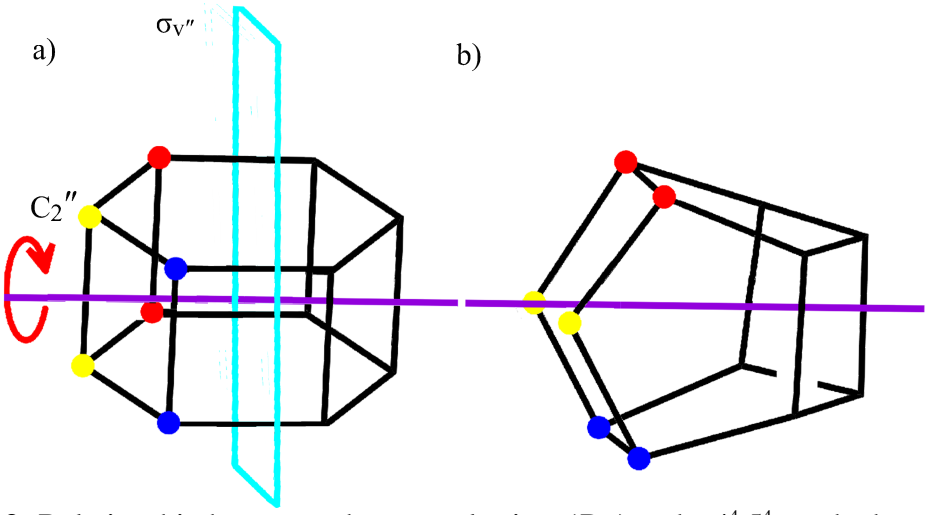

Figure 3.9: Relationship between a hexagonal prism (D_{6h}) and a $4^4.5^4$ octahedrane (D_{2d}) by distortion along one of the two-fold rotation axes (C_2'') of the hexagonal prism.

3.3.1.3 Mass spectrometric studies on $[Ru@Ge_{12}]^{3-}$ (5)

Evidence that **5** exists in solution was obtained by electrospray mass spectrometric analysis of DMF solutions of the crude reaction mixtures. In the negative ion mode spectrum, mass envelopes corresponding to $[Ru@Ge_{12}]^-$ at 972.7 Da and $\{[K(2,2,2\text{-crypt})][Ru@Ge_{12}]\}^-$ at 1387.8 Da were observed (Figure 3.10).

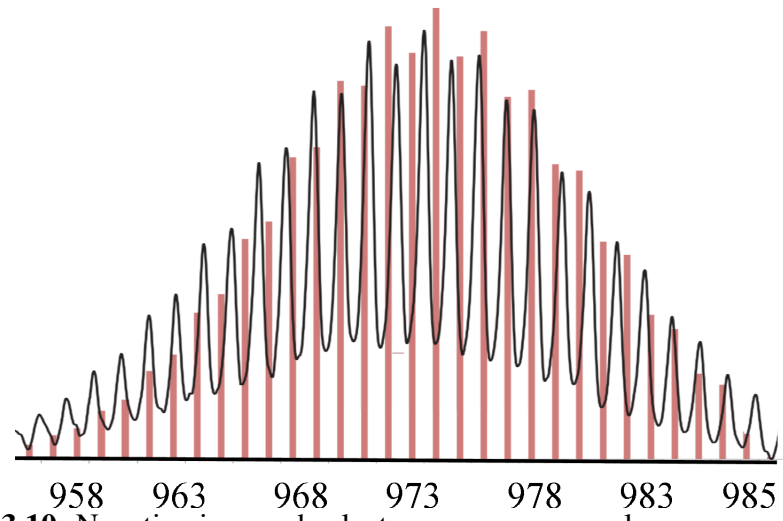

Figure 3.10: Negative ion mode electrospray mass envelope corresponding to $[Ru@Ge_{12}]^-$. Predicted isotopic distributions are shown in red and observed mass spectrometric data are shown in black.

In the positive ion mode, the ion paired species $\{[K(2,2,2\text{-crypt})]_4[Ru@Ge_{12}]\}^+$ was identified at 2632.0 Da. The presence of $[Ge_5]^{2-}$ was also observed by mass spectrometry in the negative ion mode at 364.0 Da, $\{K[Ge_5]\}^-$ at 403.4 Da and $\{[K(2,2,2\text{-crypt})][Ge_5]\}^-$ at 779.6 Da and in the positive ion mode as $\{[K(2,2,2\text{-crypt})]_3[Ge_5]\}^+$ at 1609.8 Da supporting the non-stoichiometric nature of the reaction.

3.3.1.4 EPR spectroscopic studies on $[Ru@Ge_{12}]^{3-}$ (5)

Electron paramagnetic resonance spectroscopy (X-band) was performed at isotopic natural abundance in a frozen pyridine glass of the crystalline product at 85 K to confirm its paramagnetic character (Figure 3.11). The spectrum was simulated by Dr. William Myers using axially anisotropic g values ($g_{\parallel}$ = 1.9993, $g_{\perp}$ = 2.043) and an isotropic hyperfine coupling $|A_{iso}|$ of 33 MHz with the eight symmetry related Ge_b atoms. These values are consistent with the DFT computed values (Section 3.3.1.5). The simulation used g-values of g = 2.043, 2.043 and 1.993, while $A_{iso}(^{73}Ge_b)$ was assumed to have a Gaussian distribution of FWHM = 20 MHz centred at $|A_{iso}(^{73}Ge_b)|$ = 33 MHz.

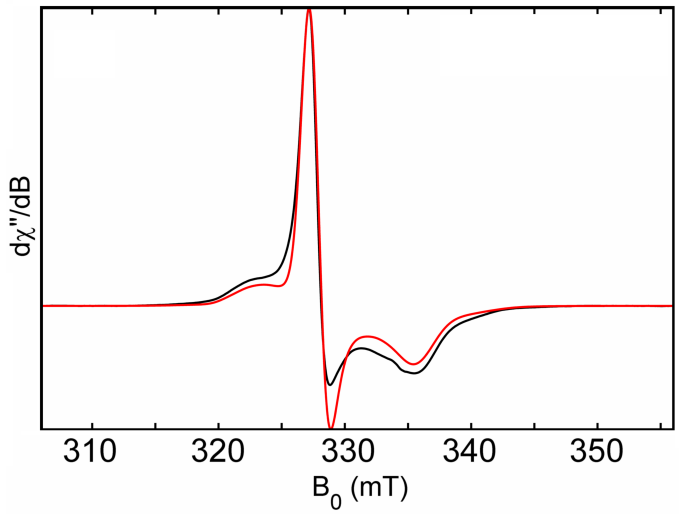

Figure 3.11: Experimental (black) and simulated (red) EPR spectra for **5**.

Non-saturating conditions were found experimentally at 85 K, with a microwave frequency of 9.3691 GHz, microwave power of 10 μW, modulation amplitude of 0.2 mT, time constant of 81.92 ms and sweep rate of 42.94 s over 50 mT.

3.3.1.5 DFT calculations on $[Ru@Ge_{12}]^{3-}$ (5)

Professor John McGrady and Jack Duckworth performed DFT calculations on $[Ru@Ge_{12}]^{3-}$. After calculating a range of different geometries for $[Ru@Ge_{12}]^{3-}$ they observed that the most stable isomer is a doublet with a D_{2d} symmetry and bond lengths very similar to those obtained by X-ray crystallography. The Ru–Ge and Ge–Ge bond lengths lie in the range of 2.81 to 2.89 Å and 2.56 to 2.72 Å, respectively. DFT calculations were used to compare the energies of the D_{2h} geometry of **5** with other possible geometries. The different geometries calculated include the deltahedral I_h, D_{5d} and D_{2h} and the three-connected D_{2d}, D_{5h}, T_d and D_{6h} (Figure 3.12).

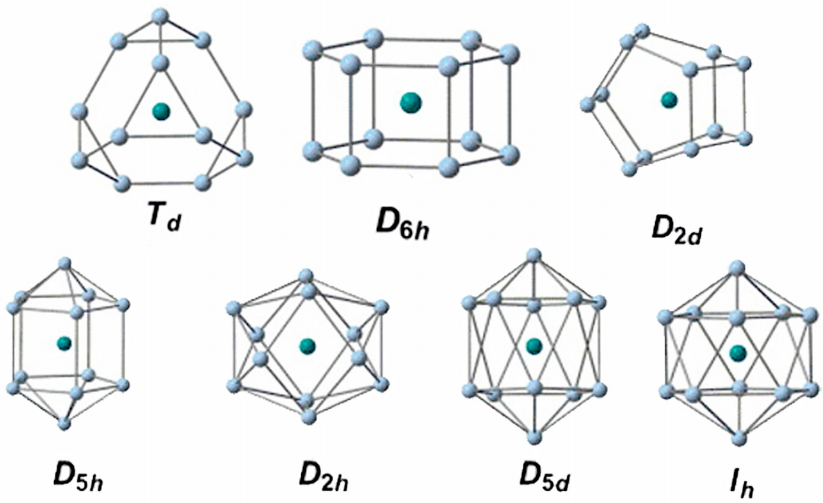

Figure 3.12: Structures of polyhedral motifs in the 12-vertex family.

	D_{2d}	D_{6h}	T_d	D_{5h}	I_h	D_{5d}	D_{2h}
Ru–Ge (Å)	2.81–2.89	2.91	3.02	2.78–3.13	2.76	2.76–3.07	2.65–2.90
Ge–Ge (Å)	2.56–2.72	2.56–2.61	2.52–2.62	2.70–3.14	2.91	2.72–3.35	2.71–3.07
ϱ(Ru)	–0.08	0.17	–0.19	0.59	0.30	0.57	0.43
ϱ(Ge_{12})	1.08	0.83	1.19	0.41	0.70	0.43	0.57
n_{imag}	0	6	12	0	5	1	1
E (eV)	0.0	+2.86	+5.86	+0.55	+1.15	+0.68	+0.99

Table 3.2: Optimised bond lengths and relative stabilities of various isomers of $[Ru@Ge_{12}]^{3-}$ (relative to D_{2d}).

The D_{2d} isomer was found to be the most stable; the D_{5h} (bicapped pentagonal prism motif) isomer had the next lowest energy, lying +0.55 eV higher in energy. This isomer has been studied computationally by Tang as a neutral molecule [M@Ge_{12}] (M = first-row transition metal) but has no precedent amongst structurally characterised species.[35]

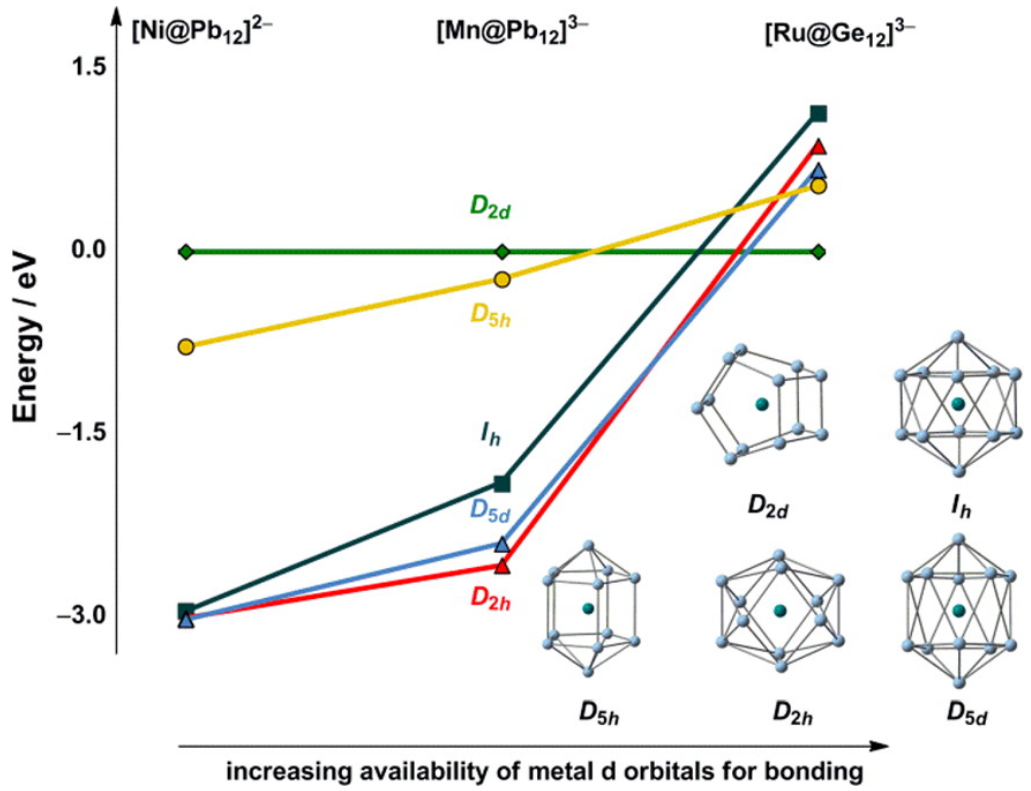

Figure 3.13: Relative energies of high-symmetry stationary points on the potential energy surfaces of representative members of the 12-vertex familiy. (D_{2d} is taken as a reference).

To extend this study, the energies of previously reported twelve-vertex cages molecules were also computed, such as $[Ni@Pb_{12}]^{2-}$ (I_h) and $[Mn@Pb_{12}]^{3-}$ (D_{2h}).[16,20] Figure 3.13 shows the results, where the horizontal axis shows a progressive destabilisation of the metal d orbitals (Ni < Mn < Ru), and this correlates with the formation of three-connected clusters for the ruthenium analogue.

Computed EPR simulations were very similar to those obtained experimentally ($g_{||}$ = 2.000, $g_{\perp}$ = 2.023). The computed isotropic hyperfine constants are for Ge_a = 3 MHz and Ge_b = –20 MHz. Only the latter can be resolved in the spectrum ($|A_{iso}|$ = 33 MHz). The very different hyperfine coupling constants at Ge_a and Ge_b are, at first glance, surprising, given that the $2a_2$ SOMO shown in Figure 3.14 is delocalised over all twelve germanium centres, giving similar spin densities at Ge_a (0.073) and Ge_b (0.098). However, the Ge_a character in the SOMO is exclusively Ge 4p (by symmetry), while for Ge_b a substantial 4s contribution leads to a much larger contact coupling.

Electronically, **5** is a very interesting compound. The electron-count consists of four electrons from each germanium, all eight valence electrons from the metallic centre d orbitals, plus three electrons for the overall charge. This sums to 59 electrons. Deltahedral electron-deficient structures $[E_{12}]$ would require 4n + 2 = 50 electrons. To provide an electron-precise structure, 60 electrons would be necessary to form 15 two-centre, two-electron bonds. This means that **5** is "one electron short". Figure 3.14 shows the electron "hole" is located on the cage and not on the ruthenium atom. Figure 3.14 also shows five doubly occupied orbitals $\{5b_2, 5a_1, 5e, 2b_1\}$ lying only 1 to 2 eV below the SOMO. This facilitates strong bonding character from the five d orbitals of the ruthenium centre towards the vacant cluster orbitals.

The ruthenium (–I) atom has a negative oxidation state, consistent with the relatively high Mulliken spin densities on the metal in these isomers. The strong interaction of the ruthenium atom with the cage is due to the availability of the D_{2d}-symmetric cage to interact with the five d orbitals of the interstitial metal atom. This allows the cluster to participate in back-donation from the electron-rich metal.

Metal-cage interactions were first observed in $[Mn@Pb_{12}]^{3-}$, where a mild distortion was seen due to back-donation from the metal centre to the cage. This is in contrast to the I_h-symmetric $[Ni@Pb_{12}]^{2-}$, where the d orbitals are low-lying and structurally inert and no distortion or back-donation is observed.

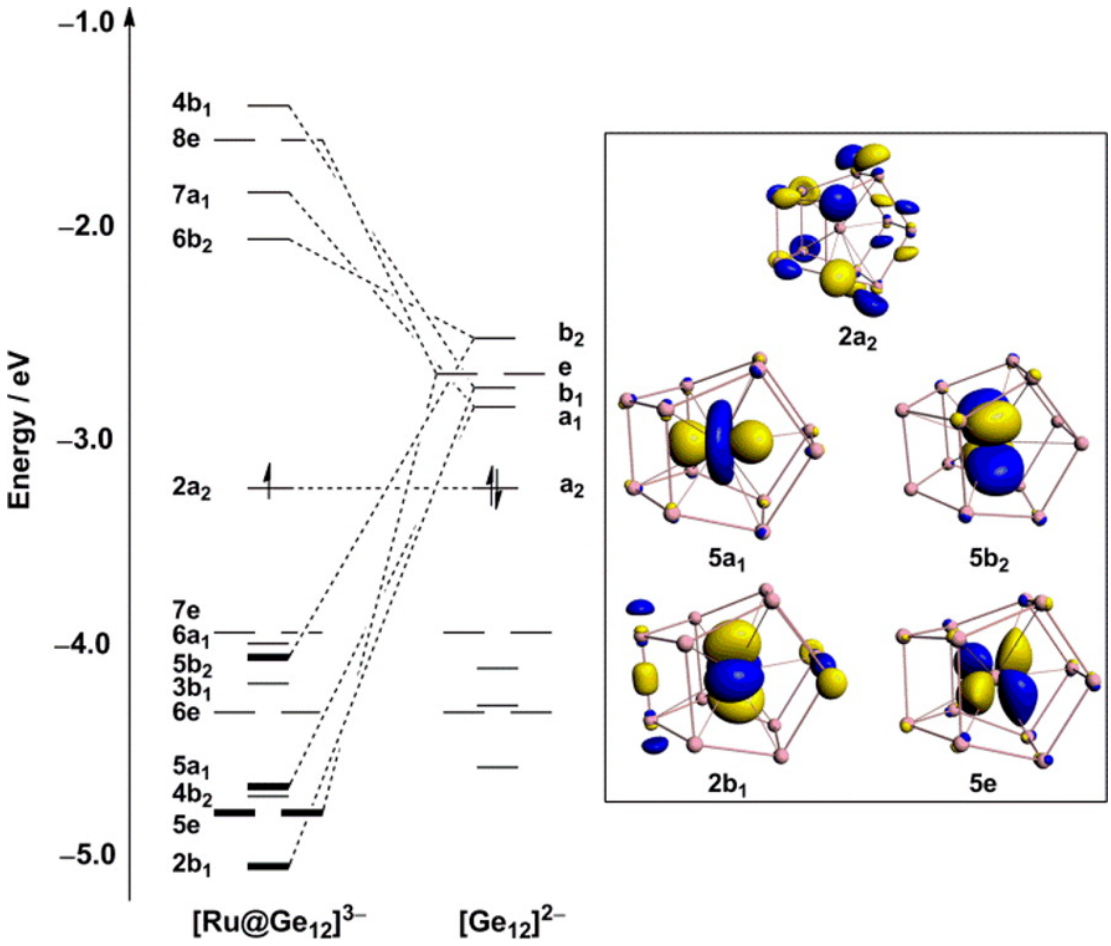

Figure 3.14: Selected frontier Kohn-Sham orbitals for D_{2d}-symmetric **5** and associated energy level diagrams.

3.3.2 Reactivity of K_4Ge_9 towards $[Co(PPhEt_2)_2(mes)_2]$

3.3.2.1 Synthesis of $[Co_2@Ge_{16}]^{4-}$ (6)

A THF solution of $[Co(PPhEt_2)_2(mes)_2]$ was added dropwise to an ethylenediamine solution of K_4Ge_9 and three equivalents of 2,2,2-crypt. After 4 hours stirring, the reaction mixture was filtered into a Schlenk tube. Toluene was added to precipitate the product $[Co_2@Ge_{16}]^{4-}$ (**6**) as a black powder which was subsequently dried under vacuum (Scheme 3.2).

Reddish-brown single crystals suitable for X-ray crystallography were grown by slow diffusion of toluene into an ethylenediamine / THF reaction mixture.

The precipitate that remained in the initial reaction vessel was dissolved in pyridine and layered with toluene to give rise to the previously reported monofunctionalised cluster $[Ge_9(mes)]^{3-}$.[36]

$$K_4Ge_9 + Co(PPhEt_2)_2(mes)_2 \xrightarrow[\text{en / THF}]{3(2,2,2\text{-crypt})} \begin{matrix}[K(2,2,2\text{-crypt})]_4[Co_2@Ge_{16}] \\ + \\ [K(2,2,2\text{-crypt})]_3[Ge_9(mes)]\end{matrix}$$

Scheme 3.2: Formation of **6**.

The presence of **6** was observed by mass spectrometry when using 18-crown-6 as a sequestering agent; however, no crystals could be obtained from such reactions. There were several attempts to synthesise **6** by using alternative cobalt precursors such as $[Co(anthracenide)_2]^-$, $CoBr_2$, $CoCp_2$ and $Co[N(SiMe_3)_2]_2$. Unfortunately all attempts were unsuccessful. It similarly was not possible to crystallise the product in the presence of alternative sequestering agents.

3.3.2.2 Structure of $[Co_2@Ge_{16}]^{4-}$ (6)

6 crystallises in space group $P2_1/c$ (No. 4) with the formula $[K(2,2,2\text{-crypt})]_4[\mathbf{6}]\cdot 2en$. X-ray crystallography studies revealed half of the cluster present in the asymmetric unit with the other half generated by symmetry. The anionic moiety is severely disordered which precludes the acquisition of a reasonable quality solution. Nevertheless, the four $[K(2,2,2\text{-crypt})]^+$ units are clearly observed, confirming the 4– charge.

During the course of the reaction, cluster enlargement from a nine-atom cage to a sixteen-atom deltahedral cage occurred. Due to the significant positional disorder of the cluster anion, the geometry of **6** cannot be defined. Nevertheless, DFT calculations have helped to elucidate its structure. The presence of two metal centres is observed in the centre of the disordered cluster, which imposes a preference for a distinctly prolate structure over a more spherical geometry.

Electronically, this cluster has 68 valence electrons, disregarding contribution from the cobalt centres (four per germanium atom and four due to the charge). The role of the cobalt atoms cannot be deduced by looking at the crystal structure, therefore DFT calculations were performed.

3.3.2.3 Mass spectrometric studies on $[Co_2@Ge_{16}]^{4-}$ (6)

The presence of the cluster in solution was confirmed by electrospray mass spectrometry. The reaction mixture was filtered, reduced to dryness and subsequently dissolved in DMF to be analysed. The negative ion mode mass spectrum shows a mass envelope corresponding to $[Co_2@Ge_{16}]^-$ at 1281.4 Da (Figure 3.15).

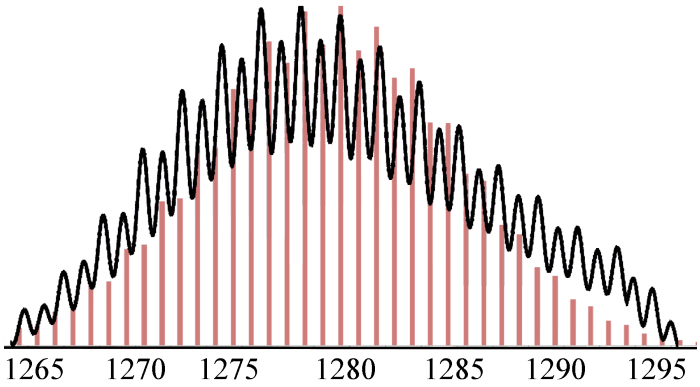

Figure 3.15: Negative ion mode electrospray mass envelope corresponding to $[Co_2@Ge_{16}]^-$. Predicted isotopic distributions are shown in red and observed mass spectrometric data are shown in black.

3.3.2.4 DFT calculations on $[Co_2@Ge_{16}]^{4-}$ (6)

Professor John McGrady's research group performed a series of DFT calculations on **6** to study its electronic properties and the nature of the interaction between the two cobalt atoms, as well between the cobalt atoms and the germanium atoms of the cage. Since in the mass spectrum the cluster appears as monoanionic and the solid-state structure as tetraanionic, calculations were performed in order to suggest the optimised structure of the anion for both cases.

A series of calculations on different $[M_2@Ge_{16}]^{x-}$ (x = 0–4) clusters revealed that an increase in electron-count stabilises both the D_{2h} and D_{4d} isomers relative to the deltahedral C_{2h} geometry (Figure 3.16). With a 4– charge, as observed in the solid-state, the $[Co_2@Ge_{16}]^{4-}$ cluster has 86 valence electrons, including four electrons per germanium atom, nine d electrons from the two cobalt centres and four from the overall charge ($16 \times 4 + 9 \times 2 + 4 = 86$).

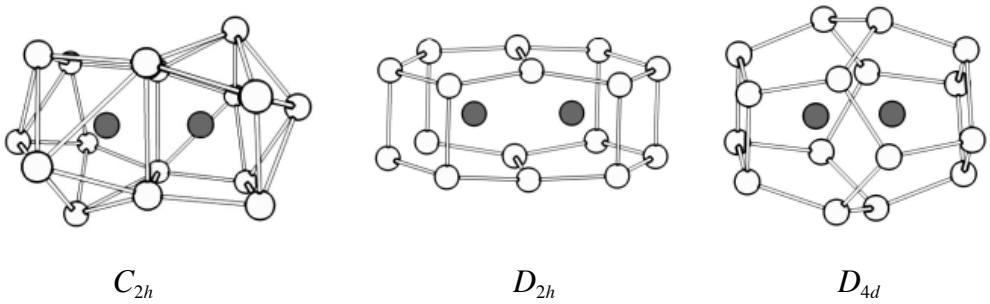

C_{2h} D_{2h} D_{4d}

Figure 3.16: Possible structures for $[Co_2@Ge_{16}]^{x-}$.

The results revealed that for both a 4– charge (found in the crystalline structure), and 1– charge (found by mass spectrometry), the three-connected D_{2h}-symmetric geometry is the lowest in energy (Figure 3.17). For $[Co_2@Ge_{16}]^{4-}$, the deltahedral C_{2h} geometry lies only 0.3 eV higher in energy and the D_{4d}-symmetric lies 1.1 eV higher in energy. The Co–Co separation gets shorter as the overall charge of the cluster decreases, going from 2.81 Å in the 4– cluster to 2.74 Å for the 1– species. In the 1– species, the four linking germanium atoms are displaced away from the centre of the cluster. This trend continues to the neutral species $[Co_2@Ge_{16}]^0$ where there would be a Co–Co bond (2.57 Å) along with puckering of the cage.

The D_{2h}-symmetric minima of **6** can be considered as two fused pentagonal prisms and the Kohn-Sham molecular orbital diagram shown in Figure 3.18 highlights the close relationship to the $[Co@Ge_{10}]^{3-}$ anion that has been studied previously.[7]

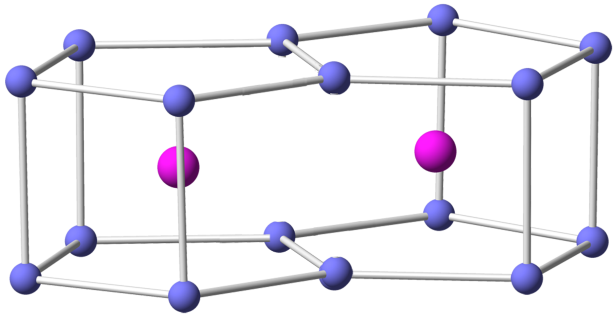

Figure 3.17: Representative diagram for a D_{2h}-symmetric isomer for **6**.

The $14b_{3g}$ symmetric HOMO of **6** contains two electrons and exhibits substantial Ge–Ge bonding character between the atoms in the five membered rings. More subtly, with a high negative charge, the energy of the metal d band is increased, such that substantial 3d character accumulates in the low-lying vacant orbitals that are primarily Ge–Ge bonding in nature, making this conformation stable. There is some degree of back-bonding from the cobalt centres to the cage because the orbitals involved have a Ge–Ge bonding character: the result is a strengthening of both the Co–Ge and the Ge–Ge bonds, particularly those in the five-membered rings.

One- and two-electron oxidations of the cluster depopulate the cluster-based $14b_{2g}$ orbital, whereas a further oxidation results in the partial depopulation of the Co–Co π* orbital, $15b_{1g}$, resulting in a net Co–Co bond order of 0.5. The 3d valence orbitals on cobalt play an integral part in controlling the structural chemistry. Just as in the monometallic endohedral cages, it appears that the stability of the cluster is associated with situations where the electron-densities on the metal and on the cluster interpenetrate, such that both attain stable configurations.

By way of comparison for the neutral species $[Pd_2@Ge_{16}]^0$, the most stable conformation was also the D_{2h} isomer. This is because it is the only geometry with cavities large enough to accommodate two palladium atoms. Nevertheless, due to its very low energy HOMO–LUMO separation (0.5 eV), probably caused by steric effects, this cluster is not very likely to be stable in a global sense. This cluster has two fewer electrons in the $14b_{3g}$ than **6** (an orbital which is entirely cluster based), with mixed Ge–Ge σ and π* character, making the HOMO-LUMO gap significantly smaller than in **6**. The Pd 4d orbital character is instead found in a narrow band of 10 linear combinations that lie ~2.5 eV

below the LUMO, and as a result, the sharing of electron-density between the metal and the cage is minimal.

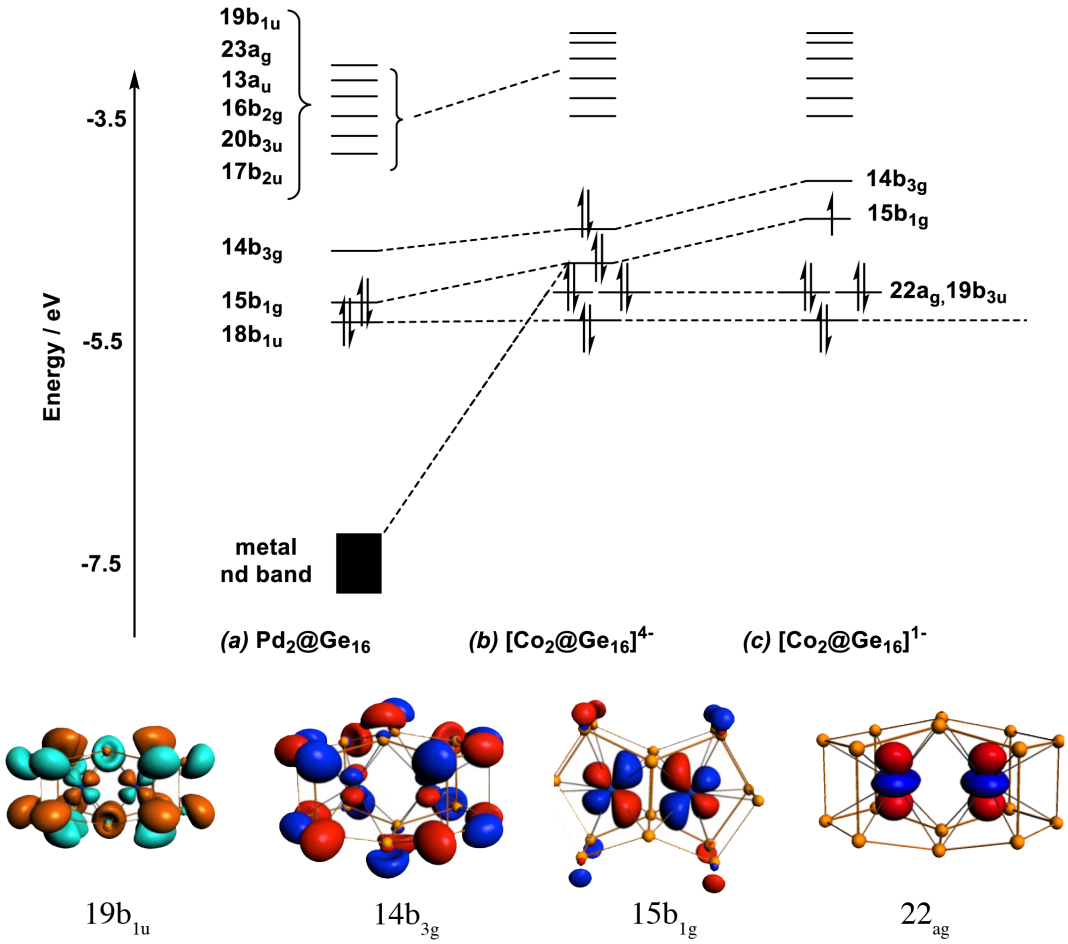

Figure 3.18: Kohn-Sham diagrams for $Pd_2@Ge_{16}$, $[Co_2@Ge_{16}]^{4-}$ and $[Co_2@Ge_{16}]^{1-}$. The levels have been shifted to bring the $18b_{1u}$ and $6a_2$'' orbitals, which are localised almost entirely on the cage, into coincidence. The contour plots emphasise the close links between the mono- and bimetallic structures.

3.4 Conclusions

This chapter detailed the synthesis and characterisation of two novel compounds. The reaction of K_4Ge_9 with $[Ru(1,5\text{-}COD)(\eta^3\text{-}CH_3C(CH_2)_2)_2]$ yielded the three-connected $[Ru@Ge_{12}]^{3-}$ (**5**) cluster which exhibits a non-deltahedral geometry. This is the first example of a three-connected $[E_{12}]$ cluster where an enlargement of the cage occurred along with the insertion of a ruthenium atom in the cluster cavity. The D_{2h} structure

elucidated by single X-ray diffraction was supported by DFT calculations, showing that the observed geometry is energetically more stable than other possible isomers. **5** is the twelve-vertex version of the pentagonal prismatic clusters $[Fe@Ge_{10}]^{3-}$ and $[Co@Ge_{10}]^{3-}$.[6,7]

EPR spectroscopy confirmed the paramagnetic character of **5**, and the *g* values were replicated using DFT calculations. DFT calculations were used to place this new cluster in the context of the wider 12-vertex family (including the icosahedral $[Ni@Pb_{12}]^{2-}$ and the distorted but still identifiably deltahedral D_{2h}-symmetric $[Mn@Pb_{12}]^{3-}$). The three clusters lie on a continuum defined by the electron-richness of the metal. In $[Ni@Pb_{12}]^{2-}$ the d orbitals are low-lying and structurally inert, while in **5** all five d orbitals are strongly mixed with vacant orbitals on the cluster. The three-connected geometry characteristic of electron-precise clusters is optimal in this case because it allows all the five d orbitals of the electron-rich metal to participate in back-bonding, giving an effective 5n electron-count at the cage.

The reaction between K_4Ge_9 and $[Co(PPhEt_2)_2(mes)_2]$ yielded the expanded cluster $[Co_2@Ge_{16}]^{4-}$ (**6**). The quality of the crystals was poor due to positional disorder of the anion and extensive DFT calculations had to be performed to support the partial structure obtained. The calculations showed that the cluster likely adopts a D_{2h}-symmetric structure based on two pentagonal prisms sharing a square face. There is no direct interaction between the cobalt centres in the tetraanion, but a three-electron oxidation results in the partial depopulation of the Co–Co π* orbital and hence the emergence of a direct Co–Co bond. The formation of **6** was supported by mass spectrometric measurements.

Table 3.3 shows a summary of all the endohedral group 14 clusters that, to my knowledge, have been reported to date. Most of them have been prepared using the Zintl phases K_4E_9, but there are a handful of examples that were prepared in the solid-state by the reaction between the relevant elements at high temperatures.

Nuclearity	Ge	Sn	Pb
Ligated	$[Ni@Ge_9Ni(PPh_3)]^{2-}$ [3]	$[Ni@Sn_9Ni(CO)]^{3-}$ [37]	
	$[Ni@Ge_9Ni(CO)]^{2-}$ [1]	$[Pt@Sn_9Pt(PPh_3)]^{2-}$ [37]	
	$[Ni@Ge_9Ni(L)]^{n-}$ [1]	$[Pd@Sn_9SnCy_3]^{3-}$ [38]	
	(L = C≡C–Ph, en)		
	$[Ni@Ge_9Pd(PPh_3)]^{2-}$ [39]	$[Pd@Sn_9PdSnCy_3]^{3-}$ [38]	
	$[Ni_6Ge_{13}(CO)_5]^{4-}$ [3]		
9	$[Ni@Ge_9]^{3-}$ [1,2]	$[Ni@Sn_9]^{3-}$ [1]	
		$[Cu@Sn_9]^{3-}$ [14]	$[Cu@Pb_9]^{3-}$ [14]
		$[Ni@Sn_9]^{4-}$ [12,40]	
		$[Co@Sn_9]^{5-}$ [40]	
	$[Ni@Ge_9Tl]^{3-}$ [13]	$[Ni@Sn_9Tl]^{3-}$ [13]	
10	*[Fe@Ge$_{10}$]$^{3-}$* [6]	$[Fe@Sn_{10}]^{3-}$ [17]	$[Ni@Pb_{10}]^{2-}$ [15]
	[Co@Ge$_{10}$]$^{3-}$ [7]		
12			$[Ni@Pb_{12}]^{2-}$ [15,15]
		$[Ir@Sn_{12}]^{3-}$ [18]	
			$[Pt@Pb_{12}]^{2-}$ [16,41]
			$[Pd@Pb_{12}]^{2-}$ [15]
			$[Mn@Pb_{12}]^{3-}$ [20]
	[Ru@Ge$_{12}$]$^{3-}$ [8]		
16		$[\{Ni@Sn_8(\mu\text{–}Ge)_{1/2}\}_2]^{4-}$ [12]	
	[Co$_2$@Ge$_{16}$]$^{4-}$ [9]		
17		$[Ni_2@Sn_{17}]^{4-}$ [21]	
		$[Pt_2@Sn_{17}]^{4-}$ [22]	
		$[Co_2@Sn_{17}]^{5-}$ [42]	
18	$[Ni_3@(Ge_9)_2]^{4-}$ [2]		
	$[Pd_2@Ge_{18}]^{4-}$ [23]	$[Pd_2@Sn_{18}]^{4-}$ [24,25]	
20(21)		$[Sn@Cu_{12}@Sn_{20}]^{2-}$ [43]	

Non-deltahedral species shown in italics

Table 3.3: Examples of endohedral clusters reported in the literature.

3.5 References

(1) Goicoechea, J. M.; Sevov, S. C. *J. Am. Chem. Soc.* **2006**, *128* (12), 4155–4161.

(2) Goicoechea, J. M.; Sevov, S. C. *Angew. Chem. Int. Ed.* **2005**, *44* (26), 4026–4028.

(3) Esenturk, E. N.; Fettinger, J.; Eichhorn, B. W. *Polyhedron* **2006**, *25* (2), 521–529.

(4) Fässler, T. F.; Hoffmann, S. D. *Angew. Chem. Int. Ed.* **2004**, *43* (46), 6242–6247.

(5) Sevov, S. C.; Goicoechea, J. M. *Organometallics* **2006**, *25* (24), 5678–5692.

(6) Zhou, B.; Denning, M. S.; Kays, D. L.; Goicoechea, J. M. *J. Am. Chem. Soc.* **2009**, *131* (8), 2802–2803.

(7) Wang, J.-Q.; Stegmaier, S.; Fässler, T. F. *Angew. Chem. Int. Ed.* **2009**, *48* (11), 1998–2002.

(8) Espinoza-Quintero, G.; Duckworth, J. C. A.; Myers, W. K.; McGrady, J. E.; Goicoechea, J. M. *J. Am. Chem. Soc.* **2014**, *136* (4), 1210–1213.

(9) Jin, X.; Espinoza-Quintero, G.; Below, B.; Arcisauskaite, V.; Goicoechea, J. M.; McGrady, J. E. *J. Organomet. Chem.* **2015**, *792*, 149–153.

(10) Gardner, D. R.; Fettinger, J. C.; Eichhorn, B. W. *Angew. Chem. Int. Ed. Engl.* **1996**, *35* (23-24), 2852–2854.

(11) Kesanli, B.; Fettinger, J.; Gardner, D. R.; Eichhorn, B. W. *J. Am. Chem. Soc.* **2002**, *124* (17), 4779–4786.

(12) Gillett-Kunnath, M. M.; Paik, J. I.; Jensen, S. M.; Taylor, J. D.; Sevov, S. C. *Inorg. Chem.* **2011**, *50* (22), 11695–11701.

(13) Rios, D.; Gillett-Kunnath, M. M.; Taylor, J. D.; Oliver, A. G.; Sevov, S. C. *Inorg. Chem.* **2011**, *50* (6), 2373–2377.

(14) Scharfe, S.; Fässler, T. F.; Stegmaier, S.; Hoffmann, S. D.; Ruhland, K. *Chem. Eur. J.* **2008**, *14* (15), 4479–4483.

(15) Esenturk, E. N.; Fettinger, J.; Eichhorn, B. W. *Chem. Commun.* **2005**, No. 2, 247–249.

(16) Esenturk, E. N.; Fettinger, J.; Eichhorn, B. W. *J. Am. Chem. Soc.* **2006**, *128* (28), 9178–9186.

(17) Krämer, T.; Duckworth, J. C. A.; Ingram, M. D.; Zhou, B.; McGrady, J. E.; Goicoechea, J. M. *Dalton Trans.* **2013**, *42* (34), 12120–12129.

(18) Wang, J.-Q.; Stegmaier, S.; Wahl, B.; Fässler, T. F. *Chem. Eur. J.* **2010**, *16* (6), 1793–1798.

(19) Downing, D. O.; Zavalij, P.; Eichhorn, B. W. *Eur. J. Inorg. Chem.* **2010**, *2010* (6), 890–894.

(20) Zhou, B.; Krämer, T.; Thompson, A. L.; McGrady, J. E.; Goicoechea, J. M. *Inorg. Chem.* **2011**, *50* (17), 8028–8037.

(21) Esenturk, E. N.; Fettinger, J. C.; Eichhorn, B. W. *J. Am. Chem. Soc.* **2005**, *128* (1), 12–13.

(22) Kesanli, B.; Halsig, J. E.; Zavalij, P.; Fettinger, J. C.; Lam, Y.-F.; Eichhorn, B. W. *J. Am. Chem. Soc.* **2007**, *129* (15), 4567–4574.

(23) Goicoechea, J. M.; Sevov, S. C. *J. Am. Chem. Soc.* **2005**, *127* (21), 7676–7677.

(24) Kocak, F. S.; Zavalij, P.; Lam, Y.-F.; Eichhorn, B. W. *Inorg. Chem.* **2008**, *47* (9), 3515–3520.

(25) Sun, Z.-M.; Xiao, H.; Li, J.; Wang, L.-S. *J. Am. Chem. Soc.* **2007**, *129* (31), 9560–9561.

(26) Sekiguchi, A.; Kabuto, C.; Sakurai, H. *Angew. Chem. Int. Ed. Engl.* **1989**, *28* (1), 55–56.

(27) Matsumoto, H.; Higuchi, K.; Hoshino, Y.; Koike, H.; Naoi, Y.; Nagai, Y. *J. Chem. Soc. Chem. Commun.* **1988**, No. 16, 1083–1084.

(28) Sita, L. R.; Kinoshita, I. *Organometallics* **1990**, *9* (11), 2865–2867.

(29) Sekiguchi, A.; Yatabe, T.; Kabuto, C.; Sakurai, H. *J. Am. Chem. Soc.* **1993**, *115* (13), 5853–5854.

(30) Wiberg, N.; Lerner, H.-W.; Nöth, H.; Ponikwar, W. *Angew. Chem. Int. Ed.* **1999**, *38* (8), 1103–1105.

(31) Matsumoto, H.; Higuchi, K.; Kyushin, S.; Goto, M. *Angew. Chem. Int. Ed. Engl.* **1992**, *31* (10), 1354–1356.

(32) Sekiguchi, A.; Yatabe, T.; Kamatani, H.; Kabuto, C.; Sakurai, H. *J. Am. Chem. Soc.* **1992**, *114* (15), 6260–6262.

(33) Pyykkö, P.; Atsumi, M. *Chem. Eur. J.* **2009**, *15* (1), 186–197.

(34) . For 203 crystallographically characterised complexes containing a Ge–Ru single bond (CSD version 5.36, November 2014): d(min) = 2.315; d(max) = 2.715; d(mean) = 2.499; var(d) = 0.004; std. dev. = 0.062; mean dev. = 0.048;

(35) Tang, C.; Liu, M.; Zhu, W.; Deng, K. *Comput. Theor. Chem.* **2011**, *969* (1–3), 56–60.

(36) Benda, C. B.; Wang, J.-Q.; Wahl, B.; Fässler, T. F. *Eur. J. Inorg. Chem.* **2011**, *2011* (27), 4262–4269.

(37) Kesanli, B.; Fettinger, J.; Gardner, D. R.; Eichhorn, B. *J. Am. Chem. Soc.* **2002**, *124* (17), 4779–4786.

(38) Kocak, F. S.; Zavalij, P.; Eichhorn, B. W. *Chem. Eur. J.* **2011**, *17* (17), 4858–4863.

(39) Sun, Z.-M.; Zhao, Y.-F.; Li, J.; Wang, L.-S. *J. Clust. Sci.* **2009**, *20* (3), 601–609.

(40) Hlukhyy, V.; Stegmaier, S.; van Wüllen, L.; Fässler, T. F. *Chem. Eur. J.* **2014**, 12157–12168.

(41) Esenturk, E. N.; Fettinger, J.; Lam, Y.-F.; Eichhorn, B. W. *Angew. Chem. Int. Ed.* **2004**, *43* (16), 2132–2134.

(42) He, H.; Klein, W.; Jantke, L.-A.; Fässler, T. F. *Z. Anorg. Allg. Chem.* **2014**, *640* (14), 2864–2870.

(43) Stegmaier, S.; Fässler, T. F. *J. Am. Chem. Soc.* **2011**, *133* (49), 19758–19768.

Chapter 4 Coordination chemistry of group 15 Zintl ions $[E'_7]^{3-}$

4.1 Summary

Coordination chemistry studies of group 15 Zintl ions have largely been limited to the interaction of the $[E'_7]^{3-}$ cages with transition metals. The most successful reactions employed organometallic reagents (MR_n) whilst reactions involving metal halides (MX_n) were less successful due to unexpected redox type reactivity. We decided to study the reactivity of $M(NR_2)_2$ reagents towards Zintl ions, in particular group 14 main group bis(amide) species. There are only a few examples of coordination of a main group element to a Zintl cluster *via* a solution-phase reaction, namely the $[ME'_{15}]^{3-}$ (M = Sn, Pb and Hg)[1,2] clusters and the *exo*-functionalised neutral molecules $E'_7(ER)_3$ (E' = P: E = Si: R = H_3, H_2Me, Me_3, Me_2PEt_3 and Ph_3; E' = P: E = Ge and Sn: R = Me_3; E' = As: E = Si: R = Me_3).[3–5]

This chapter will describe the reactivity of the $[HP_7]^{2-}$ cage towards a series of group 14 bis(amide) compounds. $[HP_7]^{2-}$ reacts with $E[N(SiMe_3)_2]_2$ to form compounds of the type $[P_7EN(SiMe_3)_2]^{2-}$ (E = Ge (**7**) and Sn (**8**)). In these compounds the $[P_7]^{3-}$ cage interacts with the main group element in an η^2 (or κ^2) fashion. The reactions proceed *via* the deprotonation of the $[HP_7]^{2-}$ precursor and the formation of the volatile

$HN(SiMe_3)_2$ amine. Additionally **7** loses a $[N(SiMe_3)_2]^-$ fragment over time and transforms to the more thermodynamically favourable product $[(P_7)_2Ge_2N(SiMe_3)_2]^{3-}$ (**10**).

4.2 Introduction

$[E'_7]^{3-}$ cages can react with d-block metal complexes to give rise to coordination compounds where the original geometry is retained and one or more E' atoms coordinate to the metal centre. There are also a handful of examples where the cage fragments and coordinates to the metal in alternative ways. There are three predominant coordination modes available for $[E'_7]^{3-}$: η^1, where one E' atom donates two electrons; η^2 (or κ^2), four electrons are donated or η^4, when the cage acts as a six-electron donor. Figure 4.1 shows the numbering scheme that will be used in this chapter.

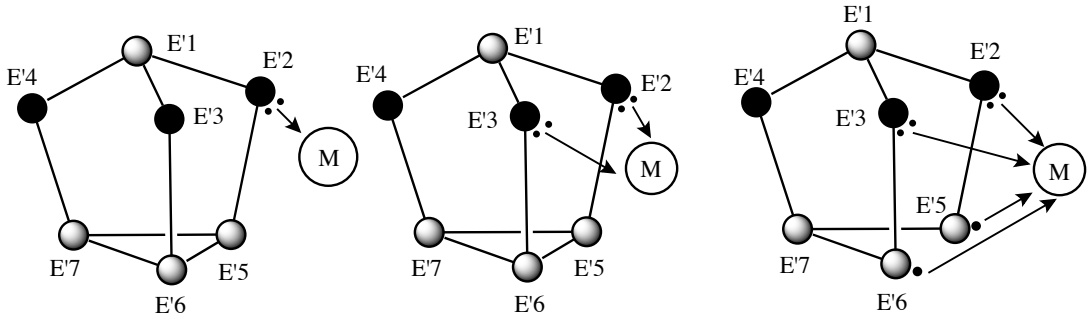

η^1 coordination mode η^2 coordination mode η^4 coordination mode

Figure 4.1: Diagram showing the three possible coordination modes of the $[E'_7]^{3-}$ cage. Atoms possessing a formal negative charge are highlighted in black.

4.2.1 η^1 coordination of the $[E'_7]^{3-}$ cage

The least common coordination mode for $[E'_7]^{3-}$ cages functionalised with metal fragments is the η^1. The *tris*functionalised neutral compound $[P_7\{FeCp(CO)_2\}_3]$ (Figure 4.2) was prepared by reacting the $[P_7]^{3-}$ cage with three equivalents of $[FeCp(CO)_2Br]$.[6] Since the $FeCp(CO)_2$ fragment is very bulky this reaction proceeds forming exclusively the symmetric isomer. This can be confirmed by ^{31}P NMR spectroscopic studies where only three resonances are observed (δ = 47.7 ppm for the apical phosphorus atom, δ = –48.7 ppm for the three basal phosphorus atoms and δ = –159.3 ppm for the three iron-bonded phosphorus atoms).

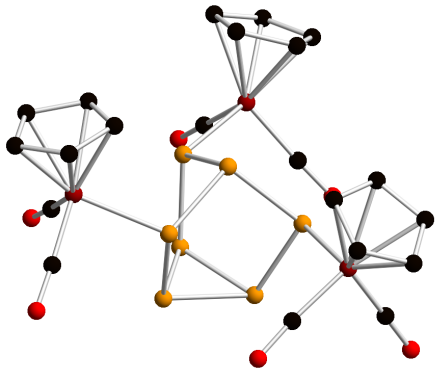

Figure 4.2: Ball and stick diagram of $[P_7\{FeCp(CO)_2\}_3]$ (P atoms are shown in orange, Fe atoms in dark red, C atoms in black and O atoms in red). H atoms are omitted for clarity.

4.2.2 η^2 coordination of the $[E'_7]^{3-}$ cage

As mentioned above, when the $[E'_7]^{3-}$ cages coordinate in an η^2 fashion, they act as a four-electron donors and the shape of the cage is retained. By ^{31}P NMR spectroscopy they exhibit five different resonances corresponding to the five inequivalent phosphorus environments. The first reaction that will be discussed is between the $[E'_7]^{3-}$ (E' = P and As) cage and the organometallic complex $[Pt(PPh_3)_2(C_2H_4)]$, which

yields $[E'_7PtH(PPh_3)]^{2-}$ (Figure 4.3).[7,8] In these compounds the platinum atom loses a PPh_3 ligand and is coordinated by two E' atoms of the cage. Additionally, the platinum atom has gained a hydride that was abstracted from the solvent. The hydride could not be located by X-ray crystallography, but it was observed by deuterium labelling studies. The platinum atom has a sixteen-electron configuration and a square planar geometry as expected for a d^8 platinum (II) species.

^{31}P NMR spectroscopic studies at –78 ºC showed seven multiplets, five of them corresponding to the different phosphorus environments of the cage, another corresponding to free unreacted $[P_7]^{3-}$, and a doublet corresponding to the PPh_3 ligand. Variable temperature studies showed that P2, P3, P5 and P6 coalesce at –20 ºC into one resonance that integrates to four, P1 and P7 coalesce to one resonance at –60 ºC, the P4 resonance remains unchanged, and finally the PPh_3 resonance changes from a doublet to a quintet at 25 ºC indicating that the structure is fluxional in solution. It was proposed by the authors that this fluxionality is due to an η^2 to η^4 type of rearrangement.

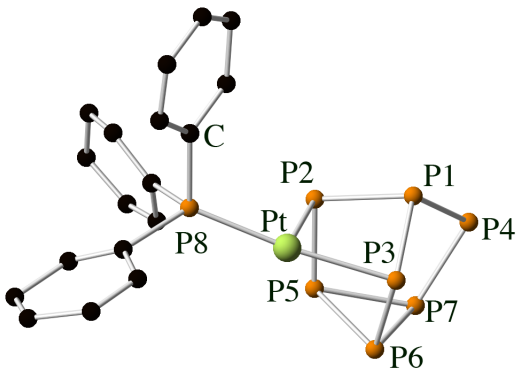

Figure 4.3: Ball and stick diagram of $[P_7PtH(PPh_3)]^{2-}$. Hydride could not located by X-ray crystallography. H atoms are omitted for clarity.

Reactions between $[E'_7]^{3-}$ cages (E' = P and As) and the homoleptic organometallic complexes MPh_2 (M = Zn and Cd) also afford compounds in which the cage chelates the metal in an η^2 fashion.[2,9,10] The products of these reactions, $[M(E'_7)_2]^{4-}$ (E = P and As: M = Zn and Cd) (Figure 4.4), consists of two $[E'_7]^{3-}$ cages bridged by a M^{2+} atom. The reaction proceeds *via* the heterolytic cleavage of both M–C bonds of the metal reagent and the formation of benzene (as observed by ^{1}H NMR spectroscopy). To synthesise the $[Cd(As_7)_2]^{4-}$ analogue, cadmium cyclohexanebutyrate was used instead of $CdPh_2$.

The central metal atoms adopt a distorted tetrahedral coordination environment and have a total of eighteen valence electrons. As expected for the η^2 coordination mode, the ^{31}P NMR spectra exhibit five resonances corresponding to each one of the inequivalent phosphorus environments.

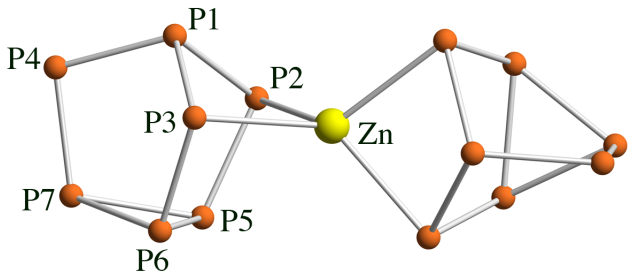

Figure 4.4: Ball and stick diagram of $[Zn(P_7)_2]^{4-}$.

A related coordination compound, $[E'_7InPh_2]^{2-}$ (Figure 4.5), was prepared by the reaction of $InPh_3$ with the $K_3E'_7$ Zintl phase (E' = P and As).[9] In these molecules the $[E'_7]^{3-}$ cage acts as a four-electron donor towards the indium centre, and one In–Ph bond is cleaved during the synthesis. The indium atom adopts a distorted tetrahedral geometry. ^{31}P NMR spectroscopy showed the presence of five different phosphorus environments.

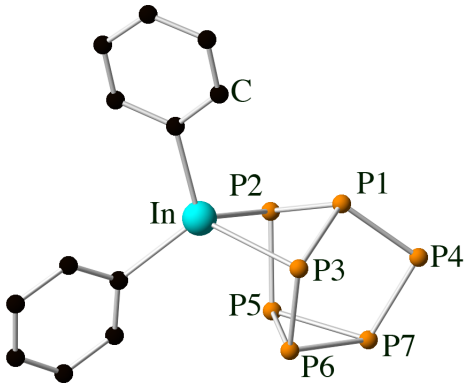

Figure 4.5: Ball and stick diagram of $[P_7InPh_2]^{2-}$. H atoms are omitted for clarity.

By contrast, $[In(E'_7)_2]^{3-}$ could be prepared by a simple salt-metathesis reaction between two equivalents of $K_3E'_7$ (E' = P and As) and $InCl_3$.[1] The bridged anion $[In(P_7)_2]^{3-}$ was studied by X-ray crystallography showing two $[P_7]^{3-}$ units bridged by an In^{3+} cation with a distorted tetrahedral geometry. Its geometry is very similar to the $[M(E'_7)_2]^{4-}$ (E' = P and As, M = Cd and Zn) compounds. The In^{3+} cation is isoelectronic with Zn^{2+} and Cd^{2+} cations and, consequently, the indium-containing compound carries a smaller negative charge.

$K_3E'_7$ (E' = P and As) react in a 1:1 ratio with TlCl to form $[E'_7Tl]^{2-}$ (Figure 4.6).[1] X-ray crystallography studies show that the $[E'_7]^{3-}$ cage coordinates to the Tl^+ cation in an η^2 fashion *via* two of the formally anionic E' atoms. In contrast to the reactions between $[E_9]^{4-}$ (E = Ge and Sn) and TlCp that form the η^4 coordination compounds $[E_9Tl]^{3-}$, $[E'_7]^{3-}$ cages coordinate in an η^2 mode to the thallium (I) atom.[11] This is supported by solid-state crystallographic studies where cleavage of the E'5–E'6 bond is not observed. Additionally, the thallium atom has a lone pair which points radially away from the cluster anion. Solution ^{31}P NMR studies of reaction mixtures at –50 ºC show only two broad resonances, as well as unreacted $[HP_7]^{2-}$ and $[P_{21}]^{3-}$. A resonance at δ = 99.0 ppm is assigned to P1 and P7 and the second resonance at δ = –147.2 ppm

is assigned to the four phosphorus atoms closest to the thallium atom (P2, P3, P5 and P6). The missing resonance corresponding to P4 is believed to be overlapping with one of the $[P_{21}]^{3-}$ resonances which was observed at δ = 58.2 ppm. This suggests that P2, P3 and P5, P6 are equivalent, similarly to P1 and P7, implying that there is a fluxionality between the η^2 and the η^4 coordination modes.

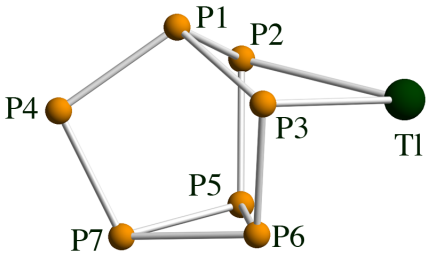

Figure 4.6: Ball and stick diagram of $[TlP_7]^{2-}$.

The reactions between K_3P_7 and $[M(nbe)_3][SbF_6]$ or MCl (M = Ag and Au), in a 1:1 ratio in the presence of 2,2,2-crypt and a two equivalents of a proton source yield the *bis*protonated cluster $[M_2(HP_7)_2]^{2-}$ (M = Ag and Au).[12] The reaction of the $[As_7]^{3-}$ Zintl ion and an alternative gold precursor, $[(PPh_3)AuCl]$, yields the deprotonated analogue $[Au_2(P_7)_2]^{4-}$ (Figure 4.7).[10,13] These compounds are light sensitive and were isolated in low crystalline yields. In these compounds two $[HP_7]^{2-}$ cages are bridged by a $[M_2]$ unit. Each metal atom is bonded to one phosphorus atom from each cage and to the other metal atom displays a "T-shape" coordination environment. The two bridging metal atoms and the phosphorus atoms which comprise their immediate coordination sphere are coplanar and give rise to an “H-shaped” motif as opposed to the other $[MP_{15}]^{3-}$ (M = Sn, Pb and Hg) species,[1,2] which are isostructural with the $[P_{16}]^{2-}$ anion and have a "bent" geometry. Additionally, both of the cages were found to be in an "up-down" configuration.

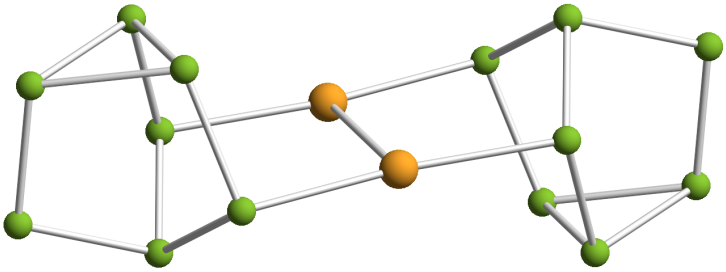

Figure 4.7: Ball and stick diagram of $[Au_2(As_7)_2]^{4-}$ (As atoms are shown in green and Au atoms in gold).

The $[ME'_{15}]^{3-}$ (E' = P and As: M = Sn, Pb and Hg) anions were prepared from reactions of the relevant $[E'_7]^{3-}$ cages with MI_2 (M = Sn and Pb) or $HgPh_2$.[1,2] The resulting anions are sixteen atom clusters which are isostructural and isoelectronic with the polyphosphide $[P_{16}]^{2-}$. One of the bridging E' atoms is replaced with a negatively charged group 14 element, and thus the cluster cage has a total charge of 3–. The metal atom is three-connected and has an *exo*-lone pair. The phosphorus containing species were studied using ^{31}P NMR spectroscopy and revealed a total of eight resonances in each case, arising from all of the magnetically inequivalent phosphorus atoms.

$[As_7]^{3-}$ reacts with $Pd(PCy_3)_2$ to form $[Pd_2(As_7)_2]^{4-}$ (Figure 4.8) as the major product and $[Pd_7As_{16}]^{4-}$ as a minor product.[14] In $[Pd_2(As_7)_2]^{4-}$ the $[As_7]^{3-}$ cage is mildly activated and the cleavage of the As5–As6 bond has taken place. The palladium atoms have a distorted square-planar geometry and with a strong bonding interaction between the two centres. A theory for the mechanism of formation of this molecule is that a complex similar to the previously discussed $[P_7PdH(PCy_3)]^{2-}$ is initially formed, and then, through a redox process, $[Pd_2(As_7)_2]^{4-}$ is generated. This hypothesis is consistent with the release of H_2 gas observed during the reaction, however, the proposed $[As_7PdH(PCy_3)]^{2-}$ intermediate has not been isolated.

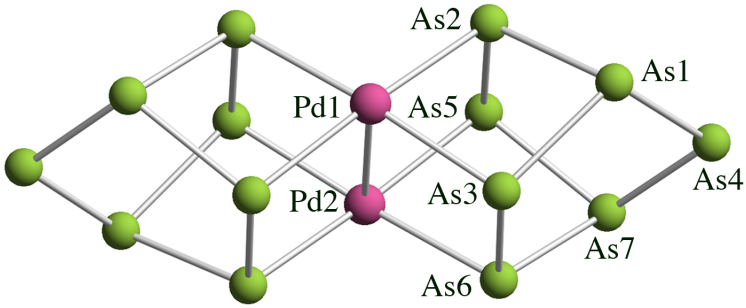

Figure 4.8: Ball and stick diagram of $[Pd_2(As_7)_2]^{4-}$.

$K_3E'_7$ reacts with $[Cu(mes)]_5$ to form another bridged compound, $[Cu_2(E'_7)_2]^{4-}$ (E' = P and As).[9] The anions consist of a $[Cu_2]^{2+}$ moiety bridging two $[E'_7]^{3-}$ units, and has a similar structure to the $[Pd_2(As_7)_2]^{4-}$ cluster discussed above. However in $[Cu_2(E'_7)_2]^{4-}$ the $[Cu_2]$ unit is not located in the middle of the structure; instead, each copper atom has strong bonding interactions with all four E' atoms of one cage and with one E' atom of the adjacent cage. This gives each copper atom a coordination number of six. ^{31}P NMR spectroscopic studies revealed that the phosphorus-containing species is fluxional in solution. At –50 ºC it shows three very broad resonances with intensities in a 1:2:4 ratio.

4.2.3 η^4 coordination of the $[E'_7]^{3-}$ cage

When $[E'_7]^{3-}$ cages act as six-electron donors and coordinate in an η^4 fashion to a metal centre, they undergo mild activation by cleavage of the basal E'5–E'6 bond. As a result there are four E' atoms coordinating to the metal (E'2, E'3, E'5 and E'6), two bridging E' atoms (E'1 and E'7), and a single two-connected E' atom (E'4).

Group 15 $[E'_7]^{3-}$ cages can react with $[M(CO)_3L]$ (M = Cr and W: L = mesitylene; M = Mo: L = cycloheptatriene) to afford coordination compounds of the type $[E'_7M(CO)_3]^{3-}$ (E' = P, As and Sb; M = Cr, Mo and W) (Figure 4.9).[15,16] The

$[Sb_7Mo(CO)_3]^{3-}$ complex was formed by reacting the $[Sb_7]^{3-}$ cage and $[Mo(CO)_4(bipy)]$.[17] In these coordination compounds the $[E'_7]^{3-}$ cage binds to the $M(CO)_3$ fragment in an η^4 fashion, donating six electrons to the zero-valent metal centre. As expected for these compounds, the ^{31}P NMR spectra exhibit only three resonances. For example, for $[P_7Cr(CO)_3]^{3-}$ the ^{31}P NMR spectrum revealed resonances at δ = 199 ppm for the single two-connected atom, δ = –21 ppm for the two two-connected bridging phosphorus atoms and δ = –143 ppm for the four metal-bonded phosphorus atoms.

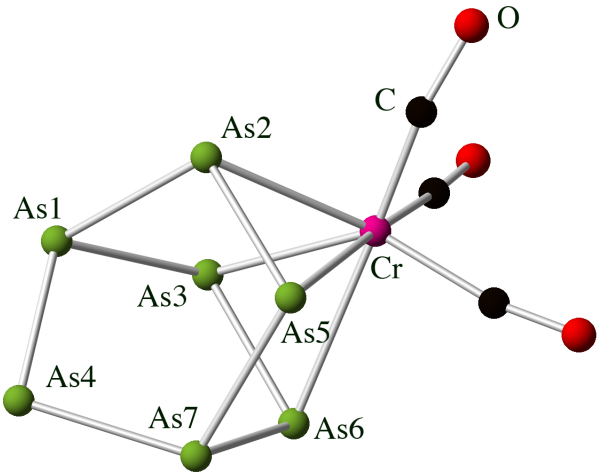

Figure 4.9: Ball and stick diagram for $[As_7Cr(CO)_3]^{3-}$.

It is possible to protonate these species using acids with pK_a values of less than eighteen to give rise to protonated species of the type $[HP_7M(CO)_3]^{2-}$. These species can in turn be deprotonated with MeO^- to generate the original complex.[18] Functionalisation reactions have also been reported for $[P_7W(CO)_3]^{3-}$ to form $[RP_7W(CO)_3]^{2-}$ (R = Me, Et, Bu, $PhCH_2$, Me_3Si, Bu_3Si, Hex_3Si, Ph_3Si, Et_3Ge, Ph_3Ge, Et_3Sn, Bu_3Sn, Cy_3Sn, Ph_3Sn, Ph_3Pb, $(C_6H_{11})_3Sn$ and $(en)(CO)_3W$).[19–21] Additional reactions that have been studied are the addition of an extra CO ligand to the metal to form $[P_7M(CO)_4]^{3-}$. In these species, the $[P_7]^{3-}$ cage is forced to change its

coordination mode, switching from η^4 to η^2 in order to preserve the eighteen-electron configuration of the metal centre. This regenerates the nortricyclane-like shape of the cluster. These carbonylated species tend to lose a CO ligand when exposed to nitrogen.[22]

The reaction of the $[P_7]^{3-}$ cage and $[Ni(CO)_2(PPh_3)_2]$ has also been studied, yielding the η^4 coordination compound $[P_7Ni(CO)]^{3-}$.[7] This anion can be protonated by slow addition of MeOH at –50 ºC to give way to the complex $[HP_7Ni(CO)]^{2-}$. As expected for the deprotonated species, there are three ^{31}P NMR resonances in the spectrum.

In 2011, Goicoechea and co-workers published a phosphorus-based Zintl ion analogue of ferrocene, namely $[Fe(HP_7)]^{2-}$ (Figure 4.10).[23] This complex was synthesised by the salt-metathesis reaction of $FeCl_2$ and the Zintl phase K_3P_7. In this molecule two $[HP_7]^{2-}$ cages are coordinated to an iron (II) centre in an η^4 fashion. The iron atom has a total of eighteen valence electrons.

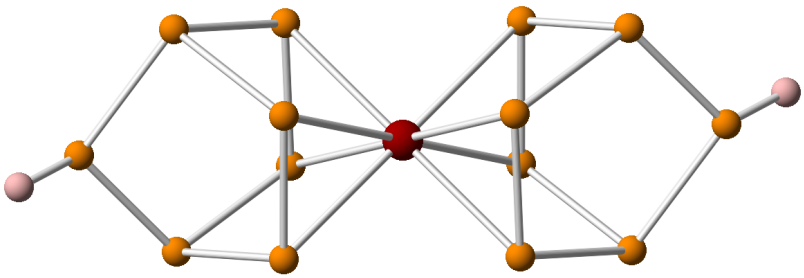

Figure 4.10: Ball and stick diagram of $[Fe(HP_7)_2]^{2-}$ (P atoms are shown in orange, the Fe atom in red and H atoms in pink).

4.3 Results and discussion

4.3.1 Reactivity of $[HP_7]^{2-}$ towards $E[N(SiMe_3)_2]_2$ (E = Ge and Sn)

4.3.1.1 Synthesis of $[P_7EN(SiMe_3)_2]^{2-}$ (E = Ge (7) and Sn(8))

The reactivity of $[K(18\text{-crown-}6)]_2[HP_7]$ towards $E[N(SiMe_3)_2]_2$ was studied in pyridine in a 1:1 molar ratio, yielding $[P_7GeN(SiMe_3)_2]^{2-}$ (**7**) and $[P_7SnN(SiMe_3)_2]^{2-}$ (**8**) (Scheme 4.1). When **7** is prepared, the reaction mixture is originally translucent orange but darkens over time to dark red. The stability of **7** was monitored by ^{31}P NMR spectroscopy over three days. This reaction rapidly gives rise to **7**, however the mixture ultimately transforms to a different thermodynamic product, which will be discussed later on. It was discovered that by keeping the reaction mixture at –35 ºC, **7** can be preserved for a period of several days allowing for its isolation.

The reaction between $[K(18\text{-crown-}6)]_2[HP_7]$ and $Sn[N(SiMe_3)_2]_2$ gives rise to an orange solution containing **8** that, unlike **7**, proved to be stable at room temperature indefinitely. Both of these reactions proceed to completion within minutes of dissolving the reactants.

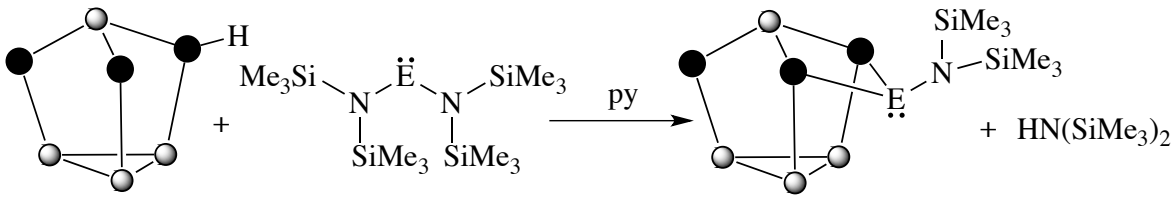

Scheme 4.1: Formation of $[P_7EN(SiMe_3)_2]^{2-}$.

Single crystals of **7** were grown over a month by vapour diffusion of toluene into a concentrated pyridine solution of **7** at –35 ºC. As mentioned previously, it was important to keep the solution at –35 ºC because **7** rapidly gives rise to a different product over the course of several hours at room temperature. Due to the low stability of **7**, the crystalline yield was very low (9%). Elemental analysis could also not be obtained due to the low stability.

Single crystals of **8** were grown overnight at room temperature as large orange blocks by the vapour diffusion of toluene into a concentrated pyridine solution of **8**. The crystalline yield was 76%. Elemental analysis confirmed the purity of this product.

4.3.1.2 Structures of $[P_7EN(SiMe_3)_2]^{2-}$ (E = Ge (7) and Sn(8))

Crystals of $[K(18\text{-crown-6})]_2[\mathbf{7}]\cdot 2py$ (Figure 4.11) and $[K(18\text{-crown-6})]_2[\mathbf{8}]\cdot 2py$ (Figure 4.12) are isomorphous, crystallising in the same space group (*P*–1) (No. 1) with similar cell parameters.

The $[P_7EN(SiMe_3)_2]^{2-}$ clusters consist of a nortricyclane-like $[P_7]^{3-}$ cage coordinated in an η^2 (or κ^2) fashion to a $[EN(SiMe_3)_2]^+$ fragment with a formally E^{2+} centre. The geometry around the E atom is distorted pyramidal, due to the stereogenic lone pair, which points away from the apical phosphorus atom of the cage. The sum of the bond angles around the E atom is notably less than 360º (Σ_{angles} = 282.2º for **7** and 279.0º for **8**). The cage acts as a four-electron donor, which, in addition to the $[N(SiMe_3)_2]^-$ substituent, gives the E atom a total of eight valence electrons. The clusters **7** and **8** possess a similar coordination mode to the previously mentioned clusters $[P_7M(CO)_4]^{3-}$ (M = Mo and W) and $[E'_7PtH(PPh_3)]^{2-}$ (E' = P and As).[7,22]

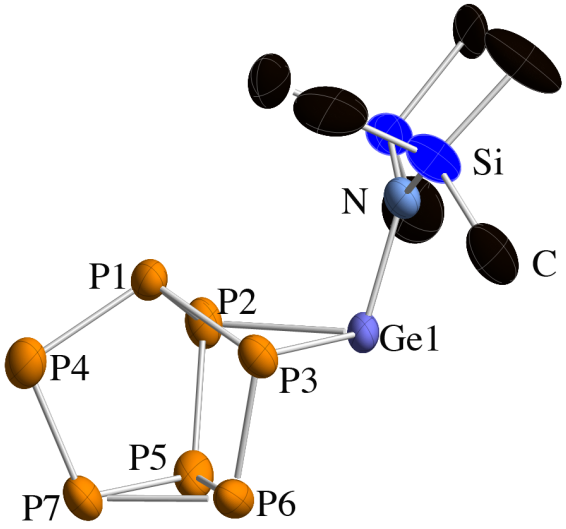

Figure 4.11: Thermal ellipsoid plot of **7** with anisotropic displacement ellipsoids pictured at 50% probability. H atoms are omitted for clarity.

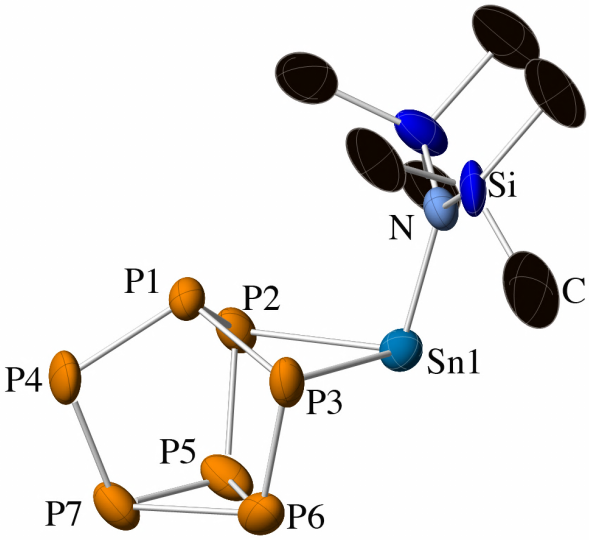

Figure 4.12: Thermal ellipsoid plot of **8** with anisotropic displacement ellipsoids pictured at 50% probability. H atoms are omitted for clarity.

Selected bond lengths and angles for **7** and **8** are provided in Table 4.1. The P–P bond lengths range from 2.139(1) to 2.265(1) Å for **7** and 2.141(1) to 2.268(2) Å for **8**. The bond metric data for the $[P_7]^{3-}$ cages is identical within experimental error. The P–P bond lengths are in good agreement with the values reported for related species such as $[P_7PtH(PPh_3)]^{2-}$ (2.14(2) to 2.26(2) Å) or $[P_7InPh_2]^{2-}$ (2.142(2) to 2.261(2) Å).[7,9]

Bond	Bond length **7** (Å)	Bond length $\mathbf{7}_{DFT}$ (Å)	Bond length **8** (Å)	Bond length $\mathbf{8}_{DFT}$ (Å)
P1–P2	2.198(1)	2.221	2.197(1)	2.225
P1–P3	2.196(1)	2.222	2.199(1)	2.223
P1–P4	2.139(1)	2.159	2.144(1)	2.165
P2–P5	2.178(1)	2.201	2.177(2)	2.200
P3–P6	2.179(1)	2.201	2.177(2)	2.199
P4–P7	2.148(1)	2.175	2.141(2)	2.173
P5–P6	2.265(1)	2.310	2.268(2)	2.309
P5–P7	2.235(1)	2.258	2.240(2)	2.264
P6–P7	2.234(1)	2.258	2.237(2)	2.263
P2–E1	2.526(1)	2.572	2.691(1)	2.751
P3–E1	2.504(1)	2.573	2.667(1)	2.753
E1–N1	2.000(2)	2.008	2.198(3)	2.220
N1–Si1	1.715(2)	1.743	1.702(3)	1.738
N1–Si2	1.708(2)	1.742	1.702(3)	1.738
Bond angles	(°)	(°)	(°)	(°)
P2–E1–P3	79.14(2)	78.60	75.33(3)	74.26
P2–E1–N1	103.26(5)	107.46	101.38(8)	104.38
P3–E1–N1	103.75(6)	107.16	102.26(8)	104.20

Table 4.1: Selected bond lengths and angles for $[P_7EN(SiMe_3)_2]^{2-}$.

The Ge–P bond lengths in **7** are 2.526(1) and 2.504(1) Å. These values are slightly longer than the mean value found in a CSD search (2.409 (av) Å) for a Ge–P single bond.[24] Compared to $Ge\{N(SiMe_3)_2\}_2P_6C_4{}^tBu_4$ (where a cluster is attached in an η^2 (or κ^2) fashion to a $Ge[N(SiMe_3)_2]_2$ fragment through two phosphorus atoms), the Ge–P bonds (2.391(1) Å and 2.409(1) Å) are shorter than those found in **7**.[25] Presumably this is due to the negative charge localised on the anionic cage. The lengthening of the bonds is also observed when compared to the sum of the covalent radii for a Ge–P single bond (2.32 Å).[26]

The Ge–N bond of **7** observed crystallographically is 2.000(2) Å. By comparison with $Ge\{N(SiMe_3)_2\}_2P_6C_4{}^tBu_4$ (1.876(4) Å and 1.883(4) Å), the Ge–N bond lengths are

longer (as are as the Ge–P bonds). The sum of the covalent radii for a Ge–N is 1.92 Å, which is shorter than the bond found in **7**.

A CSD search gives a mean Sn–P bond length of 2.625 (av) Å, while those observed for **8** are only slightly longer than this value (2.691(1) Å and 2.667(1) Å).[27] The Sn–N bond length is 2.198(2) Å. A comparison with $Sn\{N(SiMe_3)_2\}_2P_6C_4{}^tBu_4$ can be made where the Sn–N bond lengths (2.077(6) Å and 2.083(6) Å) are longer than the one found crystallographically for **8 (**2.198(3) Å).

The Sn–P bond lengths for $Sn\{N(SiMe_3)_2\}_2P_6C_4{}^tBu_4$ (2.554(2) Å and 2.624(2) Å) are only slightly shorter than **8**. This is presumably due to interelectronic repulsion due to the anionic character of **8**. The sum of the covalent radii for a Sn–P single bond is 2.51 Å and for Sn–N is 2.11 Å; both are smaller than those found for the solid-state structure of **8**.[26]

As would be expected the Ge–P bond lengths in **7** (2.526(1) Å and 2.504(1) Å) are on average 0.16 Å shorter than the Sn–P distances recorded for **8** (2.690(1) Å and 2.668(1) Å). This is consistent with the difference in covalent radius of tin relative to germanium ($r_{Sn} - r_{Ge} = 0.19$ Å). This is also reflected in the P–E–P bond angle, which is more acute for **8** (75.33(3)º) than for **7** (79.14(2)º).

DFT calculations were carried out to compute the optimised geometries of **7** and **8**. The calculated interatomic distances were found to be very similar to those observed crystallographically (Table 4.1). DFT calculations showed that the HOMOs for **7** and **8** have significant lone pair character on the E atom (31.4% and 28.6%, respectively) with some amide nitrogen atom character and mixing in of the cluster-based orbitals.

An analysis of the computed Mulliken charges revealed significant negative charges on P2, P3 and P4 as well as on the nitrogen atom. The entire cluster carries some degree of negative charge indicating charge delocalisation throughout the cluster. Interestingly, the Mulliken charges on the group 14 elements increase on the descending group (–0.082 for **7** and 0.189 for **8**). This indicates that, while formally the clusters can be interpreted as coordination complexes of a $[P_7]^{3-}$ cage with an $[EN(SiMe_3)_2]^+$ fragment, this is simply a formalism. The E–P bonding is more closely related to a strongly covalent system where the E atom is actively involved in the covalent interactions (as opposed to acting as a Lewis acid, accepting electron-density from the phosphorus atoms). The greater participation of the lighter E atoms in the cluster bonding may account for the relative instability of **7** in solution which was found to spontaneously give rise to a new cluster anion $[(P_7)_2Ge_2N(SiMe_3)_2]^{3-}$ **(10)** when left standing at room temperature. **10** will be discussed in Section 4.3.1.7.

4.3.1.3 NMR spectroscopic studies on $[P_7EN(SiMe_3)_2]^{2-}$ (E = Ge (7) and Sn (8))

The $^{31}P\{^1H\}$ NMR spectra of $[P_7EN(SiMe_3)_2]^{2-}$ show each five resonances, corresponding to a typical η^2-P_7 (or κ^2) coordination compound, with relative intensities of 1:2:1:1:2. The spectra for both compounds are very similar with minor changes to the chemical shifts of the coordinated cage. Resonances for **7** were observed at 72.3, 8.2, –46.2, –61.0 and –189.5 ppm and correspond to the P4, P2/P3, P1, P7 and P5/P6 nuclei, using the numbering scheme employed in Figure 4.11. The analogous resonances occur at 62.5, –18.1, –38.7, –81.4 and –192.0 ppm in the ^{31}P NMR spectrum of **8** and show comparable multiplet structures.

δ(ppm)		–46.2	8.2	8.2	72.3	–189.5	–189.5	–61.0
		P1	**P2**	**P3**	**P4**	**P5**	**P6**	**P7**
–46.2	**P1**		–257.4 [–234.7]	–257.4 [–234.7]	–341.4 [–249.2]	25.3 [37.0]	25.3 [37.0]	62.0 [79.9]
8.2	**P2**	–257.4 [–234.7]		18.7 [18.5]	16 [–4.6]	–370.0 [–275.8]	8.21 [–0.7]	–5.7 [–5.7]
8.2	**P3**	–257.4 [–234.7]	18.7 [18.5]		16 [–4.4]	8.21 [–0.6]	–370.0 [–275.2]	–5.7 [–5.6]
72.3	**P4**	–341.4 [–249.2]	16 [–4.6]	16 [–4.4]		10.1 [10.1]	10.1 [9.7]	373.2 [–251.3]
–189.5	**P5**	25.3 [37.0]	-370.0 [–275.8]	8.21 [–0.6]	10.1 [10.1]		–145.0 [–104.9]	–230.3 [–174.5]
–189.5	**P6**	25.3 [37.0]	8.21 [–0.7]	–370.0 [–275.2]	10.1 [9.7]	–145.0 [–104.9]		–230.3 [–174.4]
–61.0	**P7**	62.0 [79.9]	–5.7 [–5.7]	–5.7 [–5.6]	373.2 [–251.3]	–230.3 [–174.5]	–230.3 [–174.4]	

Table 4.2: ^{31}P–^{31}P NMR coupling constants in Hz taken from the $^{31}P\{^{1}H\}$ NMR spectrum of **7**. Computed values in square brackets.

δ(ppm)		–38.7	–18.1	–18.1	62.5	–192.0	–192.0	–80.4	–61.1
		P1	**P2**	**P3**	**P4**	**P5**	**P6**	**P7**	**Sn1**
–38.7	**P1**		–262.4 [–231.1]	–262.4 [–230.3]	–336.8 [–244.0]	28 [40.4]	28 [41.1]	65 [77.8]	–81.0 [30]
–18.1	**P2**	–262.4 [–231.1]		–14 [11.4]	0 [–5.9]	–368.9 [–275.1]	6.7 [–1.1]	0 [–7.1]	506.0 [280]
–18.1	**P3**	–262.4 [–230.3]	–14 [11.4]		0 [–5.9]	6.7 [–1.1]	–368.9 [–274.5]	0 [–7.0]	506.0 [278]
62.5	**P4**	–336.8 [–244.0]	0 [–5.9]	0 [–5.9]		0 [7.9]	0 [8.1]	–384.7 [–260.4]	132.0 [87]
–192.0	**P5**	28 [40.4]	–368.9 [–275.1]	6.7 [–1.1]	0 [7.9]		–143.3 [–105.4]	–223.5 [–167.4]	–259.0 [–179]
–192.0	**P6**	28 [41.1]	6.7 [–1.1]	–368.9 [–274.5]	0 [8.1]	–143.3 [–105.4]		–223.5 [–169.3]	–259.0 [–182]
–80.4	**P7**	65 [77.8]	0 [–7.1]	0 [–7.0]	–384.7 [–260.4]	–223.5 [–167.4]	–223.5 [–169.3]		288.0 [265]
–61.1	**Sn1**	–81.0 [30]	506.0 [280]	132.0 [278]	132.0 [87]	–259.0 [–179]	–259.0 [–182]	288.0 [265]	

Table 4.3: ^{31}P–^{31}P and ^{119}Sn–^{31}P NMR coupling constants in Hz taken from the $^{31}P\{^{1}H\}$ NMR spectrum of **8**. Computed values in square brackets.

Simulations were carried out by Dr. Nick Rees for **7** (Figure 4.13) and Dr. Robert Turbervill for **8** (Figure 4.14) in order to obtain the ^{31}P–^{31}P coupling constants (Table 4.2 and Table 4.3).

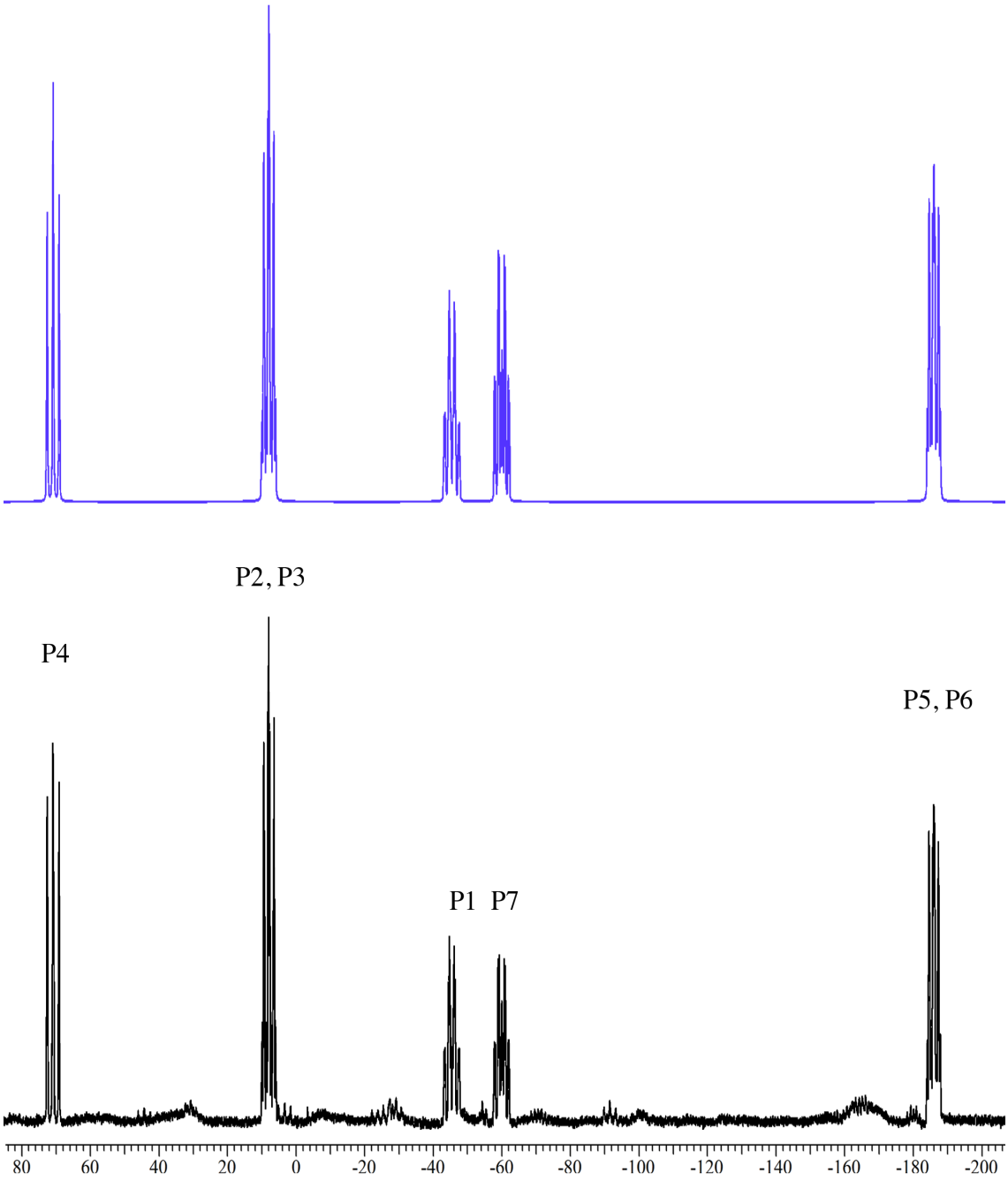

Figure 4.13: Top: simulated $^{31}P\{^{1}H\}$ NMR spectrum of **7**; bottom: recorded $^{31}P\{^{1}H\}$ NMR spectrum of **7** in d_5-pyridine.

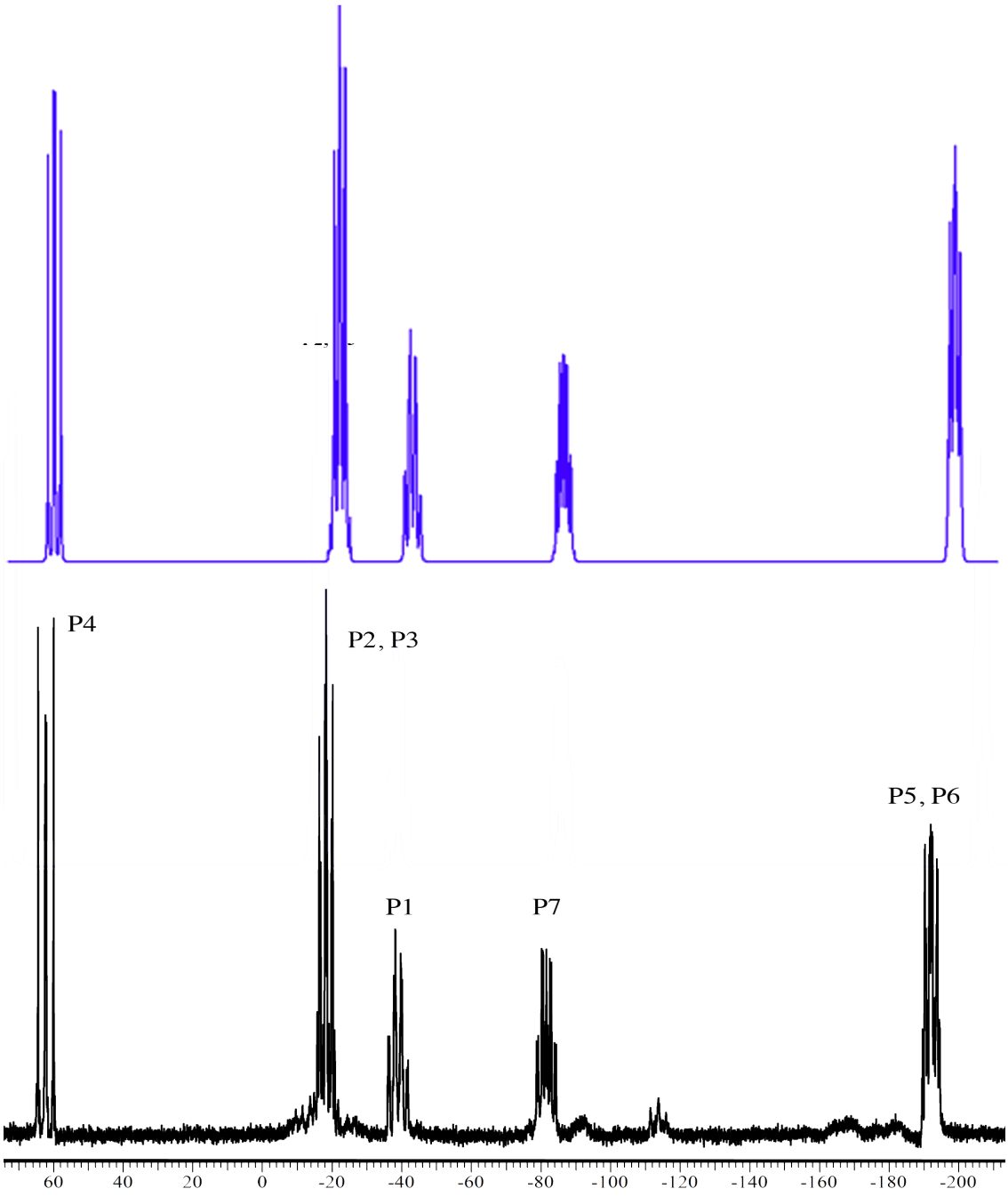

Figure 4.14: Top: simulated $^{31}P\{^{1}H\}$ NMR spectrum of **8**, bottom: recorded $^{31}P\{^{1}H\}$ NMR spectrum of **8** in d_5-pyridine.

Analysis of the resonance assigned to P4 in compound **8**, shows that tin satellites are present, corresponding to a two-bond coupling of the ^{31}P nuclei to $^{119/117}Sn$ nuclei. The coupling constant is 127.1 Hz, which is an appropriate value for a two-bond $^{31}P–^{119}Sn$ coupling (Figure 4.15). Background noise in the spectrum, combined with a large

range of possible one bond $^{31}P–^{119}Sn$ coupling values, means that satellites surrounding the P2, P3 resonance are difficult to identify.

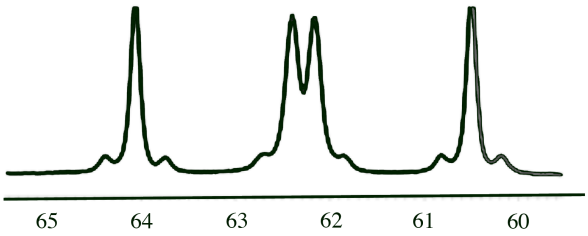

Figure 4.15: $^{31}P\{^{1}H\}$ NMR spectrum of **8** in d_5-pyridine. P4 resonance enlarged to show the tin satellites.

The ^{29}Si NMR spectrum of **7** shows a singlet at δ = –6.9 ppm (Figure 4.16) corresponding to the silicon atoms of the (bis(trimethyl)silyl)amide fragment. When compared to $Ge\{N(SiMe_3)_2\}_2P_6C_4{}^tBu_4$ (where the $[N(SiMe_3)_2]$ groups appear at δ = 6.1 ppm and δ = 5.8 ppm) the silicon atoms of **7** are more shielded, presumably due to the presence of the more electron-rich germanium atom.[25]

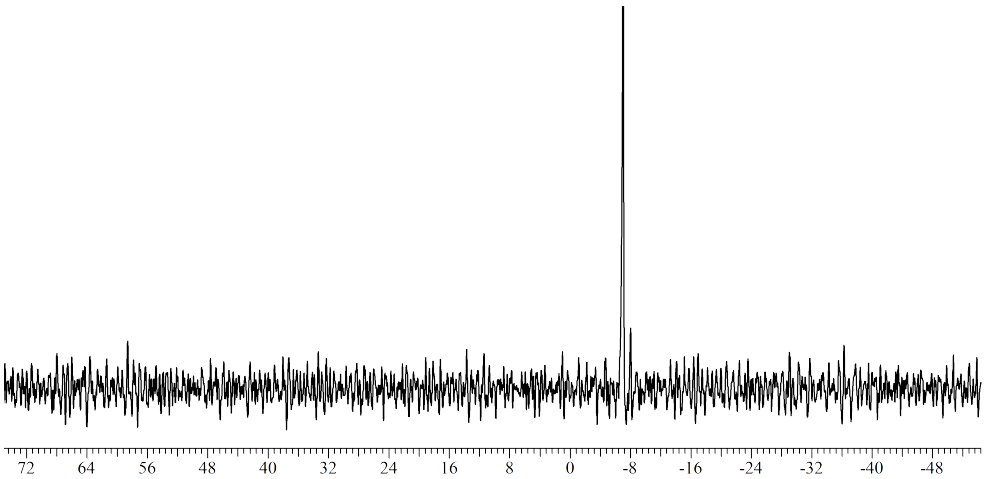

Figure 4.16: The ^{29}Si NMR spectrum of **7** recorded in d_5-pyridine.

The ^{29}Si NMR spectrum of **8** shows a singlet at δ = –7.3 ppm (Figure 4.17), which is more shielded compared to $Sn\{N(SiMe_3)_2\}_2P_6C_4{}^tBu_4$ where the (bis(trimethyl)silyl)amide groups have a chemical shift at δ = 5.4 ppm and δ = 5.2 ppm. When a ^{29}Si NMR spectrum was recorded on the crude reactions mixture, an

additional singlet at δ = –0.6 ppm was observed, corresponding to the free $HN(SiMe_3)_2$ that was generated *in situ* during the reaction. This side product could be easily removed by washing the mixture with diethyl ether or leaving the sample under dynamic vacuum overnight.

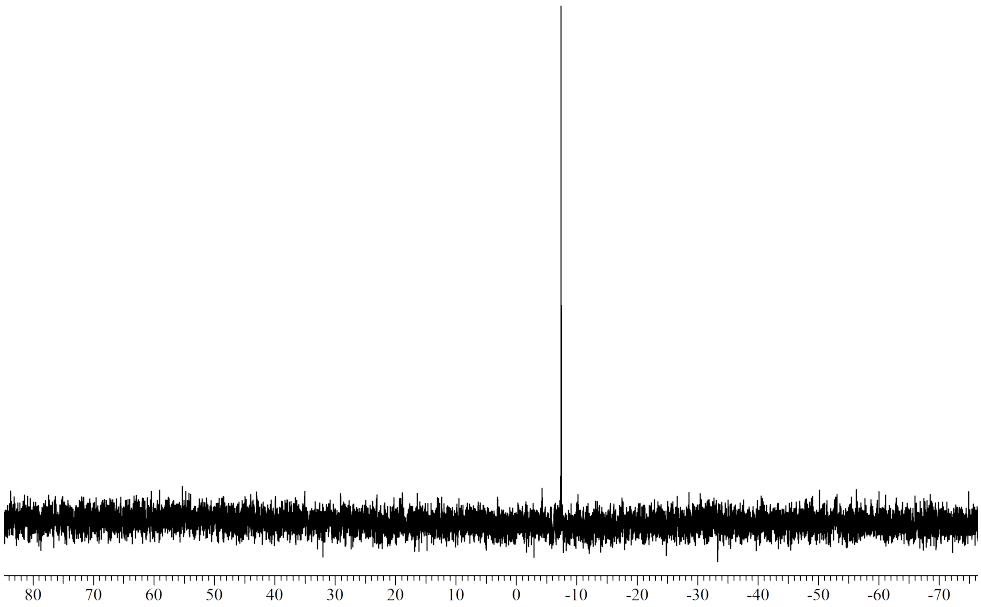

Figure 4.17: The ^{29}Si NMR spectrum of **8** recorded in d_5-pyridine.

Additionally for **8** it was possible to record the ^{119}Sn NMR spectrum. A single broad resonance was present at δ = 61.1 ppm (Figure 4.18), with no resolved multiplet structure. For reference, the starting material, $Sn[N(SiMe_3)_2]_2$, has a resonance at δ = 772 ppm.[28] This decrease in chemical shift is consistent with the increase in electron-density around the tin nucleus in **8**. $Sn\{N(SiMe_3)_2\}_2P_6C_4{}^tBu_4$ has a ^{119}Sn NMR resonance at δ = 130.4 ppm, which compared to **8** is significantly more deshielded.

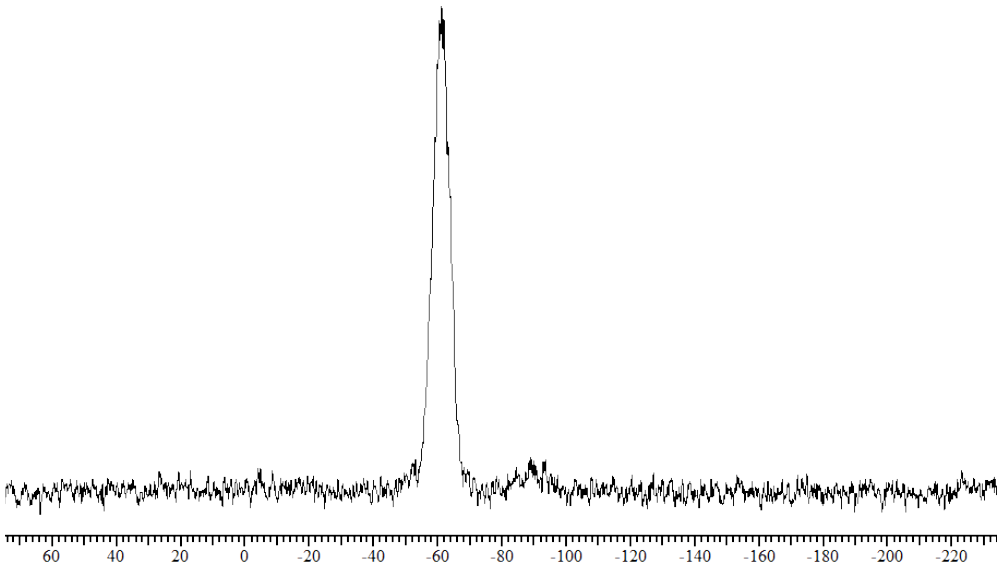

Figure 4.18: The ^{119}Sn NMR spectrum of **8** recorded in d_5-pyridine.

4.3.1.4 Mass spectrometric studies on $[P_7EN(SiMe_3)_2]^{2-}$ (E = Ge (7) and Sn (8))

Negative ion mode electrospray ionisation mass spectra of $[P_7EN(SiMe_3)_2]^{2-}$ confirmed the presence of the products in solution. Fragmentation occurs during the ionisation process and the product resulting from the loss of the amide group is observed as the major mass envelope ($[P_7E]^-$). For **7** peaks corresponding to $[P_7Ge]^-$ at 291.6 Da (100%) and $[P_7GeN(SiMe_3)_2]^-$ at 452.2 Da (43%) were observed (Figure 4.19). For **8** peaks corresponding to $[P_7Sn]^-$ at 337.4 Da (100%) and $[P_7Sn(N(SiMe_3)_2)]^-$ at 495.9 Da (18%) were also observed (Figure 4.20). Additionally, for **8**, in the positive ion mode, $[K(18\text{-crown-}6)]_3[P_7SnN(SiMe_3)_2]^+$ was observed at 1405.9 Da.

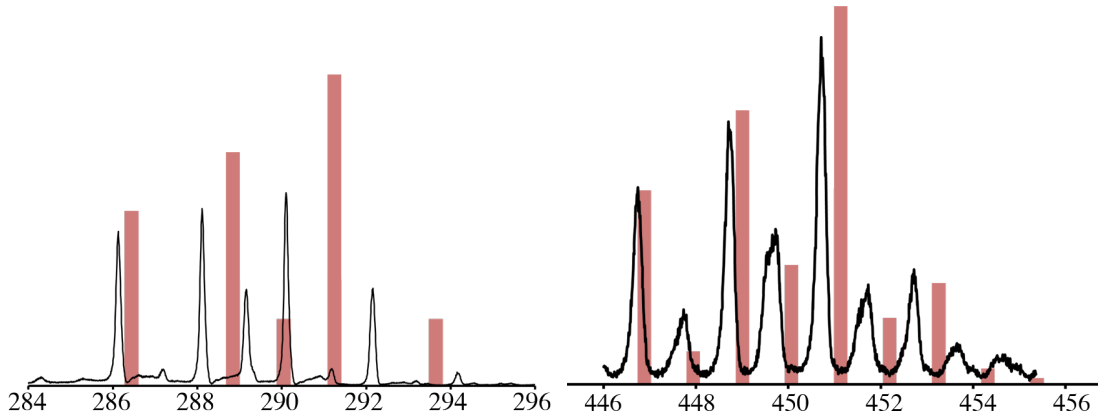

Figure 4.19: ESI-MS mass envelopes recorded in a DMF solution of **7**. $[P_7Ge]^-$ (left) and $[P_7GeN(SiMe_3)_2]^-$ (right). Predicted isotopic distributions are shown in red and observed mass spectrometric data are shown in black.

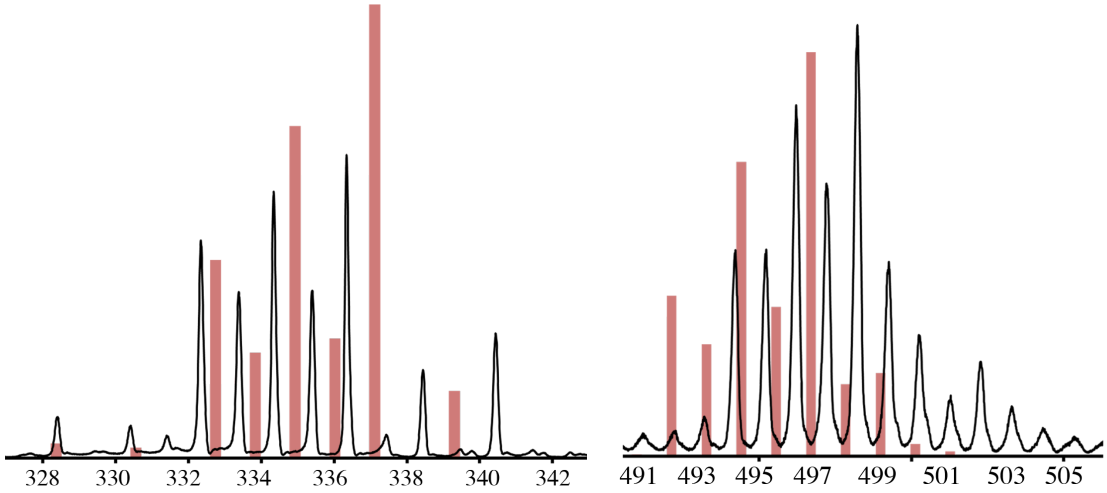

Figure 4.20: ESI-MS mass envelopes recorded in a DMF solution of **8**. $[P_7Sn]^-$ (left) and $[P_7SnN(SiMe_3)_2]^-$ (right). Predicted isotopic distributions are shown in red and observed mass spectrometric data are shown in black.

4.3.1.5 Reactions between $[HP_7]^{2-}$ and $Pb[N(SiMe_3)_2]$

In order to complete this work, the same reaction was studied with the heavier congener $Pb[N(SiMe_3)_2]$ under similar conditions, *i.e.* in a 1:1 ratio in pyridine. The reaction mixture was dark red and ^{31}P NMR spectrum showed five resonances of comparable chemical shift to those of **7** and **8** at 59.7, –17.2, –37.9, –84.5 and –197.47 consistent with the formation of $[P_7PbN(SiMe_3)_2]^{2-}$ (**9**). However, these resonances

were very broad and did not integrate to the expected ratio. ^{1}H, ^{13}C and ^{29}Si NMR spectra showed similar chemical shifts to the ones seen for the **7** and **8** analogues (Section 4.3.1.3). Additionally, mass spectrometric studies showed the presence of $[P_7Pb]^-$, but not the presence of $[P_7PbN(SiMe_3)_2]^-$. These studies also showed the formation of $[P_7(SiMe_3)_2]^-$ as a side product. Despite trying several techniques and solvent combinations, crystals of **9** could not be grown.

DFT calculations were performed on **9**, showing a comparable geometry to **7** and **8** with a pyramidal lead atom and suitable bond lengths and angles. In contrast to **7** and **8**, in **9** the orbital with the most significant lone pair character of the E atom is not the HOMO, but the HOMO–1. This orbital shows only 15.7% lone-pair character and a decreased participation of the more core-like 6s orbital. A Mulliken charge analysis revealed similar results by showing negative charges on the P2, P3, P4 and nitrogen atoms. Continuing the trend observed for the **7** and **8** analogues, **9** has the highest Mulliken charge (0.423), indicating that for **9**, the model of a $[P_7]^{3-}$ cage attached to a $[PbN(SiMe_3)_2]^+$ is more suitable.

4.3.1.6 Reactions between $[HAs_7]^{2-}$ and $E[N(SiMe_3)_2]$ (E = Ge, Sn and Pb)

Analogous reactions using $[HAs_7]^{2-}$ were attempted with partial success. When reacting $[HAs_7]^{2-}$ with $Sn[N(SiMe_3)_2]_2$ or $Pb[N(SiMe_3)_2]_2$ the formation of $[As_7E]^-$ (E = Sn and Pb) was observed in the mass spectra but not $[As_7EN(SiMe_3)_2]^-$. A possible explanation for this is fragmentation within the equipment. However the ^{1}H NMR did not show resonances that compare favourably with those observed for **7** and **8**. When reacting $[HAs_7]^{2-}$ with $Ge[N(SiMe_3)_2]_2$, the mass spectrum did not show the presence

of $[As_7Ge]^-$ unlike the other reactions, instead the formation of $[GeAs_{15}]^-$ was detected, which is analogous to the $[ME'_{15}]^{3-}$ clusters reported by Goicoechea, Sen and Weiss.[1,2] No crystals of any of these products could be obtained and, since mass spectrometry is insufficient evidence to establish the formation of a product, these results were inconclusive.

4.3.1.7 Transformation of 7 to $[(P_7)_2Ge_2N(SiMe_3)_2]^{3-}$ (10)

4.3.1.8 Synthesis of $[(P_7)_2Ge_2N(SiMe_3)_2]^{3-}$ (10)

When we first studied the reactivity of $[K(18\text{-crown-6})]_2[HP_7]$ towards $Ge[N(SiMe_3)_2]_2$, the ^{31}P NMR spectra obtained did not appear to be reproducible. It was subsequently discovered that the product that is first formed in the reaction, **7**, quickly transforms into a second thermodynamic product at room temperature $[(P_7)_2Ge_2N(SiMe_3)_2]^{3-}$ (**10**). This species results from the loss of an amide group as $[K(18\text{-crown-6})][N(SiMe_3)_2]$ (Scheme 4.2).

The reaction requires a total of 94 hours to be completed at room temperature, or it can be accelerated with mild heating (35 ºC) to reach completion in only 30 hours. After the reaction had reached completion, all volatiles were removed under vacuum and the resulting orange oil was washed with diethyl ether to remove the $[K(18\text{-crown-6})][N(SiMe_3)_2]$ that was generated, resulting in an orange powder which was characterised as **10**.

For crystallisation purposes, this reaction was carried out using the alternative $[HP_7]^{2-}$ precursor $[K(15\text{-crown-5})_2]_2[HP_7]$ as opposed to the $[K(18\text{-crown-6})]^+$ salt. Crystals

suitable for X-ray crystallography were grown by slow diffusion of diethyl ether into a concentrated pyridine solution of **10**. The crystalline yield was very high (94%).

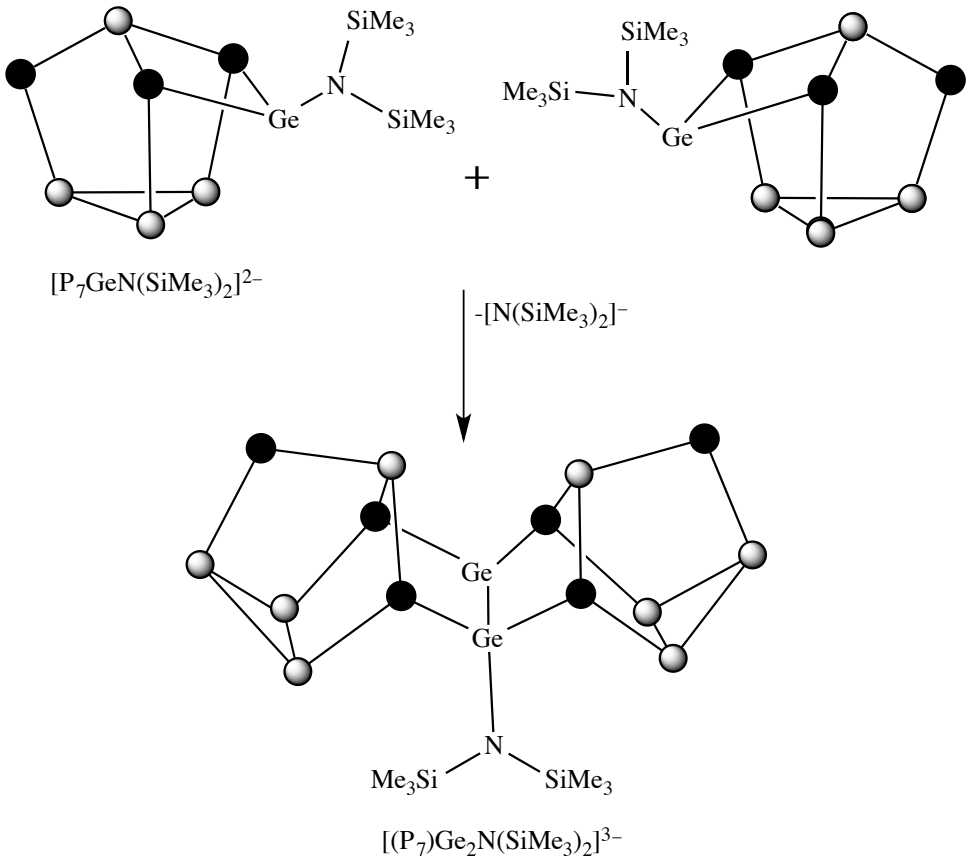

Scheme 4.2: Formation of **10**.

4.3.1.9 Structure of $[(P_7)_2Ge_2N(SiMe_3)_2]^{3-}$ (10)

The crystal structure exhibits heavy disorder of the counter cations $[K(15\text{-crown-}5)_2]^+$ and therefore a detailed bond metric analysis cannot be made. The structure of the anion can be assigned unequivocally and was confirmed by spectroscopic methods that will be discussed shortly.

10 consists of two nortricyclane-like $[P_7]^{3-}$ cages bridged by a $[Ge–GeN(SiMe_3)_2]^{3+}$ fragment (Figure 4.21). Each germanium atom bonds to one of the formally negatively charged phosphorus atoms from two different $[P_7]^{3-}$ cages and to the

second germanium atom. In addition, one of the two germanium atoms has an amide group attached to it. The structure exhibits a similar arrangement to $[P_{16}]^{2-}$ in which both of the bridging phosphorus atoms have been replaced by germanium atoms. One of them is three-connected and has a negative charge, whilst the second remains bound to an amide group and has no negative charge. The overall charge of the molecule is therefore 3–.

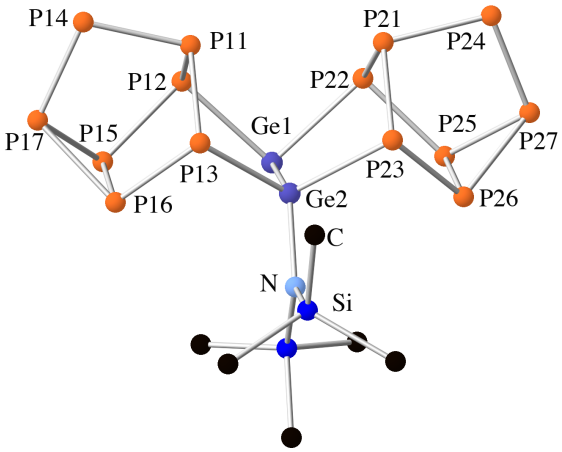

Figure 4.21: Ball and Stick diagram of **10**.

The thermodynamic instability of **7** in solution was probed using DFT computational methods. The decomposition of two molecules of **7** to give rise to **10** and one equivalent of bis(trimethylsilyl)amide, $[N(SiMe_3)_2]^-$, was found to be thermodynamically favourable by 20.43 kJ mol^{-1}. This value is the result of arithmetically combining the computed total bonding energies obtained for the optimised structures of the systems in question (*i.e.* 2(–17984.07) – (–22217.17–13771.40) = 20.43 kJ mol^{-1}). By contrast, recombination of two molecules of **8** to afford the unobserved compound $[(P_7Sn_2)_2N(SiMe_3)_2]^{3-}$ and $[N(SiMe_3)_2]^-$ is thermodynamically uphill by 27.5 kJ mol^{-1}. These values are consistent with the

observation that **7** readily affords **10** over time, whereas solutions of **8** are indefinitely stable.

The two $[P_7]^{3-}$ cages, as the $[P_{16}]^{2-}$ cluster, are in an "up-up" configuration. Each one of the cages acts as a two-electron donor towards each germanium atom; they donate four electrons in total, giving each germanium atom an eight valence electron count. Other relevant compounds are the previously mentioned $[MP_{15}]^{3-}$ (M = Sn, Pb and Hg) species in which only one of the bridging phosphorus atoms of the $[P_{16}]^{2-}$ cage has been exchanged by an alternative element.[1,2]

The germanium atom attached to the amide, Ge2, has a distorted tetrahedral structure and Ge1 has a distorted trigonal pyramidal geometry with a stereogenic lone pair pointing away from the cage.

The Ge1–Ge2 distance is abnormally short at 2.499(1) Å. A CSD search gives a mean value for a Ge–Ge single bond of 2.698 (av) Å.[29] This means that there is possibly some multiple bond character, since there is no reason for the two germanium atoms to be pushed together for steric purposes. This observation could, however, also arise due to the poor quality of the crystal structure. A similar Ge–Ge bond length is observed in $[Ge_8\{N(SiMe_3)_2\}_6]$ (2.499(1) to 2.672(1) Å).[30] The $[Ge_8\{N(SiMe_3)_2\}_6]$ molecule features a $[Ge–GeNSi(Me_3)_2]$ fragment with a bond length of 2.4987(6) Å which is very similar to the one observed in **10**.

The structure determined by X-ray crystallography was computed using DFT methods converging to give a stable trianionic species which is in good agreement with the X-ray data obtained.

4.3.1.10 NMR spectroscopic studies on $[(P_7)_2Ge_2N(SiMe_3)_2]^{3-}$ (10)

The transformation from **7** to **10** was monitored by ^{31}P NMR spectroscopy over time. After one hour a significant amount of **10** had been formed, and total completion of the transformation happens after approximately three days (Figure 4.22).

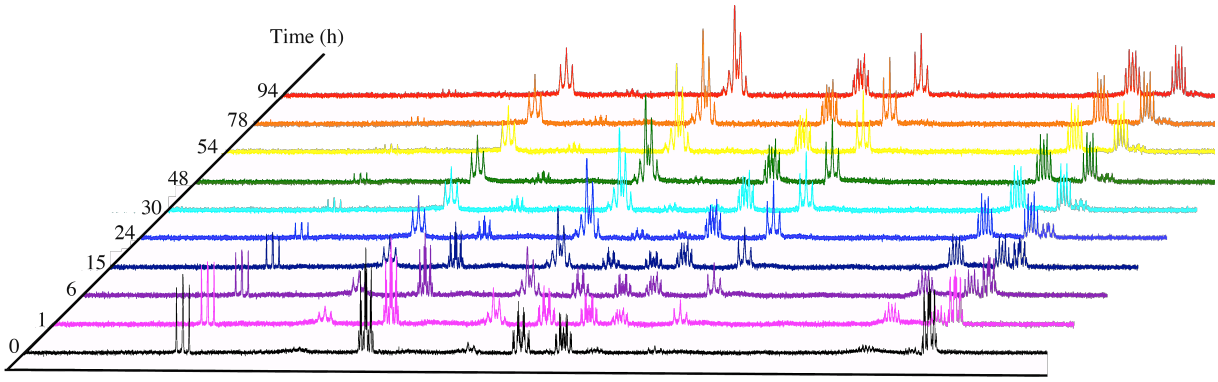

Figure 4.22: ^{31}P NMR spectra. Conversion from **7** to **10** over time.

The $^{31}P\{^1H\}$ NMR spectrum of **10** shows seven resonances, two of which overlap significantly (Figure 4.24). Resonances were found at δ = –25.8, 33.0, –27.6, –91.4, –165.9, –182.1 and –70.7 ppm correspongin to P1, P2, P3, P4, P5, P6 and P7, respectively. ^{31}P NMR resonances were assigned with the aid of a ^{31}P–^{31}P COSY (Figure 4.23). A simulation was carried out by Dr. Nick Rees for **10** (Figure 4.24) in order to obtain the ^{31}P–^{31}P coupling constants (Table 4.4).

δ(ppm)		–25.8	33.0	–27.6	–91.4	–165.9	–182.1	–70.7
		P1	***P2***	***P3***	***P4***	***P5***	***P6***	***P7***
–25.8	***P1***		–388.2 [–271.7]	–257.4 [–268.1]	–348.0 [–282.9]	31.8 [44.4]	31.8 [24.3]	71 [95.4]
33.9	***P2***	–388.2 [–271.7]		18 [5.1]	16 [–12.6]	–372.7 [–305.7]	8 [1.3]	6 [–14.0]
–27.6	***P3***	–257.4 [–268.1]	18 [5.1]		16 [–11.0]	8 [1.0]	–372.7 [–306.3]	6 [–15.1]
–91.4	***P4***	–348.0 [–282.9]	16 [–12.6]	16 [–11.0]		10 [7.2]	10 [7.7]	–368.7 [–238.7]
–165.9	***P5***	31.8 [44.4]	–372.7 [–305.7]	8 [1.0]	10 [7.2]		–187.0 [–140.6]	–218.1 [–154.9]
–182.1	***P6***	31.81 [24.3]	8 [1.3]	–372.7 [–306.3]	10 [7.7]	–187.0 [–140.6]		–200.4 [–172.9]
–70.7	***P7***	71 [95.4]	6 [–14.0]	6 [–15.1]	–368.7 [–238.7]	–218.1 [–154.9]	–200.4 [–172.9]	

Table 4.4: ^{31}P–^{31}P NMR coupling constants in Hz taken from the $^{31}P\{^{1}H\}$ NMR spectrum of **10**. Computed values in square brackets.

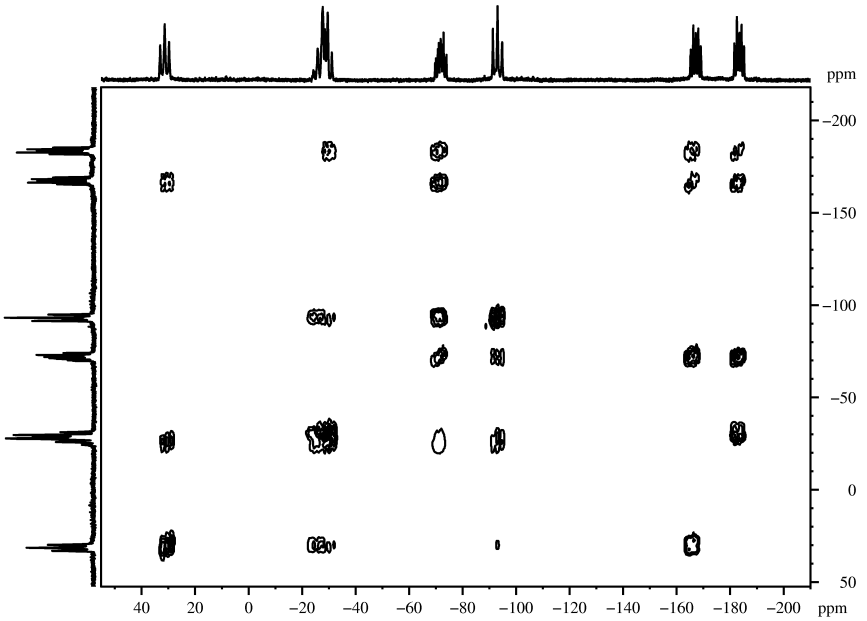

Figure 4.23: ^{31}P–^{31}P COSY spectrum for **10** recorded in d_5-pyridine.

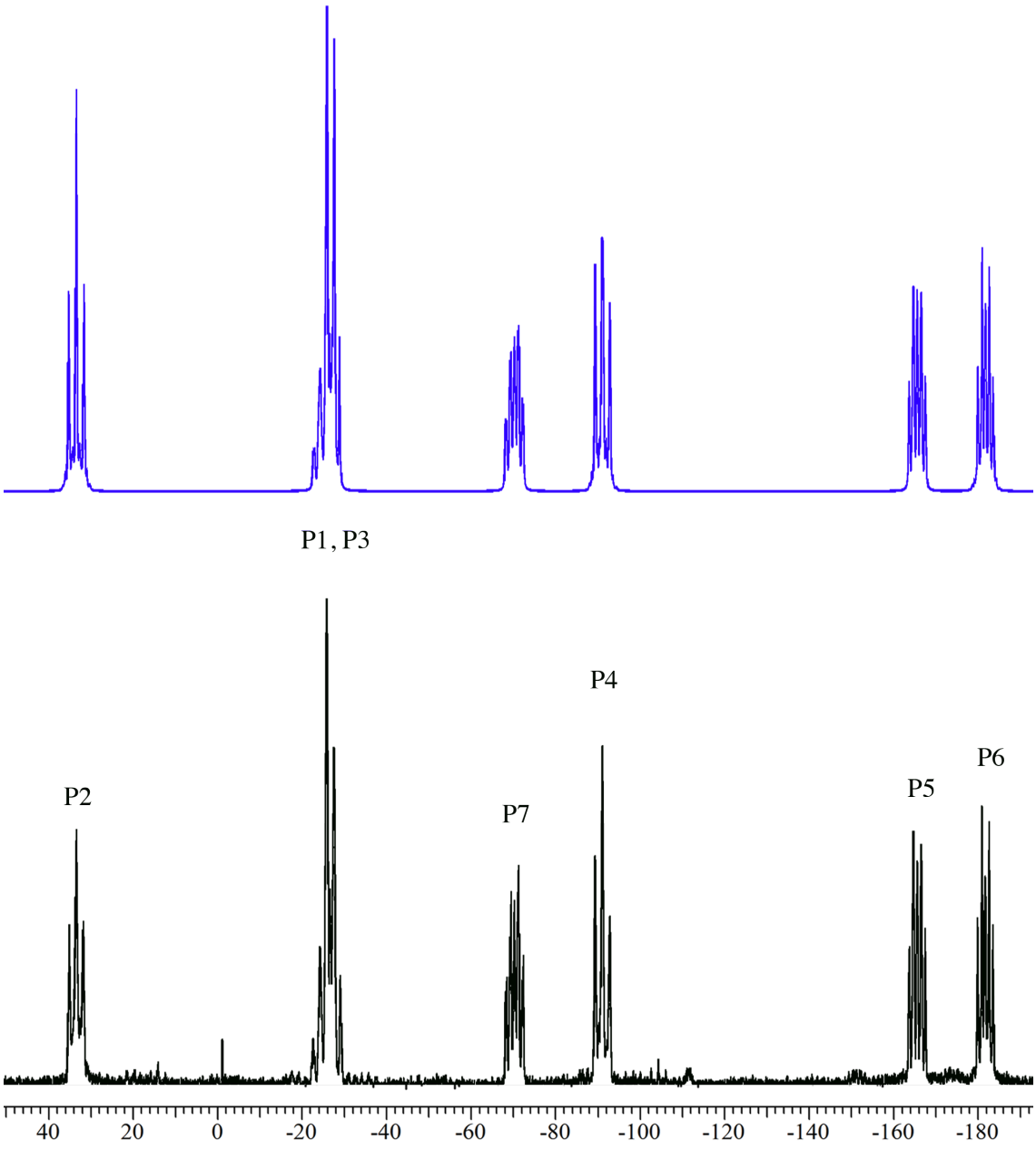

Figure 4.24: Top: simulated $^{31}P\{^{1}H\}$ NMR spectrum of **10**, bottom: recorded $^{31}P\{^{1}H\}$ NMR spectrum of **10** in d_5-pyridine.

The ^{29}Si NMR of **10** shows a singlet at δ = 2.5 ppm corresponding to the silicon atom of the bis(trimethylsilyl)amide fragment attached to the cluster (Figure 4.25). Additionally, the side product $K[N(SiMe_3)_2]$ was observed in the ^{29}Si NMR spectra at –0.8 ppm. Compared to **7** where the $N(SiMe_3)_2$ fragment appears at –6.98 ppm, **10** shows a more deshielded resonance.

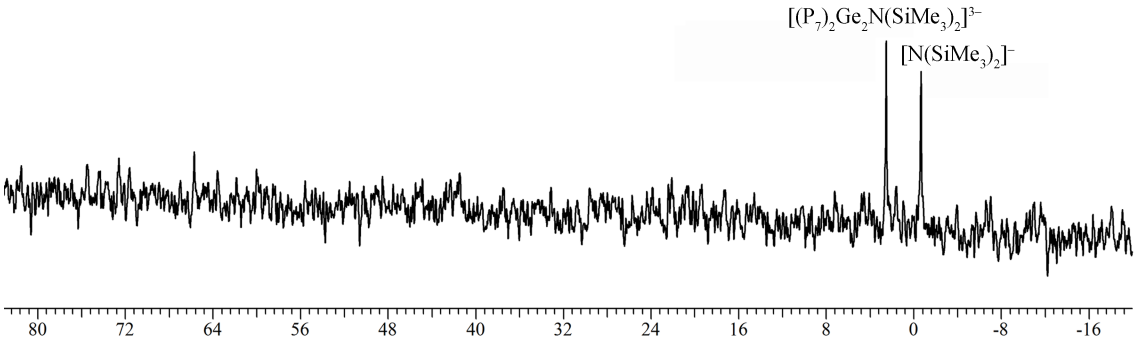

Figure 4.25: The ^{29}Si NMR spectrum of **10** recorded in d_5-pyridine.

4.3.1.11 Mass spectrometric studies on $[(P_7)_2Ge_2N(SiMe_3)_2]^{3-}$ (10)

Negative and positive mode electrospray ionisation mass spectrum of **10** confirmed that the product had been formed. $[(P_7)_2Ge_2N(SiMe_3)_2]^-$ is observed at 741.3 Da (70%) (Figure 4.26). In addition, $[P_7Ge]^-$ is also observed at 291.6 Da (99%) as is the product where both $N(SiMe_3)_2$ groups are lost ($[(P_7)_2Ge_2]^-$ at 579.7 Da (12%)). The phosphorus analogue of $[EP_{15}]^-$ (E = Sn and Pb) compounds, namely $[GeP_{15}]^-$ (545.3 Da (69%)) was also observed in the negative mode.[1]

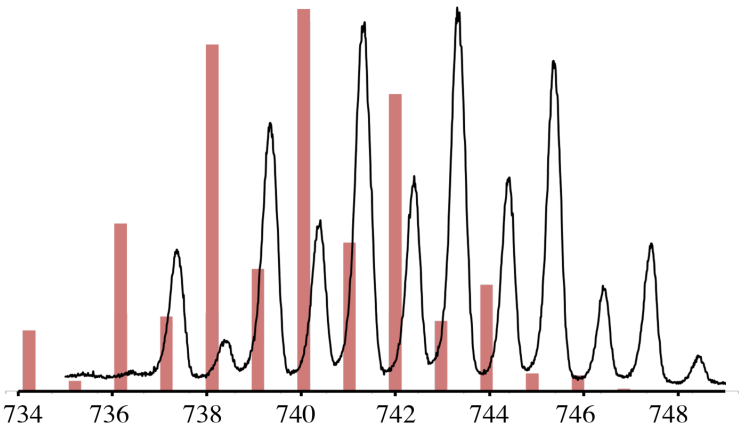

Figure 4.26: ESI-MS mass envelopes recorded in a DMF solution of $[(P_7)_2Ge_2N(SiMe_3)_2]^-$. Predicted isotopic distributions are shown in red and observed mass spectrometric data are shown in black.

When 18-crown-6 is employed as sequestering agent, a peak in the positive mode was observed at 1953.2 Da corresponding to $\{[K(18\text{-crown-}6)]_4[(P_7)_2Ge_2N(SiMe_3)_2]\}^+$, confirming the 3– charge.

4.4 Conclusions

This chapter detailed the synthesis and characterisation of three novel compounds. The reaction of $[HP_7]^{2-}$ with $E[N(SiMe_3)_2]_2$ in pyridine led to the formation of two η^2 (or κ^2) coordination compounds $[P_7EN(SiMe_3)_2]^{2-}$ (E = Ge (**7**) and Sn (**8**)). These products were characterised by ^{31}P, ^{1}H, ^{13}C and ^{29}Si NMR spectroscopy, mass spectrometry and single crystal X-ray diffraction. Furthermore, ^{119}Sn NMR spectroscopic data and an elemental analysis were obtained for **8**.

7 quickly transforms into a thermodynamic product $[(P_7)_2Ge_2N(SiMe_3)_2]^{3-}$ (**10**). This novel cluster was characterised by ^{31}P, ^{1}H, ^{29}Si, ^{13}C NMR spectroscopy, mass spectrometry, single crystal X-ray crystallography and elemental analysis. Heavy disorder in the counter cations in the crystal structure made it impossible to obtain a publishable structure, but allowed us to determine the structure and connectivity of the cluster and its overall charge.

4.5 References

(1) Knapp, C. M.; Large, J. S.; Rees, N. H.; Goicoechea, J. M. *Dalton Trans*. **2010**, *40* (3), 735–745.

(2) Mandal, S.; Reber, A. C.; Qian, M.; Liu, R.; Saavedra, H. M.; Sen, S.; Weiss, P. S.; Khanna, S. N.; Sen, A. *Dalton Trans*. **2012**, *41* (40), 12365–12377.

(3) Fritz, G.; Hoppe, K. D.; Hönle, W.; Weber, D.; Mujica, C.; Manriquez, V.; Schnering, H. G. *J. Organomet. Chem*. **1983**, *249* (1), 63–80.

(4) Fritz, G.; Schneider, H.-W. *Z. Anorg. Allg. Chem.* **1990**, *584* (1), 12–20.

(5) Von Schnering, H. G.; Fenske, D.; Hönle, W.; Binnewies, M.; Peters, K. *Angew. Chem. Int. Ed. Engl.* **1979**, *18* (9), 679–679.

(6) Ahlrichs, R.; Fenske, D.; Fromm, K.; Krautscheid, H.; Krautscheid, U.; Treutler, O. *Chem. Eur. J.* **1996**, *2* (2), 238–244.

(7) Charles, S.; Fettinger, J. C.; Bott, S. G.; Eichhorn, B. W. *J. Am. Chem. Soc.* **1996**, *118* (19), 4713–4714.

(8) Kesanli, B.; Charles, S.; Lam, Y.-F.; Bott, S. G.; Fettinger, J.; Eichhorn, B. W. *J. Am. Chem. Soc.* **2000**, *122* (45), 11101–11107.

(9) Knapp, C.; Zhou, B.; Denning, M. S.; Rees, N. H.; Goicoechea, J. M. *Dalton Trans.* **2009**, *39* (2), 426–436.

(10) Qian, M.; Reber, A. C.; Ugrinov, A.; Chaki, N. K.; Mandal, S.; Saavedra, H. M.; Khanna, S. N.; Sen, A.; Weiss, P. S. *ACS Nano* **2009**, *4* (1), 235–240.

(11) Rios, D.; Gillett-Kunnath, M. M.; Taylor, J. D.; Oliver, A. G.; Sevov, S. C. *Inorg. Chem.* **2011**, *50* (6), 2373–2377.

(12) Knapp, C. M.; Jackson, C. S.; Large, J. S.; Thompson, A. L.; Goicoechea, J. M. *Inorg. Chem.* **2011**, *50* (9), 4021–4028.

(13) Chaki, N. K.; Mandal, S.; Reber, A. C.; Qian, M.; Saavedra, H. M.; Weiss, P. S.; Khanna, S. N.; Sen, A. *ACS Nano* **2010**, *4* (10), 5813–5818.

(14) Moses, M. J.; Fettinger, J.; Eichhorn, B. W. *J. Am. Chem. Soc.* **2002**, *124* (21), 5944–5945.

(15) Eichhorn, B. W.; Haushalter, R. C.; Huffman, J. C. *Angew. Chem. Int. Ed. Engl.* **1989**, *28* (8), 1032–1033.

(16) Charles, S.; Eichhorn, B. W.; Rheingold, A. L.; Bott, S. G. *J. Am. Chem. Soc.* **1994**, *116* (18), 8077–8086.

(17) Bolle, U.; Tremel, W. *J. Chem. Soc. Chem. Commun.* **1994**, No. 2, 217–219.

(18) Charles, S.; Danis, J. A.; Mattamana, S. P.; Fettinger, J. C.; Eichhorn, B. W. *Z. Anorg. Allg. Chem.* **1998**, *624* (5), 823–829.

(19) Charles, S.; Fettinger, J. C.; Eichhron, B. W. *J. Am. Chem. Soc.* **1995**, *117* (19), 5303–5311.

(20) Charles, S.; Danis, J. A.; Fettinger, J. C.; Eichhorn, B. W. *Inorg. Chem.* **1997**, *36* (17), 3772–3778.

(21) Kesanli, B.; Mattamana, S. P.; Danis, J.; Eichhorn, B. W. *Inorg. Chim. Acta* **2005**, *358* (11), 3145–3151.

(22) Charles, S.; Fettinger, J. C.; Eichhorn, B. W. *Inorg. Chem.* **1996**, *35* (6), 1540–1548.

(23) Knapp, C. M.; Large, J. S.; Rees, N. H.; Goicoechea, J. M. *Chem. Commun.* **2011**, *47* (14), 4111–4113.

(24) For 290 crystallographically characterised complexes containing a P–Ge single bond (CSD version 5.36, November 2014): d(min) = 2.234; d(max) = 3.196; d(mean) = 2.414; var(d) = 0.012; std. dev. = 0.111; mean dev. = 0.067;

(25) Al-Ktaifani, M. M.; Hitchcock, P. B.; Lappert, M. F.; Nixon, J. F.; Uiterweerd, P. *Dalton Trans.* **2008**, No. 21, 2825–2831.

(26) Pyykkö, P.; Atsumi, M. *Chem. Eur. J.* **2009**, *15* (1), 186–197.

(27) For 645 crystallographically characterised complexes containing a P–Sn single bond (CSD version 5.36, November 2014): d(min) = 2.406; d(max) = 3.079; d(mean) = 2.625; var(d) = 0.009; std. dev. = 0.095; mean dev. = 0.066;

(28) Kravchyk, K.; Protesescu, L.; Bodnarchuk, M. I.; Krumeich, F.; Yarema, M.; Walter, M.; Guntlin, C.; Kovalenko, M. V. *J. Am. Chem. Soc.* **2013**, *135* (11), 4199–4202.

(29) For 3746 crystallographically characterised complexes containing a Ge–Ge single bond (CSD version 5.36, November 2014): d(min) = 2.052; d(max) = 3.435; d(mean) = 2.605; var(d) = 0.013; std. dev. = 0.116; mean dev. = 0.084;

(30) Schnepf, A.; Köppe, R. *Angew. Chem. Int. Ed.* **2003**, *42* (8), 911–913.

Chapter 5 Transition metal mediated activation of group 15 $[E'_7]^{3-}$ clusters

5.1 Summary

This chapter will focus on the metal mediated activation of group 15 clusters. In particular, the reactivity of the $[E'_7]^{3-}$ (E = P and As) group 15 cages towards varying stochiometric amounts of VCp_2 will be discussed. It was found that addition of 2.5 equivalents of VCp_2 yields the triple-decker species $[(CpV)_2(\eta^x\text{-}E'_x)]^-$ (E' = P: x = 6; E' = As: x = 5). When a lower loading of VCp_2 was used (0.7 equivalents) the sandwich compounds $[(CpV)(\eta^5\text{-}E'_5)]^{n-}$ (E' = P: n = 1; E' = As: n = 1 and 2) were formed. All species have been characterised by X-ray crystallography, mass spectrometry, cyclic voltammetry and EPR spectroscopy, when relevant.

5.2 Introduction

This introduction will survey the metal mediated activation of the $[E'_7]^{3-}$ (E = P, As and Sb) clusters, as well as the synthesis of $[E'_5]^-$ and $[E'_6]$ rings in sandwich and triple-decker complexes by alternative methods.

Cluster activation is the least common type of reactivity for group 15 clusters. $[Sb_7]^{3-}$ clusters tend to fragment more readily when reacted with a metal complex than

$[As_7]^{3-}$, and to date there is only one example in the literature where cluster fragmentation of the $[P_7]^{3-}$ cage occurs. This is consistent with the fact that the Sb–Sb (121 kJ/mol) bond dissociation energy is lower than for As–As (146 kJ/mol) and P–P (201 kJ/mol).[1]

The first activation compound of a $[E'_7]^{3-}$ cage was synthesised unexpectedly when Von Schnering was attempting to synthesise Rb_3As_7 as a solid-state reaction in niobium tubes and crystallised the $[NbAs_8]^{3-}$ anion instead (Figure 5.1).[2] After this, a series of compounds based on the latter were synthesised, such as $[ME'_8]^{n-}$ (E' = As: M = Mo: n = 2; E' = As: M = Cr and Nb: n = 3; E' = Sb: M = Mo, and Nb: n = 3).[3–5]

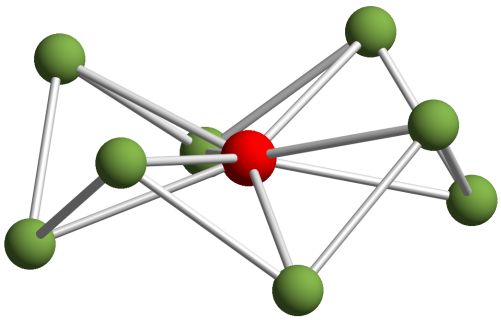

Figure 5.1: Ball and stick diagram of $[NbAs_8]^{3-}$ (The Nb atom is shown in red and As atoms in green).

The reaction of $[Ni(CO)_2(PPh_3)_2]$ and $[Sb_7]^{3-}$ yielded the activation compound $[Sb_7Ni_3(CO)_3]^{3-}$.[6] Similarly, in 2003, Eichhorn and co-workers published the synthesis of a very large cluster anion $[As@Ni_{12}@As_{20}]^{3-}$ (Figure 5.2 left) which was formed by reacting $[As_7]^{3-}$ with $Ni(COD)_2$.[7] The reaction between the $[As_7]^{3-}$ Zintl ion and the palladium (0) reagent, $Pd(Cy_3)_2$, yields the simpler $[Pd_2(As_7)_2]^{4-}$ anion and the activation product $[Pd_7As_{16}]^{4-}$ (Figure 5.2 right).[8]

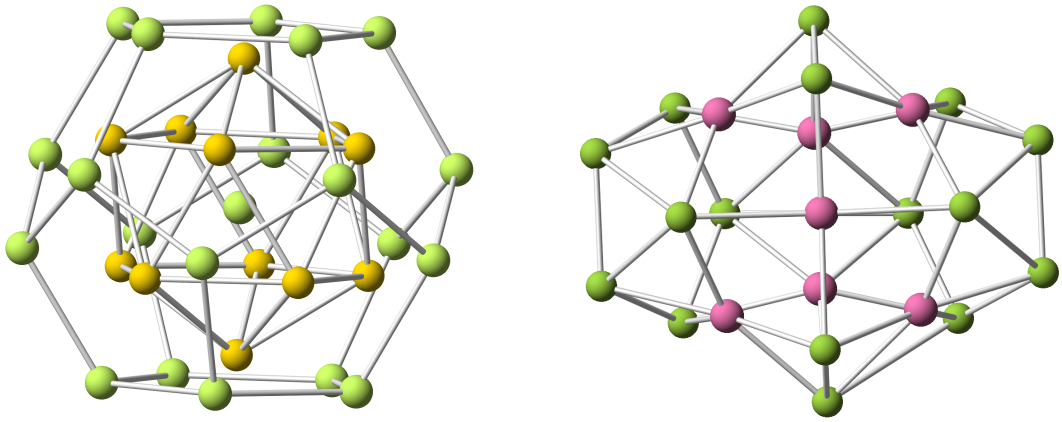

Figure 5.2: Ball and stick diagram of $[As@Ni_{12}@As_{20}]^{3-}$ (left) and $[Pd_7As_{16}]^{4-}$ (right) (As atoms are shown in green, Pd atoms in pink and Ni atoms in yellow).

Up until 2012 there were no known examples of an activated $[P_7]^{3-}$ cage. The Goicoechea group studied the reactions between $[E'_7]^{3-}$ (E' = P and As) and $Co(mes)_2(PEt_2Ph)_2$, showing that the products for the two reactions are different, but both are activation compounds with a total number of seven pnictogen atoms in the structure.

For the reaction involving $[P_7]^{3-}$, the product formed was $[Co(\eta^5\text{-}P_5)\{\eta^2\text{-}P_2H(mes)\}]^{2-}$ (Figure 5.3 left).[9] The product features a *cyclo*-$[\eta^5\text{-}P_5]^-$ ring coordinated in an η^5 fashion to a cobalt atom, and a (mes)P=PH fragment coordinated to the cobalt atom through both of the phosphorus atoms. In the analogous reaction involving the heavier arsenic cage, the activation product formed was $[Co(\eta^3\text{-}As_3)\{\eta^4\text{-}As_4(mes)_2\}]^{2-}$ (Figure 5.3 right). X-ray crystallography studies revealed the formation of a new ligand $[As_4(mes)_2]^{2-}$ (1,4-diaryltetraarsenabutadienediide) along with the previously reported *cyclo*-$[As_3]$ ring.

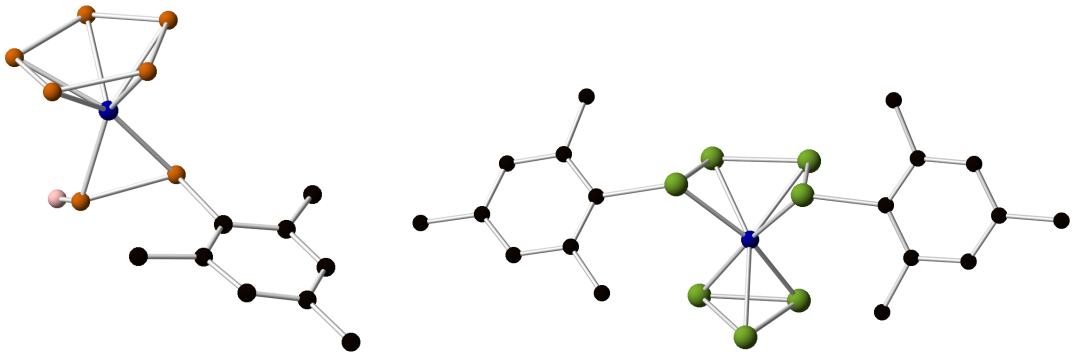

Figure 5.3: Ball and stick diagram of $[Co(\eta^3\text{-}As_3)\{\eta^4\text{-}As_4(mes)_2\}]^{2-}$ (left) and $[Co(\eta^5\text{-}P_5)\{\eta^2\text{-}HP_2(mes)\}]^{2-}$ (right) (P atoms are shown in orange, Co atoms in blue, As atoms in green, the H atom in pink and C atoms in black). H atoms in the mes groups are omitted for clarity.

5.2.1 Cyclic $[E'_5]^-$ and $[E'_6]$ ligands

There have been several sandwich and triple-decker complexes reported containing *cyclo*-$[E'_5]^-$ or $[E'_6]$ rings. Most of these have been synthesised from the activation of E'_4 (E' = P and As) with metal complexes of a variety of transition metals such as iron, molybdenum, chromium, titanium, tungsten, niobium, manganese or vanadium.

5.2.1.1 $[E'_5]^-$ ligands

5.2.1.1.1 $[E'_5]^-$ sandwich compounds

White phosphorus can react at high temperatures with group 8 organometallic compounds such as $[(\eta^5\text{-}C_5Me_4R)Fe(CO)_2]_2$ or $[(\eta^5\text{-}C_5Me_4R)Ru(CO)_2Br]$ to form sandwich complexes of the form $[(\eta^5\text{-}C_5Me_4R)M(\eta^5\text{-}P_5)]$ (M = Fe and Ru: R = Me and Et) (Figure 5.4).[10,11] These complexes can be considered as phosphorus analogues of ferrocene, in which a $[Cp]^-$ group has been replaced with the isolobal $[\eta^5\text{-}P_5]^-$ ring. $[(\eta^5\text{-}C_5Me_4R)M(\eta^5\text{-}P_5)]$ sandwich complexes have co-planar rings, which adopt a staggered conformation.

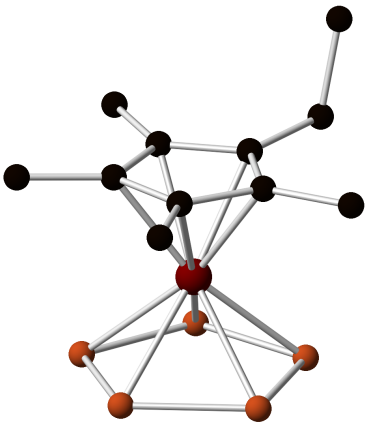

Figure 5.4: Ball and stick diagram of [(η^5-P_5)Fe(η^5-C_5Me_4Et)] (P atoms are shown in orange, the Fe atom in red and C atoms in black). H atoms are omitted for clarity.

In 1989, Scherer investigated the further reactivity of [(η^5-P_5)FeCp*]. By reacting the latter with two equivalents of [$Cr(CO)_5(THF)$] the heterobimetallic complex [Cp*Fe{(η^5-P_5)[$Cr(CO)_5]_2$}] was formed.[12]

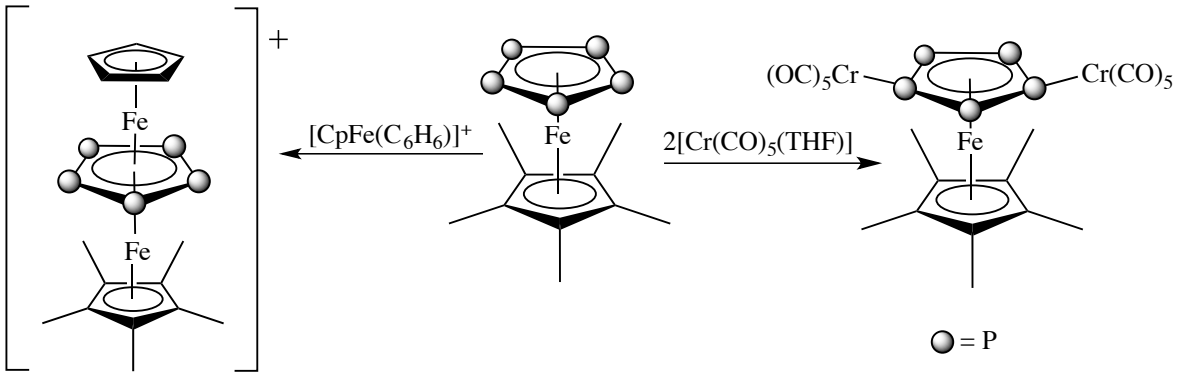

Scheme 5.1: Further reactivity of [(η^5-P_5)FeCp*].

A similar reaction performed with n equivalents of [$CpMn(CO)_2(THF)$] yielded [Cp*Fe{(η^5-P_5)[$MnCp(CO)_2]_n$}] (n = 1–4). Finally, the 30 valence electron triple-decker complex [Cp*Fe(η^5-P_5)FeCp]$^+$ was prepared by the UV irradiation of the reaction mixture of [(η^5-P_5)FeCp*] with [$CpFe(C_6H_6)$][PF_6] (Scheme 5.1). A more extensive discussion of the formation and structural properties of triple-decker complexes will be given in the Section 5.2.1.1.2 .

The related $[As_5]^-$ sandwich compound $[(C_5Me_4R)Fe(\eta^5\text{-}As_5)]$ (R = Me and Et) and triple-decker $[Cp^*Fe(\eta^5\text{-}As_5)FeCp]^+$ can be prepared by similar reactions using As_4 instead.[13]

Further reactivity of $[Cp^*Fe(\eta^5\text{-}P_5)]$ has been extensively studied where this sandwich complex has been used as a building block for 1D and 2D polymers. Spherical molecular aggregates, showing pronounced host-guest interactions have also been prepared.[14–16]

The last $[P_5]^-$ complex that will be discussed in this section is the purely inorganic sandwich complex $[(\eta^5\text{-}P_5)_2Ti]^{2-}$.[17] Schleyer *et al*. prepared $[(\eta^5\text{-}P_5)_2Ti]^{2-}$ (Figure 5.5) in 2002 by reacting white phosphorus at room temperature with a highly reduced titanium complex.

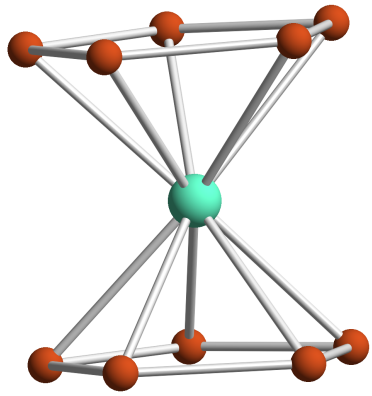

Figure 5.5: Ball and stick diagram of $[(\eta^5\text{-}P_5)_2Ti]^{2-}$ (P atoms are shown in orange and the Ti atom in green).

$[(\eta^5\text{-}P_5)_2Ti]^{2-}$ consists of two parallel and planar $[P_5]^-$ rings symmetrically positioned in a staggered conformation coordinated to a titanium centre. $[(\eta^5\text{-}P_5)_2Ti]^{2-}$ is a 16 valence electron complex with a formally zero-valent titanium centre. Rather remarkably, $[(\eta^5\text{-}P_5)_2Ti]^{2-}$ is highly stable towards heat and air.

5.2.1.1.2 $[E'_5]^-$ triple-decker compounds

In 1986, Scherer and co-workers reported the first example of a $[P_5]^-$ triple-decker $[(Cp^*Cr)_2(\eta^5\text{-}P_5)]$ (Figure 5.6). It was prepared by reacting $[(Cp^*(CO)_3Cr)_2]$ with white phosphorus in xylene at 140 ºC.[10] $[Cp^*Cr(CO)_2(\eta^3\text{-}P_3)]$ was observed as a side product. This neutral triple-decker complex features two [Cp*Cr] fragments that coordinate to a $[P_5]^-$ ligand, each in an η^5 fashion.

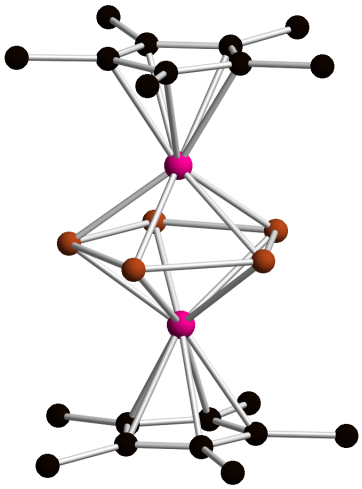

Figure 5.6: Ball and stick diagram of $[(Cp^*Cr)_2(\eta^5\text{-}P_5)]$ (P atoms are shown in orange, Cr atoms in pink and C atoms in black). H atoms are omitted for clarity.

$[(Cp^*Cr)_2(\eta^5\text{-}P_5)]$ is a paramagnetic 27 valence electrons complex. ^{31}P NMR spectroscopy showed a singlet at δ = 290.5 ppm. This is an unusual observation as this complex is paramagnetic and hints that more than one species may be present in solution. Since the $[Cp^*]^-$ and the $[P_5]^-$ ligands are isoelectronic and have a 1– charge, the chromium atoms have an average oxidation state of 1.5+, or mixed valences (*i.e.* Cr^+/Cr^{2+}). Electrochemical studies performed on $[(Cp^*Cr)_2(\eta^5\text{-}P_5)]$ revealed that it exhibits reversible one-electron oxidation and reduction steps. EPR measurements showed that the unpaired electron is shared between the two chromium atoms. A structural study revealed that the Cr–Cr separation was 2.727(5) Å.

In 1994, the oxidised analogue of $[(Cp^*Cr)_2(\eta^5\text{-}P_5)]$ was synthesised by Hughes and co-workers, namely $[(Cp^*Cr)_2(\eta^5\text{-}P_5)]^+$.[18] This complex was prepared by the oxidation of $[(Cp^*Cr)_2(\eta^5\text{-}P_5)]$ with $[FeCp_2]^+[A]^-$ (A = PF_6 and SbF_6). The 26 valence electron complex contains two Cr^{2+} centres has a Cr–Cr distance of 3.185(1) Å (0.458 Å greater than the neutral compound). They proposed that this is due to the removal of one electron from a Cr–Cr bonding orbital.

Similar chromium organometallic compounds $[(\eta^5\text{-}C_5R_4R')(CO)_2Cr)_2]$ (R = H: R' = Me; R = Me: R' = Et) react with As_4 to form the 27 valence electron $[((\eta^5\text{-}C_5R_4R')Cr)_2(\eta^5\text{-}As_5)]$ compounds, reported by Scherer in 1989.[19,20]

A triple-decker compound containing a central a $[As_5]^-$ ring was prepared by reacting $(MeAs)_5$ with $[MoCp(CO)_3]_2$ at 190 ºC for two days. This reaction ultimately afforded $[(CpMo)_2(\eta^4\text{-}As_5)]$.[21] For this 26 valence electron triple-decker complex, the interaction of the metals and the $[As_5]^-$ ring is not an η^5-type interaction but η^4 instead. The three rings are coplanar, meaning the metals are not in the centre of the rings. The Mo–Mo distance (2.764 (2) Å) is between the distance for a Mo–Mo single and a Mo=Mo double bond.[22,23] The As–As distances are not all equal; two of them (2.397(3) and 2.389(2) Å) have bond lengths close to that of a double bond,[24] and the remaining ones (2.570(2)–2.762(3) Å) are longer than any other reported As–As distances, and are assumed to have a fractional bond order.

Mixed metal cationic triple-decker complexes have been prepared by similar methods. By reacting the sandwich complex $[Cp^*M(\eta^5\text{-}P_5)]$ with $[CpM(C_6H_6)]^+$ compounds of formulae $[Cp^*M(\eta^5\text{-}P_5)M'(\eta^5\text{-}C_5R_5)]^+$ (M = M' = Fe: R = Me; M = Ru: M' = Fe: R = H; M = Fe: M' = Ru: R = H; M = Fe: M' = Ru: R = Me; M = M' = Ru: R = H; M = M'

= Ru: R = Me) can be synthesised as the $[BF_4]^-$ or $[PF_6]^-$ salts.[25] It was discovered that by reacting these triple-decker complexes with MeCN or NaI/MeCN it is possible to go back to the respective sandwich complexes *via* a nucleophilic degradation process. The electrochemistry of $[(Cp^*Fe)_2(\eta^5\text{-}P_5)]^+$ was studied finding one reversible oxidation and two separate reduction processes, one reversible and one irreversible.

Wolmershäuser *et al*. prepared mixed metal $[E'_5]^-$-containing complexes of the form $[(Cp^*M)(\eta^5\text{-}E'_5)M'(CO)_3]$ (E' = P and As: M = Fe and Ru: M' = Cr, Mo and W) (Figure 5.7) by reacting $[(Cp^*M)(\eta^5\text{-}E'_5)]$ with $[M'(CO)_3(MeCN)_3]$.[26]

Recent reports, detailed the synthesis and characterisation of the 29 valence electron triple-decker complex $[(CpBIGMn)_2(\eta^5\text{-}P_5)]$.[27] The latter was identified by X-ray crystallography and EPR.

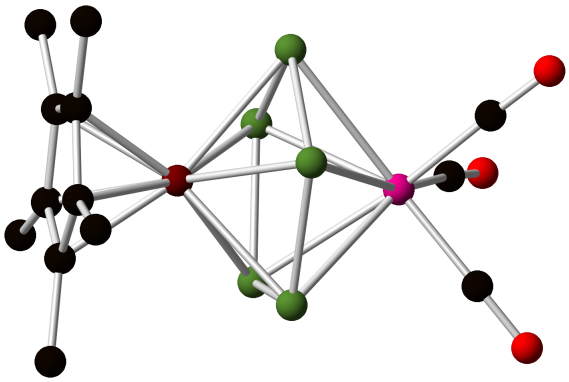

Figure 5.7: Ball and stick diagram of $[Cp^*Fe(\eta^5\text{-}As_5)Cr(CO)_3]$ (As atoms are shown in green, the Fe atom in dark red, the Cr atom in pink, C atoms in black and O atoms in red). H atoms are omitted for clarity.

5.2.1.2 $[E'_6]$ ligands

Scherer reported the thermolysis of E'_4 (E' = P and As) in 1985 to form triple-decker compounds. By reacting $[(\eta^5\text{-}C_5Me_4R)Mo(CO)_2]_2$ with E'_4, the 28 valence electron triple-decker complexes $[\{(\eta^5\text{-}C_5Me_4R)Mo\}_2(\eta^6\text{-}E'_6)]$ (E' = P: R = Me; E' = As: R =

Me and Et) were prepared.[28,29] [{(η^5-C_5Me_4R)Mo}$_2$(η^6-E'$_6$)] feature a planar [E'$_6$] ring that coordinated in an η^6 fashion to two [MoCp*] moieties. The [E'$_6$] ring is considered isoelectronic with benzene, where each CH unit has been replaced with an E' atom.

For [{(η^5-C_5Me_4R)Mo}$_2$(η^6-E'$_6$)] (R = Me: E' = P), the ^{31}P NMR spectrum revealed only a singlet at δ = –315.6 ppm showing that all six phosphorus atoms are equivalent. This reaction is not quantitative and forms a variety of complexes with different numbers of phosphorus atoms in the ligands such as [{(η^5-C_5Me_4R)Mo(CO)$_2$}(η^3-P$_3$)], [((η^5-C_5Me_4R)(CO)$_2$Mo)$_2$(η^2-P$_2$)] and [((η^5-C_5Me_4R)(CO)$_2$Mo)$_2$(η^2-P$_2$)$_2$], amongst others.

The single crystal X-ray structure of [{(η^5-C_5Me_4R)Mo}$_2$(η^6-E'$_6$)] revealed that the three rings in the structure are planar and parallel. The Mo–Mo bond lengths (2.646(1) Å for the phosphorus-containing species and 2.639(1) Å for the arsenic-containig analogue) seem to indicate the presence of a Mo–Mo single bond, which would be necessary to achieve an 18 valence electron configuration for each of the molybdenum metal centres.

Other triple-decker complexes including [(RM)$_2$(η^6-P$_6$)] (M = W: R = Cp*; M = V: R = Cp* and η^5-C_5Me_4Et; M = Nb: R = Cp* and η^5-C_5H_3-1,3(^{t}Bu)$_2$) have been prepared using similar methods (Figure 5.8).[30–32]

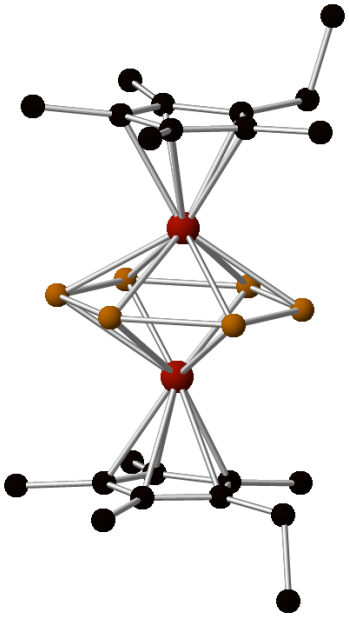

Figure 5.8: Ball and stick diagram of $[((\eta^5\text{-}C_5Me_4Et)V)_2(\eta^6\text{-}P_6)]$ (P atoms are shown in orange, V atoms in red and C atoms in black). H atoms are omitted for clarity.

In 1987, Scherer *et al*. reported a phosphorus-containing triple-decker compound where the $[P_6]$ ring is not planar. The thermolysis of P_4 with $[Cp^*Ti(CO)_2]$ leads to the formation of the 24 valence electron neutral triple-decker complex $[(Cp^*Ti)_2(P_6)]$ (Figure 5.9).[33] In contrast to other planar $[P_6]$ triple-decker complexes, this species exhibits a ^{31}P NMR resonance at δ = 386.7 ppm, consistent with a loss of aromaticity of the $[P_6]$ ring. In the mass spectrum recorded for the reaction mixture, $[P_2]$ elimination was observed, which is consistent with the fact that two equivalents of $[P_4]$ would be needed to form $[(Cp^*Ti)_2(P_6)]$.

X-ray crystallography revealed a chair conformation of the central $[P_6]$ ring with two $[Cp^*Ti]$ capping moieties. This species can be interpreted as consisting of a $[P_6]^{6-}$ ring (isoelectronic with S_6), two $[Cp^*]^-$ ligands and two titanium (IV) metal centres.

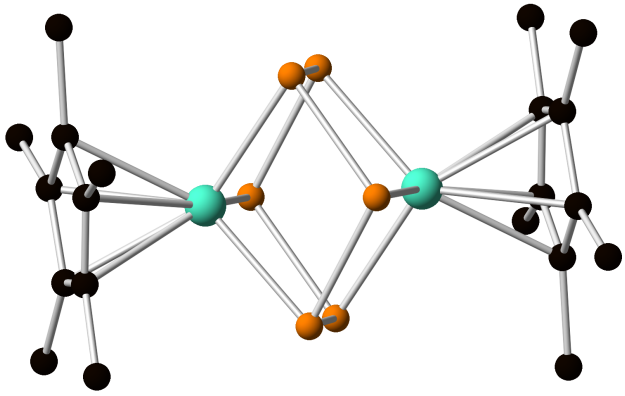

Figure 5.9: Ball and stick diagram of $[(Cp^*Ti)_2P_6]$ (P atoms are shown in orange, Ti atoms in green and C atoms in black). H atoms are omitted for clarity.

The electrochemistry of $[(Cp^*Ti)_2P_6]$ revealed an irreversible oxidation step and a reversible one-electron reduction step. The reduced 25 valence electron species, $[(Cp^*Ti)_2P_6]^-$, was prepared and studied by EPR. It exhibited a *g* factor of 1.9967 and no hyperfine coupling to the ligand. Computer simulations of $[(Cp^*Ti)_2P_6]^-$ were consistent with a delocalised mixed valence system.

5.3 Results and discussion

5.3.1 Solution reactivity of $[E'_7]^{3-}$ towards VCp_2 (E' = P and As)

Reactions of $[E'_7]^{3-}$ (E' = P and As) with VCp_2 in a 1:1 ratio showed the formation of two different products by mass spectrometry. Mass envelopes corresponding to $[CpV(\eta^5\text{-}P_5)]^-$ and $[(CpV)_2(\eta^6\text{-}P_6)]^-$ were observed in the reactions with the $[P_7]^{3-}$ Zintl ion. $[CpV(\eta^5\text{-}As_5)]^-$ and $[(CpV)_2(\eta^5\text{-}As_5)]^-$ were identified for reactions involving the $[As_7]^{3-}$ cage. It was observed that by using different stoichiometric loadings of the VCp_2 reagent, the different products could be selectively targeted.

5.3.1.1 Reactivity of $[K(18\text{-crown-}6)]_3[P_7]$ towards VCp_2

5.3.1.1.1 Synthesis of $[CpV(\eta^5\text{-}P_5)]^-$ (11) and $[(CpV)_2(\eta^6\text{-}P_6)]^-$ (12)

As mentioned previously, the product distribution for reactions between $[P_7]^{3-}$ and VCp_2 could be controlled by varying the stoichiometry of the reagents. When 0.7 equivalents of VCp_2 were added to a $[K(18\text{-crown-}6)]_3[P_7]$ solution, the sandwich complex $[CpV(\eta^5\text{-}P_5)]^-$ (**11**) was isolated, whereas a stoichiometric excess of the VCp_2 (2.5 equivalents) leads to the formation to the triple-decker complex $[(CpV)_2(\eta^6\text{-}P_6)]^-$ (**12**) (Scheme 5.2).

The reactions reach completion after an hour of stirring at room temperature in pyridine. The reactions can also be carried out in THF but longer stirring times (3 hours) are required due to the reduced solubility of $[P_7]^{3-}$ in THF.

After the reactions had reached completion, all volatiles were removed under vacuum; the resulting oils were washed with diethyl ether and the products were extracted into THF. 2,2,2-crypt was added, to exchange the sequestering agent, and the THF solutions of the products were layered with hexane. The systems were placed at –35 ºC for three days. The crystalline yields were 35% and 51% for [K(2,2,2-crypt)][**11**] and [K(2,2,2-crypt)][**12**] ·2THF, respectively.

For all of these reactions $[K(18\text{-crown-}6)]_3[P_7]$ was used as the source of the Zintl cluster. This is because the K_3P_7 precursor contains small amounts of an unknown insoluble impurity making it difficult to control precise stoichiometries. This can be removed by protonating the solution of K_3P_7 with two equivalents of H_2O to form

$[K(18\text{-crown-6})]_2[HP_7]$ and subsequently deprotonating using KHMDS to yield compositionally pure $[K(18\text{-crown-6})]_3[P_7]$.[34]

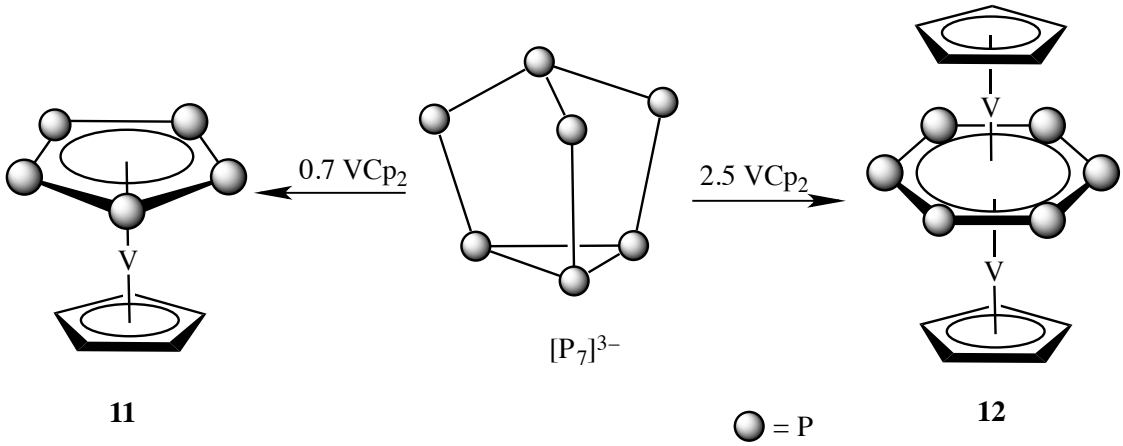

Scheme 5.2: Reactivity of $[P_7]^{3-}$ towards 0.7 and 2.5 equivalents of VCp_2 to form **11** and **12**, respectively.

5.3.1.1.2 Structures of $[CpV(\eta^5\text{-}P_5)]^-$ (11) and $[(CpV)_2(\eta^6\text{-}P_6)]^-$ (12)

Crystals of **11** were initially obtained as the $[K(18\text{-crown-6})]^+$ salt, but co-crystallised with a unit of [K(18-crown-6)][Cp]. To remove the [K(18-crown-6)][Cp] by-product a sequestering agent exchange was carried out using 2,2,2-crypt. Crystals of **12** could only be obtained by varying the cation sequestering agent to afford the $[K(2,2,2\text{-crypt})]^+$ salt.

[K(2,2,2-crypt)][**11**] contains an anionic moety which exhibits a "sandwich" conformation, with a *cyclo*-$[\eta^5\text{-}P_5]^-$ ring and a cyclopentadienyl ligand coordinated to a vanadium atom (Figure 5.10). Both ligands are coplanar. In the starting material the vanadium had an oxidation state of 2+, whereas in the product, assuming that the $[P_5]^-$ ring is isoelectronic to a $[Cp]^-$, it has an oxidation state of 1+. It crystallised in a *P*–1 (no. 2) space group.

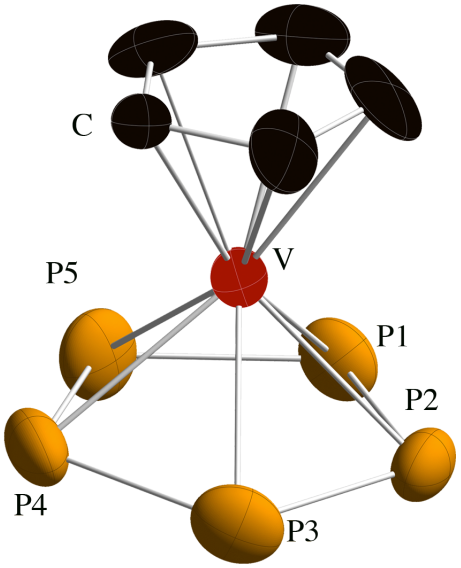

Figure 5.10: Thermal ellipsoid plot of **11** with anisotropic displacement ellipsoids pictured at 50% probability. H atoms are omitted for clarity.

This is a 16 valence electron compound, assuming that each ligand is acting as a six-electron donor. There are a number examples previously reported of transition metal compounds featuring an $[P_5]^-$ ring. **11** is the first anionic species where a $[P_5]^-$ ring is coordinated to a vanadium centre. Both of the rings are in an eclipsed conformation. Despite the even number of electrons in **11**, no NMR signal could be recorded. This could be due to a high spin nature of the molecular orbitals.

Selected interatomic distances for **11** are listed in Table 5.1. The P–P bond lengths within the $[P_5]^-$ ring lie in the very narrow range of 2.162(1) to 2.171(1) Å. These bond lengths are all in between the typical values for a P–P single bond (2.22 Å) and P=P double bond (2.04 Å).[35,36] A CSD search gave a mean P–P bond length of 2.123 (av) Å for compounds containing a $[P_5]^-$ anion.[37] The P–V bond lengths are in the very narrow range of 2.375(1) to 2.401(1) Å, indicating that the vanadium atom is centrally positioned with respect to the ring. A CSD search gave a mean length for the P–V single bond of 2.482 (av) Å, and the sum of the covalent radii is 2.45 Å, both of which are larger than those found crystallographically for **11**, presumably due to a strong

interaction between the anionc $[P_5]^-$ ring and the vanadium centre.[38] These data are consistent with a significant degree of back-bonding between the vanadium metal centre and the $[P_5]^-$ ring.

Bond in $[CpV(\eta^5\text{-}P_5)]^-$ (**11**)	Bond length (Å)
P1–P2	2.165(1)
P1–P5	2.171(1)
P2–P3	2.164(1)
P3–P4	2.162(1)
P4–P5	2.164(1)
P1–V1	2.386(1)
P2–V1	2.401(1)
P3–V1	2.383(1)
P4–V1	2.400(1)
P5–V1	2.375(1)
V1–C2	2.241(3)
V1–C1	2.243(3)
V1–C3	2.256(3)
V1–C5	2.267(3)
V1–C4	2.269(3)

Table 5.1: Selected interatomic distances for **11**.

12 crystallised as [K(2,2,2-crypt)][**12**]·2THF in the *P*–1 space group (No. 2) (Figure 5.11). **12** exhibits a triple-decker structure with a *cyclo*-$[\eta^6\text{-}P_6]$ ring sandwiched between two vanadium cyclopentadienyl fragments. It is interesting to note that for the reactions involving $[P_7]^{3-}$, the number of phosphorus atoms in the ring changes from the sandwich compound to the triple-decker species. The three rings in **12** are coplanar with the two $[Cp]^-$ rings adopting a staggered conformation.

If we assume that the $[P_6]$ ring is neutral (isoelectronic with benzene) and that the [Cp] ring has a 1– charge, the vanadium atoms should have an average charge of +1/2 to afford a monoanionc species. This must imply that the two vanadium atoms have

mixed valences, *i.e* V^{I} and V^{0}. The total number of valence electrons is 27, assuming the $[Cp]^{-}$ rings and the $[P_6]$ ring are six-electron donors.

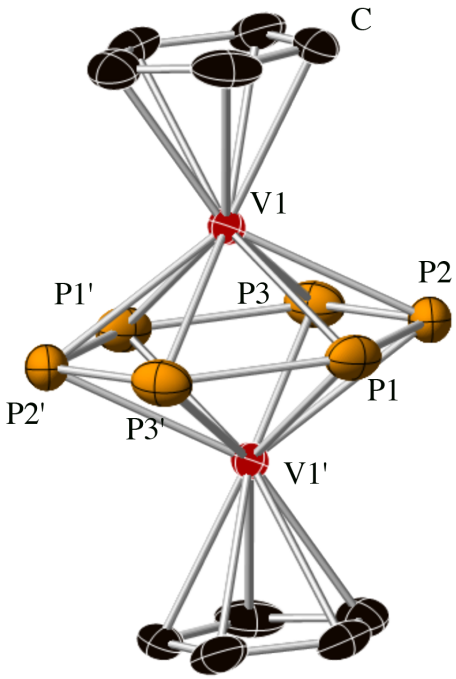

Figure 5.11: Thermal ellipsoid plot of **12** with anisotropic displacement ellipsoids pictured at 50% probability. H atoms are omitted for clarity.

There is a centre of inversion in the centre of the $[P_6]$ ring, as a result the asymmetric unit only contains half of the molecule and the other half is derived by symmetry as pictured in Figure 5.11.

Interatomic distances for **12** are provided in Table 5.2. The P–P bond lengths within the $[P_6]$ ring lie in the very narrow range of 2.146(1) to 2.178(1) Å similar to those in **11**. Comparing to the neutral compound $[\{(\eta^5\text{-}C_5Me_4Et)V\}_2(\eta^6\text{-}P_6)]$, where the P–P bond distances range from 2.085(4) to 2.163(4) Å, it is obvious that the distances in **12** are significantly larger, as a result of increased electron-density.[30] These bond lengths are all in between the typical values for a P–P single bond and P=P double

bond. The average distances for other compounds containing a [P_6] ring is 2.170 Å, which is closer to the longest P–P bond in **12**.[39]

Bond in $[(CpV)_2(\eta^6\text{-}P_6)]^-$ (**12**)	Bond length (Å)
P1–P2	2.146(1)
P2–P3	2.150(1)
P1'–P3	2.178(1)
V1–P1	2.521(1)
V1–P2	2.548(1)
V1–P3	2.506(1)
V1–C1	2.290(2)
V1–C2	2.292(2)
V1–C3	2.286(2)
V1–C4	2.280(2)
V1–C5	2.286(2)
V1–V1	2.619(1)

Table 5.2: Selected interatomic distances for **12**.

The increased ring diameter is reflected in the slightly shorter V–V distance observed for **12** (2.619(1) Å) compared to the V–V distance found in [$\{(C_5Me_4Et)V\}_2(\eta^6\text{-}P_6)$]) (2.627(2) Å). The larger ring allows the vanadium atoms to approach one another.

This follows the trend reported by Hughes where for $[(Cp^*Cr)_2(\eta^5\text{-}P_5)]$ and $[(Cp^*Cr)_2(\eta^5\text{-}P_5)]^+$, the more reduced species has a shorter M–M distance. For the neutral triple-decker $[(Cp^*Cr)_2(\eta^5\text{-}P_5)]$ the Cr–Cr distance is 2.727(5) Å whereas for the monocationic species $[(Cp^*Cr)_2(\eta^5\text{-}P_5)]^+$ it is 3.185(1) Å.[40,18,41]

A CSD search gave a mean V–V distance of 2.844 (av) Å.[42] The sum of the covalent radii for a V–V single bond is 2.68 Å and V=V double bond is 2.24 Å. The interatomic V–V distances recorded for **12** (2.619(1) Å) is consistent with a V–V single bond.

The P–V bond lengths are in the range of 2.506(1) to 2.548(1) Å. A CSD search gave a mean for P–V single bond of 2.482 (av) Å, and the sum of the covalent radii is 2.45 Å.[38] Compared to **11**, the distances observed for **12** are longer which may be simply due to the greater ring size of $[P_6]$ compared to the $[P_5]^-$. In $[\{(\eta^5\text{-}C_5Me_4Et)V\}_2(\eta^6\text{-}P_6)]$ the P–V distances lie in the range of 2.474(3) to 2.542(3) Å, which are slightly shorter than the ones found for **12**, which is consistent with the fact that **12** has a moderately expanded ring.

DFT calculations were performed by Andrew Zeng from the research group of Professor McGrady in order to study the electronic properties of **12**, in particular with regard to the interactions between the $[P_6]$ ring and the vanadium atoms. The computed optimised geometry found was found to be in good agreement with the experimental data.

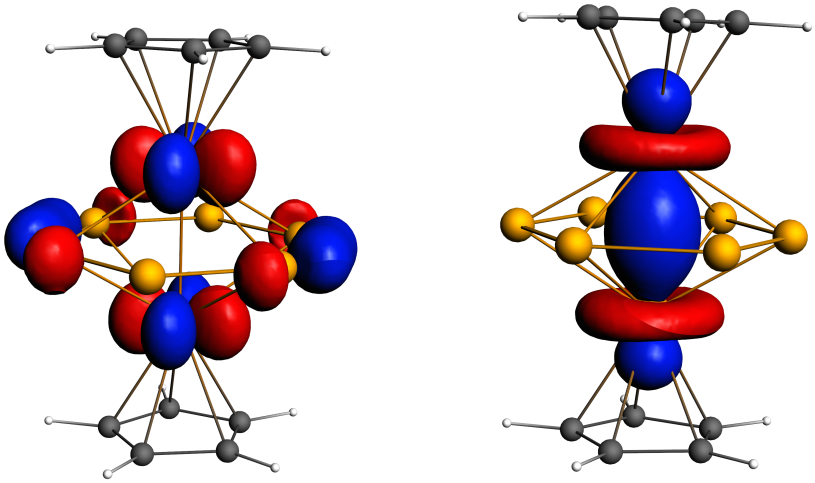

Figure 5.12: Selected frontier orbitals for the optimised structure of **12**. HOMO (left) and HOMO–2 (right).

Figure 5.12 shows that the HOMO is mainly composed of the delta-bond between the two vanadium atoms and of some phosphorus atoms of the $[P_6]$ ring. HOMO–2 is

mainly composed on the σ bond between the two vanadium atoms, corroborating the observations found by X-ray crystallography.

5.3.1.1.3 Mass spectrometric studies on $[CpV(\eta^5\text{-}P_5)]^-$ (11) and $[(CpV)_2(\eta^6\text{-}P_6)]^-$ (12)

Confirmation of the presence of **11** and **12** in solution was obtained by electrospray mass spectrometric studies of DMF solutions of the reaction mixtures. In the negative ion mode spectrum of **11**, a mass envelope corresponding to $[CpVP_5]^-$ was observed at 271.0 Da. (Figure 5.13 left), and in the positive ion mode the ion paired species $\{[K(2,2,2\text{-crypt})]_3[CpVP_5]\}^+$ was also observed at 1517.8 Da. In the negative ion mode spectrum of **12**, a mass envelope corresponding to $[Cp_2V_2P_6]^-$ was observed at 417.7 Da. (Figure 5.13 right), and in the positive ion mode, the ion paired species $\{[K(2,2,2\text{-crypt})]_3[Cp_2V_2P_6]\}^+$ was also observed at 1663.0 Da.

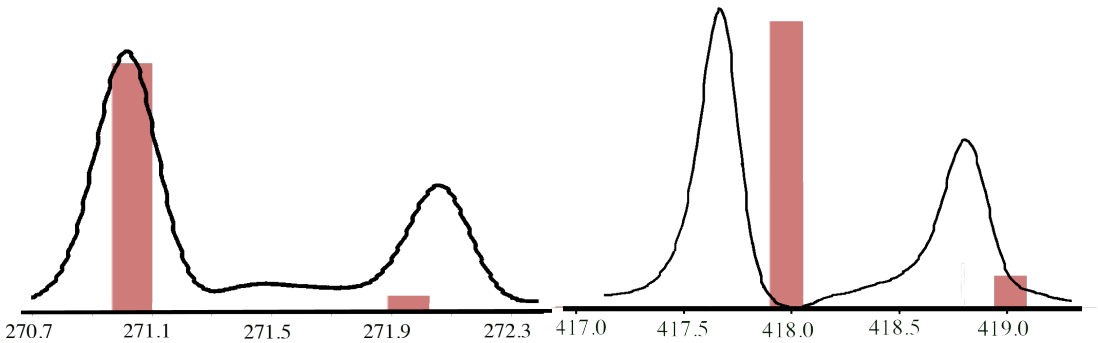

Figure 5.13: Negative ion mode electrospray mass envelopes corresponding to $[CpVP_5]^-$ (left) and $[Cp_2V_2P_6]^-$ (right). Predicted isotopic distribution is shown in red and observed mass spectrometric data are shown in black.

In the positive ion mode, an ion paired species corresponding to the anion plus the cations necessary to generate a monocationic species is typically observed. **11** and **12** would be expected to appear as $\{[K(2,2,2\text{-crypt})]_2[P_5VCp]\}^+$ and $\{[K(2,2,2\text{-crypt})]_2[P_6V_2Cp_2]\}^+$, nevertheless they are observed as $\{[K(2,2,2\text{-crypt})]_3[P_5VCp]\}^+$

and $\{[K(2,2,2\text{-crypt})]_3[P_6V_2Cp_2]\}^+$. This may imply that some additional redox processes are occurring during ionisation, although it is interesting to note that the molecular ions are observed in the negative ion mode mass spectra for both species.

5.3.1.1.4 EPR spectroscopic studies on $[(CpV)_2(\eta^6\text{-}P_6)]^-$ (12)

EPR measurements (X-band and W-band) were performed on a solid-state sample of [K(2,2,2-crypt)][**12**]·2THF to confirm the paramagnetic character of this species. X-band data constrains the hyperfine coupling and W-band provides a constraint on the spread of the *g*-values in addition to the anisotropy of the ^{51}V hyperfine interaction.

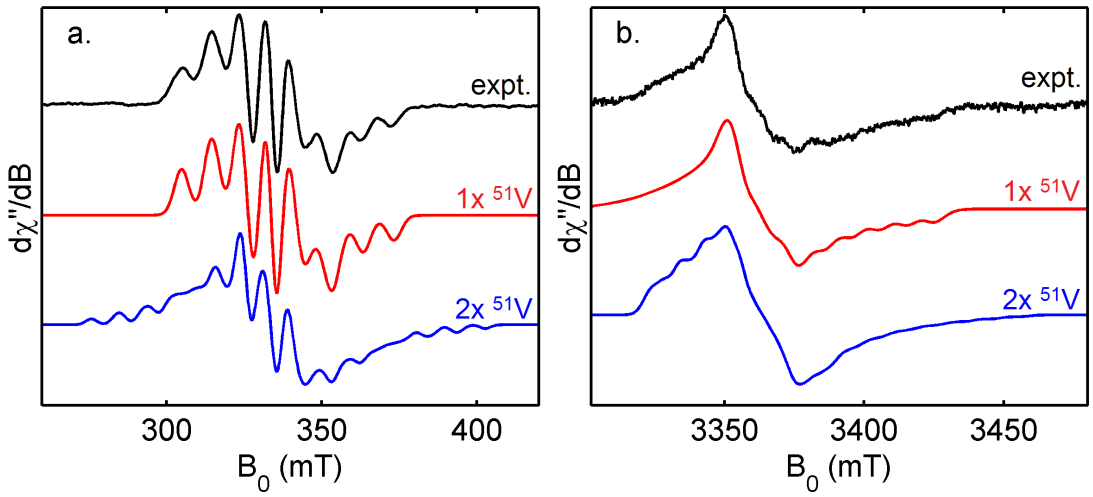

Figure 5.14: Room temperature CW-EPR of 12, measured as a neat powder at X-band and W-band, panels a. and b., respectively, with simulations below in red for one ^{51}V nucleus and in blue for two ^{51}V nuclei.

EPR spectra were fit using Nelder/Mead simplex optimisation method, varying the *g*-values, hyperfine couplings and line widths as defined by Gaussian distributions of *g*-values and energy. The best fit was obtained with a single ^{51}V nucleus contributing to the hyperfine features of the EPR spectra.

Figure 5.14 shows experimental data (black line) and simulations with one (red line) and two (blue line) ^{51}V nuclei. The central splitting in the X-band data limits the range of possible maximum hyperfine values. Following the 2n*I*+1 rule for equivalent nuclei, there are eight or fifteen hyperfine features of this maximum hyperfine value, depending on whether or not there are one or two ^{51}V nuclei. However, in the case of inequivalent hyperfine interactions, the splitting goes as n(2*I*+1). Both equivalent and inequivalent simulations were attempted; Figure 5.14 shows only the inequivalent results. Simulation with equivalent nuclei optimised simultaneously against the X-band and W-band data led to a value of 355 MHz, which is larger than the value observed for the X-band measurements. These results suggest that the unpaired electron is localised on one of the two vanadium ions. Table 5.3 lists the simulation parameters used.

Species		g_1	g_2	g_3	A_1	A_2	A_3
12	1x ^{51}V	2.0046	1.9927	1.9780	119.7	62.48	270.36
	Linewidth[a]	σ_{g1}	σ_{g2}	σ_{g3}	σ_{n1}	σ_{n2}	σ_{n3}
	value	0.0113	0.0010	0.0014	62	54	64
		g_1	g_2	g_3	A_1	A_2	A_3
12 Two ^{51}V	1st ^{51}V	1.9983	1.9943	1.9769	122.8	89.7	278
	2nd ^{51}V				123	0	224
	Linewidth[a]	σ_{g1}	σ_{g2}	σ_{g3}	σ_{n1}	σ_{n2}	σ_{n3}
	value	0.0012	0.0012	0.004	107	11	0

[a.] Linewidths are described with Gaussian distributions of both g-value (σ_g) and MHz (σ_n).

Table 5.3: Simulation parameter values for **12**.

5.3.1.1.5 Cyclic voltammetry studies on $[CpV(\eta^5\text{-}P_5)]^-$ (11) and $[(CpV)_2(\eta^6\text{-}P_6)]^-$ (12)

Electrochemical cyclic voltammetry studies were recorded at a silver quasi-reference electrode, a glassy-carbon working electrode and a platinum auxiliary electrode on a

DMF solutions containing [K(2,2,2-crypt)][**11**] and [K(2,2,2-crypt)][**12**]·2THF (Figure 5.15 and 5.16).

$[Bu_4N][PF_6]$ was used as electrolyte and ferrocene as a reference. First the samples were run without the ferrocene and then with it, showing no difference in the voltammogram, indicating no chemical interaction with the ferrocene.

Attempts to get a better quality voltammogram with different solvents, different scan rates and electrolytes failed. The best results were obtained by running the voltammograms at fast scan rates (1 V/s for **11** and 5 V/s for **12**) and for both samples after one to three cycles the "shape" of the voltammogram was completely lost. Attempts to chemically synthesise the reduced and oxidised products of **11** and **12** were made with no success. Table 5.4 shows the list of redox steps for **11** and **12** and their values with reference to ferrocene.

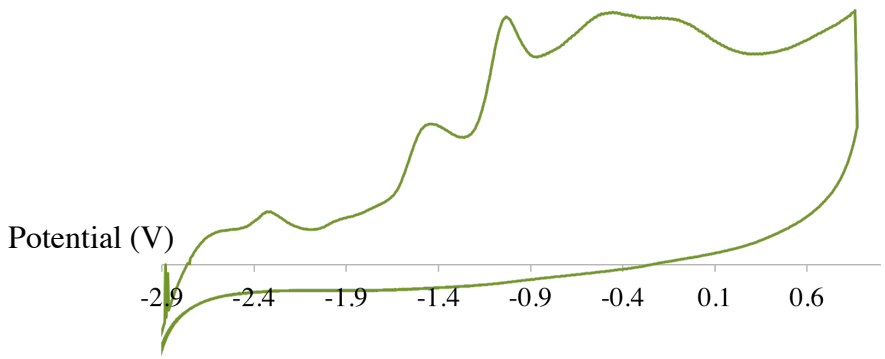

Figure 5.15: Cyclic voltammogram of **11**.

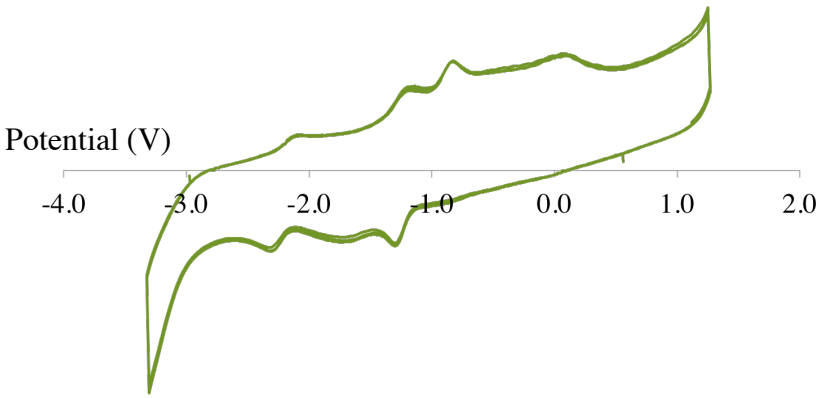

Figure 5.16: Cyclic voltammogram of **12**.

Compound	Oxidation (V)	Reduction (V)
11		–2.32 (i)
		–1.47 (i)
		–1.03 (i)
		–0.49 (i)
12		– 2.23 (r)
		– 1.25 (r)
		– 0.85 (i)
	0.01 (i)	

Table 5.4: Reduction and oxidation steps for **11** and **12**. (i = irreversible step, r = reversible step).

11 shows the possibility for four completely irreversible one-electron reduction steps. Since the redox processes are irreversible and they only seem to be present for one to three cycles, it is reasonable to assume that the redox processes may arise due to cage related phenomena and they are not occurring at the metal. The $[P_5]^-$ ring might be generating polyphosphides such as $[P_7]^{3-}$, $[P_{21}]^{3-}$, $[P_{16}]^{2-}$ or $[P_{11}]^{3-}$.

12 shows the possibility for two reversible reductions steps, one irreversible reduction step and one irreversible oxidation step. It is possible that the two irreversible steps may be due to processes occurring with the $[P_5]^-$ ring, similarly to **11**, whereas the reversible reduction steps may arise from the metal (since in **12** the vanadium atoms

have mixed valances V^{1+}/V^0 then the reductions would correspond to V^0/V^0 and V^0/V^{1-}). However after three cycles no redox steps could be observed, it might be reasonable to conclude that all redox steps observed are due to the formation of polyphosphides.

5.3.1.2 Reactivity of K_3As_7 towards VCp_2

5.3.1.2.1 Synthesis of $[CpV(\eta^5\text{-}As_5)]^{n-}$ (13) and $[(CpV)_2(\eta^5\text{-}As_5)]^-$ (14)

Similarly to the reactions with the $[P_7]^{3-}$, $[As_7]^{3-}$ reacts with VCp_2 to give two different products. K_3As_7 was stirred with three equivalents of 18-crown-6 in pyridine for 30 minutes. Subsequently, VCp_2 was added as a powder to the reaction mixture. By following the reaction using ESI mass spectrometry, it was observed that both the sandwich complex and a triple-decker complex could be prepared. These compounds are significantly different to the phosphorus species described in Section 5.3.1 (Scheme 5.3).

0.7 equivalents of VCp_2 were added to a pyridine solution of K_3As_7/18-crown-6 and the reaction mixture was left to stir for one hour. A compound with a molecular ion corresponding to $[CpV(\eta^5\text{-}As_5)]^-$ was observed by mass spectrometry. Subsequently all volatiles were removed under vacuum and the remaining oil was washed with diethyl ether. The oil was dissolved in THF and 2,2,2-crypt was added to displace the 18-crown-6 from the K^+ cation. Unlike the rest of the compounds mentioned in this chapter, **13** is only sparingly soluble in THF, so in order to grow crystals a mixture of pyridine and THF had to be used to dissolve the solid. The pyridine/THF solution was

layered with hexane and left to crystallise for three days at –35 ºC. The crystalline yield for [K(2,2,2-crypt)]$_2$[**13**] was 35%.

When 2.5 equivalents of VCp_2 were added to the K_3As_7/18-crown-6 mixture, a compound with a molecular ion corresponding to $[(CpV)_2(\eta^5\text{-}As_5)]^-$ was observed by ESI mass spectroscopy. The reaction mixture was left to stir for one hour to reach completion and all volatiles were removed under vacuum. The resulting oil was washed with diethyl ether and extracted into THF. 2,2,2-crypt was added and single crystals were obtained after three days from layering the THF solution with hexane and leaving the mixture at –35 ºC. The crystalline yield for [K(2,2,2-crypt)][**14**]·2THF was 82%. All attempts to obtain NMR data for **14** failed.

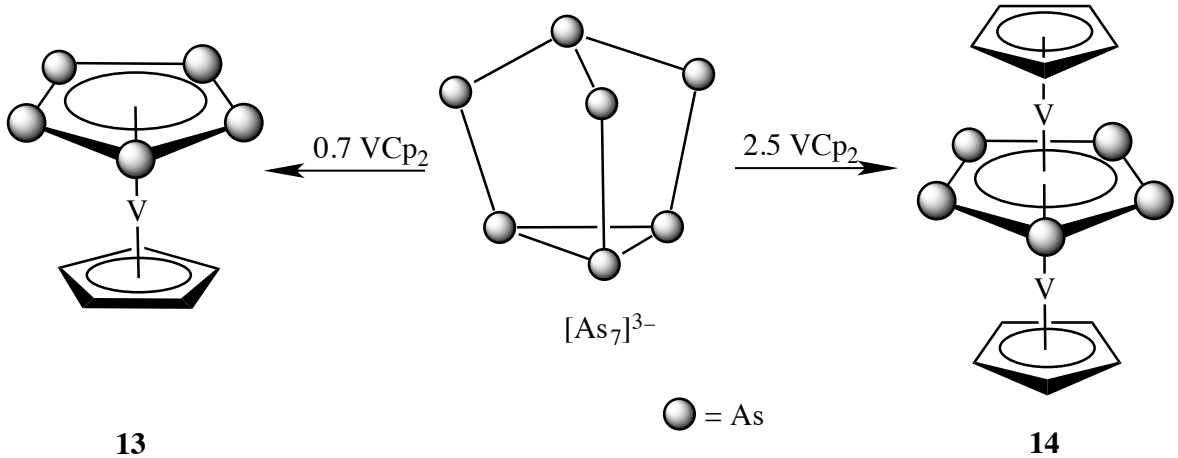

Scheme 5.3: Reactivity of $[As_7]^{3-}$ towards 0.7 and 2.5 equivalents of VCp_2 to form **13** and **14**, respectively.

5.3.1.2.2 Structures of $[CpV(\eta^5\text{-}As_5)]^{2-}$ (13) and $[(CpV)_2(\eta^5\text{-}As_5)]^-$ (14)

Crystals of **13** were grown with $[K(18\text{-crown-}6)]^+$ as the counter cation, and in an analogous manner to the phosphorus-containing system, **11**, a unit of [K(18-crown-6)][Cp] co-crystallised along with the desired product. In this crystal structure the sandwich compound had an overall charge of 1– (**13'**), but the quality of the crystal

structure was found to be very poor (R_{int} = 8.4%) due to heavy rotational disorder of one of the $[K(18\text{-crown-6})]^+$ cations. In an attempt eliminate the positional disorder of the counter-cations and the [K(18-crown-6)][Cp], a sequestering agent exchange with 2,2,2-crypt was carried out. The crystals obtained from this mixture had a formula of $[K(2,2,2\text{-crypt})]_2$[**13**], implying that the overall charge for the anion is 2–.

Similarly to **11**, **13** exhibits a sandwich conformation, with a *cyclo*-$[\eta^5\text{-As}_5]^-$ ring and a cyclopentadienyl ligand coordinated to a vanadium atom, where both ligands are coplanar (Figure 5.17). For the monoanionic species the vanadium should have an oxidation state of 1+ and a total of 16 valence electrons, assuming that the $[Cp]^-$ and $[As_5]^-$ rings have an overall 1– charge. By contrast with the dianionic system the vanadium centre should be zero-valent and the complex would have a total of 17 valence electrons. The electron counts are assuming that both the $[Cp]^-$ and the $[As_5]^-$ rings are acting as six-electron donors. Since the crystalline samples of the dianionic species were of better quality, it will form the focus of the discussioin of bond metrics. $[K(2,2,2\text{-crypt})]_2$[**13**] crystallises in a *P*–1 (No. 2) space group. The $[Cp]^-$ and the $[As_5]^-$ ring are in an eclipsed conformation.

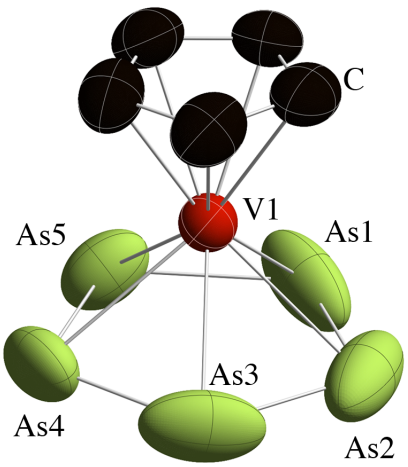

Figure 5.17: Thermal ellipsoid plot of **13** with anisotropic displacement ellipsoids pictured at 50% probability. H atoms are omitted for clarity.

There are several reports of $[\eta^5\text{-}As_5]^-$ rings in the chemical literature, as mentioned in the Section 5.2.1.1 , but this is the first example of a sandwich compound including an $[\eta^5\text{-}As_5]^-$ ring attached to a vanadium atom.

Bond	$[CpV(\eta^5\text{-}As_5)]^{2-}$ **(13)** (Å)	$[CpV(\eta^5\text{-}As_5)]^-$ **(13')** (Å)
As1–As2	2.388(1)	2.355(2)
As2–As3	2.370(1)	2.350(2)
As3–As4	2.350(1)	2.338(1)
As4–As5	2.355(1)	2.310(1)
As1–As5	2.371(1)	2.339(1)
V1–As1	2.643(1)	2.575(1)
V1–As2	2.523(1)	2.565(1)
V1–As4	2.582(1)	2.567(1)
V1–As3	2.615(1)	2.557(2)
V1–As5	2.540(1)	2.571(2)
V1–C1	2.270(5)	2.264(1)
V1–C2	2.277(4)	2.274(1)
V1–C3	2.284(4)	2.256(1)
V1–C4	2.276(4)	2.262(1)
V1–C5	2.266(4)	2.269(1)

Table 5.5: Selected interatomic distances for **13**.

Table 5.5 shows selected interatomic distances for $[K(2,2,2\text{-crypt})]_2$[**13**]. For comparison purposes selected bond lengths of $[K(18\text{-crown-}6)]_2$[**13'**][Cp] are also shown, but it is important to remark that caution should be used when analysing bond metrics for the latter. Bond lengths for $[K(2,2,2\text{-crypt})]_2$[**13**] and $[K(18\text{-crown-}6)]_2$[**13'**][Cp] are very similar, the only fact worth pointing out is the 0.142 Å difference in the perimeter of the rings ($[K(2,2,2\text{-crypt})]_2$[**13**] = 11.834 Å, $[K(18\text{-crown-}6)]_2$[**13'**][Cp] = 11.692 Å). From now on all discussions made about **13**, will refer to the structure obtained in $[K(2,2,2\text{-crypt})]_2$[**13**].

In **13** the As–As distances in the $[As_5]^-$ ring lie in the range of 2.350(1) to 2.388(1) Å. These bond lengths lie in between the typical range of an As–As single bond (2.42 Å)

and an As=As double bond (2.28 Å).[35,36] A CSD search gave a mean As–As distance in $[As_5]^-$ rings of 2.351 (av) Å, which is almost identical to the distances found.[43]

The As–V distances lie in the range of 2.523(1) to 2.643(1) Å, these distances are not very similar, implying that the vanadium is not positioned in the centre of the $[As_5]^-$ ring. A CSD search gave a mean for an As–V single bond of 2.539 (av) Å, which is somwhere between the the range found crystallographically in **13**.[44] The sum of the covalent radii for an As–V single bond is 2.55 Å, which is similar to the distances found.

For **14**, crystals of the anion were obtained with $[K(18\text{-crown-6})]^+$ counter cations co-crystallising with a [K(18-crown-6)][Cp] unit. It was also possible to obtain the crystals with $[K(2,2,2\text{-crypt})]^+$ as counter cation. The $[K(2,2,2\text{-crypt})]^+$ salt will be discussed. It crystallised as [K(2,2,2-crypt)][**14**]·2THF in the *P*–1 (No. 2) space group.

As **12**, **14** is a triple-decker complex, but the difference is that in the central ring in **14** has only five arsenic atoms (Figure 5.18), instead of six as observed when similar reactions were carried out with $[P_7]^{3-}$. The *cyclo*-$[As_5]^-$ ring is coordinated to two VCp units on each side. In **14** all the three rings are perfectly eclipsed and coplanar, in contrast to **12**, where the two $[Cp]^-$ rings are in a staggered conformation. The oxidation state of the vanadium atoms is 1+. This is a 26 valence electron compound. Despite the even number of electrons in **12**, no NMR signal could be recorded. This could be due to a high spin nature of the molecular orbitals.

Interatomic distances of **14** are shown in Table 5.6. The As–As distances lie in the range of 2.379(1) to 2.684(1) Å, as with the sandwich complex **13**, they do not lie in a narrow range. The sum of the covalent radii for an As–As single bond is 2.42 Å.[31]

This would imply that the As3–As4 (2.369(1) Å), As2–As3 (2.446(1) Å), As4–As5 (2.379(1) Å) and As1–As5 (2.477(1) Å) distances are closer to a single bond, but the As1–As2 distance, (2.684(1) Å) is surprisingly long. A CSD search gave a mean As–As distance in $[As_5]^-$ rings of 2.351 (av) Å, which is shorter than any distance in the $[As_5]^-$ ring for **14**.[43] In **13** the perimeter found was 11.834 Å, whereas for **14** the perimeter expands to 12.355 Å, which is 0.521 Å larger. This could give us a lead to explain why for the phosphous analogue the nuclearity of the ring expands from five to six when going from the sandwich complex to the triple-decker species. The perimeter for **12** is 12.948 Å, and for **11** is 10.826 Å.

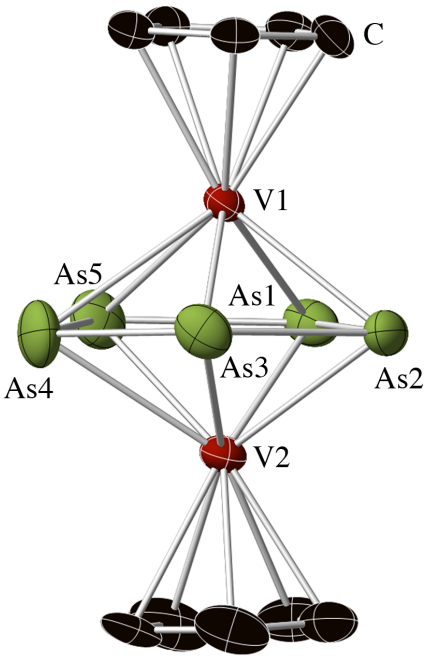

Figure 5.18: Thermal ellipsoid plot of **14** with anisotropic displacement ellipsoids pictured at 50% probability. H atoms are omitted for clarity.

In order to facilitate a V–V contact, the central ring for the phosphorus containing systems must expand. By contrast, in the arsenic analogue it is possible to keep an $[As_5]^-$ ring and accommodate the V–V bond in the central cavity. This is reflected in the shorter V–V bond distance in **12** (2.619(1) Å) than in **14** (2.862(1) Å). The V–V distance for **14** is slightly longer than the mean found from a CSD search (2.844 Å),

and longer than the sum of the covalent radii for a V–V single bond (2.68 Å). This is indicated that only a weak interaction between the two vanadium atoms is present.

The As–V distances are very dissimilar, the shortest ones As1–V1, As2–V1, As1–V2 and As2–V2 (2.459(1) to 2.476 (1) Å) are smaller than the sum of the covalent radii for an As–V single bond (2.55 Å), whereas the rest are longer (2.572(1) to 2.648(1) Å). A CSD search gave a mean value of 2.539 (av) Å for an As–V single bond.

Bond in $[(CpV)_2(\eta^5\text{-}As_5)]^-$ **(14)**	Bond length (Å)
As1–As2	2.684(1)
As2–As3	2.446(1)
As3–As4	2.369(1)
As4–As5	2.379(1)
As1–As5	2.477(1)
As1–V1	2.461(1)
As2–V1	2.459(1)
As3–V1	2.611(1)
As4–V1	2.611(1)
As5–V1	2.597(1)
As1–V2	2.471(1)
As2–V2	2.476(1)
As3–V2	2.583(1)
As4–V2	2.648(1)
As5–V2	2.572(1)
V1–C1	2.283(4)
V1–C2	2.286(4)
V1–C3	2.279(4)
V1–C4	2.281(4)
V1–C5	2.289(4)
V2–C6	2.292(5)
V2–C7	2.301(4)
V2–C8	2.297(5)
V2–C9	2.264(5)
V2–C10	2.258(5)
V1–V2	2.862(1)

Table 5.6: Selected interatomic distances for **14**.

5.3.1.2.3 Mass spectrometric studies on $[CpV(\eta^5\text{-}As_5)]^{2-}$ (13) and $[(CpV)_2(\eta^5\text{-}As_5)]^-$ (14)

Confirmation of the presence of the cluster anion **13** and **14** in solution was obtained by electrospray mass spectrometry. For **13**, crystals of $[K(2,2,2\text{-crypt})]_2[\mathbf{13}]$ were dissolved in DMF. In the negative ion mode spectrum a mass envelope corresponding to $[CpVAs_5]^-$ was observed at 490.3 Da. (Figure 5.19 left). Similarly, in the positive ion mode the ion paired species $\{[K(2,2,2\text{-crypt})]_3[CpVAs_5]\}^+$ was also observed at 1735.9 Da. In the negative ion mode spectrum of **14**, a mass envelope corresponding to $[Cp_2V_2As_5]^-$ was observed at 606.0 Da. (Figure 5.19 right). In the positive ion mode the ion paired species $\{[K(2,2,2\text{-crypt})]_3[Cp_2V_2As_5]\}^+$ could also be detected at 1851.9 Da.

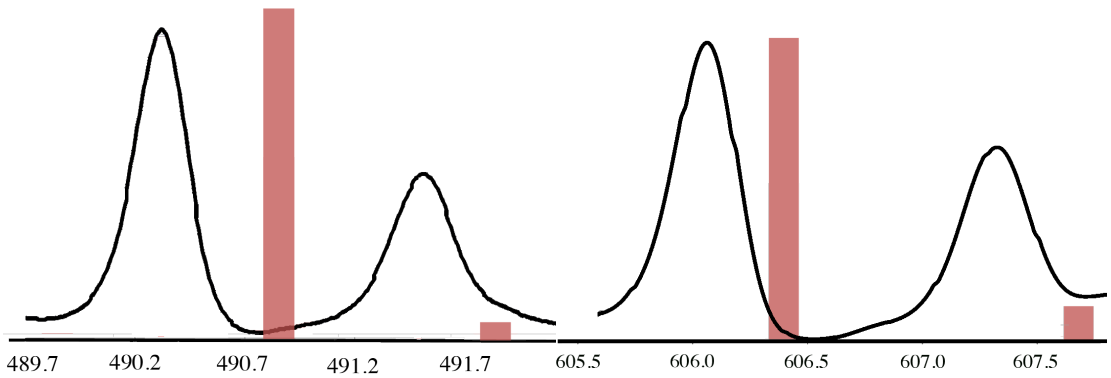

Figure 5.19: Negative ion mode electrospray mass envelopes corresponding $[CpVAs_5]^-$ (left) $[Cp_2V_2As_5]^-$ (right). Predicted isotopic distribution is shown in red and observed mass spectrometric data are shown in black.

As with **11** and **12**, in the positive ion mode the observed ion paired species have one cation more than what would be expected in order to afford a positively charged ion pair.

5.3.1.2.4 EPR spectroscopic studies on $[CpV(\eta^5\text{-}As_5)]^{2-}$ (13)

EPR measurements (X-band and W-band) were performed on the solid-state sample of $[K(2,2,2\text{-crypt})]_2$[**13**] at room temperature to confirm the paramagnetic character of this species. Simulations are shown in red and experimental data in black in Figure 5.20.

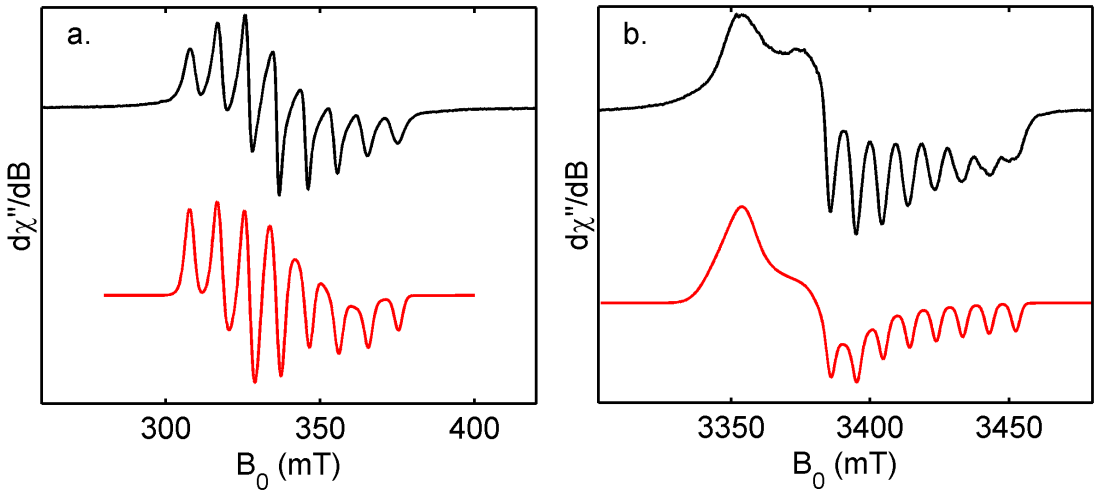

Figure 5.20: Room temperature CW-EPR of **13**, measured as a neat powder at X-band and W-band, panels a. and b., respectively, with simulations below in red.

Dr. Will Myer simulated the EPR spectra for **13**. Table 5.7 lists the simulation parameters used.

Species		g_1	g_2	g_3	A_1	A_2	A_3
13	X/W	1.9928	1.9921	1.9626	181.5	96	262
	Linewidth	σ_{g1}	σ_{g2}	σ_{g3}	σ_{n1}	σ_{n2}	σ_{n3}
	value	0.0021	0.0017	0.0004	106	68	32

[a.] Linewidths are described with Gaussian distributions of both g-value (σ_g) and MHz (σ_n).

Table 5.7: Simulation parameter values for **13**.

5.3.1.2.5 Cyclic voltammetry studies on $[CpV(\eta^5\text{-}As_5)]^{2-}$ (13) and $[(CpV)_2(\eta^5\text{-}As_5)]^-$ (14)

Electrochemical cyclic voltammetry studies were recorded at a silver quasi-reference electrode, a glassy-carbon working electrode and a platinum auxiliary electrode on THF solutions containing $[K(2,2,2\text{-crypt})]_2$[**13**] and [K(2,2,2-crypt)][**14**]·2THF (Figure 5.21 and Figure 5.22). $[Bu_4N][PF_6]$ was used as the electrolyte and ferrocene as a reference, first the samples were run without the ferrocene and then with it, showing no difference in the voltammogram, indicating no chemical interaction with ferrocene. Additionally, cyclic voltammograms for **13** and **14** were run at 0.05 V/s, and the slower they were run the greater the reversibility of the processes. Furthermore, the "shape" of the voltammogram was not lost regardless of many cycles were measured.

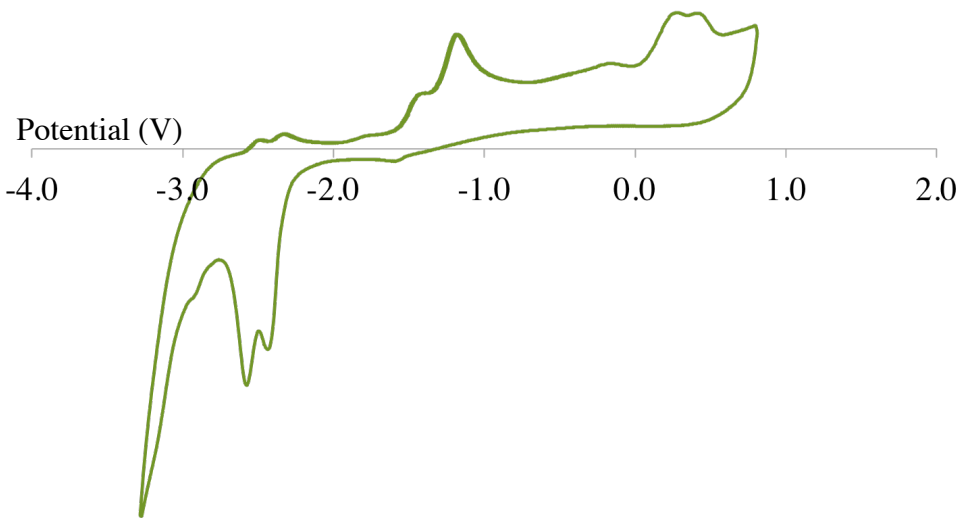

Figure 5.21: Cyclic voltammogram of **13**.

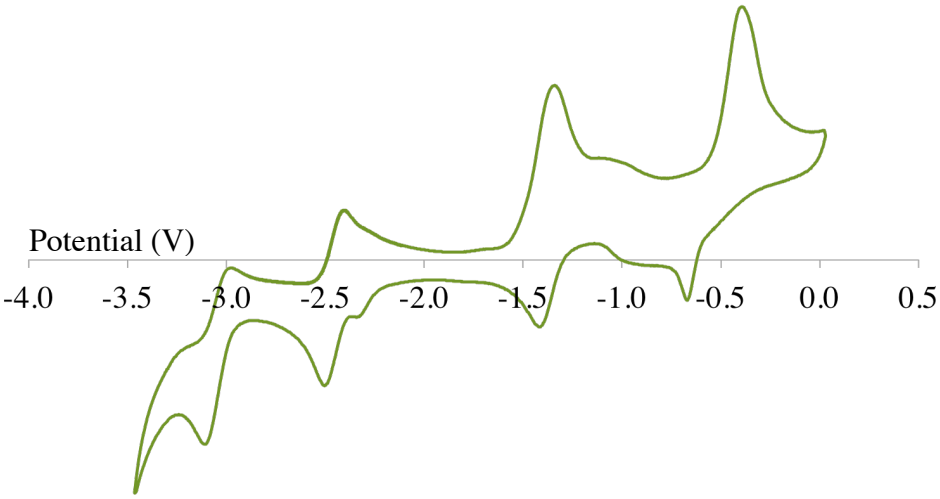

Figure 5.22: Cyclic voltammogram of **14**.

All attempts to chemically synthesise the oxidised or reduced species of **13** and **14** failed and only led to decomposition of the product. Table 5.8 shows the redox steps found for **13** and **14** with reference to ferrocene.

Compound	Oxidation (V)	Reduction (V)
13		–2.83 (qr)
		–2.53 (qr)
		–1.51 (qr)
		–1.18 (i)
	0.25 (i)	
	0.41 (i)	
14		–0.5342 (r)
		–1.3874 (r)
		–2.4562 (r)
		–3.0337 (r)

Table 5.8: Reduction and oxidation points for **13** and **14**. (qr = quasi-reversible step, i = irreversible step, r = reversible step).

The sandwich complex **13** shows three quasi-reversible reduction steps, one irreversible reduction step, plus two irreversible oxidation steps. As mentioned before, these steps were observed for long collection times at very slow scan rates, and the "shape" of the voltammogram did not change. This could be indicative that the steps

are on the metal centre, nevertheless the irreversibility of some process could be indicative that they correspond to the formation of polyarsenides clusters.

If the redox processes were occurring on the metal atom, since this cyclic voltammogram was run with crystals of $[K(2,2,2\text{-crypt})]_2$[**13**], the original oxidation state of the vanadium atoms is zero, which would imply that the reductions correspond to V^{-}, V^{2-}, $V^{3-}$and V^{4-}, whereas the oxidations would be V^{1+} and V^{2+}.

14 shows the possibility to undergo four reversible one-electron reduction steps. The reversibility and stability for long collection times could be indicative that all four redox processes are occurring on the metal. These reductions would correspond to V^{1+}/V^{0}, V^{0}/V^{0}, V^{0}/V^{1-} and V^{1-}/V^{1-}.

5.4 Conclusions

This chapter describes the characterisation of four new metal-mediated activation products of the $[E'_7]^{3-}$ cages. $[P_7]^{3-}$ reacts with 0.7 equivalents of VCp_2 to form the sandwich compound $[CpV(\eta^5\text{-}P_5)]^{-}$ (**11**), and with 2.5 equivalents of VCp_2 to form the triple-decker complex $[(CpV)_2(\eta^6\text{-}P_5)]^{-}$ (**12**). $[As_7]^{3-}$ has similar reactivity and forms $[CpV(\eta^5\text{-}As_5)]^{n-}$ (n = 1 (**13'**) and 2 (**13**)) and $[(CpV_2)(\eta^5\text{-}As_5)]^{-}$ (**14**). These novel complexes have been studied by X-ray crystallography, mass spectrometry, EPR spectroscopy (when relevant) and cyclic voltammetry. Despite having an even electron count, compounds **11** and **14**, did not show any NMR signal, this may be due to a high spin nature of the molecular orbitals. DFT calculations or SQUID measurements could help elucidate this problem.

The sandwich compounds **11** and **13** have a five-membered ring $[E'_5]^-$ and a Cp^- ligand coordinated in an η^5 fashion to a vanadium metal centre. When scaling-up to the triple-deckers, the phosphorus containing species, **12**, changes the nuclearity of the central ring from five to six atoms, whereas the arsenic system **14** does not. Also, **14** has a larger perimeter in the $[As_5]^-$ ring than **13**. Since the V–V distance in the triple-deckers can be described as a single bond in both cases, the expansion of the perimeter in the rings could be caused by the formation of a V–V interaction.

Cyclic voltammetry studies for **11** and **12** showed that these species are not very stable to the redox processes, since after two cycles no further redox character was observed, presumably due to decomposition in the complexes caused by the formation of polyphosphides. **11** shows the possibility for four completely irreversible one-electron reduction steps. **12** shows the possibility to undergo two reversible one-electron reduction steps, one irreversible reduction step and one irreversible oxidation step. On the other hand **13** and specially **14** were completely stable to the redox processes. The processes could be observed for prolongued periods of time and at a relatively slow scan rates (0.05 V/s). The sandwich complex **13** shows three quasi-reversible one-electron reduction steps, one irreversible one-electron reduction step plus two irreversible one-electron oxidation steps. **14** can undergo four reversible one-electron reduction steps.

5.5 References

(1) Huheey, J.E.; Keiter, E. A.; Keiter, R. L. New York, 1993.

(2) Von Schnering, H. G.; Wolf, J.; Weber, D.; Ramirez, R.; Meyer, T. *Angew. Chem. Int. Ed. Engl.* **1986**, *25* (4), 353–354.

(3) Kesanli, B.; Fettinger, J.; Scott, B.; Eichhorn, B. W. *Inorg. Chem.* **2004**, *43* (13), 3840–3846.

(4) Eichhorn, B. W.; Mattamana, S. P.; Gardner, D. R.; Fettinger, J. C. *J. Am. Chem. Soc.* **1998**, *120* (37), 9708–9709.

(5) Kesanli, B.; Fettinger, J.; Eichhorn, B. W. *J. Am. Chem. Soc.* **2003**, *125* (24), 7367–7376.

(6) Charles, S.; Eichhorn, B. W.; Bott, S. G. *J. Am. Chem. Soc.* **1993**, *115* (13), 5837–5838.

(7) Moses, M. J.; Fettinger, J. C.; Eichhorn, B. W. *Science* **2003**, *300* (5620), 778–780.

(8) Moses, M. J.; Fettinger, J.; Eichhorn, B. W. *J. Am. Chem. Soc.* **2002**, *124* (21), 5944–5945.

(9) Knapp, C. M.; Westcott, B. H.; Raybould, M. A. C.; McGrady, J. E.; Goicoechea, J. M. *Angew. Chem. Int. Ed.* **2012**, *51* (36), 9097–9100.

(10) Scherer, O. J.; Schwalb, J.; Wolmershäuser, G.; Kaim, W.; Gross, R. *Angew. Chem. Int. Ed. Engl.* **1986**, *25* (4), 363–364.

(11) Scherer, O. J.; Brück, T. *Angew. Chem. Int. Ed. Engl.* **1987**, *26* (1), 59–59.

(12) Scherer, O. J.; Brück, T.; Wolmershäuser, G. *Chem. Ber.* **1988**, *121* (5), 935–938.

(13) Scherer, O. J.; Blath, C.; Wolmershäuser, G. *J. Organomet. Chem.* **1990**, *387* (2), C21–C24.

(14) Bai, J.; Virovets, A. V.; Scheer, M. *Angew. Chem. Int. Ed.* **2002**, *41* (10), 1737–1740.

(15) Scheer, M.; Gregoriades, L. J.; Virovets, A. V.; Kunz, W.; Neueder, R.; Krossing, I. *Angew. Chem. Int. Ed.* **2006**, *45* (34), 5689–5693.

(16) Welsch, S.; Gröger, C.; Sierka, M.; Scheer, M. *Angew. Chem. Int. Ed.* **2011**, *50* (6), 1435–1438.

(17) Urnežius, E.; Brennessel, W. W.; Cramer, C. J.; Ellis, J. E.; Schleyer, P. von R. *Science* **2002**, *295* (5556), 832–834.

(18) Hughes, A. K.; Murphy, V. J.; O'Hare, D. *J. Chem. Soc. Chem. Commun.* **1994**, No. 2, 163–164.

(19) Scherer, O. J.; Wiedemann, W.; Wolmershäuser, G. *Chem. Ber.* **1990**, *123* (1), 3–6.

(20) Scherer, O. J.; Wiedemann, W.; Wolmershäuser, G. *J. Organomet. Chem.* **1989**, *361* (1), C11–C14.

(21) Rheingold, A. L.; Foley, M. J.; Sullivan, P. J. *J. Am. Chem. Soc.* **1982**, *104* (17), 4727–4729.

(22) Adams, R. D.; Collins, D. M.; Cotton, F. A. *Inorg. Chem.* **1974**, *13* (5), 1086–1090.

(23) DuBois, M. R.; VanDerveer, M. C.; DuBois, D. L.; Haltiwanger, R. C.; Miller, W. K. *J. Am. Chem. Soc.* **1980**, *102* (25), 7456–7461.

(24) Di Vaira, M.; Midollini, S.; Sacconi, L.; Zanobini, F. *Angew. Chem. Int. Ed. Engl.* **1978**, *17* (9), 676–677.

(25) Kudinov, A. R.; Loginov, D. A.; Starikova, Z. A.; Petrovskii, P. V.; Corsini, M.; Zanello, P. *Eur. J. Inorg. Chem.* **2002**, *2002* (11), 3018–3027.

(26) Rink, B.; Scherer, O. J.; Heckmann, G.; Wolmershauser, G. *Chem. Ber.* **1992**, *125* (5), 1011–1016.

(27) Scheer, M.; Heinl, S.; Balazs, G.; Bodensteiner, M. *Dalton Trans.* **2015**.

(28) Scherer, O. J.; Sitzmann, H.; Wolmershäuser, G. *Angew. Chem. Int. Ed. Engl.* **1985**, *24* (4), 351–353.

(29) Scherrer, O. J.; Sitzmann, H.; Wolmershäuser, G. *Angew. Chem. Int. Ed. Engl.* **1989**, *28* (2), 212–213.

(30) Scherer, O. J.; Schwalb, J.; Swarowsky, H.; Wolmershäuser, G.; Kaim, W.; Gross, R. *Chem. Ber.* **1988**, *121* (3), 443–449.

(31) Reddy, A. C.; Jemmis, E. D.; Scherer, O. J.; Winter, R.; Heckmann, G.; Wolmershaeuser, G. *Organometallics* **1992**, *11* (11), 3894–3900.

(32) Scherer, O. J.; Vondung, J.; Wolmershäuser, G. *Angew. Chem. Int. Ed. Engl.* **1989**, *28* (10), 1355–1357.

(33) Scherer, O. J.; Swarowsky, H.; Wolmershäuser, G.; Kaim, W.; Kohlmann, S. *Angew. Chem. Int. Ed. Engl.* **1987**, *26* (11), 1153–1155.

(34) Turbervill, R. S. P.; Goicoechea, J. M. *Chem. Rev.* **2014**, *114* (21), 10807–10828.

(35) Pyykkö, P.; Atsumi, M. *Chem. Eur. J.* **2009**, *15* (1), 186–197.

(36) Pyykkö, P.; Atsumi, M. *Chem. Eur. J.* **2009**, *15* (46), 12770–12779.

(37) For 192 crystallographically characterised complexes containing a $[P_5]^-$ ring (CSD version 5.36, November 2014): d(min) = 2.005; d(max) = 2.487; d(mean) = 2.123; Var(d) = 0.002; std.dev. = 0.047; mean dev. = 0.029.

(38) For 435 crystallographically characterised complexes containing a P–V single bond (CSD version 5.36, November 2014): d(min) = 2.33; d(max) = 2.826; d(mean) = 2.482; Var(d) = 0.005; std.dev. = 0.068 mean dev. = 0.051.

(39) For 2 crystallographically characterised complexes containing a $[P_6]$ ring (CSD version 5.36, November 2014): d(min) = 2.086; d(max) = 2.169; d(mean) = 2.127; Var(d) = 0.003; std.dev. = 0.059; mean dev. = 0.042.

(40) Goh, L. Y.; Chu, C. K.; Wong, R. C. S.; Hambley, T. W. *J. Chem. Soc. Dalton Trans.* **1989**, No. 10, 1951–1956.

(41) Goeta, A. E.; Howard, J. A. K.; Hughes, A. K.; O'Hare, D.; Copley, R. C. B. *J. Mater. Chem.* **2007**, *17* (5), 485–492.

(42) For 373 crystallographically characterised complexes containing a V–V bond (CSD version 5.36, November 2014): d(min) = 2.3; d(max) = 3.292; d(mean) = 2.844; Var(d)=0.037; std.dev. = 0.192; mean dev. = 0.149.

(43) For 21 crystallographically characterised complexes containing a $[As_5]^-$ ring (CSD version 5.36, November 2014): d(min) = 2.29; d(max) = 2.444; d(mean) = 2.351; var(d) = 0.002; std. dev. = 0.041; mean dev. = 0.033;

(44) For 7 crystallographically characterised complexes containing a As–V bond (CSD version 5.36, November 2014):d(min) = 2.486; d(max) = 2.646; d(mean) = 2.539; var(d) = 0.003; std. dev. = 0.052; mean dev. = 0.036;

Chapter 6 Conclusions

This thesis has focused on the reactivity of group 14 ($[E_9]^{4-}$ (E = Ge and Sn)) and 15 ($[E'_7]^{3-}$ (E'= P and As)) Zintl ions towards metal and semi-metal complexes. As was detailed in the introduction, this kind of reactivity can result in two types of products, coordination products or activation products.

This thesis has described the synthesis and characterisation of fourteen novel anionic species. Chapter two detailed the coordination chemistry of group 14 Zintl ions towards $Zn[N(SiMe_3)_2]_2$. K_4Ge_9 reacted to yield a typical $[Ge_9ZnR]^{3-}$ cluster $[Ge_9ZnN(SiMe_3)_2]^{3-}$ (**1**).[1,2] However, the tin analogue does not exhibit comparable reactivity and was found to lose a trimethylsilyl group to afford the paramagnetic cluster $[Sn_9ZnNSiMe_3]^{3-}$ (**2**). The transamination and desilylation of **1** were studied yielding $[Ge_9ZnNPh_2]^{3-}$ (**3**) and $[Ge_9ZnNSiMe_3]^{4-}$ (**4**), respectively.

Two activation products of group 14 Zintl ions are described in Chapter three. The first one is the non-deltahedral cluster $[Ru@Ge_{12}]^{3-}$ (**5**), which has an extraordinary structure with electron-precise bonds.[3] This type of connectivity has only been observed for two germanium clusters in the past ($[M@Ge_{10}]^{3-}$ (M = Fe and Co).[4,5] The second activation product described is $[Co_2@Ge_{16}]^{4-}$ (**6**).[6] The structure of this cluster

could not be determined by X-ray crystallography, but extensive DFT calculations revealed that the cluster exhibits a three-connected structure as well.

Chapter four describes coordination chemistry of $[HP_7]^{2-}$ towards group 14 amides $E[N(SiMe_3)_2]_2$ yielding the η^2 (or κ^2) coordination compounds $[P_7EN(SiMe_3)_2]^{2-}$ (E = Ge (**7**) and Sn(**8**)). **7** analogue quickly dimerises at room temperature into a more thermodynamically stable product loosing an $[N(SiMe_3)_2]^-$ group forming $[(P_7)_2Ge_2N(SiMe_3)_2]^{3-}$ (**10**).

Finally Chapter five described four activation products of the reaction of $[E'_7]^{3-}$ (E' = P and As) towards different stoichiometric amounts of VCp_2. This reaction yields the sandwich compounds $[CpV(\eta^5\text{-}E'_5)]^{n-}$ (E' = P: n = 1 (**11**); E' = As: n = 1 (**13'**) and 2 (**13**)) and the triple-decker compounds $[(CpV)_2(\eta^x\text{-}E'_x)]^-$ (E' = P: x = 6 (**12**); E' = As: x = 5 (**14**)). These clusters represent the first examples of activation compounds where the product has fewer E' atoms than the starting material.

This research could potentially be extended to other transition metals and semi-metals in the future.

6.1 References

(1) Goicoechea, J. M.; Sevov, S. C. *Organometallics* **2006**, *25* (19), 4530–4536.

(2) Zhou, B.; Denning, M. S.; Jones, C.; Goicoechea, J. M. *Dalton Trans*. **2009**, No. 9, 1571–1578.

(3) Espinoza-Quintero, G.; Duckworth, J. C. A.; Myers, W. K.; McGrady, J. E.; Goicoechea, J. M. *J. Am. Chem. Soc*. **2014**, *136* (4), 1210–1213.

(4) Zhou, B.; Denning, M. S.; Kays, D. L.; Goicoechea, J. M. *J. Am. Chem. Soc*. **2009**, *131* (8), 2802–2803.

(5) Wang, J.-Q.; Stegmaier, S.; Fässler, T. F. *Angew. Chem. Int. Ed.* **2009**, *48* (11), 1998–2002.

(6) Jin, X.; Espinoza-Quintero, G.; Below, B.; Arcisauskaite, V.; Goicoechea, J. M.; McGrady, J. E. *J. Organomet. Chem.* **2015**, *792*, 149–153.

Chapter 7 Experimental

7.1 General synthetic considerations

7.1.1 Manipulation of air- and moisture-sensitive compounds

Due to the highly air- and moisture-sensitive nature of many of the reagents and products described in this thesis, all manipulations were carried out under an inert atmosphere using standard Schlenk-line or glovebox techniques (MBraun UNIlab glovebox maintained at < 0.1 ppm O_2 and < 0.1 ppm H_2O).

Chemical	Source	Purity	Purification Procedure
K_4Ge_9	Synthesised[1]	Undetermined	Used as obtained
K_4Sn_9	Synthesised[1,2]	Undetermined	Used as obtained
K_3P_7	Synthesised[3]	Undetermined	Used as obtained
K_3As_7	Synthesised[4]	Undetermined	Used as obtained
K	Strem	99.95%	Used as received
Ge	Strem	99.99%	Used as received
Sn	Strem	99.8%	Used as received
P	Aldrich	99.99%	Used as received
As	Alfa Aesar	99%	Used as received
Ethylenediamine	Aldrich	99%	Distilled over Na metal
Pyridine	Rathburn	99.9%	Distilled over CaH_2
Toluene	Rathburn	99.9%	Purified through an MBraun MB SPS800 solvent purification system

THF	Rathburn	99.9%	Distilled over Na metal/benzophenone
Diethyl ether	Fisher	Pesticide residue grade	Purified through an MBraun MB SPS800 solvent purification system
DMF	Rathburn	99.9%	Purified through an MBraun MB SPS800 solvent purification system
Hexane	Rathburn	99.9%	Purified through an MBraun MB SPS800 solvent purification system
d_5-pyridine	Cambridge Isotope Laboratories, Inc.	99.5%	Dried over CaH_2, then vacuum distilled
2,2,2-crypt	VWR	99%	Used as received
18-crown-6	Alfa Aesar	99%	Dried under vacuum
15-crown-5	Alfa Aesar	98%	Used as received
$K[N(SiMe_3)_2]$	Aldrich	95%	Used as received
$Zn[N(SiMe_3)_2]_2$	Synthesised[5]	Undetermined	Used as obtained
$ZnCl_2$	Strem	97%	Used as received
$Li[N(SiMe_3)]$	Aldrich	97%	Used as received
$[Ru(PPh_3)_3Cl_2$	Strem	99%	Used as received
$[Ru(COD)(\eta^3$-$CH_2C(CH_3)CH_2)_2]$	Synthesised[6]	Undetermined	Used as obtained
$[Ru(COD)Cl_2]_n$	Synthesised[7]	Undetermined	Used as obtained
3-chloro-2-methylpropene	Alfa Aesar	98%	Used as received
1,5-cyclooctadiene	Aldrich	99%	Used as received
$RuCl_3$·xH2O	Alfa Aesar	99%	Used as received
$[Co(PEt_2Ph)_2(mes)_2]$	Synthesised[8]	Undetermined	Used as obtained
Mg turnings	Fisher	General purpose grade	Used as received
PEt_2Ph	Alfa Aesar	97%	Used as received
$CoBr_2$	Alfa Aesar	97%	Used as received
$Ge(N(SiMe_3)_2)_2$	Synthesised[9]	Undetermined	Used as obtained
$GeCl_2$·dioxane	Aldrich	Undetermined	Used as received
$Sn(N(SiMe_3)_2)_2$	Aldrich	98%	Used as received
$Pb(N(SiMe_3)_2)_2$	Synthesised[9]	Undetermined	Used as obtained
$PbCl_2$	Alfa Aesar	99%	Used as received
[K(18-crown-	Synthesised[10]	Undetermined	Used as obtained

$6)]_2[HP_7]\cdot py$			
$[K(15\text{-crown-}5)_2]_2[HP_7]\cdot py$	Synthesised	Undetermined	Used as obtained
VCp_2	VWR	95%	Used as received
$[K(18\text{-crown-}6)]_3[P_7]$	Synthesised	Undetermined	Used as obtained
Et_2O	Aldrich	99.9%	Used as received

Table 7.1: Chemicals used in this research.

7.2 Syntheses

7.2.1 Zintl phases

The intermetallic precursors, K_4E_9 (E = Ge and Sn) and $K_3E'_7$ (E' = P and As), were synthesised according to previously reported synthetic procedures by combining stoichiometric mixtures of the elements at hight temperatures (K_3P_7: 600 °C, K_3As_7: 550 °C and K_4E_9: 900°C) for 72 h in sealed niobium containers that were jacketed in evacuated, flame-sealed silica ampoules.[1,2,3,4]

7.2.2 Zintl Ions Precursors

7.2.2.1 $[K(18\text{-crown-}6)]_2[HP_7]$

K_3P_7 (8.00 g, 23.9 mmol) was slurried in pyridine (80 mL) and deionised water (0.96 mL, 47.8 mmol) was added dropwise, resulting in an orange solution that was stirred for 5 min. 18-crown-6 (12.62 g, 47.8 mmol) was added to the reaction mixture which was stirred for further 5 min. The solution was filtered and reduced in volume under vacuum to 20 mL. Toluene (300 mL) was added to precipitate the product as an orange microcrystalline

solid.[10] Crystals suitable for X-ray diffraction were obtained by layering a pyridine solution with toluene in an airtight crystallisation ampoule. Yield 17.9 g (89%).

7.2.2.2 $[K(15\text{-crown-}5)_2]_2[HP_7]$

K_3P_7 (400 mg, 1.19 mmol) was slurried with pyridine (30 mL) and deionised water (43 μL, 2.39 mmol) was added, resulting in an orange solution that was stirred for 1 h. 15-crown-5 (0.95 mL, 4.79mmol) was added to the reaction mixture which was stirred for further 5 min. The solution was filtered and reduced in volume under vacuum to 10 mL. Toluene (100 mL) was added to precipitate the product as an orange microcrystalline solid. Crystals suitable for X-ray diffraction were obtained by layering a pyridine solution with toluene in an airtight crystallisation ampoule. Yield 1.07g (76%).

7.2.2.3 $[K(18\text{-crown-}6)]_3[P_7]$

$[K(18\text{-crown-}6)]_2[HP_7]$ (4.0 g, 4.85 mmol), KHMDS (1.07 g, 5.36 mmol) and 18-crown-6 (1.42 g, 5.36 mmol) were weighed into a Schlenk tube and slurried with THF (40 mL). Pyridine (80 mL) was added until the slurry turned into a dark-red solution, which was stirred for 12 h. All volatiles were removed under vacuum and the remaining oil was washed with THF (3 × 40 mL) and Et_2O (3 × 40 mL) to remove amine by-products and excess base. The bright yellow powder obtained was dried under vacuum for 1 h. Yield 5.02 g (92%).

7.2.3 Organometallic precursors

7.2.3.1 $Zn[N(SiMe_3)_2]_2$

$Zn[N(SiMe_3)_2]_2$ was prepared using a modification of a reported synthetic procedure.[5] A mixture of $ZnCl_2$ (2.0 g, 14 mmol) and $LiN(SiMe_3)_2$ (4.9 g, 29 mmol) in 10 mL of diethyl ether was left to stir for 3 h. The solution was filtered into an H-cell and reduced to dryness under vacuum. It was distilled under vacuum (5.0×10^{-2} mbar, 80 ºC) to give $Zn[N(SiMe_3)_2]_2$ as a colourless liquid yielding 4.3 g (80%).

7.2.3.2 $[Ru(COD)(\eta^3\text{-}CH_2C(CH_3)CH_2)_2]$

$[Ru(COD)(\eta^3\text{-}CH_2C(CH_3)CH_2)_2]$ was synthesised from $[Ru(COD)Cl_2]_n$ and 2-methylpropenylmagnesium chloride according to a procedure reported by James and co-workers.[6] $[Ru(COD)Cl_2]_n$ was prepared according to a synthetic procedure previously reported by Gênet *et al*.[7] A mixture of $RuCl_3 \cdot xH_2O$ (2.45 g, 18 mmol) and 1,5-cyclooctadiene (9 mL, 74 mmol) in ethanol (100 mL) was heated under reflux for 3 days. The resulting brown precipitate was separated by filtration, washed twice with ethanol and dried under vacuum. 2-methylpropenylmagnesium chloride was prepared *in situ* by stirring magnesium turnings (440 mg, 18.3 mmol) and 3-chloro-2-methylpropene (1.2 mL, 12.3 mmol) in THF (6 mL) for 30 min in the presence of an iodine crystal. The solution was filtered and added dropwise to a suspension of $[Ru(COD)Cl_2]n$ (280 mg, 1 mmol) in THF:diethyl ether (15 mL:10 mL). The mixture was stirred for 20 min, after which diethyl ether (30 mL) was added, resulting in the precipitation of a white solid. The colourless solution was filtered and hydrolysed with deionised water (50 mL). The aqueous layer was washed twice with diethyl ether (50 mL), and then the organic layers were collected and

dried over $MgSO_4$. The solution was filtered through Celite, and the solvent was removed *in vacuo*, yielding 242 mg of the desired product (76% yield).

7.2.3.3 $[Co(PEt_2Ph)_2(mes)_2]$

$[Co(PEt_2Ph)_2(mes)_2]$ was synthesised according to a previously reported synthetic procedure.[8] $[Co(PEt_2Ph)_2Br_2]$ was prepared by adding PEt_2Ph (4 mL, 0.023 mol) to a solution of $CoBr_2$ (2.5 g, 0.011 mol) in ethanol (60 mL). The reaction mixture was stirred for 30 min, and then all volatiles were removed under vacuum, yielding a green solid. 2-mesitylmagnesium bromide was prepared *in situ* by stirring magnesium turnings (1.504 g, 0.062 mol) and 2-bromomesitylene (6.3 mL, 0.041 mol) in THF (30 mL) at 0 °C overnight. This solution was subsequently filtered and cooled to –30 °C. A solution of $[Co(PEt_2Ph)_2Br_2]$ in benzene (60 mL) was added dropwise, and the reaction mixture was allowed to slowly warm up to room temperature. The resulting brown solution was stirred under argon for 40 min, before being cooled to –30 °C and hydrolysed with dilute HCl. The mixture was warmed up to room temperature, and benzene (60 mL) was added. The organic layer was washed twice with deionised water, dried over $MgSO_4$ and filtered, and the solid residue was washed 3 times with benzene. The filtrate was dried under vacuum, yielding 5.24 g of the desired product (73% yield).

7.2.3.4 $Ge[N(SiMe_3)_2]_2$

$Ge[N(SiMe_3)_2]_2$ was prepared using a modified literature procedure.[9] A mixture of $GeCl_2$(1,4-dioxane)$_2$ (4 g, 12.5 mmol) and $LiN(SiMe_3)_2$ (4.2 g, 25 mmol) in diethyl ether (15 mL) was left to stir for 3 h. The solution was filtered into an H-cell and reduced to dryness under vacuum. It was distilled under static vacuum (5.0×10^{-2} mbar, 80 ºC) to

give $Ge[N(SiMe_3)_2]_2$ as an orange liquid at room temperature yielding 4.2 g of the desired product (85%).

7.2.3.5 $Pb[N(SiMe_3)_2]_2$

$Pb[N(SiMe_3)_2]_2$ was prepared using a modified literature procedure.[9] A mixture of $PbCl_2$ (4 g, 14.4 mmol) and $LiN(SiMe_3)_2$ (4.8 g, 28 mmol) in diethyl ether (15 mL) was stirred for 3 h. The solution was filtered into an H-cell and reduced to dryness under vacuum. It was distilled under static vacuum (5.0×10^{-2} mbar, 80 ºC) to give $Pb[N(SiMe_3)_2]_2$ as a yellow liquid. The liquid was frozen with liquid nitrogen under static vacuum and then thawed until a yellow low melting-point solid was obtained yielding 5.9 g of the desired product (78%).

7.2.4 Compounds discussed in Chapter two

7.2.4.1 $[K(2,2,2\text{-crypt})]_3[Ge_9ZnN(SiMe_3)_2]\cdot 3tol$ (1)

K_4Ge_9 (100 mg, 0.12 mmol) and 2,2,2-crypt (186 mg, 0.49 mmol) were dissolved in ethylenediamine (5 mL) to form a black solution, which was stirred for approximately 5 min. $Zn[N(SiMe_3)_2]_2$ (142 mg 0.37 mmol) was added dropwise and the resulting orange suspension was stirred for 2 h. The ethylenediamine solution was filtered and all volatiles were removed under vacuum. The remaining oil was washed with THF (10 mL) and the resulting orange solid dissolved in pyridine. The solution was filtered into a crystallisation ampoule and layered with toluene. After several days orange block-like crystals of $[K(2,2,2\text{-crypt})]_3[Ge_9ZnN(SiMe_3)_2]\cdot 3tol$ suitable for X-ray diffraction were obtained in a yield of 78 mg (30%). Anal. Calcd. for $[K(2,2,2\text{-crypt})]_3[Ge_9ZnN(SiMe_3)_2]$

($C_{60}H_{117}Ge_9K_3N_7O_{18}Si_2Zn$): C 33.90%; H 5.97%; N 4.63%; found C 33.95%; H 5.57%; N 4.64%. ^{1}H NMR (500 MHz, d_5-pyridine, 298 K): δ (ppm) 3.44 (s, 24H; 2,2,2-crypt), 3.37 (s, 24H; 2,2,2-crypt), 2.35 (s, 24H; 2,2,2-crypt), 1.11 (s, 6H; $[Ge_9ZnN(SiMe_3)_2]^{3-}$). $^{13}C\{^1H\}$ NMR (128.5 MHz, d_5-pyridine, 298 K): δ (ppm) 71.23 (2,2,2-crypt), 68.4 (2,2,2-crypt), 54.6 (2,2,2-crypt), 10.2 ($[Ge_9ZnN(SiMe_3)_2]^{3-}$). ESI-MS (negative ion mode) (DMF): *m/z* 876.9 (100%) $[Ge_9ZnNSi(Me_3)_2]^-$, 653.1 (96.4%) $[Ge_9]^-$, 692.0 (71.4%) $\{K(Ge_9)\}^-$, 916.0 (32.1%) $\{K(Ge_9ZnN(SiMe_3)_2)\}^-$, 809.6 (28.1%) $[Ge_9ZnNSiMe_3]^-$, 846.9 (27.1%) $\{[K(Ge_9ZnNSiMe_3)]\}^-$, 1294.2 (25%) $\{[K(2,2,2\text{-crypt})][Ge_9ZnN(SiMe_3)_2]\}^-$, 1070.1 (23.6%) $\{[K(2,2,2\text{-crypt})][Ge_9]\}^-$, 763.9 (17.14%) $\{K(Ge_{10})\}^-$, 1709.2 (10%) $\{[K(2,2,2\text{-crypt})]_2[Ge_9ZnN(SiMe_3)_2]\}^-$. ESI-MS (positive ion mode) (DMF): *m/z* 2540.9 (100%) $\{[K(2,2,2\text{-crypt})]_4[Ge_9ZnN(SiMe_3)_2]\}^+$, 1900.0 (78.3%) $\{[K(2,2,2\text{-crypt})]_4[Ge_9]\}^+$, 2968.9 (42.1%) $\{[K(2,2,2\text{-crypt})]_4[Ge_9ZnNSiMe_3]\}^+$.

7.2.4.2 $[K(2,2,2\text{-crypt})]_3[Sn_9ZnNSiMe_3]\cdot 3tol$ (2)

K_4Sn_9 (74 mg, 0.06 mmol) and 2,2,2-crypt (100 mg, 0.24 mmol) were dissolved in ethylenediamine (5 mL) to form a black solution, which was stirred for approximately 5 min. $Zn[N(SiMe_3)_2]_2$ (27 mg, 0.07 mmol) was added dropwise and the resulting brown solution was stirred for 2 h. The ethylenediamine solution was filtered into a crystallisation ampoule, layered with toluene. After several days black block-like crystals of $[K(2,2,2\text{-crypt})]_3[Sn_9ZnNSiMe_3]\cdot 3tol$ suitable for X-ray diffraction were obtained in a yield of 96 mg (55%). Anal. Calcd. for $[K(2,2,2\text{-crypt})]_3[Sn_9ZnNSiMe_3]\cdot tol$ ($C_{64}H_{125}K_3N_7O_{18}SiSn_9Zn$): C 30.30%; H 4.92%; N 3.83%; found: C 29.85%; H 4.84%; N 3.74%. ESI-MS (negative ion mode) (DMF): *m/z* 1222.8 $[Sn_9ZnNSiMe_3]^-$, 1637.2 $\{[K(2,2,2\text{-crypt})][Sn_9ZnNSiMe_3]\}^-$.

7.2.4.3 Synthesis of $Cs[K(2,2,2\text{-crypt})]_3[Ge_9ZnNSiMe_3]$ (3)

$[K(2,2,2\text{-crypt})]_3[Ge_9ZnN(SiMe_3)_2]\cdot 3tol$ (70 mg, 0.032 mmol) and CsF (10 mg, 0.066 mmol) were dissolved in pyridine (3 ml) and left to stir for one hour. All volatiles were removed under vacuum. The resulting black oil was washed with Et_2O (10 ml) and dried under dynamic vacuum. The resulting green powder $Cs[K(2,2,2\text{-crypt})]_3[Ge_9ZnNSiMe_3]$ was isolated in a yield of 45 mg (63 %). ^{1}H NMR (400 MHz, d_5-pyridine, 298 K): δ (ppm) 3.44 (s, 24H; 2,2,2-crypt), 3.37 (s, 24H; 2,2,2-crypt), 2.35 (s, 24H; 2,2,2-crypt), 1.15 (s, 9H; $[Ge_9ZnNSiMe_3]^{4-}$). $^{13}C\{^1H\}$ NMR (128.5 MHz, d_5-pyridine, 298 K): δ (ppm) 71.2 (2,2,2-crypt), 68.4 (2,2,2-crypt), 54.6 (2,2,2-crypt), 16.05 ($[Ge_9ZnNSiMe_3]^{4-}$). ESI-MS (negative ion mode) (DMF): *m/z* 806.6 (100%) $[Ge_9ZnNSiMe_3]^-$, 653.1 (50%) $[Ge_9]^-$, 691.2 (16%) $\{K(Ge_9)\}^-$. ESI-MS (positive ion mode) (DMF): *m/z* 2468.6 (100%) $\{[K(2,2,2\text{-crypt})]_4[Ge_9ZnNSiMe_3]\}^+$, 1900.0 (21%) $\{[K(2,2,2\text{-crypt})_4[Ge_9]\}^+$.

7.2.4.4 $[K(2,2,2\text{-crypt})]_3[Ge_9ZnNPh_2]$ (4)

$[K(2,2,2\text{-crypt})]_3[Ge_9ZnN(SiMe_3)_2]\cdot 3tol$ (90 mg, 0.042 mmol) and $HNPh_2$ (26 mg, 0.153 mmol) were dissolved in pyridine (3 ml) and left to stir for one hour. All volatiles were removed under vacuum. The resulting black oil was washed with Et_2O (10 ml) and dried under dynamic vacuum. The resulting black powder $[K(2,2,2\text{-crypt})]_3[Ge_9ZnNPh_2]$ was isolated in a yield of 52 mg (57 %). ^{1}H NMR (400 MHz, d_5-pyridine, 298 K): δ (ppm) 3.44 (s, 24H; 2,2,2-crypt), 3.37 (s, 24H; 2,2,2-crypt), 2.35 (s, 24H; 2,2,2-crypt), 6.80 (t, 1H; *para*-C_6H_5), 7.3 (t, 2H; *meta*-C_6H_5), 7.57 (t, 2H-*o*; *ortho*-C_6H_5). $^{13}C\{^1H\}$ NMR (128.5 MHz, d_5-pyridine, 298 K): δ (ppm) 71.23 (2,2,2-crypt), 68.4 (2,2,2-crypt), 54.6 (2,2,2-crypt), 117.57 (*para*-C_6H_5), 118.49 (*ortho*-C_6H_5), 129.98 (*meta*-C_6H_5), 149.8 (*ipso*-C_6H_5). ESI-MS (negative ion mode) (DMF): *m/z* 652.3 (100%) $[Ge_9]^-$, 885.8 (87%)

$[Ge_9ZnNPh_2]^-$, 724.1 (44%) $[Ge_{10}]^-$, 691.2 (23%) $\{KGe_9\}^-$ ESI-MS (positive ion mode) (DMF): *m/z* 2548.7 (100%) $\{[K(2,2,2\text{-crypt})]_4[Ge_9ZnPh_2]\}^+$, 1899 (34%) $\{[K(2,2,2\text{-crypt})]_3[Ge_9]\}^+$, 1971 (21%) $\{[K(2,2,2\text{-crypt})]_3[Ge_{10}]\}^+$.

7.2.5 Compounds discussed in Chapter three

7.2.5.1 $[K(2,2,2\text{-crypt})]_3[Ru@Ge_{12}]\cdot 4py$ (5)

K_4Ge_9 (81 mg, 0.1 mmol) and 2,2,2-crypt (111 mg, 0.3 mmol) were stirred in ethylenediamine (4 mL) for 5 min giving rise to a dark-brown solution. A THF (2 mL) solution of the organometallic precursor $[Ru(1,5\text{-COD})(\eta^3\text{-}CH_3C(CH_2)_2)_2]$ (31 mg, 0.1 mmol) was added dropwise to the ethylenediamine solution. The mixture was stirred at 65°C for 5 h and filtered. All volatiles were removed under reduced pressure to leave a brown powder, which was washed with THF (10 mL). The resulting solid was dissolved in pyridine (5 mL) and filtered into a crystallisation ampoule and layered with toluene. After 2 weeks dark brown block-like crystals of $[K(2,2,2\text{-crypt})]_3[Ru@Ge_{12}]\cdot 4py$ suitable for X-ray diffraction were obtained. This sample crystallised alongside orange block-like crystals of $[K(2,2,2\text{-crypt})]_2[Ge_5]$. ESI-MS (negative ion mode) (DMF): *m/z* 972.7 $[Ru@Ge_{12}]^-$, 1387.8 $\{[K(2,2,2\text{-crypt})][Ru@Ge_{12}]\}^-$; ESI-MS (positive ion mode) (DMF): *m/z* 2632.0 $\{[K(2,2,2\text{-crypt})]_4[Ru@Ge_{12}]\}^+$.

7.2.5.2 $[K(2,2,2\text{-crypt})]_4[Co_2@Ge_{16}]\cdot 2en$ (6)

K_4Ge_9 (81 mg, 0.1 mmol) and 2,2,2-crypt (111 mg, 0.3 mmol) were stirred in ethylenediamine (4 mL) for 5 min giving rise to a dark-brown solution. A THF (2 mL) solution of the organometallic precursor $[Co(PPhEt_2)_2Mes_2]$ (63 mg, 0.1 mmol) was added

dropwise to the ethylenediamine solution. The mixture was stirred for 4 h at room temperature after which it was filtered into an airtight crystallisation ampoule and layered with toluene. After 2 weeks dark brown block-like crystals of [K(2,2,2-crypt)]$_4$[Co_2@Ge_{16}]·en suitable for X-ray diffraction were obtained. ESI-MS (negative ion mode) (DMF): *m/z* 1279.4 [Co_2@Ge_{16}]$^-$.

7.2.6 Compounds discussed in Chapter four

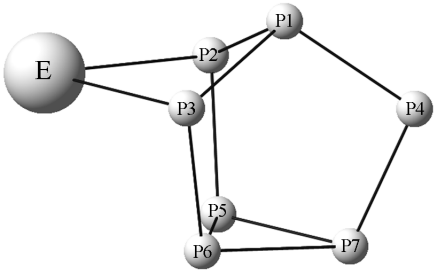

Figure 7.1: Diagram showing labelling used for ^{31}P NMR spectroscopic studies for compounds [$P_7EN(SiMe_3)_2$]$^{2-}$ (E = Ge (**7**), Sn (**8**) and Pb (**9**)).

7.2.6.1 [K(18-crown-6)]$_2$[$P_7GeN(SiMe_3)_2$]·2py (7)

Ge[$N(SiMe_3)_2$]$_2$ (38 mg, 0.097 mmol) and [K(18-crown-6)]$_2$[HP_7] (80 mg, 0.136 mmol) were dissolved in pyridine (1 mL) yielding a light orange solution. Toluene was added immediately to the pyridine solution to precipitate the product yielding an orange powder. Light-orange block-like crystals of [K(18-crown-6)]$_2$[$P_7GeN(SiMe_3)_2$]·2py were grown by vapour diffusion of toluene into a very concentrated pyridine reaction mixture at –35 ºC over a month. Yield: 12 mg (9%). CHN analysis could not be obtained due to transformation to the thermodynamic product **10**. ^{1}H NMR (500 MHz, d_5-pyridine, 298 K): δ (ppm) 3.56 (s, 24H; 18-crown-6), 0.87 (s, 18H; [$P_7GeN(SiMe_3)_2$]$^{2-}$). ^{31}P{^{1}H} NMR (202.4 MHz, d_5-pyridine, 298 K): δ (ppm) 72.3 (m, 1P; P4), 8.2 (m, 2P; P2, P3), –46.2 (m,

1P; P1), –61.0 (m, 1P; P7), –189.5 (t, 2P; P5, P6). $^{13}C\{^{1}H\}$ NMR (125.8 MHz, d_5-pyridine, 298 K): δ (ppm) 71.0 (18-crown-6), 7.9 ($[P_7GeN(SiMe_3)_2]^{2-}$). ^{29}Si NMR (99.32 MHz, d_5-pyridine, 298 K): δ (ppm) –6.9 (s, $[P_7GeN(SiMe_3)_2]^{-}$). ESI-MS (negative ion mode) (DMF): *m/z* 216.5 (98%) $[P_7]^{-}$, 291.6 (100%) $[Ge(P_7)]^{-}$, 452.2 (43%) $[P_7GeN(SiMe_3)_2]^{-}$.

7.2.6.2 $[K(18\text{-crown-6})]_2[P_7SnN(SiMe_3)_2]\cdot 2py$ (8)

$Sn[N(SiMe_3)_2]_2$ (60 mg, 0.136 mmol) and $[K(18\text{-crown-6})]_2[HP_7]$ (112 mg, 0.136 mmol) were dissolved in pyridine (1 mL) yielding an orange solution. The reaction mixture was stirred for 5 min. All volatiles were removed under vacuum and the resulting orange oil was washed with diethyl ether (10 mL) and dried under vacuum to yield an orange powder. Orange block-like crystals of $[K(18\text{-crown-6})]_2[P_7SnN(SiMe_3)_2]\cdot 2py$ were grown by vapour diffusion of toluene into a very concentrated pyridine reaction mixture with a yield of 132 mg (76%). Anal. Calcd. for $[K(18\text{-crown-6})]_2[P_7SnN(SiMe_3)_2]$ ($C_{30}H_{66}K_2NO_{12}P_7Si_2Sn$): C 32.68%, H 6.03%, N 1.27%; found: C 32.14%, H 5.67%, N 1.46%. ^{1}H NMR (500 MHz, d_5-pyridine, 298 K): δ (ppm) 3.51 (s, 24H; 18-crown-6), 0.85 (s, 18H; $[P_7SnN(SiMe_3)_2]^{2-}$). $^{31}P\{^{1}H\}$ NMR (202.4 MHz, d_5-pyridine, 298 K): δ (ppm) 62.5 (t, 1P; P4), –18.1 (m, 2P; P2, P3), –38.7 (m, 1P; P1), –81.4 (m, 1P; P7), –192.0 (t, 1P; P5, P6). $^{13}C\{^{1}H\}$ NMR (125.8 MHz, d_5-pyridine): δ (ppm) 71.0 (18-crown-6), 8.02 ($[P_7Sn(N(SiMe_3)_2)]^{2-}$). ^{119}Sn NMR (186.43 MHz, d_5-pyridine, 298 K): δ (ppm) –61.1 ($[P_7Sn(N(SiMe_3)_2)]^{2-}$). ^{29}Si NMR (99.32 MHz, d_5-pyridine, 298 K): δ (ppm) –7.3 (s, $P_7Sn[N(SiMe_3)_2]^{-}$). ESI-MS (negative ion mode) (DMF): *m/z* 337.4 (100%) $[P_7Sn]^{-}$, 495.9 (18%) $[P_7SnN(SiMe_3)_2]^{-}$. ESI-MS (positive ion mode) (DMF): *m/z* 1405.6 $\{[K(18\text{-crown-6})]_3[P_7SnN(SiMe_3)_2]\}^{+}$.

7.2.6.3 $[K(18\text{-crown-6})]_2[P_7Pb(N(SiMe_3)_2]$ (9)

$Pb[N(SiMe_3)_2]_2$ (44 mg, 0.084 mmol) and $[K(18\text{-crown-6})]_2[HP_7]$ (70 mg, 0.084 mmol) were dissolved pyridine (1 mL) yielding a dark red solution. All volatiles were removed under vacuum and the resulting oil was washed with diethyl ether (10 mL) to give a dark red powder. Crystals of this product could not be isolated. ^{1}H NMR (499.93 MHz, d_5-pyridine, 298 K): δ (ppm) 3.54 (s, 24H; 18-crown-6), 0.81 (s, 18H; $[P_7PbN(SiMe_3)_2]^{2-}$). ^{31}P{H} NMR (161.98 MHz, d_5-pyridine, 298 K): δ (ppm) 59.7 (t, 1P; P4), –17.2 (broad m, 2P; P2, P3), –37.9 (broad m, 1P; P1), –84.5 (broad m, 1P; P7), –197.5 (broad m, 2P; P5, P6). ^{13}C{^{1}H} NMR (125.8 MHz, d_5-pyridine, 298 K): δ (ppm) 70.9 (18-crown-6), 8.13 ($[P_7PbN(SiMe_3)_2]^{2-}$). ^{29}Si NMR (99.32 MHz, d_5-pyridine): δ (ppm) –7.1 (s, $[P_7PbN(SiMe_3)_2]^{-}$). ESI-MS (negative ion mode) (DMF): *m/z* 288.9 (20%) $[P_7(SiMe_3)]^{-}$, 360.1 (100%) $[P_7(SiMe_3)_2]^{-}$, 426.0 (70%) $[P_7Pb]^{-}$.

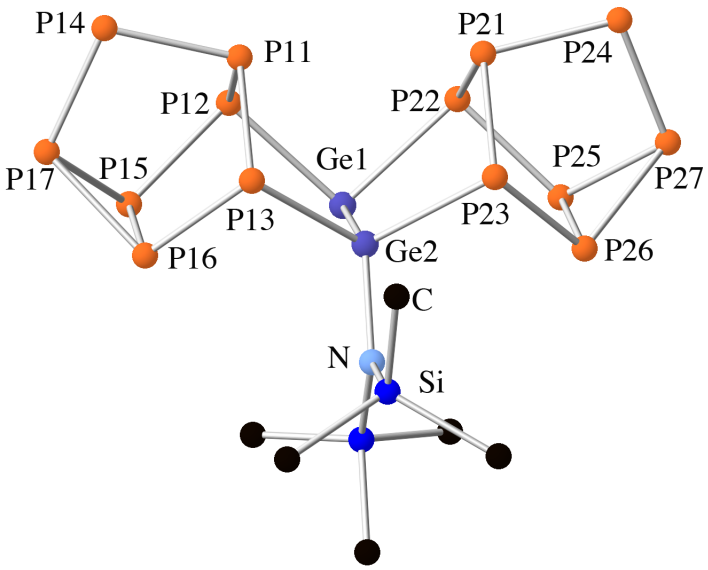

Figure 7.2: Ball and stick diagram of $[(P_7)_2(Ge)_2N(SiMe_3)_2]^{3-}$

7.2.6.4 $[K(15\text{-crown-}5)_2]_3[(P_7)_2Ge_2N(SiMe_3)_2]$ (10)

$Ge[N(SiMe_3)_2]_2$ (66 mg, 0.168 mmol) and $[K(15\text{-crown-}5)_2]_2[HP_7]$ (198 mg, 0.168 mmol) were dissolved in pyridine (2 mL) yielding a light orange solution of **7**. The reaction mixture was then monitored by ^{31}P NMR for a 94 h period and a gradual colour change from light orange to dark red was observed. All volatiles were removed under vacuum and the resulting orange oil was washed with diethyl ether (10 mL) to give rise to an orange powder. The orange powder was dissolved in pyridine and filtered into an airtight ampoule and layered with diethyl ether, after three days orange needles suitable for X-ray crystallography were found. Yield 130 mg (94%). Anal. Calcd. for $[K(15\text{-crown-}5)_2]_3[(P_7)_2Ge_2N(SiMe_3)_2]$ ($C_{66}H_{138}Ge_2K_3NO_{30}P_{14}Si_2$): C 36.40%, H 6.39%, N 0.64%; found: C 36.5%, H 6.25%, N 0.96%. ^1H NMR (500 MHz, d_5-pyridine, 298 K): δ (ppm) 3.61 (s, 40H; 15-crown-5), 1.08 (s, 18H; $[(P_7)_2Ge_2N(SiMe_3)_2]^{3-}$). $^{31}P\{^1H\}$ NMR (202.4 MHz, d_5-pyridine, 298 K): δ (ppm) 31.3 (t, 1P; P2), –27.2 (m, 1P; P1), –29.3 (m, 1P; P3), –70.9 (m, 1P; P7), –92.3 (m, 1P; P4), –164.9 (t, 1P; P5), –182.4 (m, 1P; P6). $^{13}C\{^1H\}$ NMR (125.8 MHz, d_5-pyridine, 298 K): δ (ppm) 69.4 (15-crown-5), 16.0 ($[(P_7)_2Ge_2N(SiMe_3)_2]^{3-}$). ^{29}Si NMR (99.32 MHz, d_5-pyridine): δ (ppm) 2.5 (s, $[(P_7)_2Ge_2N(SiMe_3)_2]^{3-}$). ESI-MS (negative ion mode) (DMF): *m/z* 216.5 (100%) $[P_7]^-$, 291.6 (99%) $[P_7Ge]^-$, 741.3 (70%) $[(P_7)_2Ge_2N(SiMe_3)_2]^-$.

7.2.7 Compounds discussed in Chapter five

7.2.7.1 $[K(2,2,2\text{-crypt})][CpV(\eta^5\text{-}P_5)]$ (11)

$[K(18\text{-crown-}6)]_3[P_7]$ (150 mg, 0.133 mmol) and VCp_2 (17 mg, .094 mmol) were stirred in pyridine (5 mL) for 1 h giving rise to a dark brown solution. All volatiles were removed

under reduced pressure to leave a brown oil, which was washed with diethyl ether (10 mL) with sonication to leave a brown powder. The product was extracted into THF (5 mL) and 2,2,2-crypt (75 mg, 0.199 mmol) was added while the reaction mixture was stirred for further 20 min. The resulting solution was filtered into a crystallisation ampoule and layered with hexane. After 3 days at –35 ºC days dark brown block-like crystals of [K(2,2,2-crypt)][CpV(η^5-P_5)] suitable for X-ray diffraction were obtained. Yield: 45 mg (35%). ESI-MS (negative ion mode) (DMF): *m/z* 270.9 $[CpVP_5]^-$. ESI-MS (positive ion mode) (DMF): *m/z* 1100.8 $\{[K(2,2,2\text{-crypt})]_3[CpVP_5]\}^+$. Cyclic voltammogram recorded at a silver electrode on DMF solution containing [K(2,2,2-crypt)][CpV(η^5-P_5)] (1.2×10^{-3} mol/dm^3); supporting electrolyte $[Bu_4N][PF_6]$ (0.2 mol dm^3); scan rate 1 V/s; Ferrocene as reference. No elemental analysis could be obtained for this species.

7.2.7.2 [K(2,2,2-crypt)][$(CpV)_2(\eta^6$-$P_6)$]·2THF (12)

$[K(18\text{-crown-}6)]_3[P_7]$ (200 mg, 0.177 mmol) and VCp_2 (80 mg, 0.44 mmol) were stirred in pyridine (5 mL) for 1 h giving rise to a dark brown solution. All volatiles were removed under reduced pressure to leave a brown oil, which was washed with hexane (10 mL) and diethylether (10 mL) with sonication to leave a brown powder. This was extracted into THF (5 mL) and 2,2,2-crypt (133 mg, 0.32 mmol) was added. The mixture was stirred for 20 min and then was filtered into a crystallisation ampoule and layered with hexane. After 3 days at –35 ºC dark brown block-like crystals of [K(2,2,2-crypt)][$(CpV)_2(\eta^6$-$P_6)$]·2THF suitable for X-ray diffraction were obtained. Yield 102 mg (51%). ESI-MS (negative ion mode) (DMF): *m/z* 417.9 $[(CpV)_2P_6]^-$. ESI-MS (positive ion mode) (DMF): *m/z* 1249.3 $\{[K(2,2,2\text{-crypt})]_3[(CpV)_2P_6]\}^+$. Cyclic voltammogram recorded at a silver electrode on DMF solution containing [K(2,2,2-crypt)][$(CpV)_2(\eta^6$-$P_6)$]·2THF (1.2×10^{-3} mol/dm^3);

supporting electrolyte $[Bu_4N][PF_6]$ (0.2 mol dm^3); scan rate 5 V/s; Ferrocene as reference. No elemental analysis could be obtained for this species.

7.2.7.3 $[K(2,2,2\text{-crypt})]_2[CpV(\eta^5\text{-}As_5)]$ (13)

K_3As_7 (150 mg, 0.23 mmol) and 18-crown-6 (185 mg, 0.69 mmol) were stirred in pyridine (4 mL) for 30 min. VCp_2 (30 mg, 0.16 mmol) was added slowly to the pyridine solution and the mixture was stirred for 1 h. All volatiles were removed under reduced pressure affording a brown oil which was washed with diethyl ether (10 mL) with sonication to leave a brown powder. The solid was dissolved in a mixture of pyridine (2 mL) and THF (2 mL) and 2,2,2-crypt (219 mg, 0.58 mmol) was added. The mixture was stirred for 20 min and then filtered into a crystallisation ampoule and layered with hexane. After 3 days at –35 ºC dark brown block-like crystals of $[K(2,2,2\text{-crypt})]_2[CpVAs_5]$ suitable for X-ray diffraction were obtained. Yield 110 mg (25%). ESI-MS (negative ion mode) (DMF): *m/z* 491.1 $[CpVAs_5]^-$. Cyclic voltammogram recorded at a silver electrode on THF solution containing $[K(2,2,2\text{-crypt})]_2[CpVAs_5]$ (1.2×10^{-3} mol/dm^3); supporting electrolyte $[Bu_4N][PF_6]$ (0.2 mol dm^3); scan rate 0.05 V/s; Ferrocene as reference. No elemental analysis could be obtained for this species.

7.2.7.4 $[K(2,2,2\text{-crypt})][(CpV)_2(\eta^5\text{-}As_5)]\cdot 2THF$ (14)

K_3As_7 (150 mg, 0.23 mmol), 18-crown-6 (185 mg, 0.70 mmol) and VCp_2 (100 mg, 0.58 mmol) were stirred in pyridine (5 mL) for 1 h giving rise to a dark brown solution. 2,2,2-crypt (175 mg, 0.46 mmol) was added and the mixture stirred for a further 20 min. All volatiles were removed under reduced pressure to leave a brown oil, which was washed with hexane (10 mL) and diethyl ether (10 mL) with sonication to leave a brown powder.

This was extracted into THF (5 mL), filtered into a crystallisation ampoule and layered with hexane. After 3 days at –35 ºC dark brown block-like crystals of [K(2,2,2-crypt)][$(CpV)_2(\eta^5\text{-}As_5)$]·2THF suitable for X-ray diffraction were obtained. Yield 311.3 mg (82%). ESI-MS (negative ion mode) (DMF): *m/z* 606.4 $[(CpV)_2As_5]^-$. ESI-MS (positive ion mode) (DMF): *m/z* 1438.6 $\{[K(2,2,2\text{-crypt})]_2[(CpV)_2As_5]^+$. Cyclic voltammogram recorded at a silver electrode on THF solution containing [K(2,2,2-crypt)][$(CpV)_2(\eta^5\text{-}As_5)$]·2THF (1.2 × 10–3 mol/$dm^3$); supporting electrolyte $[Bu_4N][PF_6]$ (0.2 mol dm3); scan rate 0.05 V/s; Ferrocene as reference. No elemental analysis could be obtained for this species.

7.3 Characterisation techniques

7.3.1 Single Crystal X-Ray diffraction

Crystals were mounted on micro-mount loops using Paratone-N oil and cooled to 150 K using an Oxford Cryosystems open flow N_2 cooling device.[11] Data were collected using mirror monochromated Cu Kα radiation (λ = 1.5418 Å) and processed using the CrysAlisPro package, including unit cell parameter refinement and interframe scaling (which was carried out using SCALE3 ABSPACK within CrysAlisPro).[12] Equivalent reflections were merged, and the images were processed using the CrysAlisPro suite. Corrections for Lorentz-polarisation effects were performed, and the structures were solved by direct methods and refined on F^2 using the SHELX 97-2 package.[13–15]

Single crystal diffraction data for the $[K(2,2,2\text{-crypt})]^+$ salts of **11**–**14** and the $[K(18\text{-crown-6})]^+$ salts of **7** and **8** were collected on an Enraf-Nonius Kappa CCD diffractometer and a 95 mm CCD detector. Data were collected using graphite monochromated Mo Kα

radiation (λ = 0.71073 Å), equivalent reflections were merged, and the images were processed using the DENZO and SCALEPACK programs.[16]

Single crystal diffraction data for the $[K(2,2,2\text{-crypt})]^+$ salts of **1, 2, 5** and **6** and the $[K(15\text{-crown-}5)_2]^+$ salts of **10** were collected on an Oxford Diffraction Supernova dual-source diffractometer equipped with a 135 mm Atlas CCD area detector.

7.3.2 Electrospray Ionisation Mass Spectrometry

Positive and negative ion mode electrospray mass spectra were recorded from DMF solutions (10-20 μM) on a Waters LCT mass spectrometer with a Z-spray source (150 °C source temperature, 200 °C desolvation temperature, 3.2 kV capillary voltage and 25 V cone voltage). The samples were introduced directly using a 1 mL SGE syringe and a syringe pump at 60 μL per minute.

7.3.3 NMR spectroscopy

^{31}P, ^{13}C, ^{1}H, ^{119}Sn and ^{29}Si spectra were recorded from d_5-pyridine solutions using a Bruker Avance III HD Nanobay 400 MHz spectrometer or a Bruker Avance III 500 MHz spectrometer. ^{1}H spectra were referenced to the most downfield residual protic solvent resonance (pyridine: δ = 8.74 ppm). ^{13}C spectra were referenced to d_5-pyridine (δ = 150.35 ppm). ^{31}P spectra were externally referenced to 85% H_3PO_4 (δ = 0 ppm). ^{119}Sn spectra were externally referenced to $SnMe_4$ (δ = 149.2 ppm), and ^{29}Si spectra were externally referenced to $SiMe_4$ (δ = 79.5 ppm). When provided, numbering of nuclei is identical to that in the crystal structure. ^{31}P NMR simulations were carried out using the gNMR software suite.

7.3.4 Elemental Analysis

Elemental analyses were carried out by Elemental Microanalysis Ltd. Samples (approximately 5 mg) were submitted in sealed Pyrex ampoules under vacuum.

7.3.5 DFT calculations

7.3.5.1 $[K(2,2,2\text{-crypt})]_3[Sn_9ZnNSiMe_3]\cdot 3tol$ (2) and $[K(2,2,2\text{-crypt})]_3[Ge_9ZnN(SiMe_3)_2]\cdot 3tol$ (1)

All calculations were carried out using Amsterdam Density Functional 2014.01 (ADF) by Michael Connolly and Professor John McGrady. Geometries were fully optimised without imposing any symmetry constraints (**C**$_1$symmetry) unless otherwise specified. All quantum chemical results were visualised using the Chemcraft 1.7 software or ADF GUI. Computational geometries were optimised at the TZVP level of basis set for all atoms. The local density approximation (LDA) was used with a generalised gradient approximation (GGA) through the exchange and correlation functional of Becke (BP86). Relativistic effects were treated using scalar coupling in the Zeroth Order Regular Approximation (ZORA). Vibrational modes were calculated using the frequencies software in the ADF suite of programs using the same level of calculation as in the geometry optimisations, and were used to identify the structures as minima. The effects of solvent were modelled using the conductor like screening model (COSMO) as implemented by the ADF software, and were used in the geometry optimisations of the two functionalised clusters.

7.3.5.2 $[K(2,2,2\text{-crypt})]_3[[Ru@Ge_{12}]\cdot 4py$ (5)

All calculations were performed with the Amsterdam Density Functional package (ADF2012.01) by Jack Duckworth and Prof. John McGrady (University of Oxford).[17–19] A TZ2P Slater-type basis set of triple-ζ quality, extended with two polarisation functions, was used to describe all transition metal elements (Ru, Mn, Ni) as well as the Group 14 elements (E = Ge, Pb). Electrons in orbitals up to and including 2p for the 1st row transition metals, 3p on Ge, 3d on Ru and 5d on Pb were considered part of the core and treated in accordance with the frozen core approximation (M.2p, Ge.3p, Ru.3d, Pb.5d). All calculations employed the Local Density Approximation (LDA) to the exchange potential,[20] along with the local exchange-correlation potential of Vosko, Wilk and Nusair (VWN)[21] and gradient corrections to non-local exchange and correlation proposed by Becke and Perdew BP86).[21,22] All calculations were unrestricted. Relativistic effects were incorporated using the Zeroth Order Relativistic Approximation (ZORA).[23–25] The confining effect of cations in the crystal lattice was modelled by surrounding the clusters with a continuum dielectric model (COSMO).[26] The chosen dielectric constant ε = 78.4 corresponds to that of water although structural parameters are not strongly dependent on this choice. All structures were optimised using the gradient algorithm of Versluis and Ziegler.[27]

The calculations for the icosahedral structures merit a brief comment as ADF does not support I_h point symmetry. The calculations were therefore performed using a sub-group of I_h (D_{5d}) with all M–E bonds constrained to be equal and all E–M–E angles fixed at 63.43°. Moreover, the d electrons (8, 9 and 10 in $[Mn@Pb_{12}]^{3-}$, $[Ru@Ge_{12}]^{3-}$ and $[Ni@Pb_{12}]^{2-}$, respectively) were distributed evenly over the corresponding representations in D_{5d} symmetry (e_{1g}, e_{2g} and a_{1g}). This leads to fractional occupations in the first two cases.

7.3.5.3 $[K(2,2,2\text{-crypt})]_4[Co_2@Ge_{16}]\cdot 2en$ (6)

All calculations were performed with the Amsterdam Density Functional package (ADF2013.02) by Prof. John McGrady's group.[17–19] A Slater-type basis set of triple-ζ quality, extended with one polarisation function (TZP), was used to describe all transition metals and a DZP basis was used for silicon and germanium. Electrons in orbitals up to and including 2p and 3p for first and second row transition metals, respectively were considered part of the core and treated in accordance with the frozen core approximation. Likewise, orbitals up to 2p and 3d on slicon and germanium, respectively, were considered as core. All calculations employed the non-local exchange and correlation functional proposed by Becke and Perdew (BP86).[21,22] For the anionic species, a continuum dielectric salvation model (COSMO) with ε = 78.4 was imposed. All structures were optimised using the gradient algorithm of Versluis and Ziegler.[26,27]

7.1.1.1.1 $[K(18\text{-crown-6})]_2[P_7EN(SiMe_3)_2]\cdot 2py$ (E = Ge (7), Sn (8), Pb (9)) and $[K(15\text{-crown-5})_2]_3[(P_7)_2Ge_2N(SiMe_3)_2]$ (10)

All geometry optimisations were performed using the Amsterdam Density Functional package (ADF2013.01).[17–19] An all-electron TZ2P Slater-type basis set of triple-ζ quality, extended with two polarisation functions, was used to describe all atoms (ATZ2P). All calculations employed the Local Density Approximation (LDA) to the exchange potential,[20] along with the local exchange-correlation potential of Vosko, Wilk and Nusair (VWN)[28] and gradient corrections to non-local exchange and correlation proposed by Becke and Perdew (BP86).[21,22] Relativistic effects were incorporated using the Zeroth Order Relativistic Approximation (ZORA).[23,24,29] A continuum dielectric to model solvation was employed using COSMO.[26] The chosen dielectric constant ε = 78.4 corresponds to that of

ammonia, although structural parameters are not strongly dependent on this choice. All structures were optimized using the gradient algorithm of Versluis and Ziegler.[27]

7.1.1.1.2 [K(2,2,2-crypt)][$(CpV)_2(\eta^6\text{-}P_6)$]·2THF (12)

All calculations of the gas-phase electronic structure were performed using the Amsterdam Density Functional package ADF2013 package. A double-ζ Slater-type basis set, extended with a single polarization function (DZP) was used to describe carbon and hydrogen, while vanadium and phosphorus were modelled with a triple-ζ basis set with a single polarisation function (TZP). B3LYP functional was employed for the optimisation.

7.3.6 EPR

CW-EPR spectra were collected in the Centre for Advanced Electron Spin Resonance (CAESR) in the Inorganic Chemistry Laboratory at the University of Oxford. X-band measurements performed with a Bruker-Biospin EMXplus spectrometer equipped with a Premium X microwave bridge, a cylindrical TE011-mode resonator (SHQE-W), an ESR-900 liquid helium cryostat, and an ITC-503s temperature controller (Oxford Instruments). CW-EPR measurements at W-band were performed on a Bruker EleXsys E680 pulsed/CW-EPR spectrometer. Custom simulation scripts were written in MatLab™ to make use of matrix diagonalisation functions of the EasySpin EPR software package.[30]

7.3.7 Cyclic Voltammetry

Electrochemical measurements were performed within a Saffron Omega Scientific glovebox under anhydrous Nitrogen on a PARAMETEK® VersaSTAT 3 potentiostat. Cyclic voltammetry measurements were carried out as outlined in the literature, with a silver quasi-reference electrode, a glassy-carbon working electrode and a platinum auxiliary electrode, all sourced from Bioanalytical Systems®. The supporting electrolyte for the measurements was a 0.2 M solution of tetrabutylammonium hexafluorophosphate. The quasi-reference electrode was immersed in the electrolyte solution for 48 h prior to the experiment and ferrocene (Fc/Fc^+) was used as an internal references.

7.4 References

(1) Von Schnering, H. G.; Baitinger, M.; Bolle, U.; Carrillo-Cabrera, W.; Curda, J.; Grin, Y.; Heinemann, F.; Llanos, J.; Peters, K.; Schmeding, A.; Somer, M. *Z. Anorg. Allg. Chem.* **1997**, *623* (7), 1037–1039.

(2) Hoch, C.; Wendorff, M.; Rohr, C.,. *Acta Crystallogr. Sect. C-Cryst. Struct. Commun.* **2002**, *58*, I45.

(3) Santandrea, R. P.;Mensing, C.; von Schnering, H.G. *Thermochim. Acta* **1986**, *98*, 301–311.

(4) Emmerling, F.; Rohr, C. *Z. Naturforsch. 57 b* **2002**, 963–975.

(5) Cowley, A. H. *Inorganic Syntheses*; John Wiley & Sons, 2009.

(6) MacFarlane, K. S.; Rettig, S. J.; Liu, Z.; James, B. R. *J. Organomet. Chem.* **1998**, *557* (2), 213–219.

(7) Genêt, J. P.; Pinel, C.; Ratovelomanana-Vidal, V.; Mallart, S.; Pfister, X.; De Andrade, M. C. C.; Laffitte, J. A. *Tetrahedron Asymmetry* **1994**, *5* (4), 665–674.

(8) Chatt, J.; Shaw, B. L. *J. Chem. Soc. Resumed* **1961**, No. 0, 285–290.

(9) Chorley, R. W.; Hitchcock, P. B.; Lappert, M. F.; Leung, W.-P.; Power, P. P.; Olmstead, M. M. *Inorg. Chim. Acta* **1992**, *198–200*, 203–209.

(10) Turbervill, R. S. P.; Goicoechea, J. M. *Organometallics* **2012**, *31* (6), 2452–2462.

(11) Cosier, J.; Glazer, A. M. *J. Appl. Crystallogr.* **1986**, *19* (2), 105–107.

(12) *CrysAlisPro 1.171.35.8; Agilent Technologies, Yarnton, Oxfordshire, 2011.*

(13) Sheldrick, G. M. *Acta Crystallogr. A* **1990**, *46* (6), 467–473.

(14) Sheldrick, G. M. *Acta Crystallogr. A* **2008**, *64* (1), 112–122.

(15) *Sheldrick, G. M. SHELX97 - Programs for Crystal Structure Analysis 7.2; University of Gottingen, Germany, 1998.*

(16) Otwinowski, Z.; Minor, W. In *Processing of X-ray Diffraction Data Collected in Oscillation Mode*; Academic Press: New York, 1997.

(17) Guerra, C. F.; Snijders, J. G.; Velde, G. te; Baerends, E. J. *Theor. Chem. Acc.* **1998**, *99* (6), 391–403.

(18) Te Velde, G.; Bickelhaupt, F. M.; Baerends, E. J.; Fonseca Guerra, C.; van Gisbergen, S. J. A.; Snijders, J. G.; Ziegler, T. *J. Comput. Chem.* **2001**, *22* (9), 931–967.

(19) ADF2010, E. J. Baerends et. al. *SCM, Theoretical Chemistry, Vrije Universiteit,*; Amsterdam, The Netherlands,.

(20) Parr, R. G.; Yang, W. *Density Functional Theory of Atoms and Molecules Oxford*; Oxford University Press: Oxford, 1989.

(21) Becke, A. D. *Phys. Rev. A* **1988**, *38* (6), 3098–3100.

(22) Perdew, J. P. *Phys. Rev. B* **1986**, *33* (12), 8822–8824.

(23) Lenthe, E. van; Baerends, E. J.; Snijders, J. G. *J. Chem. Phys.* **1993**, *99* (6), 4597–4610.

(24) Lenthe, E. van; Baerends, E. J.; Snijders, J. G. *J. Chem. Phys.* **1994**, *101* (11), 9783–9792.

(25) Lenthe, E. van; Ehlers, A.; Baerends, E.-J. *J. Chem. Phys.* **1999**, *110* (18), 8943–8953.

(26) Klamt, A.; Schüürmann, G. *J. Chem. Soc. Perkin Trans. 2* **1993**, No. 5, 799–805.

(27) Versluis, L.; Ziegler, T. *J. Chem. Phys.* **1988**, *88* (1), 322–328.

(28) Vosko, S. H.; Wilk, L.; Nusair, M. *Can. J. Phys.* **1980**, *58* (8), 1200–1211.

(29) Lenthe, E. van; Ehlers, A.; Baerends, E.-J. *J. Chem. Phys.* **1999**, *110* (18), 8943–8953.

(30) Stoll, S.; Schweiger, A. *J. Magn. Reson.* **2006**, *178* (1), 42–55.

Appendix I Selected data collection and refinement parameters

Compound	**[K(2,2,2-crypt)]$_3$[Ge$_9$ZnN(Si(Me$_3$)$_2$)$_2$]·3tol (1)**	**[K(2,2,2-crypt)]$_3$[Sn$_9$ZnNSiMe$_3$]·3tol (2)**
Chemical formula	$C_{81}H_{150}Ge_9K_3N_7O_{18}Si_2Zn$	$C_{78}H_{141}K_3N_7O_{18}SiSn_9Zn$
Formula weight (g mol^{-1})	2402.24	2743.94
Temperature (K)	150	150
Crystal system	Triclinic	Triclinic
Space group	*P*–1	*P*–1
a (Å)	14.1476(3)	14.54430(10)
b (Å)	15.3700(3)	15.58710(10)
c (Å)	26.9871(7)	25.7435(2)
α (°)	79.809(2)	77.30(3)
β (°)	74.984(2)	82.67(3)
γ (°)	71.566(2)	71.77(3)
Volume (Å^3)	5348.1(2)	5396.5(11)
Cell formula units, Z	2	2
ρ calcd (g/cm^3)	1.492	1.689
Radiation, λ (Å)	Cu Kα (1.54180)	MoK\α (0.71073)
μ (mm^{-1})	4.794	2.447
No. parameters refined	1141	1216
Reflections collected	59761	34210
Independent reflections	22130	18832
R(int)	0.0433	0.0266
R_1/wR_2, $I \geq 2\sigma I$ (%)	4.46/11.11	7.53/19.07
R_1/wR_2, all data (%)	5.70/11.82	9.55/20.15
GOF	1.025	1.024
residual e– Å–3 max./min.	2.435/–1.137	4.623/–2.024

[a] $R_1 = [\sum||F_o| - |F_c||]/\sum|F_o|$; $wR_2 = \{[\sum w[(F_o)^2 - (F_c)^2]^2]/[\sum w(F_o^2)^2]\}^{1/2}$; $w = [\sigma^2(F_o)^2 + (AP)^2 + BP]^{-1}$, where $P = [(F_o)^2 + 2(F_c)^2]/3$ and the A and B values are 0.0480 and 9.7343 for [K(2,2,2-crypt)]$_3$[**1**]·3tol and 0.0881 and 59.8354 for [K(2,2,2-crypt)]$_3$ [**2**]·3tol.

Compound	**[K(2,2,2-crypt)]$_3$ [Ru@Ge$_{12}$] ·4py (5)**	**[K(18-crown-6)]$_2$ [P$_7$GeN(SiMe$_3$)$_2$]·2py (7)**
Chemical formula	$C_{74}H_{128}Ge_{12}K_3N_{10}O_{18}Ru$	1214.79
Formula weight (g mol^{-1})	2535.31	$C_{40}H_{76}GeK_2N_3O_{12}P_7Si_2$
Temperature (K)	150	150(2)
Crystal system	monoclinic	triclinic
Space group	$P2_1$	P–1
a (Å)	14.1424(1)	13.0810(2)
b (Å)	26.0428(2)	15.6526(3)
c (Å)	14.2684(1)	15.7164(3)
α (°)	90.00	87.7490(10)
β (°)	107.754(1)	72.7480(10)
γ (°)	90.00	77.0530(10)
Volume (Å^3)	5004.88(6)	2993.78(10)
Cell formula units, Z	2	2
ρ calcd (g cm^{-3})	1.682	1.348
Radiation, λ (Å)	Cu Kα (1.54180)	MoK\α (0.71073)
μ (mm^{-1})	6.790	0.930
No. parameters refined	1052	791
Reflections collected	51928	23615
Independent reflections	19737	13670
R(int)	0.0467	0.0215
R_1/wR_2, $I \geq 2\sigma I$ (%)	5.74/15.52	3.93/9.55
R_1/wR_2, all data (%)	6.15/16.21	5.76/10.57
GOF	1.022	1.006
residual e– Å–3 max./min.	1.478/–0.469	0.963/–0.581

[a] $R_1 = [\sum||F_o| - |F_c||]/\sum|F_o|$; $wR_2 = \{[\sum w[(F_o)^2 - (F_c)^2]^2]/[\sum w(F_o^2)^2]\}^{1/2}$; $w = [\sigma^2(F_o)^2 + (AP)^2 + BP]^{-1}$, where $P = [(F_o)^2 + 2(F_c)^2]/3$ and the A and B values are 0.1120 and 3.43 for [K(2,2,2-crypt)]$_3$[**5**]·4py and 0.0526 and 1.2658 for [K(18-crown-6)]$_2$[**7**]·2py

Compound	**[K(18-crown-6)]$_2$ [$P_7SnN(SiMe_3)_2$]·2tol (8)**	**[K(2,2,2-crypt)] [$CpV(\eta^5\text{-}P_5)$] (11)**
Chemical formula	$C_{42}H_{79}K_2N_2O_{12}P_7Si_2Sn$	$C_{23}H_{41}N_2O_6P_5V$
Formula weight (g mol^{-1})	1273.93	686.47
Temperature (K)	150(2)	150(2)
Crystal system	Triclinic	triclinic
Space group	*P*–1	*P*–1
a (Å)	13.1078(2)	13.2162(2)
b (Å)	15.7005(2)	14.8467(3)
c (Å)	15.9468(3)	16.9167(3)
α (°)	88.9580(10)	103.8270(10)
β (°)	72.6670(10)	92.3980(10)
γ (°)	77.3110(10)	90.6500(10)
Volume (Å^3)	3052.36(9)	3219.55(10)
Cell formula units, Z	2	4
ρ calcd (g/cm^3)	1.386	1.416
Radiation, λ (Å)	MoK\α (0.71073)	MoK\α (0.71073)
μ (mm^{-1})	0.830	0.724
No. parameters refined	699	685
Reflections collected	23003	24857
Independent reflections	13918	14658
R(int)	0.0272	0.452
R_1/wR_2, $I \geq 2\sigma I$ (%)	4.47/9.97	4.77/10.35
R_1/wR_2, all data (%)	7.22/11.19	10.07/12.59
GOF	1.022	1.027
residual e– Å–3 max./min.	0.722/–0.891	0.462/–0.502

[a] $R_1 = [\sum||F_o| - |F_c||]/\sum|F_o|$; $wR_2 = \{[\sum w[(F_o)^2 - (F_c)^2]^2]/[\sum w(F_o^2)^2]\}^{1/2}$; $w = [\sigma^2(F_o)^2 + (AP)^2 + BP]^{-1}$, where $P = [(F_o)^2 + 2(F_c)^2]/3$ and the A and B values are 0.0431 and 2.7326 for [K(18-crown-6)]$_2$[8]·2tol and 0.0542 and 0.0000 for [K(2,2,2-crypt)][11].

	[K(2,2,2-crypt)] [(CpV)$_2$(η^6-P$_6$)]·2THF (12)	**[K(2,2,2-crypt)]$_2$ [CpV(η^5-As$_5$)] (13)**
Chemical formula	C36 H62 K N2 O8 P6 V2	$C_{41}H_{77}As_5K_2N_4O_{12}V$
Formula weight (g mol^{-1})	977.68	1321.81
Temperature (K)	150(2)	150(2)
Crystal system	triclinic	Tricinic
Space group	*P*–1	*P*–1
a (Å)	10.53900(10)	11.1452(2)
b (Å)	11.48520(10)	11.7975(2)
c (Å)	21.3999(3)	20.5463(4)
α (°)	93.5980(10)	91.1960(10)
β (°)	102.8100(10)	91.5560(10)
γ (°)	114.3570(10)	92.3440(10)
Volume (Å^3)	2266.08(4)	2697.63(8)
Cell formula units, Z	2	2
ρ calcd (g/cm^3)	1.433	1.627
Radiation, λ (Å)	MoK\α (0.71073))	MoK\α (0.71073)
μ (mm^{-1})	0.764	3.439
No. parameters refined	496	586
Reflections collected	35193	47520
Independent reflections	10322	12326
R(int)	0.0325	0.1032
R_1/wR_2, $I \geq 2\sigma I$ (%)	3.21/7.51	4.83/10.85
R_1/wR_2, all data (%)	4.73/8.07	9.27/12.51
GOF	1.052	0.964
residual e– Å–3 max./min.	0.425/–0.345	0.974/–0.893

[a] $R_1 = [\sum||F_o| - |F_c||]/\sum|F_o|$; $wR_2 = \{[\sum w[(F_o)^2 - (F_c)^2]^2]/[\sum w(F_o^2)^2]\}^{1/2}$; $w = [\sigma^2(F_o)^2 + (AP)^2 + BP]^{-1}$, where $P = [(F_o)^2 + 2(F_c)^2]/3$ and the A and B values are 0.0356 and 0.4805 for [K(2,2,2-crypt)]**12**]·2THF and 0.0632 and 0.0000 for [K(2,2,2-crypt)]$_2$[**13**].

Compound	**[K(2,2,2-crypt)] [$(CpV)_2(\eta^5\text{-}As_5)$]·2THF (14)**
Chemical formula	$C_{30}H_{50}As_5KN_2O_{6.50}V_2$
Formula weight (g mol^{-1})	1058.30
Temperature (K)	150(2)
Crystal system	triclinic
Space group	*P* –1
a (Å)	13.5024(2)
b (Å)	14.9949(2)
c (Å)	20.7654(3)
α (°)	81.7130(10)
β (°)	75.8820(10)
γ (°)	78.5790(10)
Volume ($Å^3$)	3976.23(10)
Cell formula units, Z	4
ρ calcd (g/cm^3)	1.768
Radiation, λ (Å)	MoK\α (0.71073)
μ (mm^{-1})	4.746
No. parameters refined	883
Reflections collected	67817
Independent reflections	17991
R(int)	0.0887
R_1/wR_2, $I \geq 2\sigma I$ (%)	4.87/11.26
R_1/wR_2, all data (%)	8.17/12.77
GOF	0.997
residual e– Å–3 max./min.	0.986/–1.410

[a] $R_1 = [\sum||F_o| - |F_c||]/\sum|F_o|$; $wR_2 = \{[\sum w[(F_o)^2 - (F_c)^2]^2]/[\sum w(F_o^2)^2]\}^{1/2}$; $w = [\sigma^2(F_o)^2 + (AP)^2 + BP]^{-1}$, where $P = [(F_o)^2 + 2(F_c)^2]/3$ and the A and B values are 0.0700 and 0.0000 for [K(2,2,2-crypt)][**14**]·2THF.

Appendix II

Number	Formula	Structure
1	$[Ge_9ZnN(Si(Me_3)_2]^{3-}$	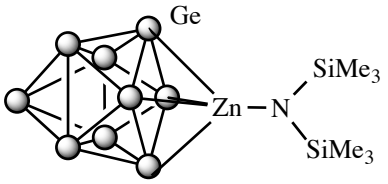
2	$[Sn_9ZnNSiMe_3]^{3-}$	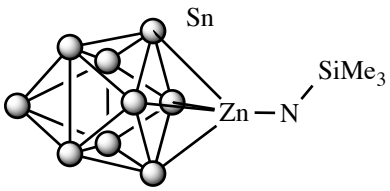
3	$[Ge_9ZnNSiMe_3]^{4-}$	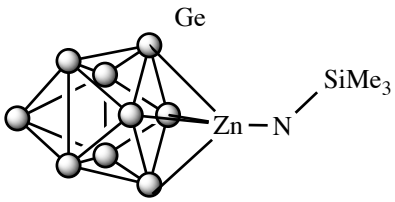
4	$[Ge_9ZnNPh_2]^{3-}$	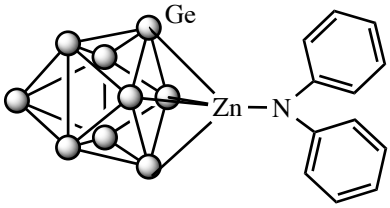
5	$[Ru@Ge_{12}]^{3-}$	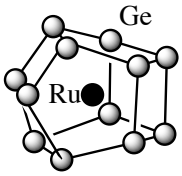

6 $[Co_2@Ge_{16}]^{4-}$

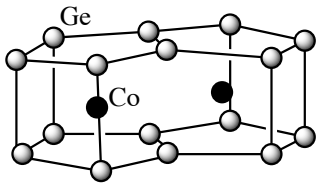

7 $[P_7GeN(SiMe_3)_2]^{2-}$

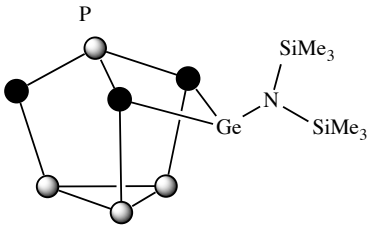

8 $[P_7SnN(SiMe_3)_2]^{2-}$

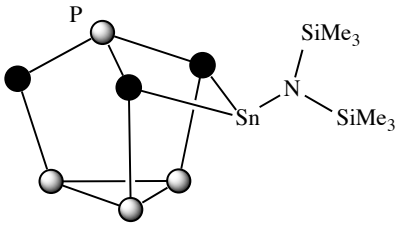

9 $[P_7Pb(N(SiMe_3)_2]^{2-}$

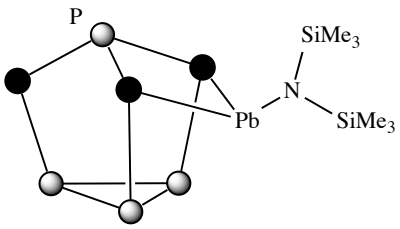

10 $[(P_7)_2Ge_2N(SiMe_3)_2]^{3-}$

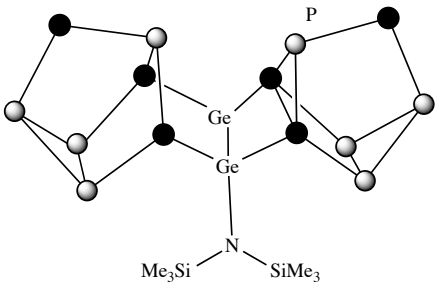

11	$[CpV(\eta^5\text{-}P_5)]^-$	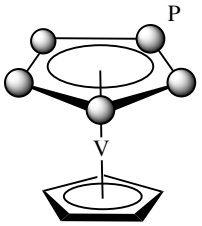
12	$[(CpV)_2(\eta^6\text{-}P_6)]^-$	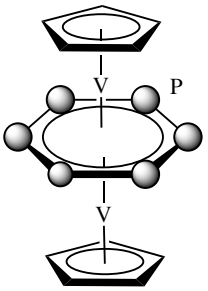
13	$[CpV(\eta^5\text{-}As_5)]^{2-}$	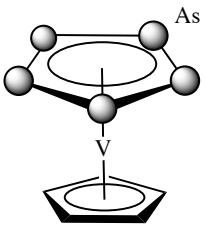
14	$[(CpV)_2(\eta^5\text{-}As_5)]^-$